Novel dilute nitride semiconductor materials for mid-infrared applications

by

Aurélien Maxime Renaud Godenir

M.Sc. in Optoelectronics Engineering

M.Sc. in Telecommunications

A thesis submitted in part fulfilment for the degree of
Doctor of Philosophy at the University of Lancaster

No part of this thesis has been or is being submitted
to any other university or other academic institution

July 2008

"*Only the curious have something to find*"

Sean Watkins

To Jola, for her love and patience,

To my family, for their unfailing support,

To the dear ones I have lost,

To the friends I have made.

Novel dilute nitride semiconductor materials for mid-infrared applications

by

Aurélien Maxime Renaud Godenir

M.Sc. in Optoelectronics Engineering

M.Sc. in Telecommunications

Abstract

A new approach to room temperature mid-infrared applications in the 3 - 5 μm spectral range has been proposed through the development of novel dilute nitride materials. InAsN shows a large bandgap reduction with a small lattice mismatch when a small amount of nitrogen is introduced into the host InAs. Because the InAsN reported so far had generally poor crystalline quality and exhibited weak luminescence that quenched far below room temperature due to poorly understood localised states, the present thesis investigated the optimisation of the MBE growth of InAsN. The nitrogen incorporation was shown to be inversely dependent on the growth temperature, the growth rate and the arsenic flux, as was interpreted by a kinetic model. Luminescence from InAsN material showed two peaks, originating in bandgap- and localised state-related transitions. The emission related to the bandgap undergoes hardly any energy shift with increasing laser excitation power while it redshifts with increasing temperature. The emission from the localised states

blueshifts with increasing laser excitation power and temperature. Rapid thermal annealing on InAsN layers improved the photoluminescence intensity and blueshifted the transition energy.

InAsN was successfully grown with high crystalline quality. It showed strong photoluminescence which persisted up to room temperature with a reduced influence of the localised states and wavelength up to 4.5 μm was achieved when 2.5 % N were incorporated. An explanation of the temperature and nitrogen incorporation dependences of the InAsN bandgap was successfully proposed using Varshni's equation and an adapted band anticrossing model, where the nitrogen level energy is dependent on temperature and nitrogen composition. The crystalline quality and luminescence were both further improved by incorporating antimony into InAsN and strain balance in material for 4.2 μm applications was achieved with the novel InAsNSb alloy. A method to determine the composition of the quaternary was derived from bandgap models and lattice constant equation and the addition of antimony in InAsN was shown to enhance the nitrogen incorporation in InAsNSb. Finally, attempts at prototype InAsN and InAsNSb devices were reported, InAsNSb LEDs were demonstrated and electroluminescence from InAsNSb diodes at 3.88 μm at 4 K was obtained.

Major technical conclusions

Nitrogen incorporation in InAsN :

	Achievable nitrogen composition ([N])	Growth temperature (T_g) (°C)	Growth rate ($g.r$) (µm/h)	As flux	RF power (W) / N flux (mbar)
[N] increases with decreasing T_g	0.7 - 1.4 %	optimum : 380 - 400	1.0	As_{min}	160 / 5.5×10^{-7}
[N] increases with decreasing *g.r.*	0.3 - 0.8 %	420	optimum : 0.3 - 0.5	As_{min}	210 / 5.2×10^{-7}
[N] increases with decreasing As flux	0.4 %	420	1.0	optimum : As_{min}	210 / 5.3×10^{-7}
High nitrogen conditions	2.52 %	380	0.3	As_{min}	210 / 5.3×10^{-7}

Table summarising the MBE growth conditions for high material quality and high nitrogen incorporation in InAsN. As_{min} is the minimum arsenic flux defined in Section 4.1.4

Rapid thermal annealing of InAsN :

Typical nitrogen composition	Typical blueshift	Annealing temperature	Annealing time	Effect
0.95 %	19 meV	optimum : 600°C	optimum : 30 s	Homogenisation of the nitrogen profile

Table summarising the rapid thermal annealing conditions of InAsN epilayers

Effect of antimony incorporated into InAsN :

- improvement of InAsNSb material quality due to the surfactant effect of Sb
- control of the strain up to lattice matching to InAs for any nitrogen composition. For instance, a ratio of As / Sb = 169 when growing InAsNSb can balance the tensile strain observed in InAsN with 0.65 % N

- the addition of Sb increases the amount of N incorporated in InAsNSb relatively to that incorporated in InAsN grown under identical conditions

Materials for 4.2 µm wavelength :

	InAsN	InAsNSb
For low temperature applications	2.52 % N (A0156)	1.2 % N, 5.9 % Sb (A0209)
For room-temperature applications	1.6 % N (A0207)	0.9 % N, 2.9 % Sb (A0220)

Table summarising the nitrogen content and nitrogen and antimony contents in InAsN and InAsNSb respectively for 4.2 µm applications. Numbers into brackets are sample references

Acknowledgements

What does a Frenchman need when going to the United Kingdom ? Legs like a frog's to leap over the Channel, a good sense of (British) humour and self-derision to shine through the laughable weather, a heart as stout as a famous Irish beer and obviously good company. What will he will bring back from there ? Memories of great people. What I have achieved (a bit of novelty in physics told in a long story), I owe it to the people that I met during this three year stay in my Little Britain. *They* made me feel home in this diverse country. They made Lancaster a wonderful place to live, made milk tea a daily need and bitter an evening delicacy.

I would like to thank my supervisors, colleagues, friends and acquaintances who made this stay, anything but a Napoleonian exile on an island, an amazing experience indeed. Sincere thanks to Qian, for helping me, directing and supporting me, believing in me and trusting me. I do thank Prof. Krier, for his kind advice, his Olympian calm and his justified demands to help me achieve a meaningful research. No worthwhile days would have started without the smile of Carole and Pam, the cleaning ladies, the hellos from John and Richard (how available you have always been to any of my needs, thank you) and the sleepy faces of my workmates. A good crew over three years, and every year had its own vintage ! Many thanks to Gavin, my personal squash coach and then victim ; Matt, my fellow until the end of the earth (I mean, Scotland or Taiwan) ; Suleiman, a nonpareil specimen from Syria and the greatest one Medicine could ever study ; Peter, alias Mister B, thanks for reading the newspaper out loud, sharing a house with me and inculcating me British subtleties. For the "new" crew, that is when I became the eldest, thanks to Neil, always ready to

give a helping hand ; Pete, aka Mister C, the kindest and most learned Green Giant ; Nana, with a big heart and a bright smile ; Martin and Kieran, our promising newbies.

No technical progress could have been made possible or sustained without Graham, as fast as a Le Mans race car ; John, the most valuable player of the team, as he would be rated by the NBA ; Steve and Shonah, for giving such a human face to the electronics world ; Stuart, more than a legend, the incarnation of happiness in science ; Duncan, a brave heart and the pride of Scotland ; Andy, Peter, Ian and Tad, for their gold fingers in the workshop ; Stevee and Tim, without whom the Physics Department would not be standing. Thanks to Bob and Azzedine for their precious help in measurements and teaching, my warm greetings to Oleg for the interesting discussions. The research team gave me a lot, from ideas to advice, from one-liners to support, thanks to Susan, Valeryi, Min, Victor. National and international collaborations were fruitful thanks to their actors, I do thank Rob Airey and Geoff Hill for processing, Prof. Mark Hopkinson for the growth of MBE samples, Dr Hosea and Dr Tim Veal for scientific advice and Dr Khue Tian Lai for FTIR measurements. Warm greetings go to Prof. Lin at National Taiwan University, along with Jin Tsai and Da-Jung Ma, who made work a question of friendship.

The research resembled sometimes a montypythonesque quest for the Holy Grail. Nevertheless, I always found my way thanks to the support I have been given, in the Physics Department or through the hills of the Lake District, the green and orange peaks of Scotland or the sharp mountains of Wales. Cheers for making this experience an unforgettable memory !

Contents

Chapter 1. Introduction

Most of the current electronic devices are based on semiconductor materials. Optoelectronic applications in effective light emission/detection devices and high speed optical switches are mainly based on III-V compound materials. Gallium arsenide- and indium phosphide-based compounds are preferred to access the near-infrared window (0.8 μm - 2 μm), such as AlGaAs lasers (780 nm) in widely-used compact disc players and InGaAs/InP (1.55 μm) photodiodes in fibre optic telecommunications. Accessing the mid-infrared spectral range is of great technological interest because of the potential applications in ecological monitoring, remote sensing, absorption spectroscopy, free-space communications and medical applications.

Most of the important molecular gases, from methane to carbon monoxide, show strong absorption features in the mid-infrared spectral range, as shown in Figure 1.1. For example, carbon dioxide has strong absorption features in the 3 - 5 μm spectral range. The effects of greenhouse gases on climate change is a matter of concern for the public and industry nowadays and carbon dioxide (CO_2), reckoned to be a major contributor, is released from the combustion of carbonaceous fuels and is a by-product of sodium phosphate, used in the manufacture of food additives, chemicals and medicines. Monitoring CO_2 from car exhausts or factory chimneys has become of vital importance for the protection of the environment. Recent medical research has shown that measuring the isotope ratio of $^{13}CO_2/^{12}CO_2$ around 4.3 μm can be used in early detection of ulcers. In 1998, gas detectors represented already 1.6 % of the sales of sensors in Japan and CO_2 detectors are undoubtedly already part of a major market for air-quality sensors in towns, factories and houses [1].

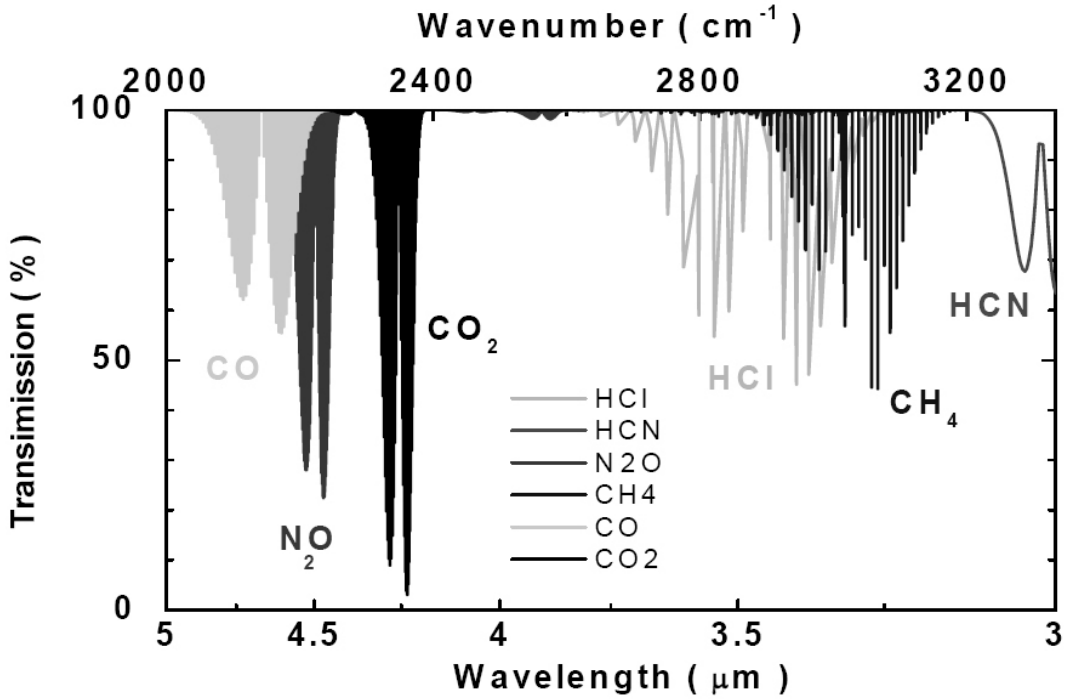

Figure 1.1 Absorption spectra of common gases in the mid-infrared spectral range [2]

A typical infrared gas sensor unit is shown in Figure 1.2. Light at a specific wavelength of interest is shone through a gas to be monitored and consequently absorbed. The decrease in the light intensity is measured by a detector at the end of the optical path. Using Beer-Lambert's law $I_{measured} = I_{source}\, 10^{-\alpha l C}$ where α is the absorption coefficient, l the path length and C the concentration of the gas, the latter can easily be computed from the light intensities at the source and detector (I_{source} and $I_{measured}$). Our interest is focused on a new approach to detectors for use in these gas sensing units. The leading technology in commercially available detectors uses pyroelectric detectors because they are cheap to produce. However, they are slow and suffer from low sensitivity. Photodetectors made of mercury cadmium telluride (HgCdTe) II-VI compound on cadmium zinc telluride (CdZnTe) substrates can be an alternative since the material can be tailored for detection at any region of the infrared spectrum with little lattice mismatch. Nevertheless, they tend to have a non-uniform response across the active region and suffer from high non-radiative processes. Their

operation wavelength is relatively sensitive to the temperature and their broad response is not suitable for *monochromatic* detection of a single gas. Moreover, they are fragile and are based on costly substrates, thus limiting large-scale production. The IV-VI compound PbSe was successfully developed for mid-infrared photoconductors but suffers from a high thermal expansion coefficient and slow response.

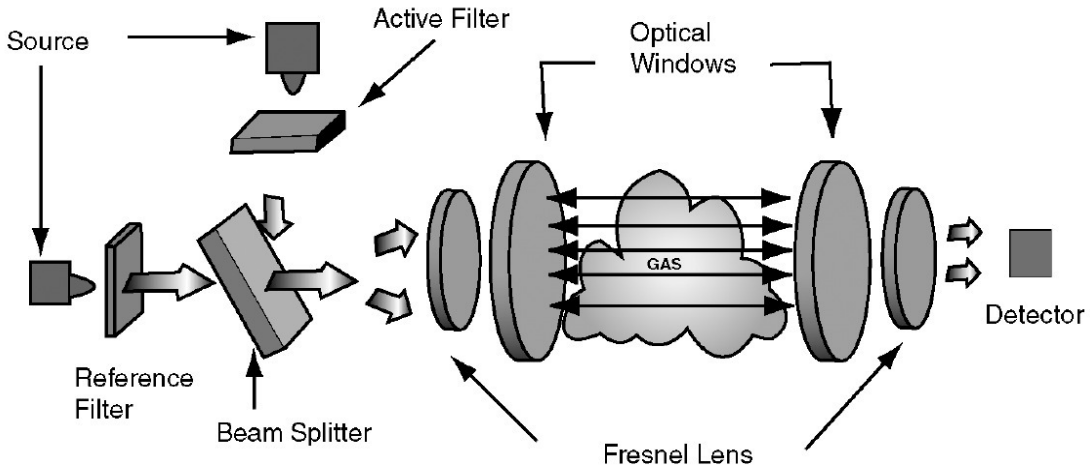

Figure 1.2 Architecture of a typical infrared gas sensor [3]

III-V compounds are promising materials and the engineering of these, grown by molecular beam epitaxy, shows prospects for improved device properties. InAs is particularly well-suited for the 3 - 5 μm range because of its bandgap energy around 0.354 eV (3.5 μm) at room temperature. InAsSb photodetectors can operate in the 3 - 5 μm spectral range at room temperature but the material suffers from high lattice mismatch when tailored for 4.2 μm wavelength. There is a need for another approach to mid-infrared sensing, which could be fulfilled by a new material. Progress in the mature technology for GaInNAs material showed that the introduction of nitrogen can cause a drastic reduction of the bandgap. By introducing a small amount of nitrogen into InAs, InAsN has the potential to be a robust novel material that can be tailored with a small lattice mismatch to InAs for the mid-infrared range. Addition of

antimony in InAsN could improve further the material quality and balance the strain. InAsN and InAsNSb could open the way to fast detectors with high current response.

The performances of current photodetectors for mid-infrared applications at room temperature are still far from theoretical limits despite the maturity in the technology employed. A new approach to room temperature photodetection of CO_2 at 4.2 μm is proposed through the development of a novel material InAsN, whose large bandgap reduction with the incorporation of a small amount of nitrogen into InAs and reduced lattice mismatch are promising assets. InAsN was first grown by MBE in 1995 and is still in its infancy. The work in this thesis aims at mastering the growth of InAsN, studying some of its properties and showing its potential for mid-infrared applications such as gas monitoring. The first chapter presents the fundamental concepts used throughout this thesis, from a crystallographic and electronic point of view, as well as device-oriented considerations. A literature review presents the technology in use in current infrared detectors, the state-of-the-art in InAsN and related dilute nitride materials and the (not so well) established growth conditions and postgrowth treatments. After a review of the experimental apparatus and procedures used for characterisation, the first part of this study focuses on the key parameters (growth temperature, growth rate, arsenic flux) controlling material quality and nitrogen incorporation in InAsN. The observed trends are explained by kinetic models. The second part of this work shows the potential of InAsN material for mid-infrared applications ; structural and electronic properties are studied. An enhanced model of the dependence of the bandgap with temperature and nitrogen content is proposed. The addition of antimony further improves InAsN material and InAsNSb alloys are demonstrated and developed. Finally, attempts at prototype InAsN and InAsNSb devices are reported and some further improvements are proposed.

Chapter 2. Theory and fundamental concepts

"*He who loves practice without theory is like the sailor who boards ship without a rudder and compass and never knows where he may cast.*"
Leonardo da Vinci

The progress of the last two decades in the growth of semiconductor materials allows nowadays the fabrication of electronic and optoelectronic devices for a wide range of applications : electronic and logic with integrated circuits, generation and detection of light, computing (and research teams are already working on all-optical computers), memory storage (flash memories and ever-increasing capacity hard drives), telecommunication. All these technologies are based on the mastering of the growth of high-quality materials with engineered properties. The following chapter highlights the crystal structure and condensed matter considerations of semiconductors, the electronic properties and parameters of III-V materials, dilute nitride materials considerations and applications to photodetector heterostructures.

2.1 Semiconductors

Semiconductors are a particular state of the matter whose main properties can be summed up as follows. They show a resistivity between metals and insulators, in the range of 10^{-3} Ω.cm and 10^{9} Ω.cm respectively. They have a negative temperature coefficient of resistance and their electrical conductivity can be varied over several orders of magnitude with temperature, by the incorporation of impurities, by the injection of excess charge carriers or by optical excitation [4]. Common semiconductors, presented in Figure 2.1, include group-IV elemental material, such as

Si or Ge, II-VI binaries ZnTe, CdSe, III-V binary compounds GaAs, InAs, ternaries such as $Hg_{1-x}Cd_xTe$ or $InAs_{1-x}N_x$ and much more.

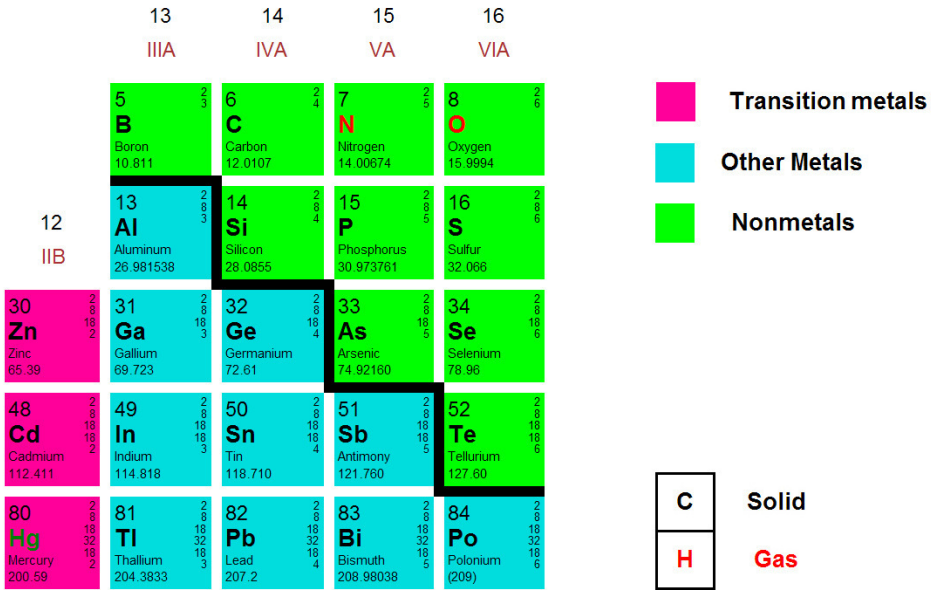

Figure 2.1 Periodic table excerpt for the common group-II to -IV elements, adapted from [5]

2.2 Crystal structure and properties of semiconductors

2.2.1 Atom size and electronegativity

The size of an atom can be considered by the atomic radius. Electronegativity quantifies the ability of an atom to attract electrons and form a chemical bond. It is generally quantified between 0 and 4 (no unit) in the Pauling scale. Indium (In) was discovered in 1863 by F. Reich and H.T. Richter in Germany. It is a rather big atom moderately electronegative, with atom size of 2 Å and electronegativity of 1.78. Arsenic (As), known for its toxic properties since the 1200's, is rather similar in size and electronegativity, 1.33 Å and 2.18 respectively. Nitrogen (N) was discovered in the so-called "mephitic air" by D. Rutherford in Scotland (and others, independently) in 1772. Contrary to In and As, N is much smaller (0.75 Å) with a strong

electronegativity (3.04), and these differences are acknowledged to cause drastic change in the electronic structure of InAs as will be seen later (see Section 3.5).

2.2.2 Crystal structure

Most semiconductors used for optoelectronic applications are crystalline materials, as opposed to polycrystalline or amorphous solids. At the microscopic scale, the solid is a periodic three-dimensional arrangement of a regularly-repeated pattern of atoms named a lattice. The lattice can be seen as the repetitive translation of a primitive cell. The energy of a crystal is a balance of repulsion and attraction between nearest neighbour atoms. The binding energy of a crystal is defined as the energy required to dissociate a solid into separate atoms or ions.

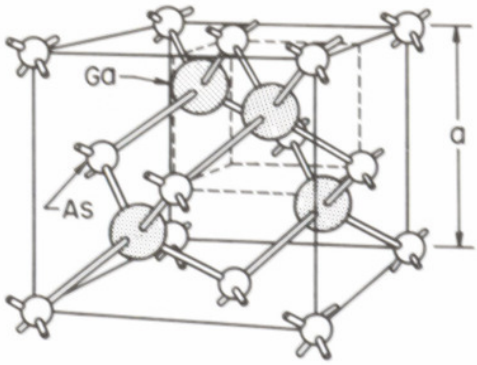

Figure 2.2 Zincblende crystalline structure for GaAs [6a]

Several group IV elemental semiconductors, of which Si is the most widely used, crystallise in the diamond or face-centred cubic (fcc) structure : atoms are at each corner of a simple cubic unit cell and in the middle of each face. Some III-V binaries such as InAs and GaAs have a zincblende structure, shown in Figure 2.2 : two fcc lattices displaced from each other by the quarter the cube body diagonal distance. Although InN can crystallise either in the wurtzite (hexagonal) or the cubic system,

InAsN is considered to be of zincblende structure. The regular fcc arrangement of In and As in InAs sees some As atoms being replaced by N, the second V-group element within the ternary.

Direct lattice sites (or cells) can be defined by [6a] :

$$\mathbf{R} = m'\mathbf{a} + n'\mathbf{b} + p'\mathbf{c} \qquad (2.1)$$

In the case of cubic systems, $m' = n' = p' = a_0$, where a_0 is the lattice constant or lattice parameter. Reciprocal lattice basis vectors **a***, **b***, **c*** can be defined by :

$$\mathbf{G} = h\mathbf{a}^* + k\mathbf{b}^* + l\mathbf{c}^* \qquad (2.2)$$

$$\mathbf{a}^* \equiv 2\pi \frac{\mathbf{b}\times\mathbf{c}}{\mathbf{a}\bullet\mathbf{b}\times\mathbf{c}}, \qquad \mathbf{b}^* \equiv 2\pi \frac{\mathbf{c}\times\mathbf{a}}{\mathbf{a}\bullet\mathbf{b}\times\mathbf{c}}, \qquad \mathbf{c}^* \equiv 2\pi \frac{\mathbf{a}\times\mathbf{b}}{\mathbf{a}\bullet\mathbf{b}\times\mathbf{c}} \qquad (2.3)$$

where h, k, l are integers and so that $\mathbf{G}\bullet\mathbf{R} = 2\pi\times\text{integer}$. Each vector of the direct lattice is normal to a set of planes (*hkl*) in the reciprocal lattice. Miller indices are used to define crystal directions (e.g. [001] for the z-axis) or crystallographic planes (e.g. (004)). The lattice plane spacing d_{hkl} depends on the geometry chosen for XRD measurements (see Section 4.2.1), and observation of the (004) diffraction planes ((115) respectively) corresponds to a lattice spacing of ¼ the lattice constant in the direct lattice space ($^1/_{\sqrt{27}}$ respectively), as illustrated in Figure 2.3.

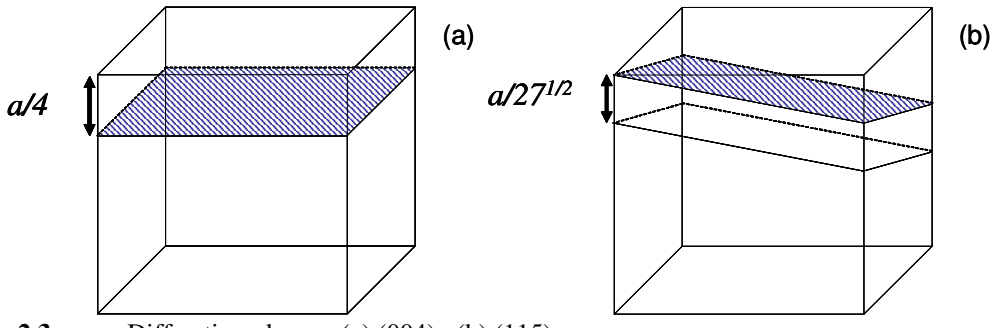

Figure 2.3 Diffraction planes : (a) (004) ; (b) (115)

2.2.3 Vegard's law

III-V binaries such as InAs, InN, GaAs or InP crystallise in the zincblende structure. The lattice size is described by the lattice constant, as shown in Table 2.1, that varies with the atom size and the strength of the atomic bonding.

Material	InAs	InN (cubic)	InSb	GaAs	InP
Lattice constant a_0 (Å)	6.0584	4.96	6.4794	5.6533	5.8686

Table 2.1 Lattice constant at 300 K of common III-V compounds [6c, 7, 8]

Vegard's law applied to crystallography states that the lattice constant of a ternary is the average of the lattice constants of the component binaries. $InAs_{1-x}N_x$ lattice constant can thus be expressed as a function of a_{InAs} and a_{InN_cubic}, InAs and InN (cubic) lattice constants respectively :

$$a_{InAsN}(x) = x\,a_{InN\_cubic} + (1-x)\,a_{InAs} \qquad (2.4)$$

The incorporation of N in InAs host lattice reduces the InAsN lattice constant.

2.3 Electronic structure of semiconductors

While the crystal structure of a semiconductor is determined by the positions of the ions (with a larger mass than that of the electrons), the valence electrons and their mutual interactions determine the electrical properties of the material [4].

2.3.1 Density of states

In a solid, atoms are close enough for their respective electric field to interact with each other and lead to a splitting of energy levels into a finite number of

electronic states [9a]. Energy bands arise from the gathering of closely spaced sublevels. Electrons tend to occupy all the lower energy levels and the two highest energy bands are the valence band (VB) and conduction band (CB). An excited electron can reach the conduction band and thus take part in the conduction process, its absence from the valence band creates a local positive charge, a hole. Electronic states can be populated or vacant, and the dependence on energy of states in the bands is described by the density of states.

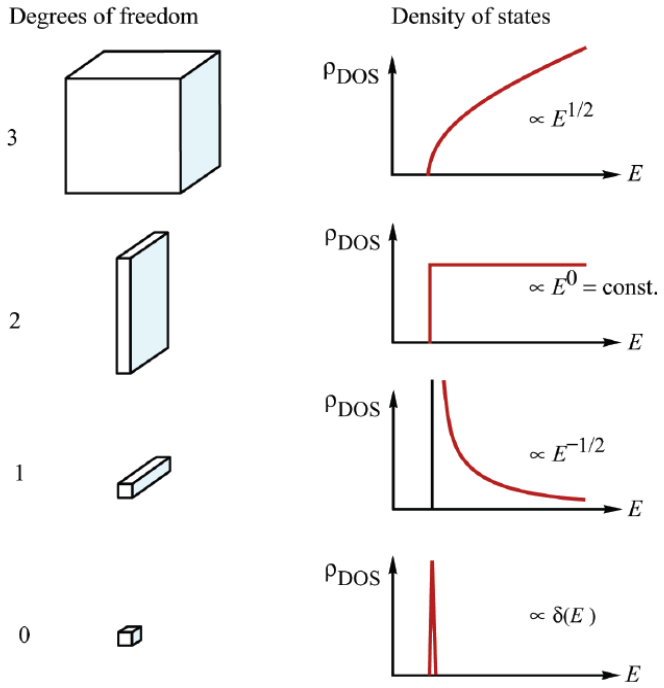

Figure 2.4 Degrees of freedom for bulk (3), QW (2), quantum wire (1) and QD (0) and related density of states [10a]

The thickness of the crystal, whether grown in the microscopic or nanoscopic scale, alters the confinement of the carriers and thereby the density of states of the material, as shown in Figure 2.4. A bulk layer is a plain and generally thick layer and its thickness often varies between a few hundreds of nanometers to a few micrometers. The carriers have three degrees of freedom (3D semiconductor) and the associated

density of states has square-root dependence on energy. Thinner planar structures can be grown in the tens of nanometers scale in so-called quantum wells, whether isolated in single quantum wells (SQW) or in the periodic structure of multiple quantum wells (MQW). The related density of states is constant as a function of the energy for this two-dimensional confinement (2D). Further confinement can be achieved in quantum wires and quantum dots (QD), where the degrees of freedom are reduced to 1 and 0 respectively, and the density of states has inverse square-root or dirac-function dependence on energy. The density of states increases when the dimension of the system decreases. Thus, quantum wells tend to trap carriers and quantum dots structures are preferred in lasers since a smaller number of carriers take part in lasing.

2.3.2 Bandgap

The band structure of a semiconductor is generally represented by an energy - wave vector relationship E - $\boldsymbol{k}$: the upper and lower bands are respectively the conduction band (*CB* at energy E_C) and the valence band (*VB* at energy E_V), separated by a forbidden energy region where allowed states cannot exist. The separation between the lowest conduction band and the highest valence band is the bandgap energy E_g.

Close to the band edges, the semiconductor conduction and valence bands can be approximated respectively by parabolic functions of $\boldsymbol{k}$:

$$E_C = E_g + \frac{\hbar^2 k^2}{2m_e} \qquad (2.5)$$

$$E_V = -\frac{\hbar^2 k^2}{2m_h} \qquad (2.6)$$

where $\hbar$ is the reduced Planck's constant $\hbar = \frac{h}{2\pi}$, h is Planck's constant, m_e and m_h are the electron and hole masses respectively. This approximation is accepted for GaAs and InAs. According to the location of the conduction band minimum compared to the valence band maximum (see Figure 2.5), a semiconductor material is said to have an indirect bandgap when these are misaligned in the ***k***-direction and direct-gap when these extrema are at the same k value. Semiconductors with direct bandgaps allow transitions with conservation of the electron momentum ($p = \hbar k$) and are favoured for mid-infrared optoelectronics because of the higher recombination probability. Figure 2.5 shows the Γ, L, X valleys of the material according to their positions on the ***k***-axis.

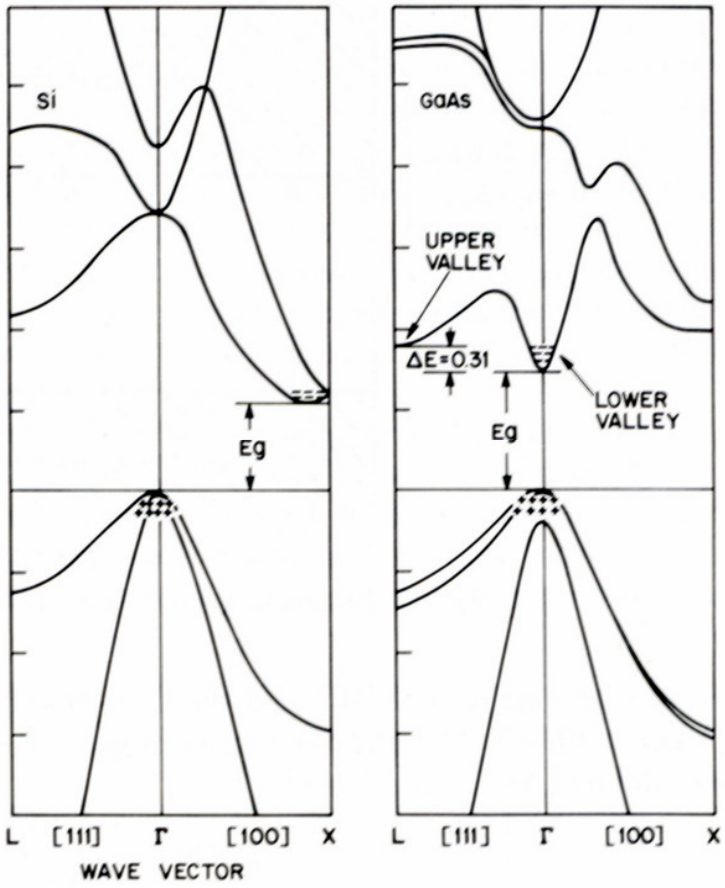

Figure 2.5 Indirect and direct bandgaps of Si and GaAs respectively [6a]

2.3.3 Recombination processes

Radiative transitions in semiconductors can take place between the conduction band, the valence bands and intermediate energy levels due to impurities as shown in Figure 2.6. Interband or band-to-band transition (a) gives birth to the intrinsic luminescence of a material for which an electron in the conduction band recombines with a hole in the valence band. At cryogenic temperatures, electron-hole pairs can couple in a bound state – via Coulomb attraction – called an exciton (X), with a generally sharp emission (b). Emissions from or to localised states of impurities (donors and acceptors) are illustrated in processes (c)-(e) : donor-to-free-hole transition D^0h (c), free-electron-to-acceptor eA^0 (d) and donor-acceptor pair transition DAP (e). Similar transitions can occur between excitons and impurities (D^0X and A^0X).

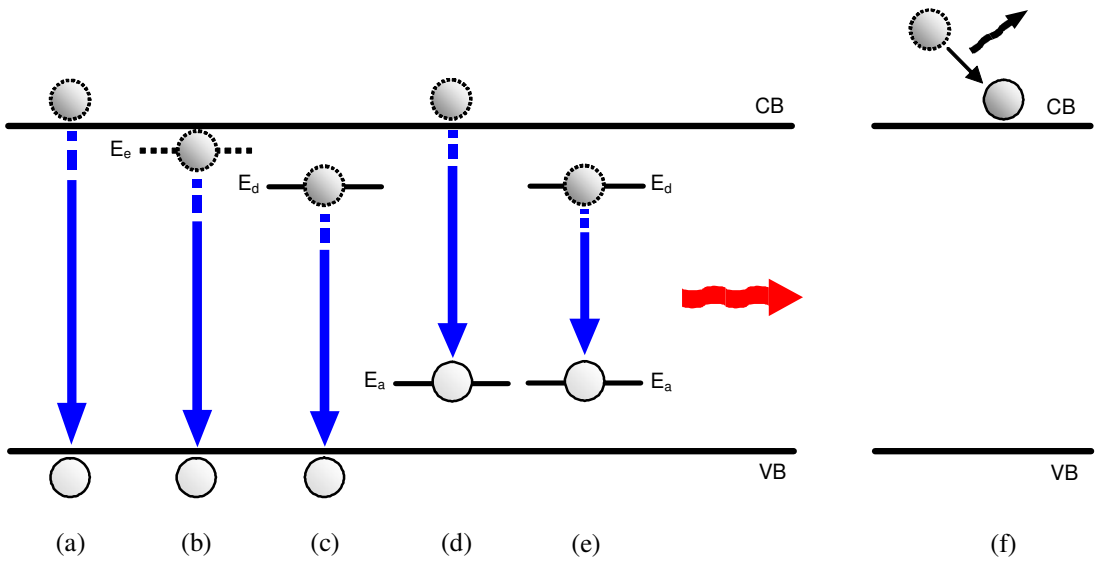

Figure 2.6 Recombination processes between the conduction band E_C, the valence band E_V and exciton E_e, donor E_d and acceptor E_a levels (a) to (e) ; (f) : non-radiative transition

Main non-radiative processes in narrow-gap semiconductors include thermal recombinations, Shockley-Read-Hall recombinations and Auger processes. An

electron excited far above the conduction-band edge can reach thermal equilibrium by releasing its energy in a generally non-radiative way : it emits a phonon (f) – a thermally excited quantum of lattice vibration. Thermal processes are responsible for the presence of free carriers. Shockley-Read-Hall recombinations can originate from deep levels in semiconductors – due to impurities or native lattice defects – and account for transitions from the conduction band to a trap state or from a trap state to the valence band. Auger recombinations are three-particule processes involving an interband and an intraband transition. CHCC in n-type material, CHLH and CHSH in p-type material, and CHHH are the main processes in narrow-gap materials [11].

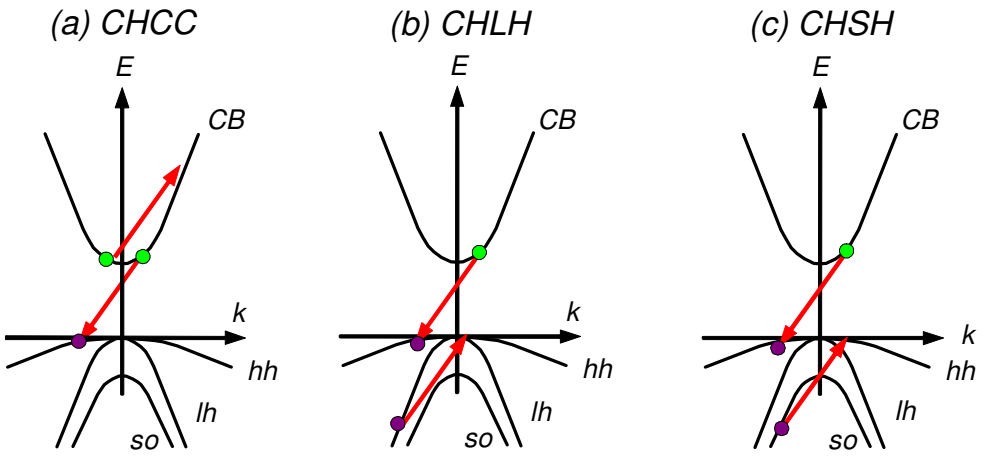

Figure 2.7 Main Auger recombinations : (a) CHCC process ; (b) CHLH process ; (c) CHSH process. *CB*, *hh*, *lh* and *so* stand for conduction band, heavy hole band, light hole band and spin orbit split-off band

As pictured in Figure 2.7, CHCC (CHLH, CHSH and CHHH respectively) is a mechanism involving an interband transition from the conduction band to the valence band (CH) and an intraband transition in the conduction band – CC for CHCC (respectively light hole band to heavy hole band – LH for CHLH, spin-orbit split-off band to heavy hole band – SH for CHSH and in the heavy hole band – HH for

CHHH). Auger recombinations are detrimental to device performances and need to be avoided.

For k-conserving transitions assuming parabolic bands, e.g. in binaries such as InAs and InSb [12], the photon energy $E_{h\nu}$ of a band-to-band transition can be expressed as [12] :

$$E_{h\nu} = h\nu = E_g + \tfrac{1}{2} k_B T \qquad (2.7)$$

For k-non conserving transitions assuming parabolic bands, e.g. in GaAs and ternaries such as InAsSb or HgCdTe [12], the photon energy is :

$$E_{h\nu} = h\nu = E_g + 2k_B T \qquad (2.8)$$

The factor $k_B T$ is particularly important in narrow gap semiconductors since it is ~ 25 meV at room temperature (compared to bandgap energies of ~ 300 meV).

2.3.4 Temperature dependence of the bandgap : Varshni's equation

The temperature dependence of the bandgap arises from two mechanisms. They originate in the shift of the relative position of the conduction band (CB) and valence band (VB) due to the dilatation of the lattice with temperature for one and due to the temperature dependence of the electron lattice interaction for the other. The temperature dependence of the bandgap can be fitted by the Varshni's equation [13] :

$$E_g(T) = E_{g0} - \frac{\alpha T^2}{\beta + T} \qquad (2.9)$$

where E_{g0} is the bandgap energy at 0 K, α and β are two empirical parameters relating to the material (α is generally near 0.5 meV/K and β is in the order of the Debye temperature [12]).

2.3.5 Doping : intrinsic and extrinsic semiconductor

From a crystallographic point of view, a group-IV atom of an intrinsic semiconductor shares its four valence electrons with its four neighbouring atoms as pictured for silicon in Figure 2.8 (a). Doping tends to modify this equilibrium in consequently-named extrinsic semiconductors. The introduction of a group-V atom (phosphorous) with five valence electrons in the place of Si provides an extra electron to the conduction band. Silicon is n-type (Figure 2.8 (b)) due to the presence of P as a donor of negative charge. Similarly, a group-III atom boron (B) in place of a silicon atom can only share three valence electrons. The lattice provides an electron to B, creating thus a hole in the valence band. Silicon is p-type in the case presented in Figure 2.8 (c) because of B being an acceptor of negative charge. A similar explanation is valid for III-V semiconductors, namely InAs : using Be or Zn, a group-II element, to substitute In the group-III element, results in p-type doping of InAs, while the group-VI S or Te makes InAs n-type.

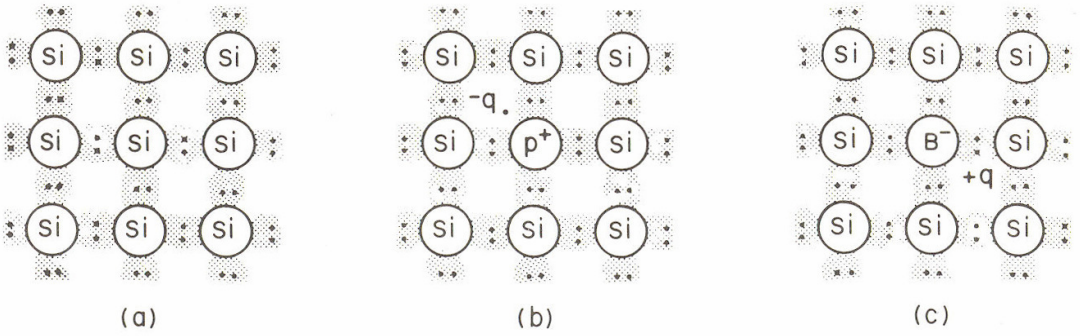

Figure 2.8 Bond pictures of a group-IV semiconductor : (a) intrinsic silicon ; (b) n-type silicon with phosphorous ; (c) p-type silicon with boron [6a]

The Fermi energy E_F is the energy at which the probability of finding an electron is ½. Under the Boltzmann statistics conditions, that is for the Fermi level far below the conduction band $E_C - E_F \gg k_B T$ and far above the valence band $E_F - E_V \gg k_B T$

in nondegenerate semiconductors, the number of occupied conduction band levels n near the bottom of the CB and the number of occupied valence band levels p near the top of the VB can be approximated [6a].

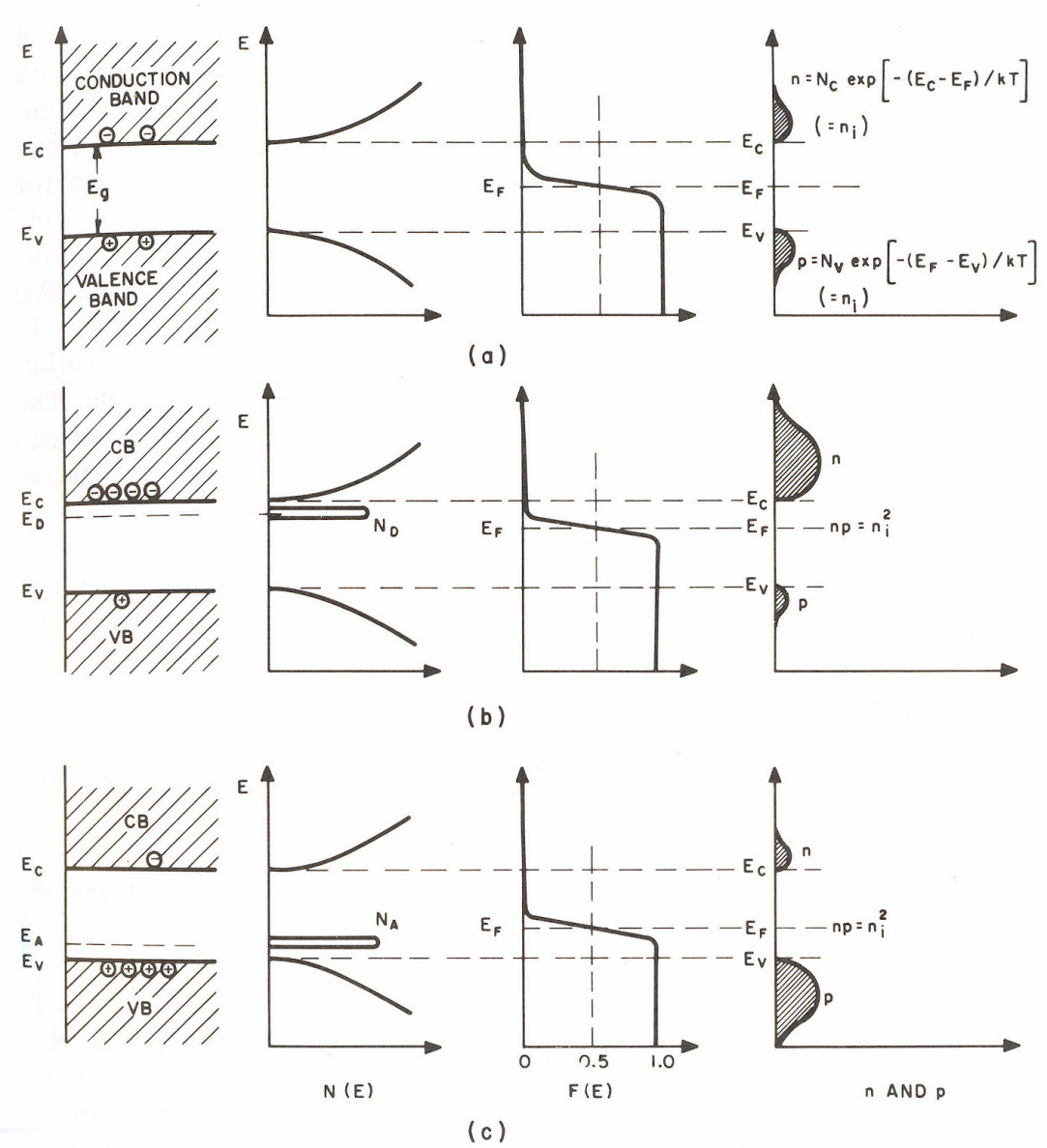

Figure 2.9 Schematic band diagram, density of states N(E), Fermi-Dirac distribution F(E) and carrier concentrations for : (a) intrinsic, (b) n-type, (c) p-type material [6a]

The occupation of conduction and valence bands follows ($T > 0$ K) :

$$n = N_C \exp\left(-\frac{E_C - E_F}{k_B T}\right) \qquad (2.10)$$

$$p = N_V \exp\left(-\frac{E_F - E_V}{k_B T}\right) \qquad (2.11)$$

where N_C and N_V are respectively the effective density of states in the conduction and the valence bands, k_B the Boltzmann constant, T the absolute temperature. Equations (2.10) and (2.11) are obtained from the integration of the density of states $N(E)$ and Fermi-Dirac distribution $F(E)$ over the appropriate band energy range shown in Figure 2.9. n and p are by extension the density of electrons and holes respectively.

A semiconductor with negligible impurities is said to be intrinsic when thermal agitation excites electrons from the valence band (VB) to the conduction band (CB) and generates an equal number of holes in the VB : $n = p = n_i$ the intrinsic carrier density. Electrons in the CB recombine with holes in the VB to reach equilibrium.

2.4. Dilute nitride materials

2.4.1 Nitrogen configurations

Nitrogen atoms can incorporate in the InAs lattice in different ways similarly to GaAsN as shown in Figure 2.10. Substitutional nitrogens N_{As} take the place of As atoms whereas interstitial nitrogens sit within the zincblende structure as extra atoms. Split interstitial N can bond with As (As-N) or with another nitrogen atom (N-N).

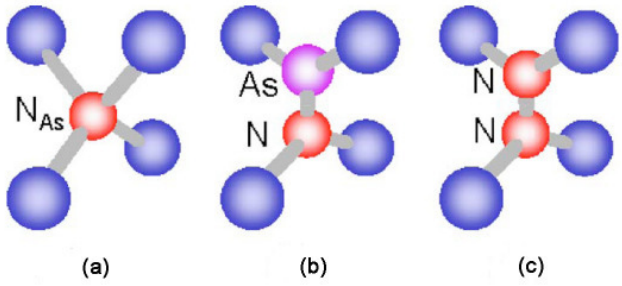

Figure 2.10 Possible configurations of nitrogen in GaAsN : (a) substitutional nitrogen N_{As} ; (b) split interstitial As-N ; (c) split interstitial N-N [14]

2.4.2 Band anticrossing model (BAC)

The incorporation of N, because of its higher electronegativity in III-V alloy lattice, create a large local perturbation of the crystal lattice potential by the introduction of a localised state with energy level E_N close to the conduction band edge. The band anticrossing (BAC) model, applicable to dilute nitride alloy systems with large band gap bowing parameters such as GaAsN [15], InAsN [16], GaInAsN [17, 18], considers the interaction between the localised N states E_N and the extended states $E_M(k)$ of the host semiconductor matrix. This interaction leads to the splitting of the conduction band into two highly non-parabolic subbands $E_+(k)$ and $E_-(k)$, as shown in Figure 2.11. The new transition from the downward-shifted lower subband E_- shows a large decrease in the bandgap.

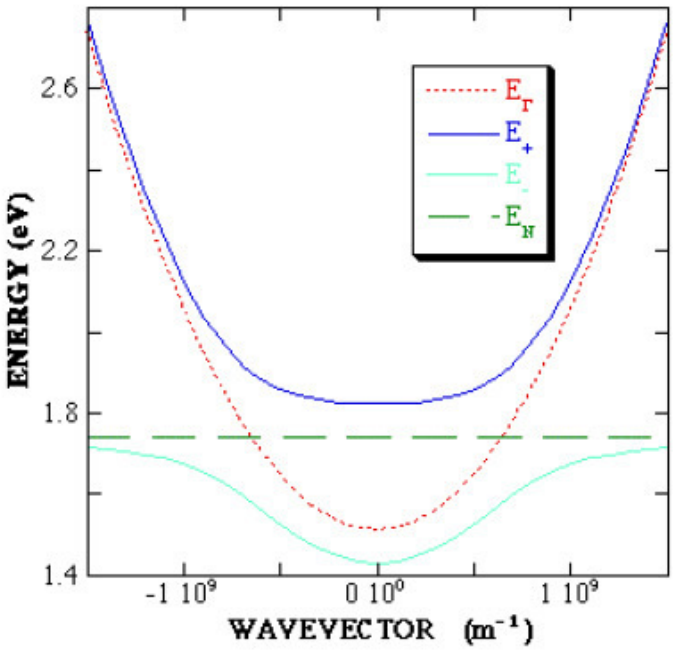

Figure 2.11 Schematic of dispersion relations for $E_+(k)$ and $E_-(k)$ in GaAsN, with E_Γ the host material (GaAs) conduction band and E_N the nitrogen related level [19]

The energy of the subbands modelled by the band anticrossing model can be written as follows :

$$E_{\pm}(k) = \frac{1}{2}\left(\left[E_M(k) + E_N \right] \pm \sqrt{\left[E_M(k) - E_N \right]^2 + 4V_{NM}{}^2} \right) \qquad (2.12)$$

where E_N is the energy of the nitrogen state and $E_M(k)$ the dispersion relation for the conduction band of the nitrogen-free semiconductor matrix. The hybridisation strength or coupling factor between $E_{\pm}$ and E_N is modelled by [16] :

$$V_{NM} = C_{NM} x^{1/2} \qquad (2.13)$$

where C_{NM} is a constant dependent on the semiconductor host and x the nitrogen fraction in the alloy. This band anticrossing model is considered to be an approximation to the single-impurity case of the many-impurity Anderson model [20] that more generally takes into account the broadening of the energy levels and resulting optical transitions described by the imaginary part of the dispersion relations.

2.5. Photodetection

Photodetectors are devices than can detect photons over a specified spectral range and generate electronic signals proportional to the absorbed energy. The processes involved are chronologically the generation of carriers by absorption of the incident light, the transport of carriers and the generation of an output signal by the current flowing through the associated external circuit. The simplest structure of a photodetector, called a photoconductor, consists of a bulk semiconductor slab with ohmic contacts at both ends and whose surface between the contacts is illuminated (see Section 3.1.1).

Photodiodes, which include p-n junctions, p-i-n diodes, metal-semiconductor diodes (or Schottky barriers) and heterojunction diodes, have a depletion region with

high electric field that separates photogenerated electron-hole pairs. If they are operated without bias and connected to a load impedance, photodiodes are said to be photovoltaic : this is the case for solar cells, that have a broad spectral range and a large detection area. In the near- and mid-infrared, photodiodes are generally reverse-biased to increase the response speed, with a small area to decrease the junction capacitance.

2.5.1 Absorption processes

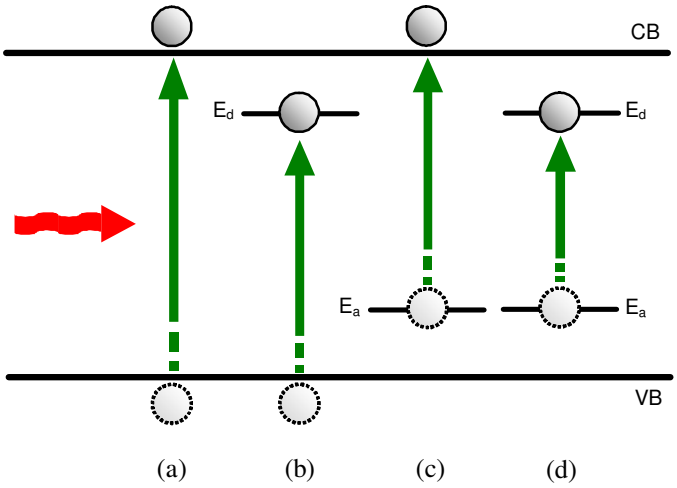

Figure 2.12 Main absorption processes in semiconductors

The illumination of a semiconductor with a photon of greater energy than the bandgap results in the generation of a hole-electron pair by the mechanisms of absorption illustrated in Figure 2.12. The absorption in a photodetector can mainly be band-to band (a) as for intrinsic detectors, between the valence band and a donor (b) or an acceptor as for extrinsic detector, and the conduction band or between two impurities (d). For direct transitions, the absorption coefficient α follows [6a] :

$$\alpha \sim (h\nu - E_g)^{1/2} \qquad (2.14)$$

where $h\nu$ is the photon energy and E_g the bandgap energy of the material.

2.5.2 Photodiodes : p-i-n diodes

Contrary to a photoconductor, a p-i-n structure can be described as an intrinsic layer (generally undoped, named i-region or depletion region) surrounded by two doped regions respectively p- and n-type as pictured in Figure 2.13 (a). The advantage of such a structure lies in the fact that tailoring the depletion region thickness allows the optimisation of the quantum efficiency and frequency response. If the n-, i- and p-regions are made of the same semiconductor, the structure is a homojunction. An alternative to it are heterojunctions which are junctions made of semiconductors with different bandgaps. For low leakage current, the lattice constants of the two materials must be closely matched.

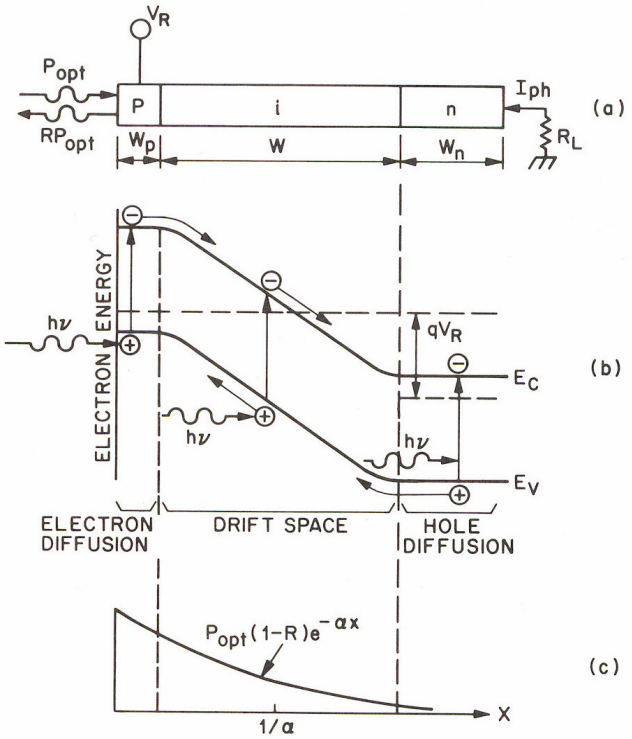

Figure 2.13 Homojunction p-i-n diode : (a) cross-sectional view ; (b) energy-band diagram under reverse bias ; (c) generation-recombination characteristics [6b]

The mechanisms involved in the generation of a photocurrent are illustrated in Figure 2.13 (b). In a p-i-n, the light is absorbed and produces hole-electron pairs. The

pairs produced in the depletion region and within the diffusion length ($1/\alpha$) are separated by the electric field. The drift of the carriers across the structure generates a current.

In a reverse-biased depletion region, assuming that the thermal generation current can be neglected and that the width of the p-region W_p verifies $W_p \ll 1/\alpha$, the total photogenerated current density J_p is :

$$J_p = J_{drift} + J_{diff} \qquad (2.15)$$

where J_{drift} is the drift current density due to carriers generated inside the intrinsic region W and J_{diff} the diffusion current density from carriers outside W diffusing into the junction. The hole-electron generation rate $G(x)$ as a function of the distance within the semiconductor is :

$$G(x) = \Phi_0 \alpha \exp(-\alpha x) \qquad (2.16)$$

where α is the absorption coefficient, Φ_0 the incident photon flux described by $\Phi_0 = \frac{P_{opt}(1-R)}{\mathcal{A} h\nu}$, R the reflection coefficient at the air-photodetector interface, $\mathcal{A}$ the area of the illuminated surface. The drift current density J_{drift} is proportional to the integral of $G(x)$ over the intrinsic region width W :

$$J_{drift} = -q\int_0^W G(x)\,dx = q\Phi_0\left(1 - e^{-\alpha W}\right) \qquad (2.17)$$

and the diffusion current density J_{diff}, also a function of the absorption coefficient, can be expressed in an analogous way.

The total current in a diode is the contribution of the photogenerated current, due to the absorption, and the dark current, due to the thermal generation-recombination of electron-hole pairs in the depletion region The current I for an ideal

diode under illumination is expressed (for a current-voltage (I-V) characteristic e.g.) in the form [9b] :

$$I = I_0\left(\exp\left(\frac{qV}{k_B T}\right) - 1\right) - I_p \qquad (2.18)$$

where I_0 is the reverse-bias saturation current, V the applied voltage, T the absolute temperature, and I_p is the photogenerated current ($I_p = J_p \mathcal{A}$, where J_p the total photogenerated current density (2.15) and $\mathcal{A}$ the area of the device).

The zero-bias resistance area product $R_0\mathcal{A}$ is a common criteria of comparison for photodiodes (see Section 2.5.6 for a relation between $R_0\mathcal{A}$ and the specific detectivity). It is derived from (2.18) as :

$$R_0 = \frac{dV}{dI} \qquad (2.19)$$

2.5.3 Charge carriers

Charge carriers in semiconductors acquire velocity in an electric field and create a drift current [9a]. At low electric field, the drift velocity v_d can be written as [6a] :

$$v_d = \mu E_{elec} \qquad (2.20)$$

where μ is the mobility and E_{elec} is the electric field strength. At high field, the drift velocity approaches the saturation velocity v_s [6a] that was simply modelled [21].

Mobility depends on the type of carriers and is generally expressed as [9a] :

$$\mu = \frac{q\tau_{th}}{m^*} \qquad (2.21)$$

where q is the electron charge, τ_{th} is the mean lifetime between collisions and m^* the carrier effective mass.

The resistivity ρ of a material defines the proportionality between electric field and current density :

$$E_{elec} = \rho J \qquad (2.22)$$

where J the current density. It is also defined as :

$$\rho = R\frac{A}{d} \qquad (2.23)$$

where R is the resistance, A the area of the surface normal to the current density vector $\boldsymbol{J}$ and d the thickness of the material across which the current flows. The reciprocal value of the resistivity is the conductivity σ. Semiconductors with both electrons and holes are characterised by :

$$\rho = \frac{1}{\sigma} = \frac{1}{q\left(\mu_n n + \mu_p p\right)} \qquad (2.24)$$

where q is the electron charge, μ_n and μ_p are the mobility of electrons and holes respectively, and n and p the electron and hole (carrier) concentrations respectively.

2.5.4 Quantum efficiency

The quantum efficiency η corresponds to the ratio of photogenerated electron-hole pairs per incident photon. It can be defined as [6b] :

$$\eta = \frac{I_p / q}{P_{opt} / h\nu} \qquad (2.25)$$

where I_p is the photogenerated current, P_{opt} the incident optical power, $h\nu$ the photon energy (in eV). Because of the dependence of J_{drift} and J_{diff} on the absorption coefficient, the quantum efficiency can be expressed as [6b] :

$$\eta(\alpha) = (1 - R)\left(1 - \frac{e^{-\alpha W}}{1 + \alpha L_p}\right) \qquad (2.26)$$

where $L_p = \sqrt{D_p \tau_p}$, D_p is the diffusion coefficient for holes and τ_p the lifetime of excess carriers. One can see that at an adapted depletion region width $W = 1/\alpha$, the quantum efficiency increases with increasing absorption coefficient α.

2.5.5 Noise equivalent power (NEP)

The noise equivalent power *NEP* (in W) is defined as the rms (root-mean-square) incident power required to produce an output signal *S* as intense as the detector noise *N* (*S* / *N* = 1) in a bandwidth of 1 Hz.

2.5.6 Specific detectivity

The specific detectivity D^* (in cm.Hz$^{1/2}$.W^{-1}) is probably the most important figure of merit given for a photodetector. It is defined as :

$$D^* = \frac{\mathcal{A}^{1/2} \Delta f^{1/2}}{NEP} \qquad (2.27)$$

where $\mathcal{A}$ is the area of the illuminated surface and Δf the bandwidth of the source. In double heterostructure detectors, the specific detectivity is a function of the net $R_0\mathcal{A}$ (net zero-bias resistance area product, $(R_0\mathcal{A})_{\text{net}}$) that takes into consideration the respective zero-bias resistance area products related to diffusion, generation-recombination in the depletion region and possible tunnelling across the heterointerface. In this case, the specific detectivity is written as [22] :

$$D^* = \frac{q\eta\lambda}{hc}\left(\frac{(R_0\mathcal{A})_{net}}{4k_B T}\right)^{1/2} \qquad (2.28)$$

For background-limited photoconductors with unit quantum efficiency, the ideal detectivity is [6b] :

$$D^*(\lambda, f_{\mathrm{mod}}, \eta = 1) = \frac{c.\exp(\zeta/2)}{2\sqrt{\pi h k_B T}.\nu^2 (1 + 2/\zeta + 2/\zeta 2)^{1/2}} \qquad (2.29)$$

where λ is the source wavelength, f_{mod} the frequency of modulation of the source, c is the velocity of light, ζ such that $\zeta \equiv h\nu/k_B T$ with, T the blackbody temperature (see Section 4.2.3).

2.5.7 Responsivity

The responsivity $\mathcal{R}$ (in $A.W^{-1}$) is the ratio of photocurrent to optical power and is written :

$$\mathcal{R} = \frac{I_p}{P_{opt}} = \frac{\eta q}{h\nu} \qquad (2.30)$$

For an ideal photodiode with unit quantum efficiency, $\mathcal{R} = \frac{\lambda}{1.24}$ where λ is the wavelength (μm).

2.6. Heterojunctions

2.6.1 Band alignment

Contrary to p-i-n homojunctions made of the same material, the layers of a heterojunction can be made of different materials to improve the properties of a detector. In Figure 2.14 (a), a material of narrower bandgap between two materials of larger bandgap results in a type-I band alignment where both band discontinuities ΔE_C and ΔE_V are positive. The first alloy acts as a window or a barrier and confines the carriers in the second alloy. When band discontinuities are of opposite sign, the material is type-II. In the example shown in Figure 2.14 (b), electrons are preferably

located in the narrow bandgap material (alloy 2) and holes in the wide bandgap material.

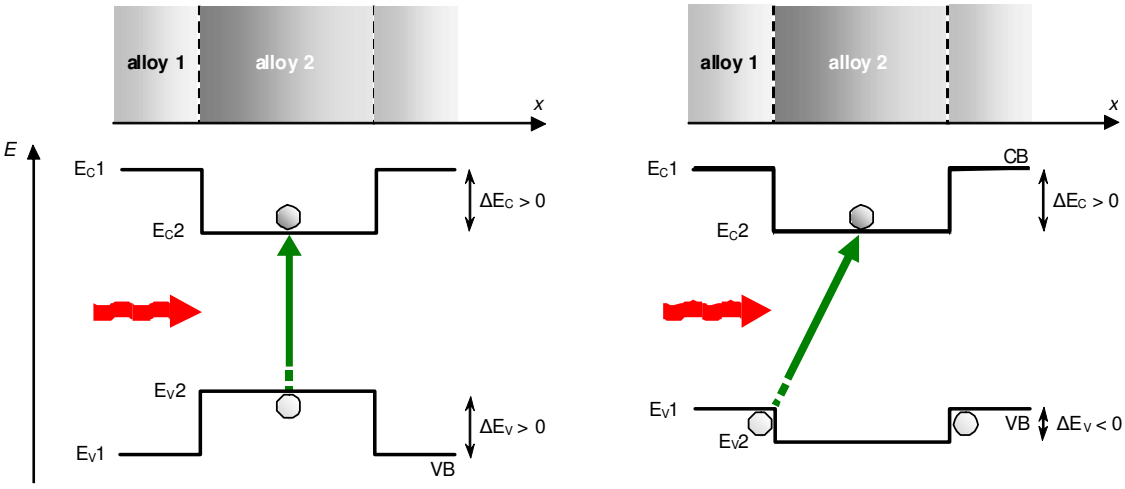

Figure 2.14 Band alignment : (a) type-I ; (b) type-II

For the realisation of a photodiode, band alignments and lattice mismatch at the interface must be taken into account. The design of windows and barriers and choice of the bandgap energy will generally try to be satisfied with lattice matching. Figure 2.15 shows the relation between the lattice constant and the conduction and valence band offsets (respectively CBO and VBO) for the Γ-valley with reference to InSb valence band minimum (VBM).

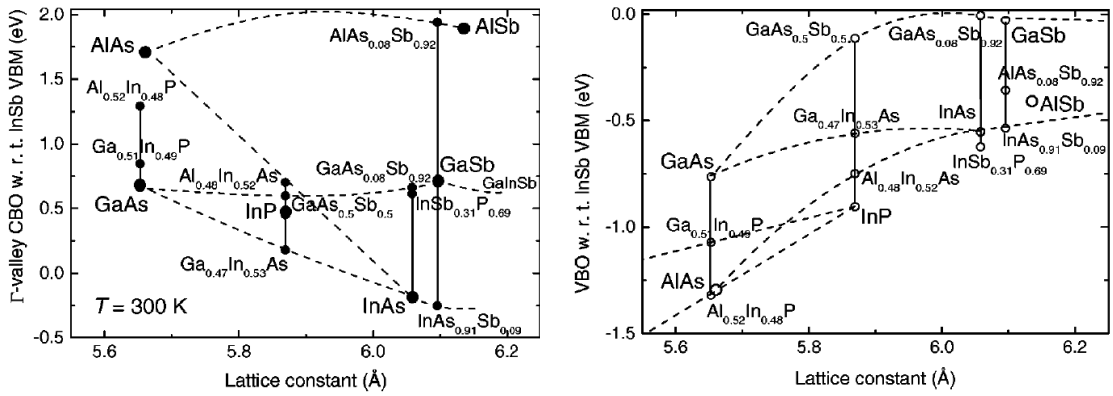

Figure 2.15 Conduction and valence band offsets as a function of the lattice constant [23]

2.6.2 Lattice mismatch

The lattice mismatch expresses the change in lattice constants at the interface of two different materials. It is given by :

$$\frac{\Delta a}{a} = \frac{a_{layer} - a_s}{a_s} \qquad (2.31)$$

where a_s and a_{layer} are respectively the substrate and "fully" relaxed epilayer lattice constants. A layer grown on another of smaller lattice constant is under compressive strain, and inversely, a layer grown on another of bigger lattice constant is under tensile strain. InAsN grown on InAs is tensile, as shown in Table 2.2.

N composition in InAsN	0.0 %	0.5 %	1.0 %	1.5 %	2.0 %	2.5 %	3.0 %
Lattice constant (Å)	6.0583	6.0529	6.0475	6.0421	6.0367	6.0313	6.0260
Mismatch to InAs	0	-8.9×10^{-4}	-1.8×10^{-3}	-2.7×10^{-3}	-3.6×10^{-3}	-4.5×10^{-3}	-5.3×10^{-3}
Mismatch to GaAs	7.2×10^{-2}	7.1×10^{-2}	7.0×10^{-2}	6.9×10^{-2}	6.8×10^{-2}	6.7×10^{-2}	6.6×10^{-2}
Mismatch to InP	3.2×10^{-2}	3.1×10^{-2}	3.1×10^{-2}	3.0×10^{-2}	2.9×10^{-2}	2.8×10^{-2}	2.7×10^{-2}

Table 2.2 Lattice mismatch of $InAs_{1-x}N_x$ epilayer on various substrates

2.6.3 Critical thickness

The critical thickness h_c is schematically the minimum thickness necessary for an epilayer to adapt its lattice constant to that of an underlying layer. It is thus thought to be the thickness above which dislocations will be generated at the interface between the two layers [24]. Assuming that the misfit dislocation generation is solely determined by the balance between the interfacial energy and the areal strain energy density, the critical thickness h_c can be derived from the following equation :

$$h_c \approx \left(\frac{1-\nu}{1+\nu}\right)\left(\frac{1}{16\pi\sqrt{2}}\right)\left(\frac{b^2}{a(x)}\right)\left[\left(\frac{1}{f^2}\right)\ln\left(\frac{h_c}{b}\right)\right] \qquad (2.32)$$

where ν is Poisson's ratio, b the slip distance, $a(x)$ the lattice constant of the material function of x the element fraction in the alloy, f the misfit (see (2.31)). Poisson's ratio is defined as $\nu = \frac{C_{12}}{C_{11}+C_{12}}$ where C_{11} and C_{12} are tabulated elastic constants of the material. A layer thinner than h_c is considered fully strained in XRD analysis. A layer thicker than the critical thickness is subject to strain relaxation, misfit and thread dislocations [25].

Chapter 3. Literature review

Photodetection in the mid-infrared is a mature field with commercially available devices. Room-temperature operation is challenging though and a few materials can achieve this target. Nevertheless, a new approach to mid-infrared applications can be considered with InAsN material. The state-of-the-art in mid-infrared photodetection at room temperature is presented in this chapter. An overview of dilute nitrides and particularly InAsN is given with emphasis on their properties and growth conditions.

3.1 Infrared detectors

3.1.1 Developments in infrared detectors

Infrared (IR) radiation was discovered in 1800 by Herschel through experiments to measure the distribution of energy in sunlight with a basic monochromator and a thermometer as a detector. By 1880, after twenty years improvement, Langley's bolometer – measuring the change in electrical resistance – could detect the heat of a cow at a distance of a quarter of a mile [26]. The beginnings of infrared detection are connected with thermal detectors, that are based on the ability of absorbed incident radiation to change the temperature of a material and consequently some other physical properties of a material leading to the generation of an electrical output. Current thermal detectors or pyroelectric detectors operate at room temperature in the mid- and long infrared spectral range with modest sensitivity and slow response (in the order of a millisecond).

Photon detectors (also referred to as photodetectors) are detectors where the radiation is absorbed within the material by interaction with electrons and the change in electronic energy distribution results in an electrical output. The first infrared photoconductor was introduced by Case in 1917 and the common architecture consists of a slab of semiconductor with ohmic contacts at each end, as shown in Figure 3.1 (a). The generation of carriers by band-to-band transitions or transitions involving the forbidden-gap energy levels (intrinsic and extrinsic photoconductors respectively) increase the conductivity of the material. Current infrared photoconductors are based whether on PbS for the spectral range 1 - 3.3 μm, on PbSe for the 3 - 4.6 μm range at room temperature, or on HgCdTe for the 2 - 5 μm range with thermoelectric (TE) coolers and up to 20 μm with liquid nitrogen cooling [27].

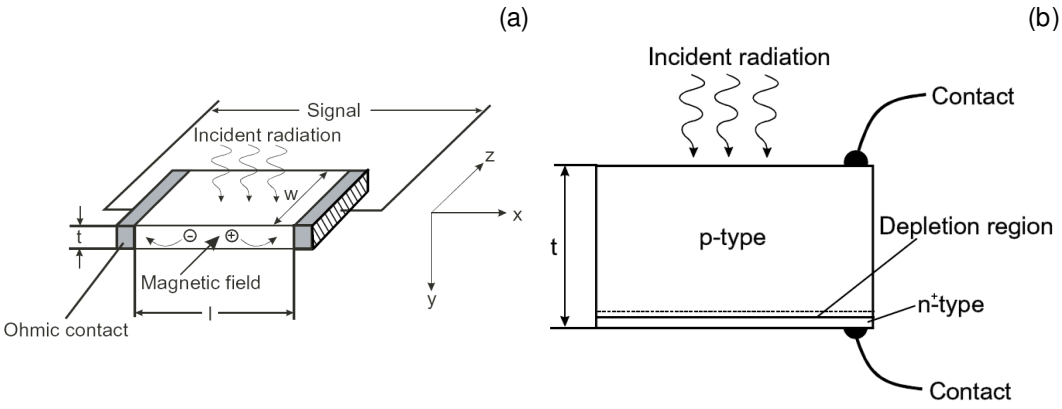

Figure 3.1 Photodetectors : (a) photoconductor ; (b) photodiode

The photodiode, as illustrated in Figure 3.1 (b), is a type of photodetector that can be designed to have a narrow wavelength range. It has a depleted semiconductor region where a high electric field separates photogenerated electron-hole pairs. The depletion region must be thin to reduce the transit time and thick enough to maximise the amount of absorbed light (refer to equations (2.17) and (2.26)) ; this tailoring can also optimise the quantum efficiency of the detector [6b]. Small device area is advised

to minimise the junction capacitance. Commercial devices such as Ge photodiodes can detect below 1.8 µm with TE coolers ; InGaAs detectors show room temperature (RT) detection below 2.6 µm ; InAs photodiodes can operate at RT in the photovoltaic mode (no bias needed) up to 3.8 µm wavelength. Detection up to ~ 5 µm can be achieved with liquid nitrogen-cooled InSb photodiodes (spectral range 1 - 5.5 µm) or TE cooled-HgCdTe photovoltaic photodiodes (spectral range 0.5 - 5 µm) [27].

3.1.2 Competing technologies for mid-infrared sensing and limitations

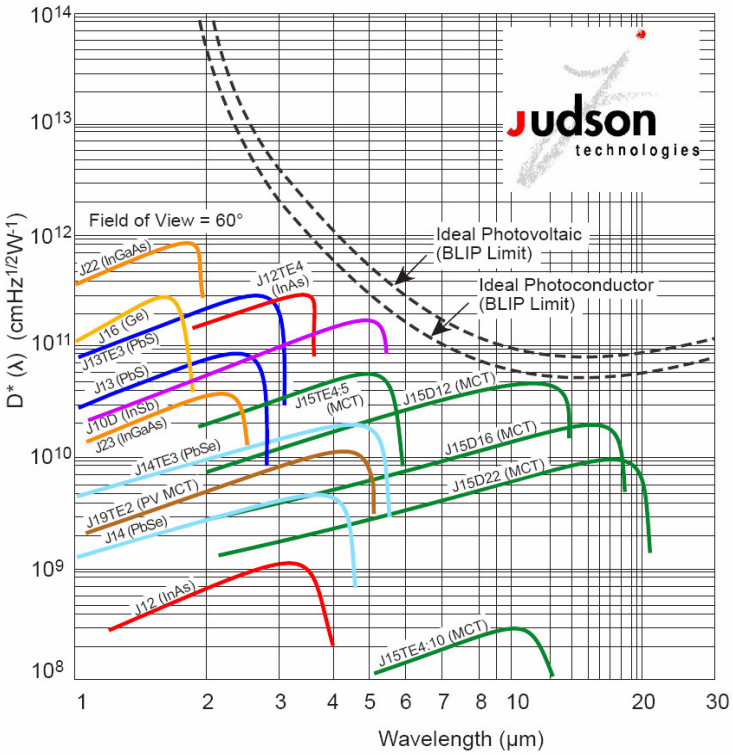

Figure 3.2 Infrared photodetectors : detectivity and spectral range [27]

The variety and range of infrared photodetectors is huge as shown in Figure 3.2 and an exhaustive review is out of the scope of this thesis. Attention will be focused on mid-infrared photodetectors in the 3 - 5 µm spectral range operating at

room temperature with high sensitivity to low level signals. Ideally, the detector would need to be cheap, work without applied bias (photovoltaic mode) and have a narrow spectral range around 4.2 μm (to limit the detection to the sole CO_2 molecule) allowing simple data processing of the signal.

Materials that compete for 3 - 5 μm range photodetection are PbSe, HgCdTe, InAs, InSb and InAsSb. PbSe photoconductors, in typical packaging pictured in Figure 3.3, show spectral detectivity $D^* > 3\times10^9$ cm.Hz$^{1/2}$.W^{-1} in the 3 - 4.6 μm range at room temperature. Nevertheless, they generally have a slow response speed, which limits modulation time and integration time of a gas sensing unit, a broad spectral range and their operation requires bias and thus bias power dissipation elements. Mercury cadmium telluride HgCdTe is the leading semiconductor for IR detectors. This II-VI alloy is flexible to be tailored for optimised detection at any region of the IR spectrum and dual or multicolour devices are easily constructed and commercially available [28]. One of its advantages is that the whole IR spectrum can be covered with roughly the same lattice parameter and a lattice mismatch not exceeding 0.2 % on CdZnTe substrates [26]. The highest performances in the 3 - 5 μm range are obtained between 77 K and 200 K (with spectral detectivity D^* of ~ 1×10^{11} and ~ 5×10^{10} cm.Hz$^{1/2}$.W^{-1} respectively) but cooling systems (with liquid nitrogen or Peltier elements) increase both price and size of infrared sensing units. The need for low-cost efficient sensors operating at room-temperature is partially met by uncooled HgCdTe detectors. Latest HgCdTe photoconductors and photodiodes from Vigo Systems show 295 K spectral detectivity of D^* ~ 2×10^9 cm.Hz$^{1/2}$.W^{-1} and 8×10^8 cm.Hz$^{1/2}$.W^{-1} respectively, with a broad response spectrum around 4 μm [29]. Optical immersion can improve these values three-fold and only thermoelectric coolers (TE) can bring their detectivity to levels ~ 6×10^{10} cm.Hz$^{1/2}$.W^{-1}.

Unfortunately, these detectors tend to have non-uniform response across the active region and suffer from high level of Auger recombination processes. There are lattice, surface and interface instabilities intrinsically due to the weak bonding in II-VI semiconductors, resulting in bad mechanical properties and difficulties in material processing.

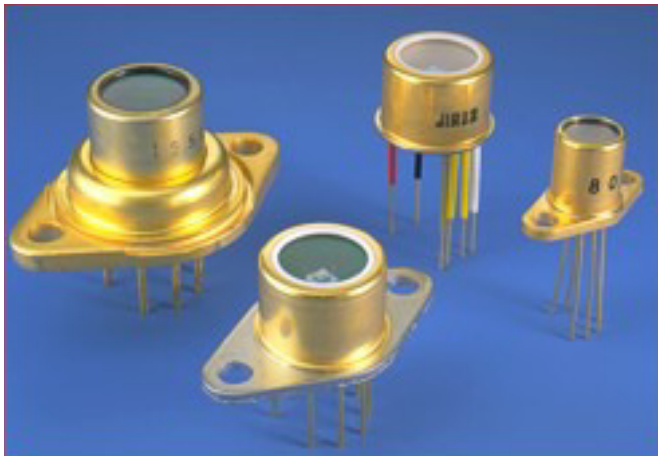

Figure 3.3 Typical commercial photodetectors for room temperature operation [27]

Photoconductors, namely based on the II-VI semiconductors PbSe and HgCdTe, suffer from 1/f noise and are generally slow. Photodiodes based on p-n or p-i-n junctions offer higher speed and higher signal-to-noise ratio than photoconductors, which is an advantage for low level detection. III-V materials can offer an alternative for mid-infrared photodetection. InAs photovoltaic photodiodes operate at room temperature in the 2.4 - 3.5 µm range with detectivity $D^* \sim 1\times10^9$ cm.Hz$^{1/2}$.W^{-1}. Nevertheless, InAs photodiodes need temperature stabilisation with TE coolers for low level signal detection and fall short of the 4.2 µm target. InSb photodiodes would be a good alternative to reach 4.2 µm wavelength target since spectral detectivity of $\sim 1\times10^{11}$ cm.Hz$^{1/2}$.W^{-1} are given by the manufacturer at ~ 4.7 µm and 77 K but all current commercial devices still require nitrogen cooling [30].

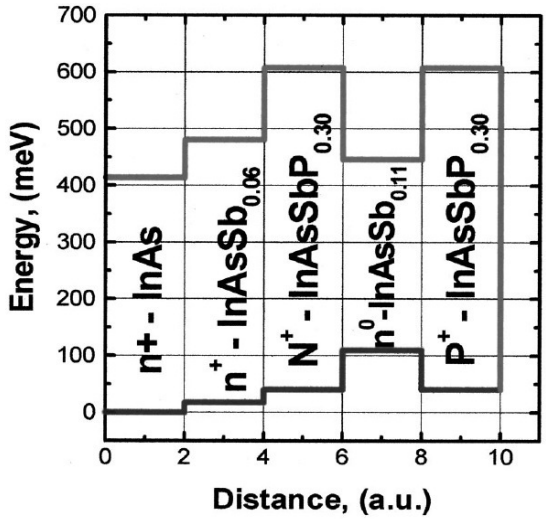

Figure 3.4 Schematic energy band diagram of a p-i-n structure with intermediate composition $InAs_{0.94}Sb_{0.06}$ buffer layer [31]

The recent developments in InAsSb photodetectors showed the high potential of this material for room temperature applications at 4.2 μm and 4.6 μm wavelengths. $InAs_{0.89}Sb_{0.11}$ heterojunctions were grown on InAs by LPE with an InAsSb buffer layer and doped InAsSbP cladding layers [31] as shown in Figure 3.4. Peak responsivity of 0.8 A/W and D^* of 1.26×10^9 cm.$Hz^{1/2}$.W^{-1} at 4.6 μm were achieved at room temperature. Cladding layers provided carrier confinement and prevented loss of electrons to InAs. Nevertheless, $InAs_{0.89}Sb_{0.11}$ is subject to high lattice mismatch and an InAsSb buffer layer of intermediate antimony composition ([Sb] = 6 %) was required to limit the strain and reduce the number of Shockley-Read recombination centres, responsible for low quantum efficiency of the device.

Indeed, the lattice mismatch in $InAs_{0.89}Sb_{0.11}$ generates threading dislocations and a 9 μm-thick buffer was needed to decrease the etch pit density by one order of magnitude [32]. To alleviate this problem, $InAs_{0.91}Sb_{0.09}$ was grown lattice matched to GaSb substrate. An $InAs_{0.91}Sb_{0.09}$ p-i-n grown by MBE showed operation at 3.39 μm and 250 K, namely with the use of a high bandgap AlGaSb confining barrier (lattice-

matched to GaSb substrate as well) [33]. The p-AlGaSb confining barrier was introduced for electron confinement, as shown in Figure 3.5. Nevertheless, the InAlAsSb barrier failed to confine holes and the noise of the photodetector was dominated by diffusion currents. From calculations, no material lattice matched to GaSb could reasonably be proposed for hole confinement [34].

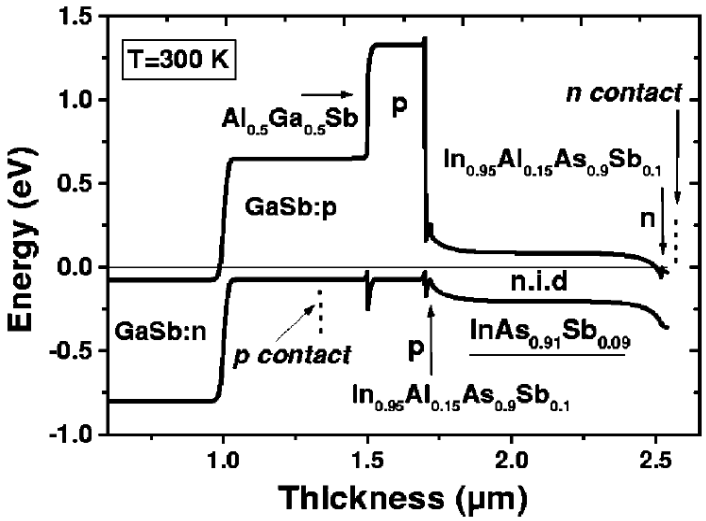

Figure 3.5 Photovoltaic p-i-n junction with high gap p-type confining barrier lattice-matched to GaSb [33]

Quantum wells and quantum dots are structures that could be considered for mid-infrared photodetection [35, 36]. Indeed, quantum well infrared photodetectors (QWIP) make use of intersubband absorption within the wells and mid-infrared applications were demonstrated in wider gap materials such as InGaAs. InGaAs/InGaP MQW grown strain-compensated on InP substrate shows a peak detectivity of 3.2×10^{10} cm.Hz$^{1/2}$.W^{-1} at 110 K [37]. InGaAs/GaAs MQW processed in a one mega pixel focal plane array (FPA) showed peak response around 4.6 μm at 77 K for back illumination through a 45^{o} facet [38]. Unfortunately, QWIP do not easily allow normal incidence detection and show low quantum efficiency [39]. Quantum dots infrared photodetectors (QDIP) do not suffer from normal incidence

limitation and show low thermal generation. GaAs/InAs QDIP demonstrated a peak detectivity at 3.7 μm $D^* \sim 3\times10^9$ cm.Hz$^{1/2}$.W^{-1} at 100 K [40]. However, efficient photodetection from quantum dots require a high density of dots only obtained through careful growth conditions [36]. Last, both QWIP and QDIP technologies are not mature yet to produce room temperature devices in the 3 - 5 μm spectral range [41]. The development in mid-infrared photodetectors is summarised in Table 3.1.

device	T_{op} (K)	λ_{op} (μm)	material	D^* (cm.Hz$^{1/2}$.W^{-1})	reference
pyroelectric	300	2 - 20	VO_x	$< 1\times10^9$	[26]
PC	300	3 - 4.6	PbSe	$> 3\times10^9$	[27]
PC	77	5	HgCdTe	$\sim 1\times10^{11}$	[27]
PC TE	20	5		$\sim 5\times10^{10}$	[27]
PC	295	4		$\sim 2\times10^9$	[29]
PC TE OI	295	4		$\sim 6\times10^{10}$	[29]
PD	295	4		$\sim 8\times10^8$	[29]
PD TE OI	295	4		$\sim 6\times10^{10}$	[29]
PD PV	300	2.4 - 3.5	InAs	$\sim 1\times10^9$	[27]
PD	77	4.7	InSb	$> 1\times10^{11}$	[27]
PD	300	4.6	InAsSb on InAs	$\sim 1.3\times10^9$	[31]
PD	250	3.39	InAsSb on GaSb	$\sim 4.5\times10^9$	[33]
QWIP	110	4.9	InGaAs/InGaP	$\sim 3.2\times10^{10}$	[37]
QDIP	100	3.7	GaAs/InAs	$\sim 3\times10^9$	[40]

Table 3.1 Summary of developments in mid-infrared photodetectors, where T_{op} is the operation temperature, λ_{op} the operation wavelength and D^* the spectral detectivity. PC stands for photoconductive, PD for photodiode, PV for photovoltaic, TE for thermo-electric cooling and OI for optically immersed

3.1.3 Proposed approach with InAsN

Whereas InAsSb seemed to be a good candidate for mid-infrared photodetection in the 3 - 5 μm spectral range, it suffers from high lattice mismatch

when grown on InAs substrate. InAsSb photodetectors grown on GaSb substrates suffer from high dark current. Quantum structures do not seem to offer yet solutions for room temperature operation. InAsN could be another approach to access the mid-infrared spectral range.

InAsN is a promising dilute nitride material for 3 - 5 μm range because of the strong bowing effect related to the incorporation of nitrogen. A bandgap reduction between 15 to 40 meV/at.% N is expected at room temperature, therefore only a small amount of nitrogen (1 - 2 % N) should be needed to reach 4.2 μm with a limited lattice mismatch to InAs substrates. The poor quality observed in dilute nitride materials such as GaInNAs [42] shows the importance to determine the growth parameters that control material quality and nitrogen incorporation in InAsN. Moreover, the incorporation of Sb in InAsN may offer the possibility to balance the strain and achieve lattice matching to InAs substrate.

3.1.4 Further optimisations of photodetectors

For high performance photovoltaic detectors, the structure of the photodetector must be optimised to maximise the amount of absorbed radiation, limit non-radiative processes, such as Shockley-Read-Hall (SRH) or Auger recombinations, and reduce noise and dark current. For instance, limitation of the non-radiative processes and reduction of the dark current can be achieved through doping optimisations [34, 43]. Achieving a compromise for the thickness of the active region can help maximising the absorption of light (thick material) and minimising SRH generation-recombination processes. Strain-related non-radiative processes can be reduced by the use of a buffer layer as previously mentioned, and a barrier with a suitable thickness can help reduce the contribution of diffusion currents [32]. Passivation of the structures is another

means to improve the performances of a photodetector. Passivation (by sulphidisation) was found to reduce surface leakage currents due to oxidisation and dangling bonds at the surface of InAsSb photodetectors [43]. The I-V characteristics was improved and $R_0\mathcal{A}$ increased (refer to equation (2.28)). Silicon dioxide (SiO_2) passivation was also shown to be efficient in increasing the resistivity of the device and reduce the dark current [44]. Last, the amount of light absorbed can be increased if multiple passes of radiation are used : a backside reflector allows absorption over an active region with twice as thick an apparent thickness ; the addition of two layers sandwiching the active region can also be designed to set up constructive interference [45]. Moreover, the use of various optical concentrators can increase the apparent optical size of the detection area.

3.2 Epitaxial growth techniques

Liquid Phase Epitaxy (LPE) is a thermodynamic equilibrium growth technique using components in liquid solution at temperature below their melting point [46] and controlled essentially by diffusion processes near the surface of the substrate. Inside a hot furnace, liquid melts contained in sliding graphite boats set onto a heated substrate when cooling down. The quality of bulk materials achieved is generally good, but LPE-grown materials suffer from high surface roughness and poor thickness uniformity [47]. High growth rates do not allow abrupt interfaces which are beneficial and the use of boats and sliders makes the growth of sub-micron structures difficult despite a few successful attempts [48, 49].

Metal Organic Chemical Vapour Deposition (MOCVD), referred to as Metal Organic Vapour Phase Epitaxy (MOVPE), uses vapour metal organic species – alkyl compounds for group-III elements and hydride compounds for group-V elements. The

gases are directed over a heated substrate in a near atmospheric pressure reactor where they decompose, in the 500 - 800^{o}C temperature range for III-V materials. It is an advantageous technique for phosphorous-containing materials [50a], but the presence of organic precursors complicates the growth and can limit the achievable purity.

Molecular Beam Epitaxy (MBE) is an evaporation growth technique [50b] producing molecular beams by the decomposition of gases (Gas Source MBE or GSMBE) or by the sublimation of solids contained in crucibles (Solid Source MBE or SSMBE) to supply the elements of the alloy to be grown (see Section 4.1). The growth on a rotating heated substrate takes place in a reactor under ultra-high vacuum, to improve the purity of the films and prevent reaction between the different precursors [51]. Ultra-high vacuum conditions make this technology a non-equilibrium growth technique governed by the kinetics of the surface processes [47]. The growth can be monitored by Reflection High-Energy Electron Diffraction (RHEED) and the ability to operate quickly the shutters of the cells makes abrupt interface and single atomic layer growths (and below) possible, as demonstrated widely in the literature on quantum wells and quantum dots.

3.3 Dilute nitride materials

The discovery in the mid-1960s of a bound state in the forbidden bandgap of GaP introduced by nitrogen doping was a decisive step to foster interest in dilute nitride materials [52]. Isolated nitrogen states and nitrogen pair states were brought to light and the N level was investigated by the application of hydrostatic pressure in GaPN in the 1970s. The same method led to the observation of a nitrogen level in GaAs in the early 1980s. From the early 1990s, GaAsN and InGaAsN alloys were

grown by MBE and by 1994, the Hitachi group reported operational laser diodes based on III-V nitride semiconductor materials.

Growth conditions such as growth temperature, growth rate, nitrogen plasma power and element fluxes strongly influence the surface quality, nitrogen incorporation and luminescence in dilute nitride materials. For instance, bulk InGaAsN grown by MBE at temperatures between 390^{o}C and 460^{o}C shows a smooth surface : the root-mean-square (rms) roughness measured by AFM (see Section 4.2.4) is only 0.6 nm. The surface is found to be rougher for a growth temperature of 520^{o}C with an rms roughness three times higher [51]. It is also reported that the luminescence gets brighter and the emission peak becomes narrower for growth at 460^{o}C, leading to a narrow window for good crystallinity. N plasma radio-frequency (RF) power, between 300 W and 400 W, and fluxes used, of 0.3 to 0.5 sccm, can be jointly varied with growth rates in the range of 1.5 μm/h to 3.0 μm/h to change efficiently the supply of nitrogen radicals. The nitrogen content in bulk MBE-grown InGaAsN decreases linearly with increasing growth rate independently of the In/Ga ratio [51]. It is also reported that in InGaAsN/GaAs SQW, increasing the growth rate (see Section 4.1.5) reduces the full-width at half maximum (FWHM) of the PL. The flux ratio between the group-V and the group-III elements, referred to as V/III ratio, is normally kept to values between 5 and 7 as an optimum to improve the crystalline quality whereas bulk GaAsN on GaAs is best grown by MBE with unity V/III ratio [53].

Nitrogen has strong repercussions on the electronic and optical properties of the material. The nitrogen atom reduces the size of the lattice in InGaAsN and GaAsN and a huge bowing effect along with a reduction of the bandgap are observed as shown in Figure 3.6. The calculation of the lattice size is based on Vegard's law,

shown to be valid for dilute nitrides with nitrogen contents up to 10 % [54 and references therein]. Bandgap reduction in the order of 0.15 eV/at.% N are reported for InGaAsN [19] and of 0.13 to 0.18 eV/at.% N for GaAsN [55]. The blueshift of the PL as the excitation power increases is a signature of the presence of nitrogen localised states (no explanation has been given about this effect) [14]. The temperature sensitivity of the bandgap decreases with the addition of N in GaAs as well [56]. The optical properties of the GaInAsN and GaAsN degrades with the incorporation of nitrogen [53, 57]. In GaAsN and InGaAsN, the electron effective mass increases with nitrogen content [58, 59], hence the mobility decreases with higher nitrogen content. Consequently, the CB gets flatter at the Γ-point and a high non-parabolicity can be deduced. It can be estimated that up to 15 % N would be needed in GaAsN to achieve 4.2 µm (0.295 eV) at room temperature [60] whereas 1.5 % N would be sufficient in InAsN [61].

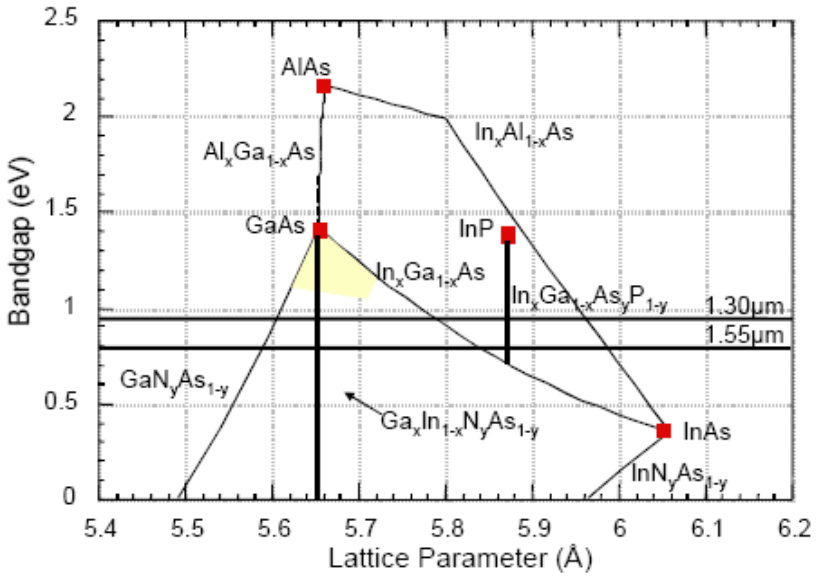

Figure 3.6 Bandgap versus lattice constant for GaAsN, InGaAsN and InAsN [57]

Several models have been proposed to describe the dependence of the electronic properties (and namely the bandgap energy) on the nitrogen composition in dilute nitrides, GaAsN and InGaAsN in particular. The empirical pseudopotential method describes the crystal in a polymorphous approach instead of a single pattern for the atomic distribution and takes relaxation into account [56]. It is used to simulate the optical and electronic properties of a supercell, i.e. a collection of several tens of thousands atoms. It nevertheless requires the specification of the size of the nitrogen chain or cluster and predicts mainly qualitative but reliable results.

The tight-binding and ***k.p*** models suggest that nitrogen introduces a resonant defect level above the conduction band edge and the repulsion of the two is the cause of the bandgap bowing [62, 63]. It takes into account the dependence on the atomic nearest neighbour. This method adds two states to the eight-band conventional ***k.p*** model and manages to model the bandgap energy as a function of the nitrogen composition or of the wave vector.

The band anticrossing model (BAC, see Section 2.4.2), that considers the hybridisation of the localised nitrogen states with the extended states of the conduction band, was successfully applied to InGaAsN [17, 18] and GaAsN [15]. Its two states-approach is both simple and consistent and manages to explain the E_+ and E_- bands observed by absorption measurements. The composition and wave-vector dependences of the bandgap, absorption coefficient and density of states are modelled for bulk and QW [60].

The progressive mastering of GaAsN and InGaAsN growth opened the way to a wide variety of commercial applications. The introduction of 4.5 % of nitrogen in bulk GaAsN enables one to reach 1.33 μm at room temperature [53] and the addition of In allows growth lattice-matched to GaAs. Indeed, InGaAsN VCSEL (vertical-

cavity surface-emitting lasers) were demonstrated at 1.3 μm and InGaAsN edge-emitting lasers have even reached 1.5 μm as required for telecommunication applications [57]. InGaAsN can also be used advantageously over InGaAs in the base of heterojunction bipolar transistors (HBT) to reduce the turn-on voltage [64].

It can be seen that nitrogen has the potential to extend the wavelength of GaAsN and InGaAsN materials, but to keep the good crystallinity of the alloys its incorporation must not exceed a few percent. It thus makes GaAsN and InGaAsN poor candidates to achieve wavelengths above 3 μm.

3.4 Growth conditions of InAsN

InAs has a bandgap energy of about 415 meV at 4 K [12], which corresponds to a wavelength of 3 μm. Introducing nitrogen is expected to increase the material wavelength and this is encouraged by the much higher calculated solubility of nitrogen in InAsN compared to GaAsN [65]. Some epitaxial growth difficulties are to be expected though, due to the miscibility gap which originates from the large difference in atomic size and electronegativity.

3.4.1 Recent developments in InAsN research

MOCVD growth of InAsN bulk, quantum wells and dots on GaAs substrate were reported from 1997 on by Osiński *et al.* [66, 67], Lee *et al.* [68] and Naoi, Sakai *et al.* [69, 70]. From 1998, the latter attempted one of the early MBE growths of bulk InAsN on GaAs [71], along with Beresford *et al.* [72].

Growth by MBE was first reported in 2001 by Lin *et al.*, who grew InAsN by GS-MBE and various InAsN structures on InP substrate at National Taiwan

University (Taiwan, ROC) [73-80]. During this project, strong collaboration with Prof. Lin's group in Taipei was pursued. Bulk, SQW and MQW have been grown from 2003 by Onabe, Kuroda *et al.* at the University of Tokyo (Japan) who reported InAsN by RF-MBE on GaAs substrate [61, 81-83]. The latest reported MBE growths of bulk InAsN, on *InAs* substrate this time, date from 2005 and were achieved by Harmand *et al.* [84] and Veal, Hopkinson *et al.* [85].

In the following, the growth of *bulk* InAsN for infrared photodetection applications was favoured to quantum wells and quantum dots structures (see Section 3.1.2). Indeed, quantum well infrared photodetectors (QWIP) in wider gap materials do not easily allow normal incidence detection [39] and show low quantum efficiency [35]. While quantum dots infrared photodetectors (QDIP) do not suffer from normal incidence limitation and show low thermal generation, the technology is not mature yet to produce room temperature devices in the 3 - 5 μm spectral range [41]. The little information available on bulk InAsN material led to broaden the research of growth conditions to all types of structures.

3.4.2 Alternative growth techniques

Efforts to grow InAsN were initially put in MOCVD and nitridation of InAs. An early attempt to grow InAsN by MOCVD failed to grow a continuous film ; the linearity of the absorption coefficient at high photon energy demonstrated the direct bandgap of InAsN though [69]. It was proposed to misorientate the GaAs substrate by 2^{o} towards [001] but this did not seem to improve the layer that often showed separated phases of InAs or InN [70]. The influence of the MOCVD growth temperature was also studied. In the growth temperature range 450^{o}C - 550^{o}C, InN was always and predominantly formed (along InNAs) ; no InAsN was formed *below*

475°C. Reduction in the N incorporation from 13 % to 7 % with an increasing temperature between 500°C to 550°C was attributed to lower N solubility at higher temperature. Quantum structures were reported by MOCVD. InAsN/GaAs QW on GaAs were reported from 2001 [66, 67] with an alleged 18 % N composition and very broad luminescence (65 meV) around 7 μm at 193 K. In this case though, the calculated lattice mismatch was higher than 3.7×10^{-2}. InAsN QD were successfully grown by MOCVD on GaAs substrate with a narrow PL emission at the telecom wavelength 1.3 μm at room temperature [68]. Despite these results, MOCVD growth of InAsN was not favoured due to the rough surface obtained for bulk material as shown in Figure 3.7.

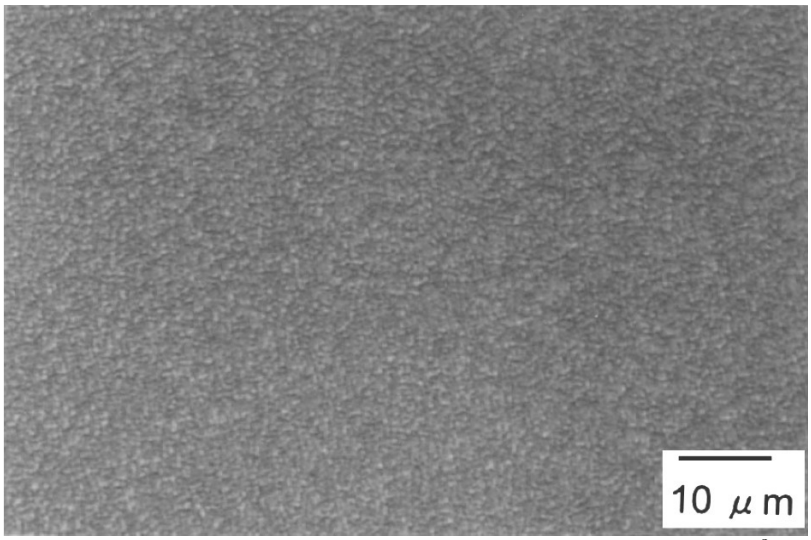

Figure 3.7 Surface micrograph of an InAsN sample grown by MOCVD at 500°C [70]

Attempts to produce InAsN by nitridation of InAs surfaces were performed by annealing substrates at temperatures ranging from 450°C to 600°C under NH_3 flow [86]. A compound with N, In and As was formed at temperatures below 500°C, but only in an amorphous phase.

3.4.3 MBE growth conditions

From the literature, it seems that molecular beam epitaxy is the favoured growth technique to realise InAsN. Apart from the group-IV silicon substrate widely used in the chip semiconductor industry, the most conventional III-V substrates that could be used are GaAs and InP.

The first MBE growth of bulk InAsN was reported in 1995 on *GaAs* substrate [87], but the nitrogen content was not measured. Three years later, V/III BEP ratios > 1 were shown to prevent InAsN from growing on GaAs while unity V/III ratio and growth temperature between 450°C and 500°C led to a metastable InAsN alloy phase simultaneously obtained with InAs [72]. A rough surface with triangular-shaped islands was observed for an InAsN layer containing supposedly ~ 38 % N under comparable growth conditions [71], as shown in Figure 3.8.

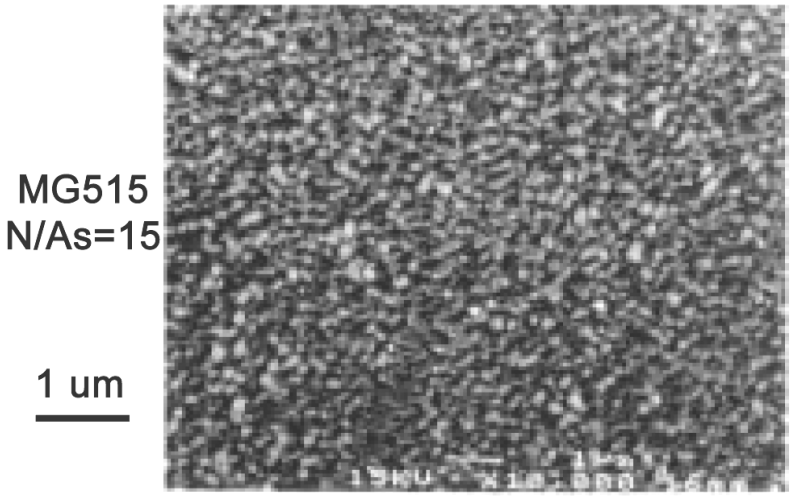

Figure 3.8 Early InAsN grown by MBE on GaAs substrate with alleged nitrogen composition of 38 % [71]

In 2003, Nishio, Onabe *et al.* [82] obtained bulk InAsN epilayers with mirror surface quality thanks to the use of a 0.8 µm-thick InAs buffer on GaAs : it reduced the lattice mismatch to 10^{-3} and the roughness measured by AFM was lower than 9 nm

in the growth temperature range 420°C - 510°C. They reached a nitrogen composition of 1.62 % with As/In ratio of 20 and 0.8 μm/h growth rate. Later InAsN growths on GaAs used similar As/In ratios and a nitrogen plasma power in the range 175 W - 250 W [61, 81]. The room temperature absorption band edge lies below 400 meV for a sample containing about 2.3 % N. As far as quantum structures are concerned, Kuroda, Onabe *et al.* obtained the growth of one monolayer-thick InAsN/GaAs SQW by RFMBE on GaAs substrates [83] with PL emission below 1.3 eV at 10 K [61].

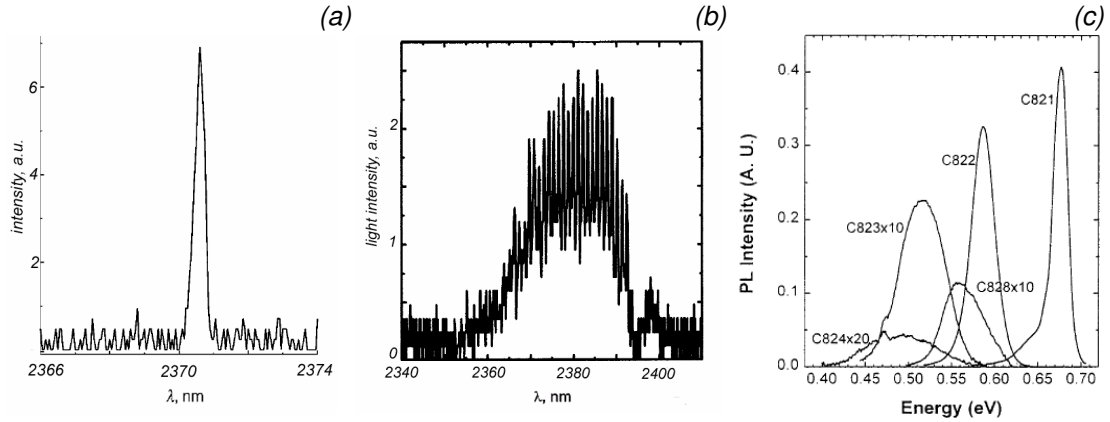

Figure 3.9 InAsN MQW-based structures grown on InP substrates : (a) 200 K laser emission from 8 QW [90] ; (b) 260 K laser emission at 2.38 μm from 4 QW [75] ; (c) 10 K PL from annealed MQW with nitrogen composition 0 %, 1.1 %, 2.5 %, 3.5 %, 5.9 % (right to left) [73]

Prof. Lin's group at National Taiwan University reported several growths of bulk InAsN on *InP* substrates ((100)-oriented) by GSMBE [74, 88]. With an initial InP buffer, InAsN was grown without growth interruption, with N plasma power ranging from 200 W to 480 W and As/N ratio of about 2 to 3. Up to 3.0 % nitrogen was incorporated [16] and absorption measurements were systematically performed. No luminescence from bulk material was evidenced though. A variety of QW structures were successfully grown on InP substrates. Prof. Lin's group produced GSMBE-grown InAsN/InGaAs MQW lasers emitting at 2.38 μm up to 260 K [75], as

shown in Figure 3.9 (a) and (b). In InAsN/InGaAsP MQW structures, the nitrogen composition, found to increase with decreasing growth temperature, reached 5.9 % and 480 meV PL emission (2.6 μm) was demonstrated at 10 K [73], as shown in Figure 3.9 (c). InAsN/InGaAs SQW were grown on InP with low nitrogen content (< 0.5 %) and the absence of room temperature luminescence is attributed to high concentration of radiative centres [89].

The choice of the substrate turned out to be critical but none of the aforementioned structures, from bulk to quantum wells, whether on GaAs or InP substrates, seemed to easily demonstrate luminescence below 400 meV (that is above 3 μm), maybe because of the high lattice mismatch between InAsN and the substrates. Choosing InAs substrate could alleviate the strain issue. It seems preferable to grow dilute nitrides by solid source MBE since some nonradiative recombination centres (traps) in GaInNAs grown by MOCVD and gas source MBE can be attributed to hydrogen impurities originating in the supplied hydrogen [91].

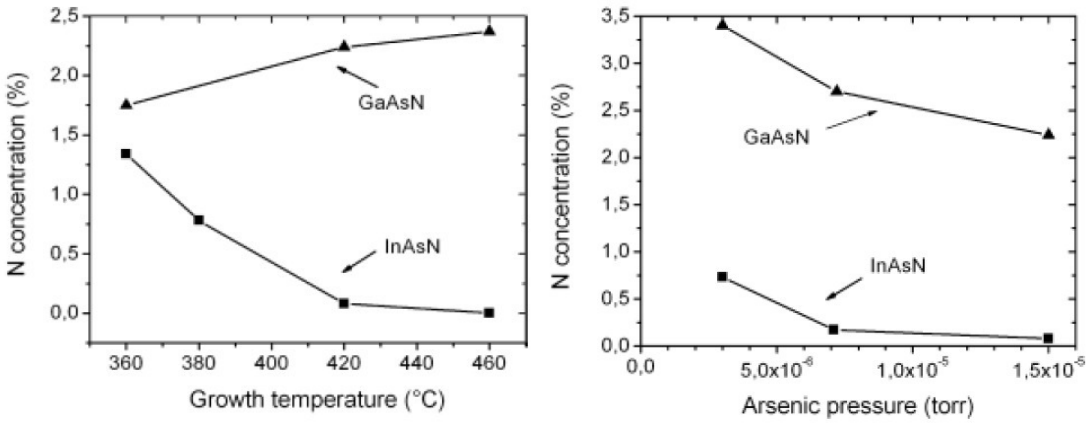

(a) (b)

Figure 3.10 N composition in InAsN and GaAsN as a function of : (a) the growth temperature ; (b) the arsenic pressure [84]

To the best of our knowledge, only two papers report the growth of bulk InAsN on InAs substrates (100-oriented) by plasma-assisted MBE and these were

published in 2005 after the start of this research project. Sallet, Harmand *et al.* [84] succeeded in the growth of InAsN films on 0.3 μm-thick InAs buffer at 450 W plasma power, V/III ratio of 20, growth rate of 2 Å/s (0.72 μm/h) in the temperature range 360°C - 420°C. As shown in Figure 3.10, the nitrogen content increases with decreasing growth temperature and arsenic flux (hence decreasing V/III ratio) and reached 1.4 %. Veal, Hosea, Hopkinson *et al.* [85] grew InAsN at 375°C with an identically thick InAs buffer, which allowed them to incorporate up to 2.8 % N. Luminescence below 350 meV at 77 K was measured by Fourier transform infrared spectroscopy (FTIR).

Finally, optimal MBE growth conditions of InAs can just be mentionned. InAs is best grown by MBE at growth temperatures between 470°C and 490°C when a 2×4 RHEED pattern is observed [84, 92, 93].

It can be seen that InAsN grown by MBE on InAs substrate is a novel dilute nitride material that has the potential to reach mid-infrared wavelengths above 3 μm suitable for gas sensing. A low growth temperature is required, but there is no consensus on the optimal V/III ratio, growth rate or nitrogen plasma power. The intrinsic close lattice matching to the substrate is expected to produce good crystallinity. Room-temperature luminescence will hopefully be demonstrated once the growth conditions are optimised.

3.5 InAsN characteristics

First and foremost, let us briefly review *InAs* properties. This III-V alloy can be obtained with high crystal quality. The bright luminescence transition in InAs is assumed to conserve the wave vector ; its bandgap energy at absolute zero temperature is estimated to be 415 meV (2.99 μm) [12] and reaches 350 meV

(3.54 μm) at 300 K [6]. Very narrow XRD FWHM is observed from bulk InAs buffer (19 arc sec) that compares favourably with InAs substrate (14 arc sec) [84]. A few electronic parameters for InAs are compared to GaAs and InP in Table 3.2 (Si is mentioned for reference). InAs is naturally n-type. Electron mobility and electron saturation velocity at the Γ-point and 300 K are higher in InAs than in GaAs and InP, pointing out potential improved electronic transport. Electron effective mass at the Γ-point in InAs is almost three times lighter than that of GaAs. The Γ-valley is thus much narrower in InAs. InAs intrinsic resistivity is extremely low compared to GaAs and InP (eight orders of magnitude higher), which makes it a better conductor. Nevertheless, the intrinsic carrier concentration in InAs is very high at 1×10^{15} cm^{-3} (only 2.1×10^{6} cm^{-3} in GaAs), which will make high doping levels required.

Parameter / Material	InAs	GaAs	InP	Si	*reference*
Bandgap energy at 300 K (eV)	0.354	1.424	1.344	1.12	[6]
Electron mobility ($cm^2.V^{-1}.s^{-1}$)	4.0×10^{4}	8.5×10^{3}	5.4×10^{3}	1.4×10^{3}	[6]
Electron saturation velocity ($cm.s^{-1}$)	0.90×10^{7}	0.72×10^{7}	0.68×10^{7}	1.02×10^{7}	[21]
Electron effective mass	0.023 m_0	0.063 m_0	0.080 m_0	0.980 m_0	[6]
Heavy hole effective mass	0.41 m_0	0.51 m_0	0.60 m_0	0.49 m_0	[6]
Intrinsic resistivity (Ω.cm)	1.6×10^{-1}	3.3×10^{8}	8.6×10^{7}	3.2×10^{5}	[6]
Intrinsic carrier concentration (cm^{-3})	1.0×10^{15}	2.1×10^{6}	1.3×10^{7}	1.0×10^{10}	[6]

Table 3.2 Selected electronic parameters of usual substrate materials

3.5.1 Optical and structural properties

Contradictory results about InAsN absorption coefficient were published by Lin *et al.* [16, 74] and Kuroda *et al.* [81]. The high residual carrier concentration is indeed an issue to determine precisely the absorption band edge. The up-to-date

results [61] are those shown in Figure 3.11. The absorption edge unexpectedly shifts to higher energy with increasing nitrogen content, whereas the contrary occurs in GaAsN [94], and its tailing becomes more important.

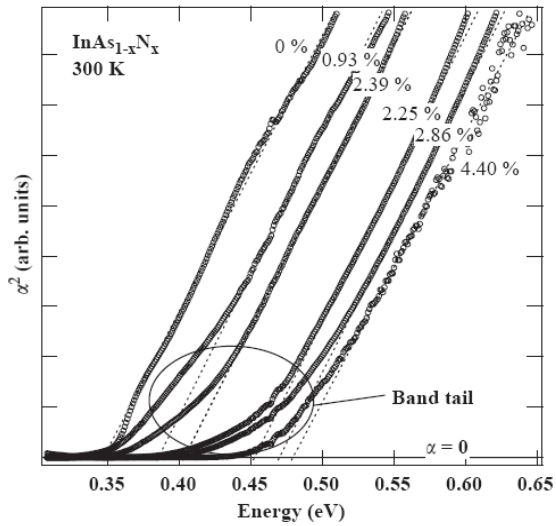

Figure 3.11 FTIR absorption spectra of bulk InAsN with increasing nitrogen content [61]

XRD rocking curves for bulk InAsN with up to 2.8 % nitrogen [85] are shown in Figure 3.12. The epilayer peak is at higher diffraction angle than that from the InAs substrate. It indicates a smaller lattice constant and InAsN thin films grown on InAs substrates are under tensile strain. The epilayer peak gets wider and less intense with increasing nitrogen content. It is a sign of the degradation of InAsN quality when more nitrogen is incorporated into the crystal.

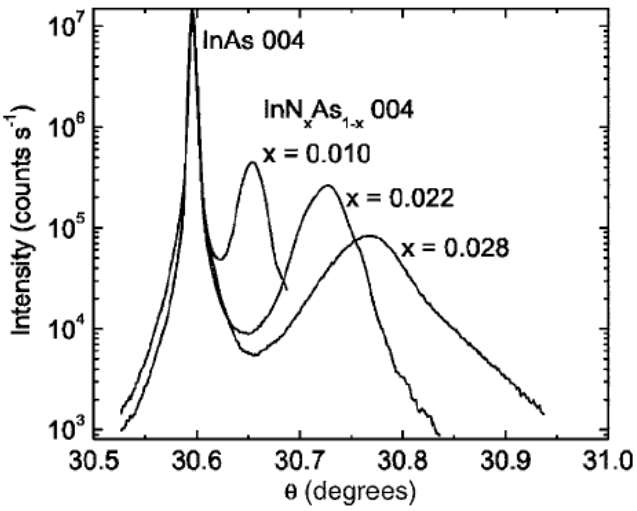

Figure 3.12 XRD rocking curves of bulk InAsN with different nitrogen composition [85]

Luminescence from bulk InAsN on InAs [85] is shown in Figure 3.13 (a). A blueshift is observed between 77 K and ~ 175 K before the emission redshifts at higher temperatures. This is attributed to the localisation of electrons in potential fluctuations due to inhomogeneous nitrogen distribution in the layer. The broad emission is alleged to result from contributions due to localised excitons (LE) at low energy and free excitons (FE) at high energy. The PL emission redshifts with higher nitrogen composition. It is quite noticeable that the absorption edge shown in Figure 3.11 behaves oppositely. It must be acknowledged that this observation is anomalous and unclear. Figure 3.13 (b) demonstrates the decrease in PL intensity and widening of the PL spectrum of InAsN/InGaAs SQW with increasing N flux. Reasons of degradation of the material quality with higher nitrogen composition rest on the growth conditions, as will be demonstrated in Section 5.2.

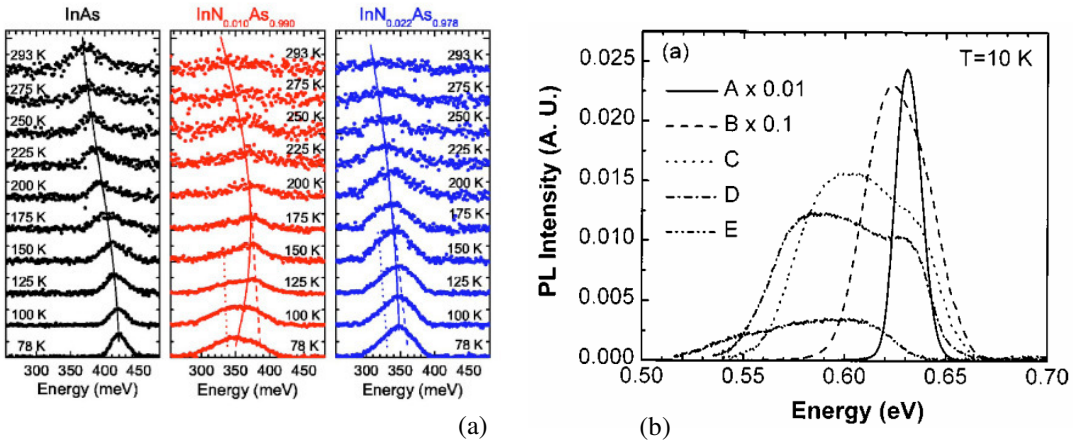

Figure 3.13 (a) Temperature-varied PL of bulk InAsN for different nitrogen content [85] ; (b) 10 K PL of InAsN/InGaAs SQW with no nitrogen (A) and increasing N flux (B to E) [89]

3.5.2 Electrical properties

Hall effect measurements were carried out on bulk InAsN films grown on GaAs substrate without InAs buffer to avoid carrier parallel conduction [81]. Figure 3.14 shows temperature-dependent electron concentration and Hall mobility for different nitrogen composition compared with silicon-doped InAs. Electron concentration increases with increasing N concentration while Hall mobility decreases. Both are less sensitive to the temperature with increasing N content. Even for layers containing as much as 2.26 % N, nitrogen seems to behave very similarly to a donor impurity in InAs:Si.

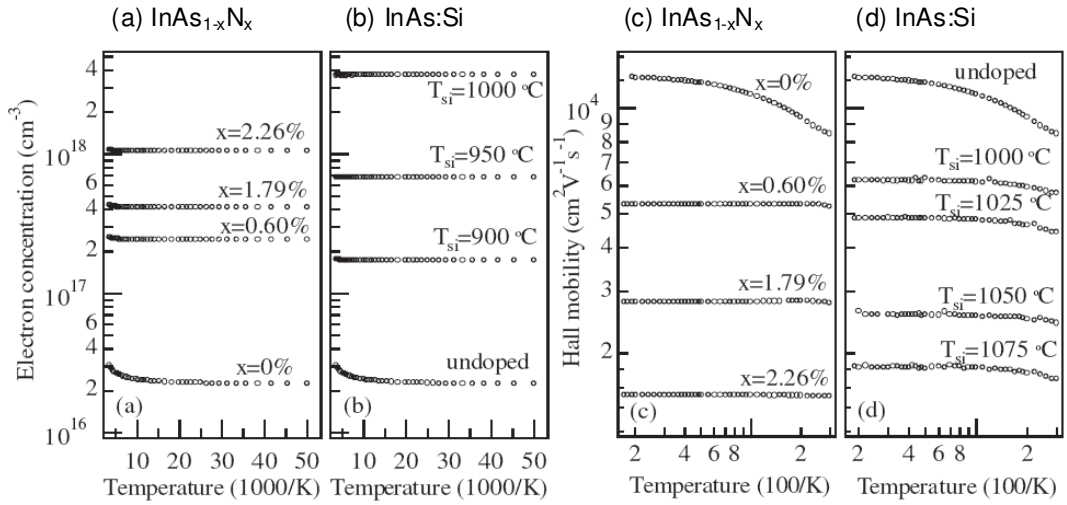

Figure 3.14 Electron concentration vs. inverse temperature for : (a) $InAs_{1-x}N_x$ and (b) InAs:Si ; Hall mobility vs. inverse temperature for (c) $InAs_{1-x}N_x$ and (d) InAs:Si [81]

Electron effective mass was demonstrated to increase with increasing nitrogen composition in bulk InAsN and MQW [16, 80, 88] as shown in Figure 3.15, because of a strong interaction of the conduction band minimum with upper states as explained by the band anticrossing model (see Section 2.4.2). The increasing value of the electron effective mass results in a flattening of the conduction band.

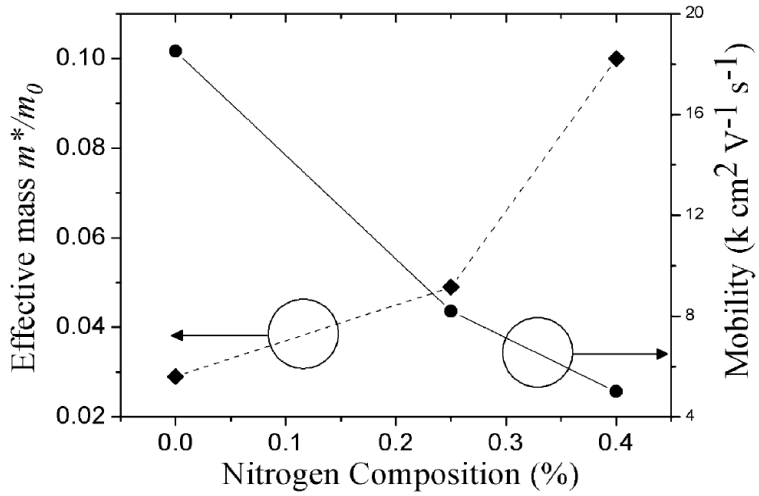

Figure 3.15 Electron effective mass and estimated carrier mobility as a function of nitrogen composition near the liquid-helium temperature [80]

3.5.3 Bandgap

InAsN alloy has a direct bandgap [69] and the valence band is unaffected by small amounts (< 1.2 %) of nitrogen [17]. As far as the bandgap reduction with nitrogen content is concerned, a room temperature energy shrinkage of 39 meV/at.% N can be deduced from absorption measurement by linear fitting in bulk InAsN grown on GaAs [61] over the compositional range 0 to 2.8 % N. This is in excellent agreement with 38 meV/at.% N that can be calculated from Naoi's *et al.* work [69] (over a wider compositional range), while only 15 meV/at.% N (0 to 2.8 % N) is reported for InAsN on InP substrates [16] and 23 meV/at.% N can be deduced from InAsN study on InAs substrates [85].

The bandgap for InAsN on InAs was unsuccessfully modelled by the dielectric method and the tight-binding model [16]. It appears that the band anticrossing model is the only suitable model [61] as shown in Figure 3.16. It must be noted that the composition was obtained from XRD measurements and the room-temperature bandgap energy from absorption measurements.

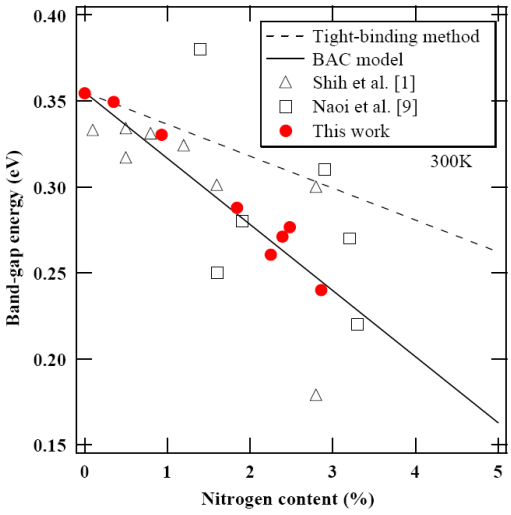

Figure 3.16 Bandgap energy of InAsN derived from absorption measurements and theoretical curves of the tight-binding method and BAC [61]

A bowing parameter is sometimes mentioned for conventional ternary and nitride alloys when the dependence of the energy bandgap on alloy composition is described by a quadratic form [23]. This formulation is *not* applicable to dilute nitrides [18] for which the BAC is preferred, since only the latter describes correctly the behaviour of nitride materials with a few percent of nitrogen.

3.6 Annealing and rapid thermal annealing

Dilute nitrides often show poor properties. In GaInAsN, they were attributed to the presence in the as-grown material of Ga vacancies, due to insufficient migration of the atoms during growth at low temperature, and nitrogen interstitials and split interstitials, energetically favoured under certain growth conditions [95]. To overcome this shortcoming, a post-growth baking technique named annealing is used to improve the crystal quality of low quality material. Characterisations of the improved material can help determine the origin of the defects in the as-grown material and the mechanisms responsible for their reduction during annealing.

3.6.1 Thermal annealing

Long time in-situ annealing was proposed for GaInAsN grown at 550^{o}C [96]. Baking the crystal in the MOCVD chamber for 30 min at 700^{o}C or for 100 min at 600^{o}C helps the formation of In-N bonds instead of the majority Ga-N bonds, reducing the local strain. Crystallographic changes are achievable through annealing.

Annealing is more commonly performed in a rapid thermal annealer where high temperatures can be reached with extremely fast temperature ramps. The equipment consists of a lamp-heated quartz chamber, under nitrogen atmosphere, with accurate temperature and heating time control. Long-time annealing with such

apparatus was reported for various InAsN-containing MQW. Long time annealing conditions range from 5 min at 550°C for InAsN/GaAs MQW on GaAs substrates [66, 67] to 15 min at ~ 525°C for InAsN/InGaAsP MQW [73] and InGaAs/InAsN SQW (Si-capped) grown on InP substrate [89]. The latter study reported a 10 K PL intensity improved by 230 times with a reduction in the linewidth, as shown in Figure 3.17 ; an increasing blueshift with annealing temperature was observed though and attributed to quantum well intermixing.

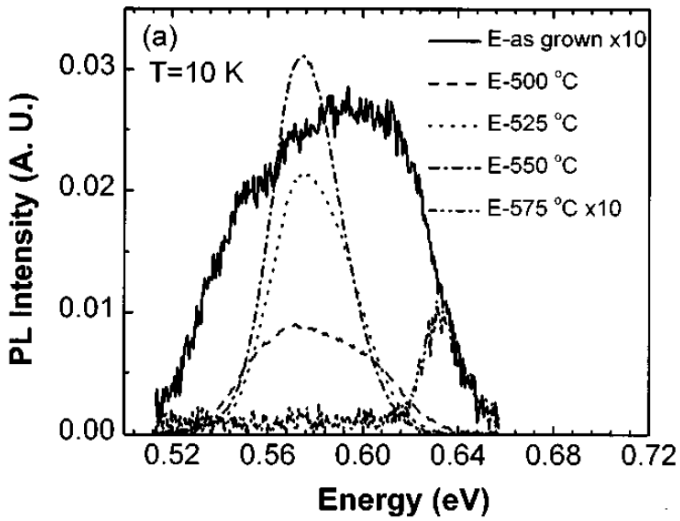

Figure 3.17 10 K PL after long time annealing on InAsN/InGaAs SQW grown on InP [89]

3.6.2 Rapid thermal annealing

A recent interesting study on GaInAsN compared long-time annealing and rapid thermal annealing (RTA), a short-time annealing technique [97]. It demonstrated that a strong blueshift regime is followed by a weak blueshift regime with increasing annealing temperature. Long-time annealing (up to 140 min) led to slightly wider PL spectrum than short-time annealing (60 s). It also showed that the blueshift of the bandgap and the PL intensity improvement are unrelated effects.

RTA was previously applied successfully to GaNAs [98] and GaInNAs materials [95, 99, 100]. The use of GaAs wafers face-to-face with the sample was

advised to prevent arsenic evaporation from the surface. Annealing times shorter than one minute are generally reported for RTA of bulk GaInAsN, annealed for 30 s at 750°C [95], and GaInAsN quantum wells, annealed for up to 20 s at temperatures between 650°C and 850°C [99, 100]. The annealing temperature is generally higher than the MBE growth temperature but RTA of GaN at too high temperature led to surface decomposition [101].

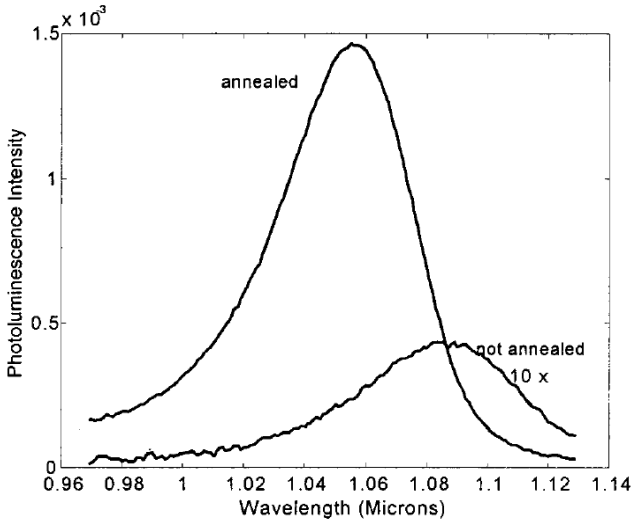

Figure 3.18 Typical PL improvement and blueshift after annealing, for annealed GaNAs/GaAs MQW [102]

RTA of dilute nitride materials at optimal annealing temperature improves the PL intensity but a blueshift of the peak wavelength is often observed, as shown in Figure 3.18. The improvement of the luminescence by RTA is generally attributed to the annealing out of defects or the elimination of some grown-in competing non-radiative channels [98]. Unfortunately, a blueshift is commonly observed, namely because of interdiffusion of group III or As-N split interstitials [95, 99]. A recent detailed study of annealed GaInNAs identified several additional mechanisms responsible for the blueshift : reduction of N-related defects, homogenisation of the nitrogen profile, outdiffusion of N at the interface or short-range ordering [100]. A

compensation redshift for interstitial N entering substitutional sites is also proposed in the lower part of the annealing temperature range. Last, a reduction of the PL dependency to the laser excitation power was observed as one of the effects of RTA on GaAsN and attributed to a better uniformity in the nitrogen distribution [14].

As a summary, short time annealing at relatively high temperature is preferred to longer time procedures to limit the PL broadening of the annealed sample. PL intensity and linewidth in dilute nitride materials can generally be improved by RTA but a blueshift is often observed. RTA is best performed under nitrogen atmosphere for a sample sandwiched between GaAs wafers. One will make sure not to use too high temperature to avoid damage of the crystal or its surface. Last, RTA can help identify the as-grown defects.

3.7 Surfactant effect of antimony and InAsNSb material

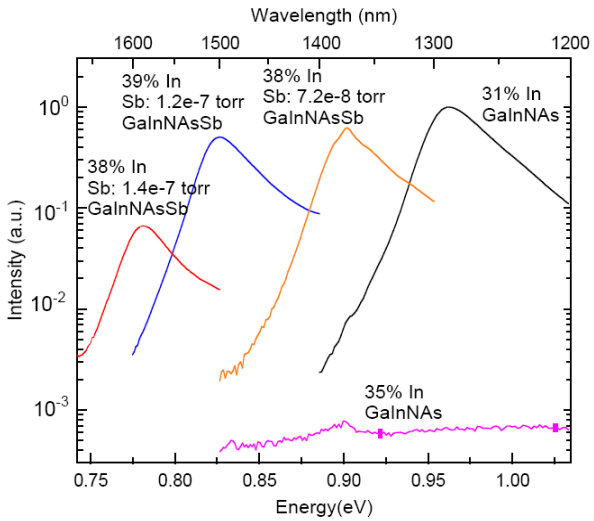

Figure 3.19 PL of GaInNAs(Sb) comparing the best 1.3 µm GaInNAs material and the drastic improvement with the addition of Sb [104]

Antimony is commonly used in GaInNAs(Sb) lasers to improve material and device properties [103, 104], as shown in Figure 3.19. Sb acts as a surfactant by

reducing the surface diffusion length in heteroepitaxial growth and preventing the formation of three-dimensional islands [105]. It avoids structural degradation and improves the luminescence of GaInNAs(Sb) material [106]. Concerning InAsNSb, very little has been published so far. Nevertheless, InAsNSb QW lasers were successfully grown on InP substrates by MBE with a wavelength up to ~ 2.3 μm with operation temperature up to 210 K [107, 108] as shown in Figure 3.20 (a).

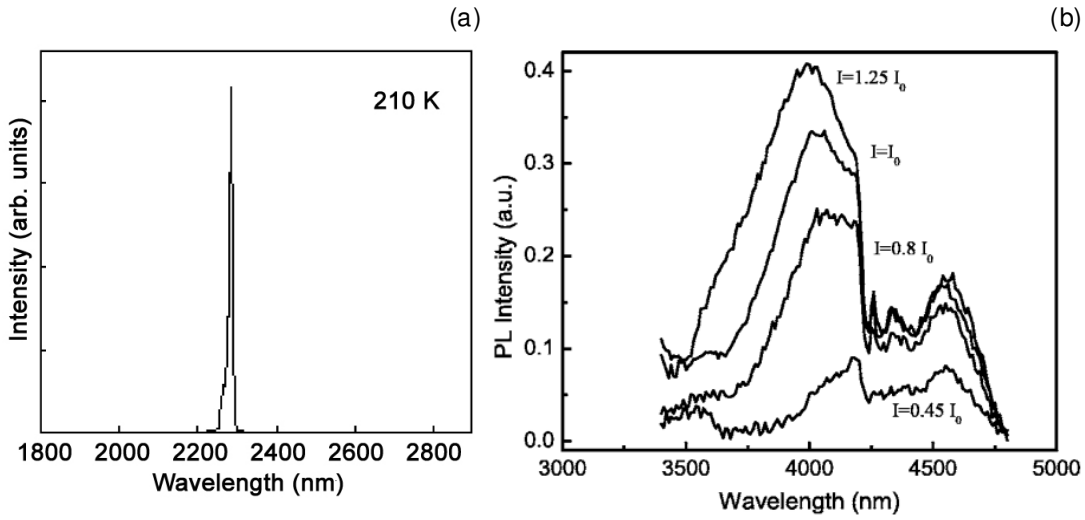

Figure 3.20 (a) 210 K spectrum of an InAsNSb QW laser diode grown on InP substrate [108] ; (b) 10 K PL of an InAsNSb SQW with various excitation powers [109]

On InAs substrates, one attempt of bulk InAsNSb material grown by melt epitaxy – a similar technique to LPE – was reported with no observed luminescence [110]. There is only one report which mentions the growth of InAsNSb, in which a SQW demonstrated PL around 4 μm at 10 K as shown in Figure 3.20 (b) and luminescence up to 220 K [109]. The same paper showed that the interface InAsNSb/InAs was a type-I band alignment. From that perspective, the growth of InAsNSb on InAs substrates opens the way for type-I devices, with the potential to reach 4.2 μm. The addition of antimony into InAsN can help in reducing the amount

of nitrogen required and balance the strain in the material to improve the material quality.

3.8 Summary

Mid-infrared photodetectors can be grown with various materials and structures and show typical spectral detectivity of ~ 2-3×10^9 cm.$Hz^{1/2}W^{-1}$ for uncooled operation. The limitations of HgCdTe, PbSe, InSb and InAsSb for room temperature photodetection, namely broad spectral response, lack of material uniformity or high lattice mismatch, show the possibility of a novel approach to reach the 3 - 5 μm spectral range. InAsN is a promising dilute nitride material for mid-infrared sensing applications in 3 - 5 μm spectral range because of the strong bowing effect related to the incorporation of nitrogen. The small amount of nitrogen needed in the material to achieve 4.2 μm wavelength allows a reduction of the lattice mismatch. Choices of V/III BEP ratios, nitrogen plasma power, growth temperature and growth rate are likely to alter nitrogen incorporation and material quality of MBE-grown InAsN. These growth conditions thus need to be optimised to obtain high quality material (characterised by luminescence up to room temperature and narrow XRD rocking curves) with a view on accurately controlling the nitrogen content. Some electronic properties were already reported but further investigations in nitrogen localisation states and InAsN bandgap are of interest to the dilute nitride community. Annealing InAsN material by RTA at high temperature for a short time may improve the bulk material and allow the study of potential defects. The addition of antimony in InAsN is likely to reduce the strain and improve the material quality. Photodiodes based on bulk InAsNSb lattice matched to InAs substrates are then imaginable for CO_2 detection at 4.2 μm wavelength.

Chapter 4. Experimental apparatus and procedures

"*Measure what is measurable, and make measurable what is not so.*"
Galileo

4.1 Molecular-beam epitaxy (MBE)

Molecular beam epitaxy (MBE), in its infancy in the early 1970s, became a high volume production technique in the late 1980s as a result of the advances in surface physics and ion generation technology [111]. Molecular beams produced by effusion cells were successfully made to stick to the solid surface of a substrate and growth of thin films was made possible by the control of the substrate temperature and flux ratio of group-III and -V elements (namely Ga and As_2). MBE growth is often referred to as a non-equilibrium growth technique since under ultra high vacuum, the kinetics of the surface mechanisms govern the growth. The main growth mechanisms shown in Figure 4.1 include the deposition of an atom, its nucleation with another already present on the surface and the aggregation, source of three-dimensional growth if the downward tunnelling mechanism is not efficient enough.

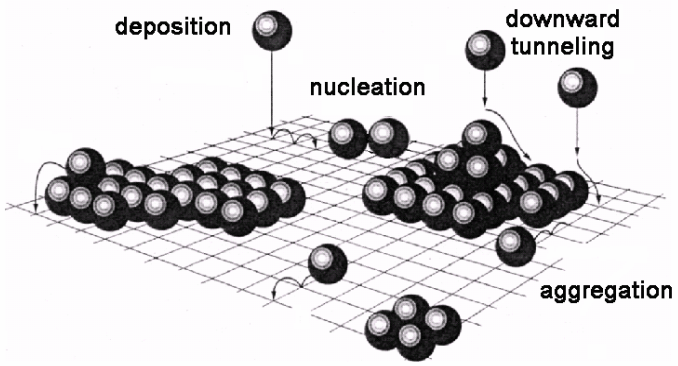

Figure 4.1 Main surface mechanisms in MBE growth

4.1.1 MBE apparatus

An MBE system is a voluminous equipment with different chambers for each stage of the growth as shown in Figure 4.2. Ultra high vacuum is maintained by the combined use of a cryopump, an ion pump and a turbopump and each chamber can be isolated by actionning gate valves. Epiready (001)-oriented substrates mounted on molybdenum holders are introduced in the system in a rack through the loading chamber and can be transferred to the outgasing stage or the growth chamber with the carrier on the transfer rod. Inside the growth chamber is a substrate holder that is heated and rotated during growth. Apart from a view window port, the growth chamber is equipped with effusion cells and crackers, to supply group-III and group-V elements, and a nitrogen plasma for the supply of nitrogen.

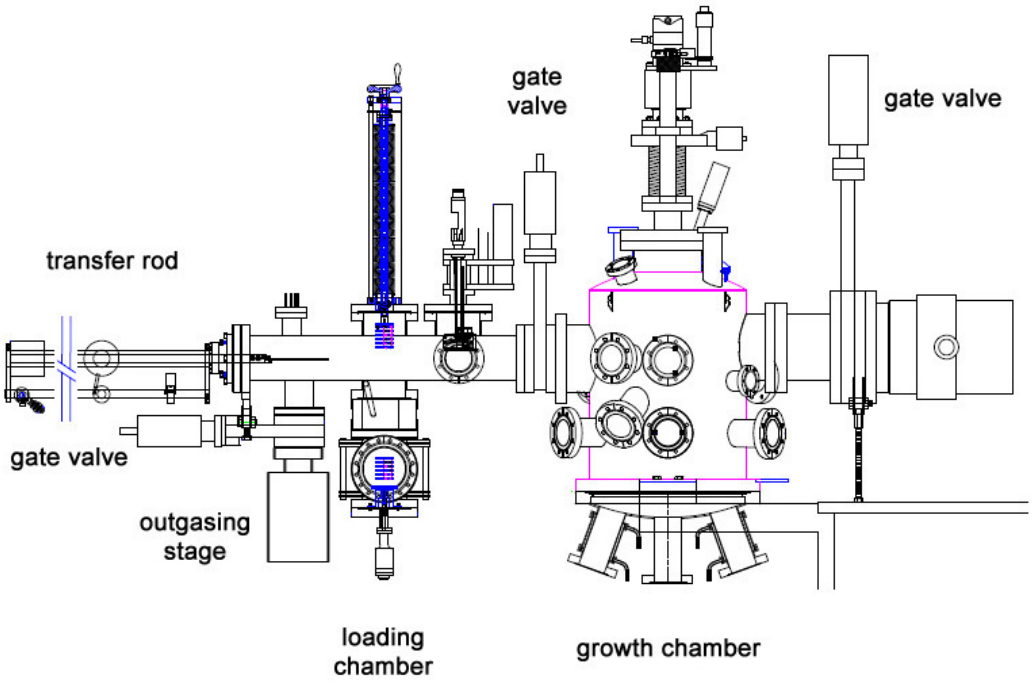

Figure 4.2 Front view of a typical MBE system, adapted from SVT Associates systems [112]

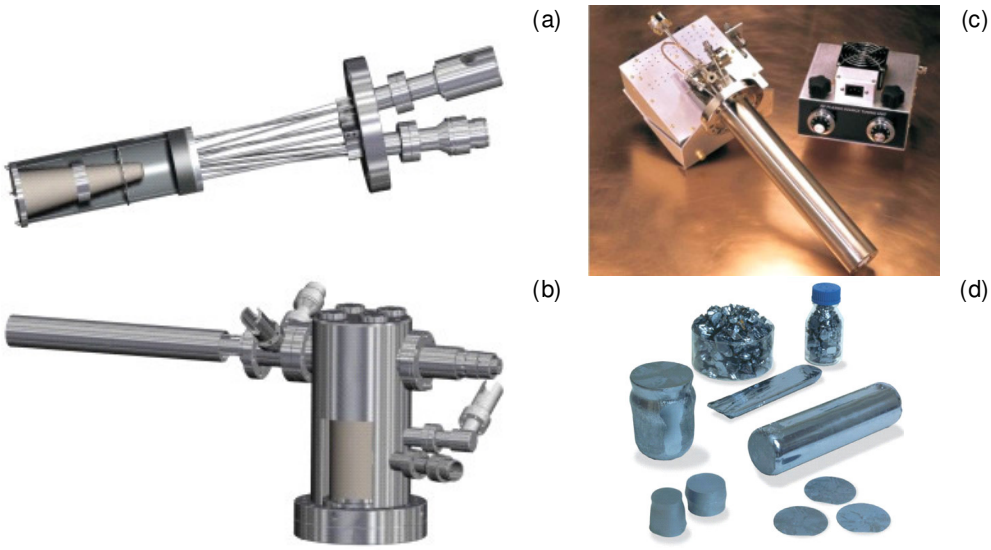

Figure 4.3 Equipment and materials for MBE systems : (a) thermal effusion cell [113a] ; (b) valved thermal cracker [113a] ; (c) UNI-bulb RF plasma source [113b] ; (d) source materials [114]

Group-III elements such as indium or gallium are produced by thermal effusion cells as illustrated in Figure 4.3 (a). A dual-filament cell is used for indium, the power of the tip filament is set to 25 % and the temperature of the bottom filament set to 780 - 890°C to maintain a high temperature to sublimate solid In and hence generate the indium flux. Group-V elements such as arsenic and antimony need a thermal cracker, as shown in Figure 4.3 (b), to provide dimeric species. While the cracker temperature is fixed to 950°C, the base temperature, in the temperature range 360 - 380°C for arsenic and 580 - 590°C for antimony, and the position of the mechanical needle valve set the flux of the group-V element. As far as nitrogen is concerned, inert N_2 molecules supplied by nitrogen gas (filtered through a purifier) require a radio-frequency (RF) plasma source, pictured in Figure 4.3 (c), to be broken into reactive nitrogen atoms. The N_2 flux is controlled by a leak valve and the plasma power can be varied between 160 W and 380 W (taking care to minimise the reflected power). The reflected power is set to zero through capacitances adjusted with the two-dial unit. MBE growth with a RF plasma source is often referred to as RFMBE or

plasma assisted-MBE (PAMBE). Ultra pure source materials, as shown in Figure 4.3 (d), are initially loaded in the solid form in the crucibles of the In, As, and Sb cells, hence the qualificative of solid-source MBE (SSMBE).

Each cell is equipped with a shutter commanded by an actionner. Out of growth, cells are kept at relatively low idle temperatures by a water-cooling system. Because of high temperature of the cells during growth (up to 1100^{o}C for Ga), the temperature of the growth chamber and cells is regulated by nitrogen-cooled cryopanels placed all around the chamber as shown in Figure 4.4. They help to maintain an ultra-high vacuum, for high purity epitaxial growth. An automated valve controls the supply of liquid nitrogen from a pressurised dewar (160 to 200 L). Before growth, the cooling down of the system greatly reduces the background pressure to values from 10^{-9} to ~ 10^{-11} mbar. An ion gauge is used to measure the molecular beam fluxes, referred to as beam equivalent pressures (BEP). A reflection high-energy electron diffraction (RHEED) set-up is used to monitor the surface during growth through the pattern observed on a fluorescent phosphorous screen.

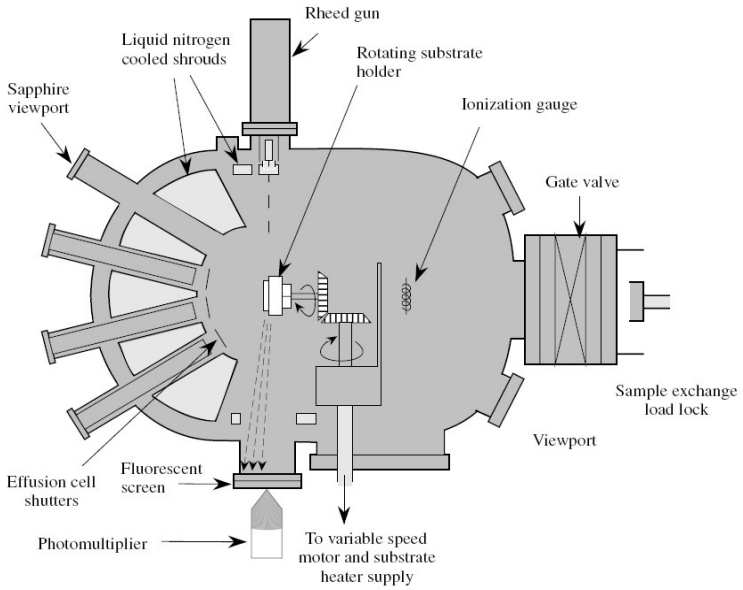

Figure 4.4 Top view of an MBE system evidencing cryopanels and RHEED [115]

4.1.2 Exploiting RHEED

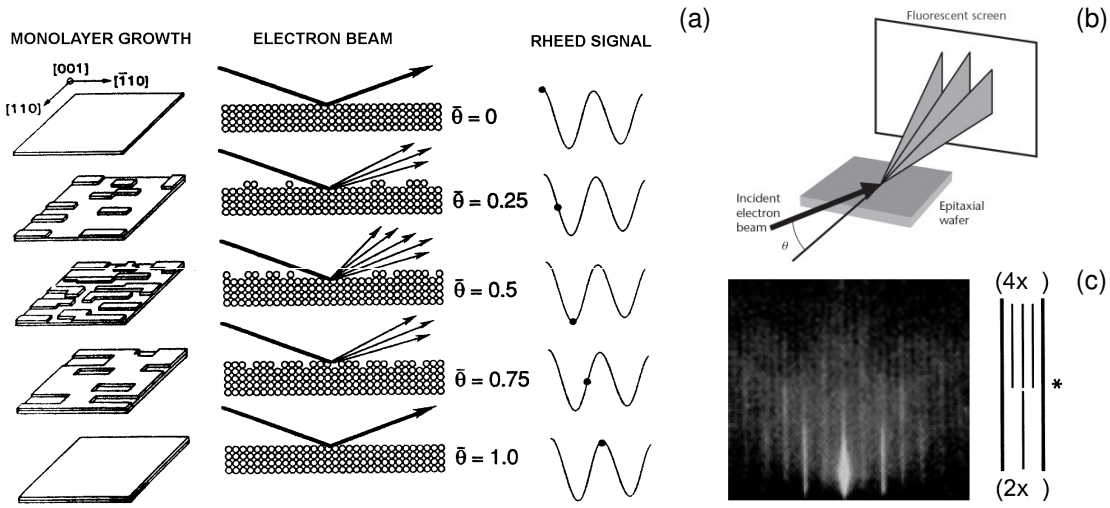

Figure 4.5 Mechanisms and nomenclature of RHEED patterns : (a) RHEED intensity as a function of the surface morphology ($\overline{\theta}$ is fractional layer coverage) [116] ; (b) formation of a RHEED pattern [47] ; (c) " $2\times$ " RHEED pattern picture and (2×4) sketch, (*) corresponds to a 90 degree rotation of the substrate holder [117, 47]

Reflection high-energy electron diffraction (RHEED) was used from the early days of MBE as a tool for surface monitoring. A RHEED gun, operated at a current of 2.25 A and a voltage of 12.5 to 13 kV, produces a beam striking substrate at a shallow angle (0.5 - 2 degrees) and reflected to a phosphorous screen. As shown in Figure 4.5 (a), the intensity of the light on the screen is proportional to the coverage of the surface by adatoms and progressively decreases period after period. More precisely, a RHEED diffraction pattern is formed as illustrated in Figure 4.5 (b) and can be spotty in the case of rough bulk material or streaky for relatively smooth surfaces. The RHEED pattern corresponds to a surface state and well-ordered structures can often be understood with thermodynamic models. For instance, an arsenic-terminated (001)-oriented GaAs surface exhibits typically a (2×4) pattern. It corresponds to the observation of two *half* patterns on the $[1\,1\,0]$ and $[1\bar{1}\,0]$ crystal

directions [116]. Indeed, primary lines are easily seen in the picture of Figure 4.5 (c). Secondary lines form between the primary lines, and with a spacing of ½ that of the primary lines in this case ; the denominator of this spacing is used to name the *half* pattern " 2 × ". A rotation of 90 degrees of the substrate holder presents the second mentioned crystal direction with its own *half* pattern " 4 × " made of three secondary lines with a spacing of a ¼ that of the primary lines, as illustrated by the sketch in Figure 4.5 (c).

4.1.3 Setting and calibrating the temperature

The temperature is a critical parameter to control material quality and incorporation of nitrogen in the MBE growth process. A poor lab-to-lab reproducibility is acknowledged and growth temperatures in the literature are generally given as a rough guide. Three temperatures need to be considered. The setpoint temperature or T_{sub} is the temperature to which the substrate is set by the computer interface of the MBE system from a temperature controller reading. Since a direct measurement of the substrate temperature with a thermocouple is not reliable (reported variation of up to 140°C [118]), a pyrometer (a non-contacting detector of thermal radiation) gives the actual temperature of the substrate T_{pyro} within a limited range of a few hundreds of degrees centigrade (emissivity ~ 0.55 for InAs). If there is no shift between the temperature measured by the pyrometer and the actual temperature (up to 40°C with a previous pyrometer, providing an additional shift to consider when targeting a given growth temperature), T_{pyro} is equal to the growth temperature T_g.

When an outgased InAs substrate is introduced into the growth chamber, its temperature is progressively raised by 25°C steps from $T_{sub} = 200$°C to about

600 ~ 700°C, where the surface starts to show a spotty RHEED pattern and the pyrometer can measure a temperature (T_{pyro} ~ 450°C). A further increase in the setpoint temperature with finer steps of 10°C allows one to obtain a streaky RHEED pattern with bulk lines, corresponding to the smooth surface obtained at the deoxidation temperature (T_{pyro} = 460 ~ 520°C). The surface is exposed to a high flux of arsenic to protect it and calibrations of the temperature as a function of the setpoint temperature are then performed around the deoxidation temperature as shown by the blue lines in Figure 4.6. The temperature calibration is repeated at the start of every growth, since different holders and substrates show different linear relations. The linear fit is then used to compute the setpoint temperature for the desired growth (~ 400°C for InAsN). The substrate is calibrated and kept at a much higher temperature than that used for the dilute nitride growth, since a ~ 0.2 µm-thick InAs buffer is generally grown at T_g = 480°C before the epilayer or structure of interest. The shift in the measured temperature after the buffer layer growth (red line) may be due to a change in the emissivity of the surface (related to the morphology of the latter).

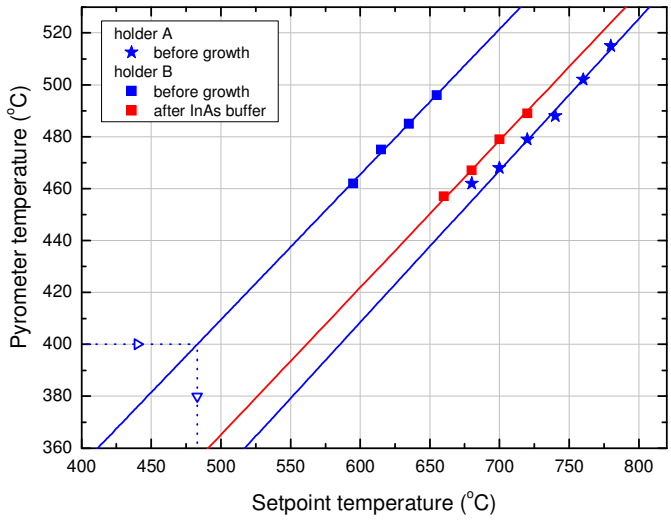

Figure 4.6 Typical growth temperature calibration by a pyrometer as a function of the setpoint temperature for different holders. Solid lines are linear fit

4.1.4 Fluxes

Beam equivalent pressures (BEP) measured by the ion gauge are also not reproducible between laboratories because of differences in ion gauge geometry, progressive coating of the filament, *etc* [117] and data given in the literature are only a rough guide. The low value of the background pressure (~ 2×10^{-10} mbar) allows to take the BEP (~ 10^{-6} mbar) as actual fluxes. The temperature of the effusion cell sets the flux of the group-III element (In for instance) as shown in Figure 4.7 (a). Thermal cracker cells set at a given base temperature (360°C and 580°C e.g. for As and Sb respectively) with a cracker temperature (950°C for dimeric species) and the tip position set in the range 0 - 300 mm, allows a finer tuning of the group-V fluxes. Because of the decreasing amount of material in the crucible with the number of growths and the small flux values which need to be achieved precisely, flux calibrations are performed at the start of each growth run as shown in Figure 4.7 (b).

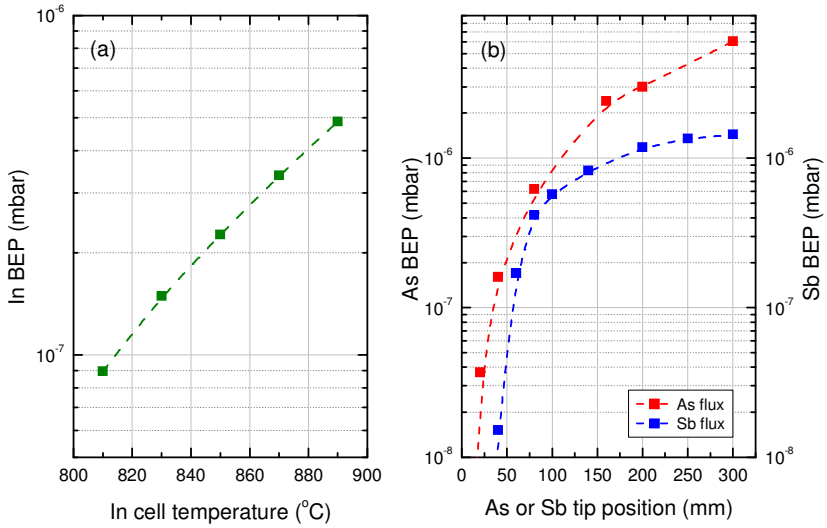

Figure 4.7 Typical flux calibrations of : (a) In BEP as a function of the cell temperature ; (b) As and Sb BEP as a function of the valve tip position. Dashed lines are a guide to the eye

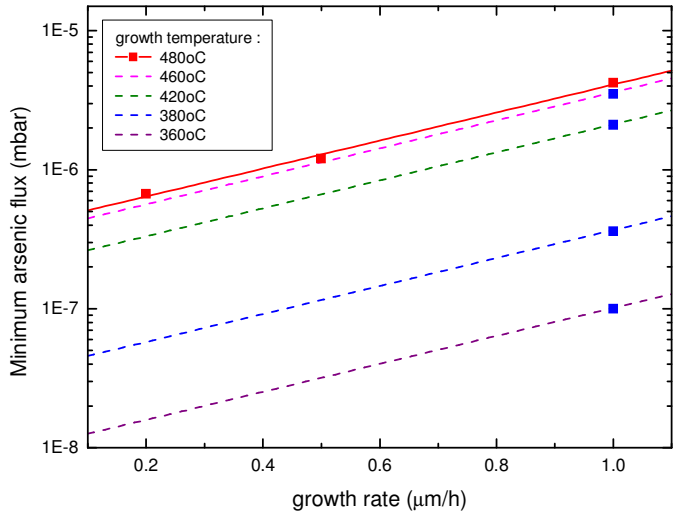

Figure 4.8 Typical dependence of the minimum arsenic flux on the growth rate and temperature. Data were measured on the same growth run

InAs, which is usually grown at temperatures of 420 - 520°C, exhibits a (2×4) RHEED pattern. As for GaAs, a stable (2×4) pattern – away from other phase transitions, and referred to as β-(2×4) in the literature – is synonymous of a flat InAs surface [118]. A more careful observation reveals that a phase transition from (2×4) to (4×2) occurs with increasing substrate temperature at fixed As flux, which reflects As- and In-terminated growth conditions respectively [92, 117]. Alternatively, the same transition can be obtained by decreasing the As flux at fixed substrate temperature. This reconstruction transition is independent of the dopant type and concentration of the substrate [118]. For III-V semiconductors, a group V-rich surface (group III-rich, respectively) means that the growth of a layer is limited by the supply of group III (V, respectively). The minimum arsenic flux As_{min} can therefore be defined as the lowest As flux required to have an As-terminated InAs surface. Practically, the substrate is set to the desired growth temperature under relatively high As flux to obtain a " $2\times$ " RHEED pattern and InAs growth is initiated by opening the In shutter. The As flux is reduced until a " $4\times$ " pattern appears ; the As flux allowing the recovery of the " $2\times$ " RHEED pattern is As_{min}. In that case, the growth rate (see

Section 4.1.5) is determined by the supply of indium, the group-III element. The minimum arsenic flux changes with the growth rate and temperature as illustrated in Figure 4.8. A linear dependence of As_{min} as a function of the growth rate was demonstrated at 480°C and it is reasonable to assume a similar behaviour for other temperatures based on the growers' experience.

4.1.5 Growth rate

The kinetics on the growing surface governing the formation of an atomic layer make molecular beam epitaxy a growth technique where the thickness of the deposited material is commanded by the growth duration given a growth rate. The growth rate can be expressed as the number of monolayers or layer thickness deposited per unit time. In the case of a slightly As-rich growth condition, InAs growth rate is fixed by the amount of indium arriving on the surface. Practically, the growth rate can be set by the choice of the In cell temperature, as demonstrated in Figure 4.9 (a). If the RHEED pattern is fixed by stopping the rotation of the substrate holder, it is possible to observe a few oscillations of the intensity (10-12) of the specular spot (refer to Figure 4.5 (a)). The period of oscillation corresponds to the time needed to grow a monolayer, defined as one complete layer of the group III-element (In) plus one complete layer of the group V-element (As), hence a thickness of half the lattice constant a_0 [119]. Practically, a number N_{osc} of oscillations is measured until extinction of clear oscillations for a time t_{osc} (in seconds). The growth rate in μm/h is calculated as :

$$growth\ rate(\mu m/h) = \frac{N_{osc}\frac{a_0}{2}}{\frac{t_{osc}}{3600}} \qquad (4.1)$$

which can be approximated to $\sim 1.0905 \frac{N_{osc}}{t_{osc}}$ in the case of InAs growth rate (μm/h).

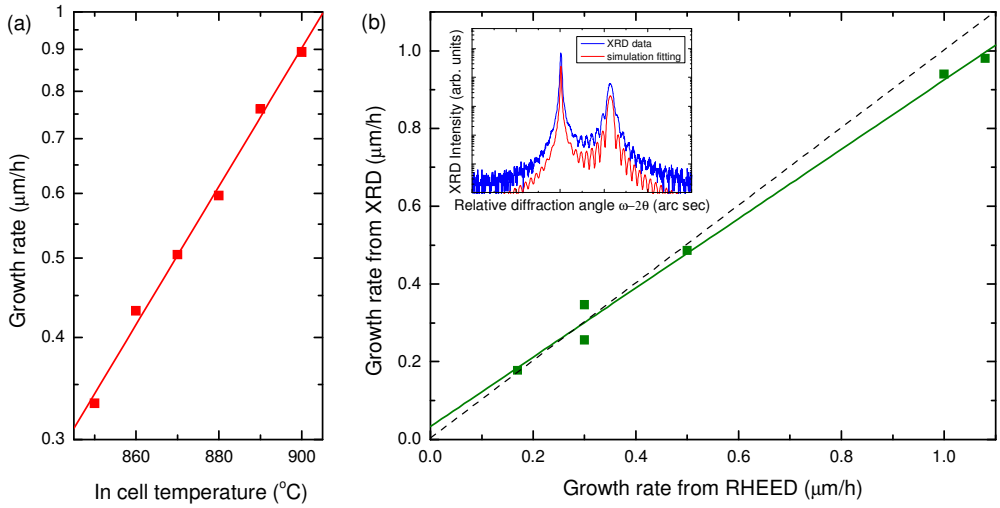

Figure 4.9 (a) InAs growth rate as a function of In cell temperature. The solid line is an exponential fit ; (b) Comparison of growth rate measured by RHEED oscillations and simulated by XRD analysis. Inset : Typical XRD rocking curve showing Pendellösung fringes (blue line) and simulation fitting (red line)

In the case of thin epilayers (typically 0.2 to 0.5 μm-thick), XRD rocking curves show interferences named Pendellösung fringes, as shown in the inset of Figure 4.9 (b), whose spacing is determined by the exact thickness of the epilayer. Given that the growth duration is a known parameter, fitting the Pendellösung fringes by adjusting the thickness allows the computation of the actual growth rate. As shown in Figure 4.9 (b), growth rates between 0.2 and 1.1 μm/h measured from RHEED oscillations of InAs monolayers and growth rates calculated by XRD are in good agreement with a slight deviation at higher growth rate.

4.1.6 Nitrogen plasma

The use of a nitrogen plasma in SSMBE opens the way to the growth of dilute nitride materials but adds to the difficulty of the epitaxy. It is advised to ignite it just before the growth of the dilute nitride layer to prevent contamination of the growth chamber by volatile nitrogen particles [120]. To protect the surface from impinging nitrogen species, the substrate is rotated away from the plasma during the initial striking and calibration of the latter, as shown in Figure 4.10, while the arsenic cell is closed to allow the measurement of the nitrogen BEP. The brightness of the plasma goes from the dark mode to the bright mode according to the settings of the plasma and a stable bright mode must be maintained for quality growth. Once desired plasma power and nitrogen flux are reached with minimised reflected power, the plasma is left to stabilise for about 15 min with the shutter closed. The substrate is then rotated back in the growth position and the growth of a dilute nitride layer can start.

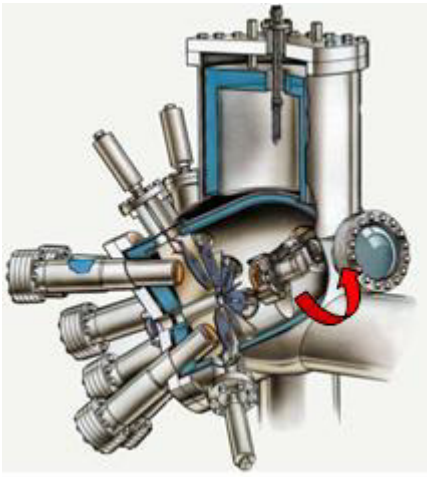

Figure 4.10 MBE growth chamber and rotation of the substrate during nitrogen plasma calibration

Molecular nitrogen is inert at low growth temperatures as used for the growth of InAsN, a more reactive nitrogen species is hence required. N_2 molecules from pure N_2 gas can be cracked by a nitrogen plasma source that produces a mixture of neutral

and charged molecular nitrogen (N_2, N_2^+), neutral and ionic atomic nitrogen (N, N^+) and free electrons. The nature of the species contained in a nitrogen plasma can be determined by optical spectroscopy. In the case of nitrogen, the optical spectrum contains broad lines in the range of 540 - 880 nm associated with the first positive series transitions of the neutral N_2 molecule [121]. The second positive series transitions of the neutral N_2 molecule are in the range of 316 - 420 nm. Weak broad emission peaks of the first negative series of the N_2^+ ion are between 390 and 430 nm. Strong sharp atomic lines can be observed in the range 700 - 1100 nm [122]. Radio frequency (RF) plasma sources, producing an RF discharge in N_2 gas, are generally preferred to electron cyclotron resonance (ECR) microwave sources since they produce more neutral atomic nitrogen, favourable to the nitrogen incorporation in a host material when growing ternary alloys [122].

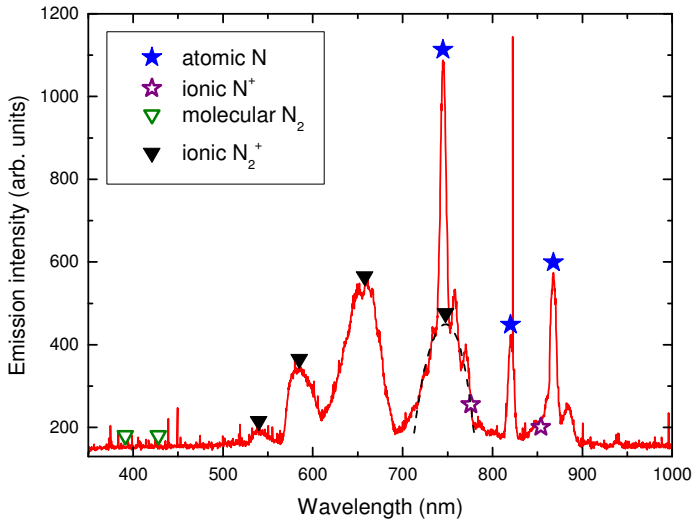

Figure 4.11 Emission spectroscopy of the nitrogen plasma source at N plasma power of 210 W and N flux of 5×10^{-7} mbar

The Veeco UNI-bulb$^{(C)}$ RF nitrogen plasma source in use in our MBE system was calibrated by emission spectroscopy at different nitrogen plasma powers and fluxes and a typical optical spectrum is shown in Figure 4.11. The intensity of each

spectral line is considered proportional to the generation rate of each species. Sharp and intense emissions at 745 nm, 821 nm and 869 nm are attributed in the literature to atomic N [121]. No report was made about the extremely sharp emission that can be seen at 823 nm and we attribute it to an experimental artefact. The broad peaks at 540 nm, 580 nm, 655 nm and 750 nm are related to molecular N_2 [121, 123, 124]. Emissions at 391 nm and 428 nm, associated with ionic N_2^+, are non-existent throughout the nitrogen plasma power and flux ranges, as are sharp emissions expected around 776 nm and 854 nm for ionic N^+ (emission wavelengths were computed from [125]).

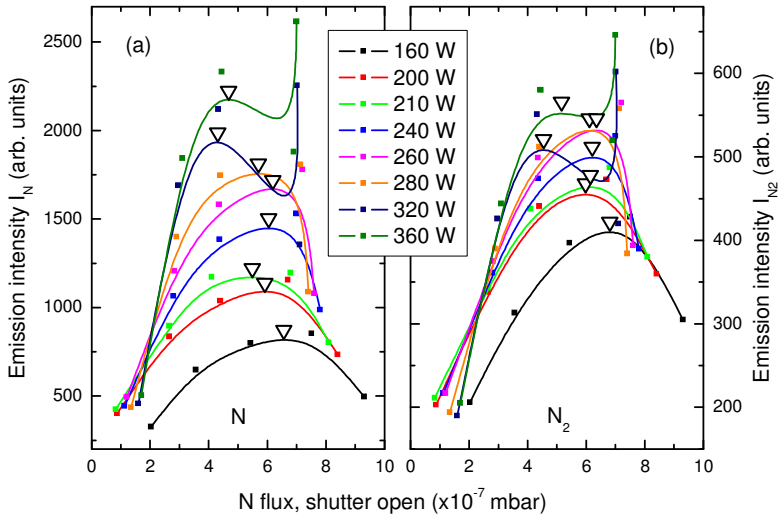

Figure 4.12 Peak intensity of the N plasma as a function of the N flux at various fixed powers for atomic N 745 nm line (a) and molecular N_2 750 nm line (b). Triangles show the flux for a maximised intensity and lines are guide to the eye

At fixed plasma power in bright mode operation, both N- and N_2-related peak intensities vary with nitrogen flux as shown in Figure 4.12. Atomic and molecular nitrogen intensities, I_N and I_{N2} respectively, increase from low to medium nitrogen flux and decrease at higher flux. Similar behaviour with various RF plasma cells was reported [122, 126] and the decrease at high flow was attributed to increased

recombination in the plasma volume at higher pressure. The atomic line intensity I_N at 745 nm (Figure 4.12 (a)) is generally 1.5 to 4 times bigger than the molecular line intensity I_{N2} at 750 nm (Figure 4.12 (b)), which shows a predominant generation of atomic species by the plasma. The anomalous behaviour around 7.5×10^{-7} mbar nitrogen flux for high powers 320 W and 360 W is probably due to a strong decrease in the mode brightness, leading to a lower dissociation efficiency of the plasma. For each nitrogen plasma power, the nitrogen flux for maximum I_N roughly corresponds to the one maximising I_{N2}. On one hand, it means that there is a particular nitrogen flux setpoint maximising atomic nitrogen for a given plasma power ; the required N flux corresponding to this maximum decreases with increasing RF power. On the other hand, the generation of molecular nitrogen, though low, cannot be avoided in the present configuration.

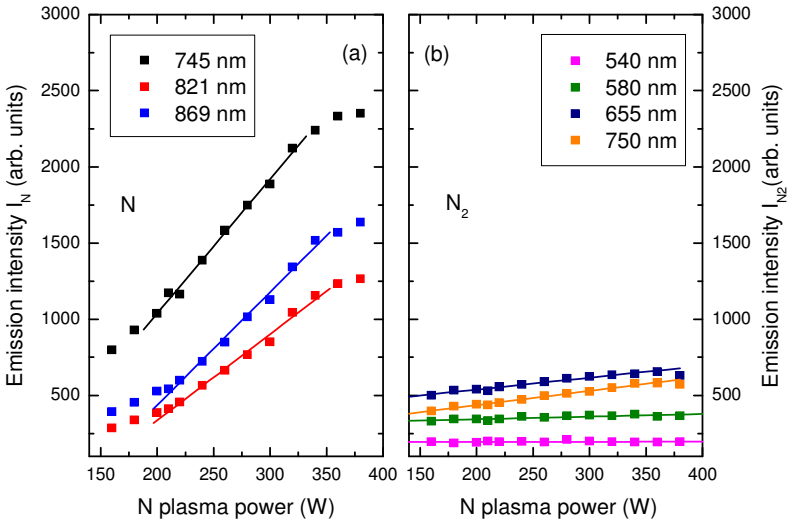

Figure 4.13 Peak intensity of the N plasma at fixed N flux (5×10^{-7} mbar) for atomic N lines (a) and molecular N_2 lines (b). Lines are linear fit

The emission intensities I_N and I_{N2} are plotted as a function of the nitrogen plasma power at fixed nitrogen flux, as shown in Figure 4.13. Atomic N (Figure 4.13 (a)) varies linearly on a wide RF power range with increasing nitrogen

plasma power before saturating slightly. Strong broad molecular lines (Figure 4.13 (b)) behave the same while the weakest ones remain constant with increasing nitrogen plasma power. Identical trends were widely reported [121, 122, 126]. From this graph, varying nitrogen plasma power seems a good way to control the amount of atomic nitrogen. Nevertheless, the RF power used strongly affects the kinetic energy of the generated species. On one hand, too high RF power produces energetic ionic species that can damage the surface. In fact, groups of ions with energies of 15 and 50 eV according to the RF power used were identified in RF plasma sources [122]. They can easily break bonds with regard to InAs and InN cohesive energies of 1.55 eV and 1.93 eV [127]. On the other hand, energetically low species lead to chemical reactions that are not vigorous enough. A medium power is probably advisable.

The RF plasma source was calibrated by optical spectroscopy but as mentioned by Wistey [123], this technique can only be a rough guide to the optimisation of the plasma settings (gas flow and RF power) to achieve high cracking efficiency. Extensive analysis could be misleading since this method hardly pictures changes in the bright mode stability of the plasma. An optimum flux at fixed RF power enhances the generation of atomic nitrogen and a linear variation of atomic N was found with increasing power at fixed N flux. Although the generation of molecular nitrogen is unavoidable, the RF plasma is a rich source of atomic nitrogen.

4.1.7 Dilute nitride material growth

An MBE growth run starts by filling the cryopanels with liquid nitrogen to improve the growth chamber vacuum. A background pressure of ~ 10^{-11} mbar can be reached in about 30 min. Flux calibrations can then be performed. Before growth (or

earlier), a substrate is moved to the outgasing stage or deoxidation chamber to be outgased of impurities and oxides, for about two hours at 300°C generally in the case of InAs substrates. The substrate is transferred to the growth chamber where its temperature is progressively increased from 200°C to 500°C. From then, RHEED is checked until the deoxidation temperature – indicated by a spotty RHEED pattern for outgased wafers – is reached. The As cell is opened (and is only shut during the nitrogen calibration) to protect the surface. Wafer temperature and InAs growth rate calibrations can be performed. For InAsN epilayers, a ~ 0.2 μm-thick InAs buffer is first grown at a growth temperature of 480°C. Under As flux, the temperature is lowered to the InAsN growth temperature and the nitrogen plasma is struck with the substrate facing away from the nitrogen plasma cell. The substrate is rotated back to the growth position at the end of the plasma calibration and InAsN growth can start. When the growth of InAsN layer is completed, the nitrogen plasma is turned off immediately to prevent the damage of the surface and contamination of following layers [70]. If a heterostructure is being grown, care must be taken to minimise the ramp time needed to reach the growth temperature of the following layer. At the end of the growth, the temperature of the substrate holder is lowered to its minimum value under As flux and cells are set to their idle temperatures.

4.2 Spectroscopic characterisation techniques

4.2.1 X-ray diffraction (XRD)

X-rays have a wavelength in the order of the atomic spacing and the periodical arrangement of atoms in crystals acts as a two-dimensional diffraction grating for this light. Lattice planes in the reciprocal lattice space (see Section 2.2.2) act in turn as

reflectors and Bragg's law (first proposed in 1912) illustrates constructive interferences with incidence angle (its complement angle to be accurate) verifying the condition :

$$2d_{hkl}\sin\theta_B = n\lambda \qquad (4.2)$$

where d_{hkl} is the lattice plane spacing, θ_B the Bragg angle dependent on the material, n an integer and λ the emission wavelength of the source [128]. Materials with different lattice plane spacing will diffract X-rays at different angles.

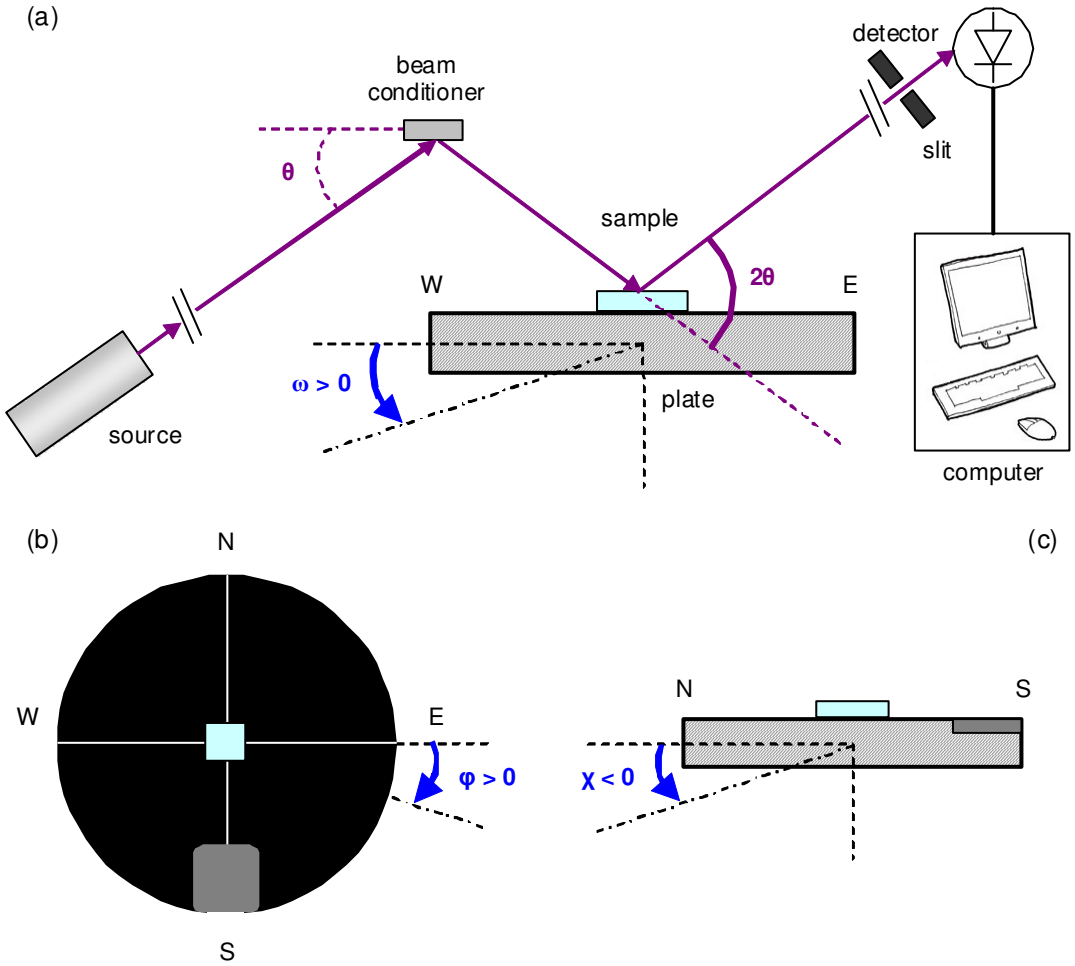

Figure 4.14 XRD system and angle orientations (a) Front view of a typical XRD system in the ω-2θ configuration ; (b) and (c) : Top and side views showing angle orientations

X-ray diffraction (XRD) is a non-destructive technique to analyse the structure and composition of a crystal that can be performed for epilayers of thickness between

50 Å and 10 μm. In a double crystal XRD system (DCXRD) as shown in Figure 4.14 (a), the sample is illuminated by a beam produced by an X-ray source (operated at 38 kV and 1.5 mA) and reflected by a GaAs beam conditioner. ω and χ angles are tilt angles of the plate, while φ is the azimuth angle (used for measurement of the relaxation). An X-ray source with a copper target produces a doublet, Cu $\kappa\alpha_1$ and Cu $\kappa\alpha_2$, and both radiations are visible when beam conditioner and substrate are of different material ; a slit in front of the detector is used to screen Cu $\kappa\alpha_2$ radiation. The use of a beam conditioner makes the measurement independent of the X-ray beam geometry and divergence.

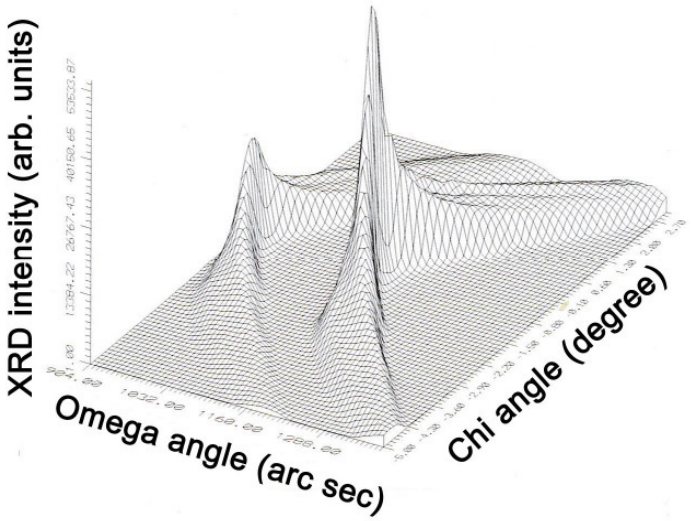

Figure 4.15 XRD mapping of a thick epilayer on a substrate for optimisation of ω and χ angles, adapted from [129]

With the QC200$^{(C)}$ DCXRD system from Bede Scientific Instruments Ltd., source and detector are rotated to verify the Bragg angle of the substrate material ($\theta_B = 30.5687^o$ in (004) geometry for InAs) in an ω-2θ configuration. An ω scan is performed over several hundreds of arc seconds to adjust the difference of lattice spacing between the GaAs beam conditioner and the substrate and generally shows two peaks as illustrated in Figure 4.15. An additional adjustment can be performed by

optimising the χ angle (optional) to obtain a brighter and narrower main XRD peak to truly represent the level of crystalline perfection of the material. This does not affect (to first order) the peak separation. Optimisation of ω and χ angles sets the relative diffraction angle to zero for the substrate (InAs) in an ω-2θ scan.

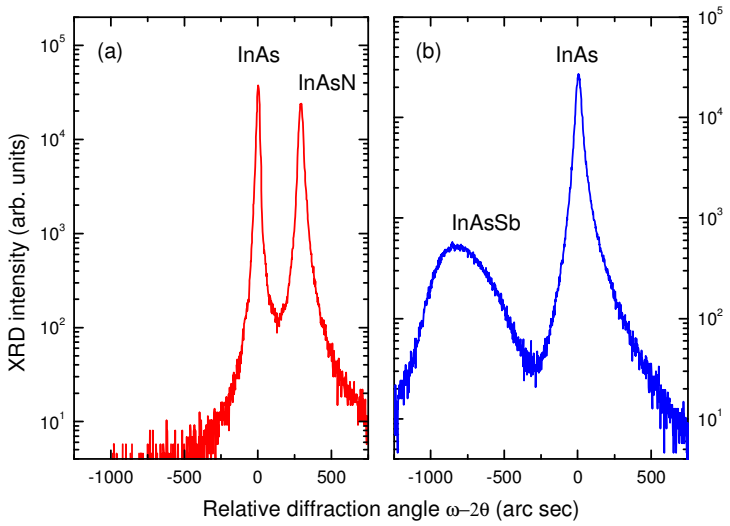

Figure 4.16 Typical XRD rocking curves in the (004) geometry for samples grown on InAs substrates : (a) good quality InAsN ; (b) poor quality InAsSb

An ω-2θ scan performs XRD measurements by the joint rotation of the plate and the detector. The rocking curve obtained in the (004) geometry – the most widely used – from the measurement of a sample composed of an epilayer grown on a substrate shows two respective peaks as shown in Figure 4.16. InAsN has a smaller lattice constant than InAs and exhibits a peak at higher diffraction angle than InAs (as light would be diffracted with a wider angle through a narrower slit) as shown in Figure 4.16 (a). Inversely, InAsSb with a bigger lattice constant than InAs exhibits a peak at lower diffraction angle than InAs. Peak intensity and width reflect the crystal perfection and weak and broad peaks are synonymous of poor quality sample, as shown in Figure 4.16 (b). The peak separation, related to the lattice plane spacing d_{hkl}

by Bragg's law, is used to compute the lattice constant with RADS Mercury(C) analysis software.

4.2.2 Photoluminescence (PL) and electroluminescence (EL)

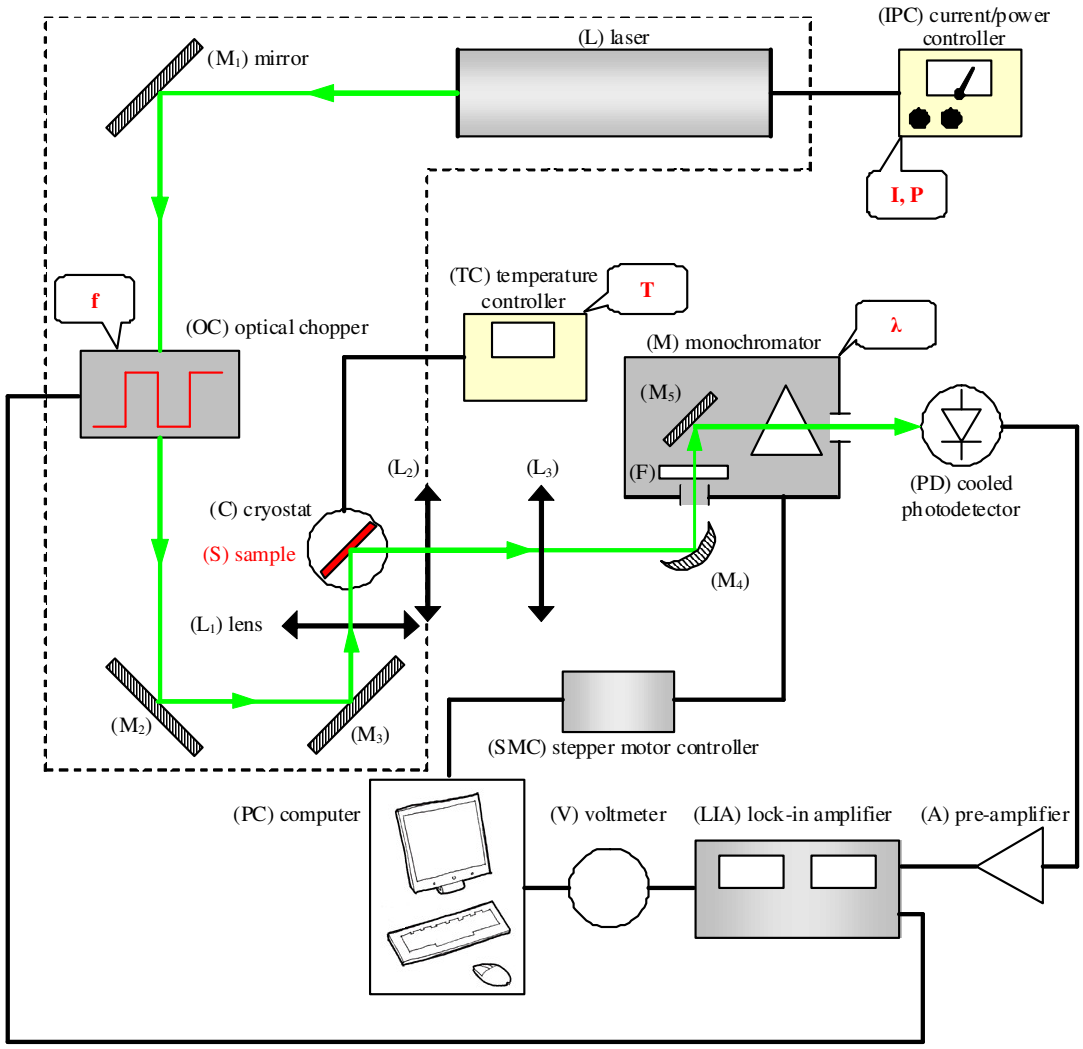

Figure 4.17 Top view of a PL system

The photoluminescence measurement (PL) is a useful non-destructive technique that provides valuable information about the optical properties of a material. By illuminating a sample with a laser beam, radiative emissions can be observed, mostly in the infrared range for narrow gap semiconductors, and reveal characteristics of the conduction and valence bands as well as of the defects, impurities and dopants

present in the material. Photons with higher energy than the bandgap of the material being measured are absorbed and photo-generated electrons relax (non-radiatively) until they reach the conduction and valence bands where they recombine radiatively by spontaneous emission of photons [130].

A PL system is illustrated in Figure 4.17. A class 4 Ar-ion laser (L) (Spectra-Physics Stabilite 2017$^{(C)}$) is operated at a driving current of $I = 20$ A and the output power P can be adjusted between 0.2 W and 1.6 W by the current/power controller (IPC). The laser emits a green light composed of lines at 488 nm and 514 nm. The laser beam is modulated by an optical chopper (OC) at the frequency f ~ 310 Hz (away from the mains frequency of 50 Hz and its orders) and reflected by mirrors (M_1, M_2, M_3) before being focused by a first CaF_2 lens (L_1) onto the sample (S). The sample is mounted on a cold finger placed in a temperature-controlled (TC) cryostat (C), cooled by liquid helium. The generated radiations are focused through a set of lenses (L_2, L_3) and directed (M_4, M_5) onto a monochromator (M). With a 300 lines/mm grating (with blaze wavelength at 3 μm), the Bentham TMc300$^{(C)}$ monochromator has a dispersion of 10.8 nm/mm (related to the slit width) and a resolution of 1.2 nm and can discriminate light up to ~ 5.5 μm wavelength. The width of its slits can be adjusted to increase details in the PL spectrum if needed. Filters (F) with cut-off wavelengths in the mid-infrared spectral range are automatically inserted to eliminate the orders of the laser. At the exit of the monochromator, a 2 mm-diameter photodetector (PD) (InSb for detection between 1.5 μm and 5.5 μm), cooled to 77 K with liquid nitrogen to improve its performance, detects the discriminated radiation. The output of the detector is connected to a pre-amplifier (A) and the signal is transmitted to a Stanford Research Systems SR810$^{(C)}$ lock-in amplifier (LIA). With the chopper frequency f as reference, the LIA can

recover the signal from the noise. A Labview(C) program drives the monochromator through a stepper motor controller (SMC) and collects the signal passing through a voltmeter (V) to record the PL spectrum. The laser and beam before the sample are enclosed for safety reasons.

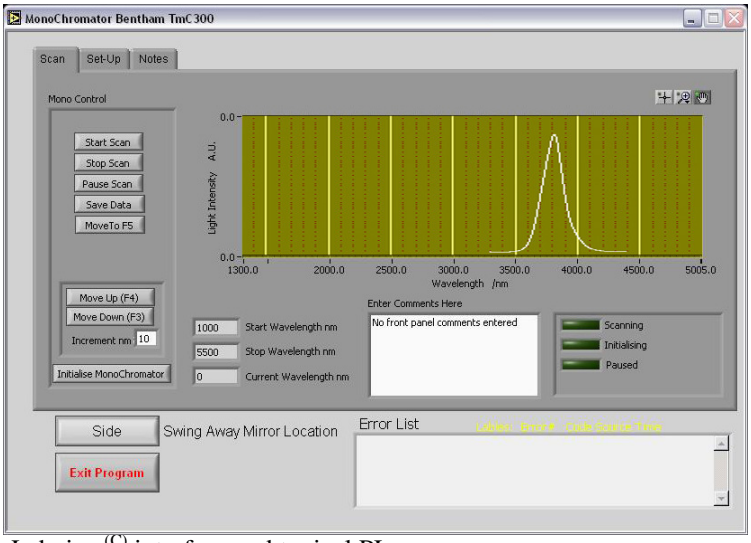

Figure 4.18 Labview(C) interface and typical PL scan

Practically, the inner jacket of the helium cryostat is first evacuated to ~ 5×10^{-2} torr before being filled with helium gas ; the outer jacket is maintained under vacuum by a rotary pump throughout the measurement. The laser needs ~ 15 min warming up before operation. The cooling down of the cryostat with liquid helium (~ 30 min from 300 K to 4 K) is controlled by the proportional, integral and derivative (P, I, D) parameters of the temperature controller (Oxford Instruments ITC 501(C)) and adapted according to the desired temperature. Positions of the lenses (L_2, L_3) must be slightly adjusted for every sample since the cryogenic high vacuum grease (Apiezon(C) N grease) used to stick the sample on the cold finger can induce a minor tilt. From experience, (L_2, L_3) can initially be arranged to allow the laser beam reach the sample (with the monochromator at the zero position) ; a slight horizontal translation of the photodetector (PD) perpendicularly to the beam should allow the detection of the mid-

infrared signal. After an initial scan over a wide range with a large monochromator step, the signal should be optimised at the peak emission wavelength by further adjustment of (L_2, L_3) and (PD). The noise of the detected signal is reduced by the choice of an adapted sensitivity of the voltmeter and a time constant of 1 s on the lock-in amplifier helps smoothing the measured spectrum. A typical scan is shown in Figure 4.18.

The optical spectrum of a light emitting diode (LED) can be measured by electroluminescence (EL). Instead of photo-excitation, a current provides electrons and holes that can recombine between conduction and valence bands of a p-i-n structure. The same setup is used with laser and chopper turned off and an LED, mounted on a cold finger with electronic connectors, is driven by the current from a pulse generator (Agilent 8114A$^{(C)}$) passing through a 10 Ω resistor. Pulses have a frequency of 1 kHz, 50 % duty cycle and the current can be varied between 33 mA and 1 A, though currents around 300 mA are recommended to prevent the damage of the device. The reference frequency for the lock-in amplifier is given by the pulse generator.

4.2.3 Photoresponse

A photoresponse set-up is used to measure the optical spectrum that the photodetectors grown by MBE can detect. As shown in Figure 4.19, a blackbody source (B) emits a beam, with a wide spectrum covering the infrared region, that is modulated by an optical chopper (OC) and focused by lenses (L_1, L_2) into a monochromator. The beam is diffracted by the grating of a monochromator (M) and focused by lenses (L_3, L_4) onto the photodetector (PD) being measured. The

photodetector is placed in a liquid nitrogen-cooled cryostat – the rest of the electronic equipment is similar to the PL system and the same considerations apply.

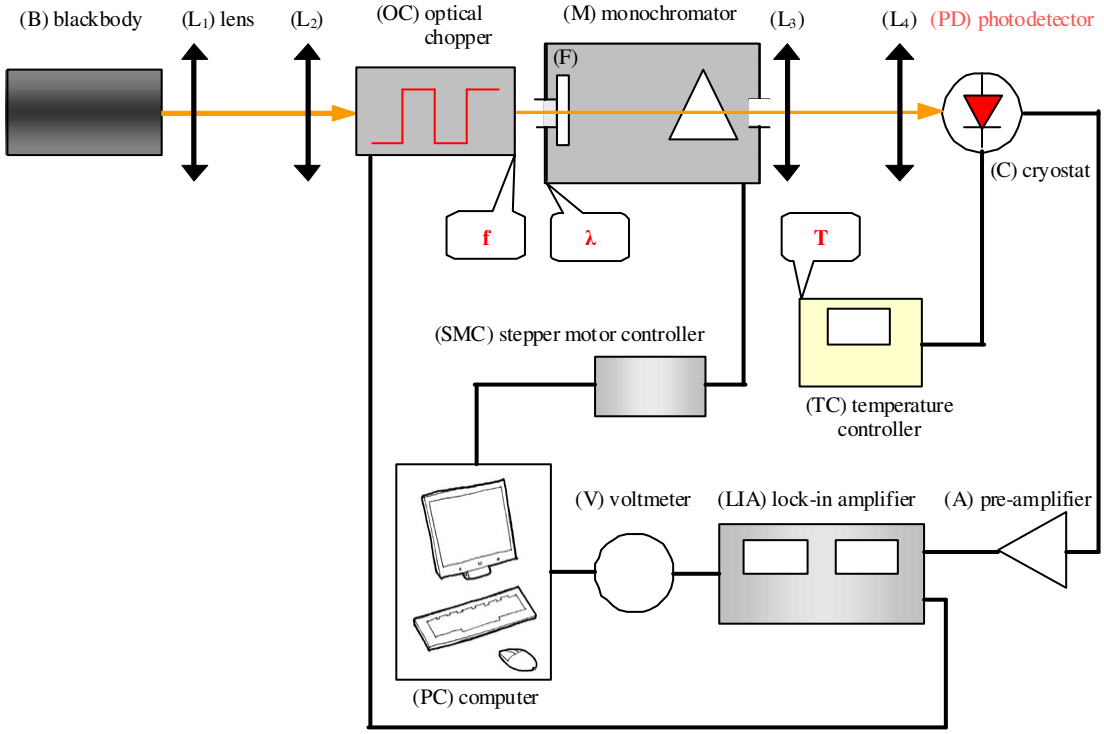

Figure 4.19 Top view of a photoresponse system

Practically, lenses (L_3, L_4) are adjusted in position and height once the photodetector is inserted in the cryostat. The system is enclosed to prevent the detector from picking undesirable signals. Additionally to the measurement, a pyroelectric detector with a flat response is placed instead of the photodetector (PD) to measure the system response and this signal is divided from the measured response of the photodetector.

4.2.4 Surface characterisation

Surface analysis of MBE-grown samples was performed by a Vickers M17[(C)] Nomarski microscope with optical interference contrast and capable of 2.5 to

100 times magnification ; best pictures using a JVC$^{(C)}$ camera were obtained in the 800×600 resolution (saved with WinTV$^{(C)}$ software with setting "quality 100 %"). The surface of samples and edge of p-i-n structures were pictured by FEI Sirion$^{(C)}$ scanning electron microscope (SEM) to check the surface aspect and thickness of the grown layers ; samples were mounted on metallic holders with silver dag. This equipment can also perform energy-dispersive X-ray spectroscopy (EDAX) to determine compositions (of quaternaries for instance). It must be noted though that EDAX is not calibrated to detect nitrogen, whose light mass makes it difficult to detect by this technique. Fine surface analysis at the micron scale (up to 12.5 μm^2) was performed by Multimode$^{(C)}$ atomic force microscopy (AFM) in tapping mode with silicon probes ; samples were mounted on holders with phenyl salicilate. Pictures were analysed using Digital Instruments Nanoscope IIIa$^{(C)}$ software capable of evaluating the root mean square (rms) roughness.

4.3 Electrical characterisation techniques

4.3.1 Van der Pauw's measurement system (Hall effect)

Van der Pauw's measurement is a useful technique for determining resistivity, mobility and concentration of carriers. The resistivity ρ of a sheet of conducting material with thickness d can be measured from the potential drop between two contact points C and D when a current is driven through A to B, as illustrated in Figure 4.20 (a). Four unconnected lines scribed in the shape of a "+" on the sample surface can help reduce leakage currents. Under the assumption of a flat, solid, uniformly doped lamella, the resistance values of the quadrupole *ABCD* are linked by the Van der Pauw theorem [131, 132] :

$$\exp\left(\frac{-\pi R_{AB,CD}\, d}{\rho}\right)+\exp\left(\frac{-\pi R_{BC,DA}\, d}{\rho}\right)=1 \qquad (4.3)$$

where $R_{ij,kl}$ is the quadrupole resistance with current entering at i and exiting the sample at j and voltage taken as the difference of potential between l and k as shown in Figure 4.20 (b). Under the assumption of a symmetrical sample such as a square, a circle, a four-leaf clover shape, the resistivity can be derived as :

$$\rho=\frac{\pi\, d}{\ln 2}\frac{\Sigma R}{2} \qquad (4.4)$$

where $\Sigma R = R_{AB,CD} + R_{BC,DA}$.

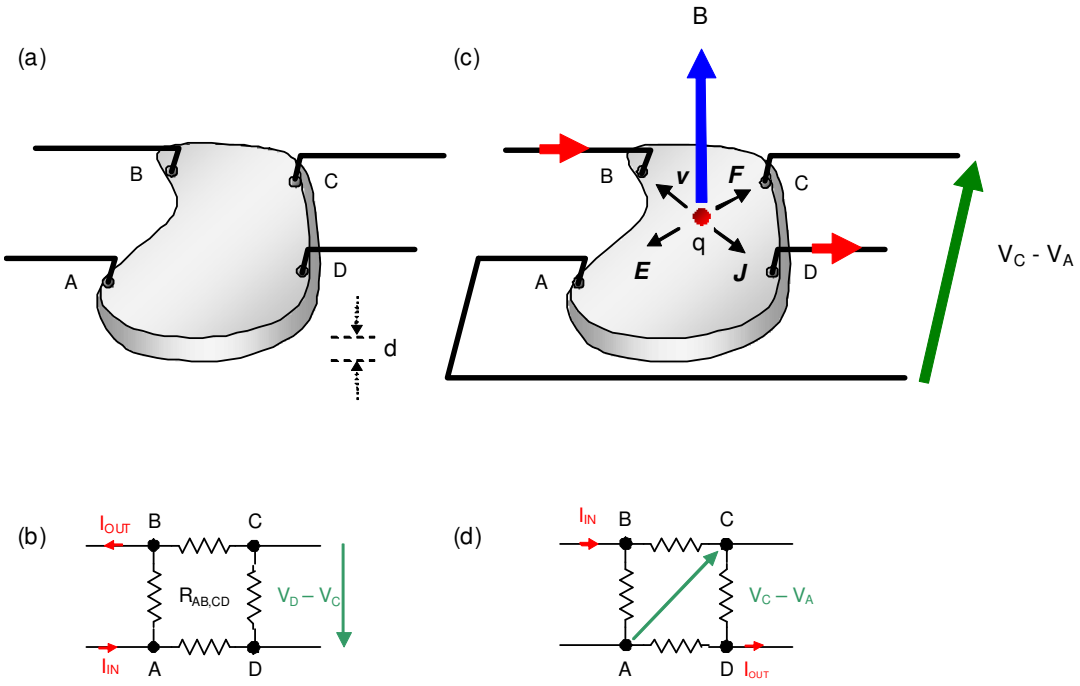

Figure 4.20 (a) Layer of arbitrary shape with point contacts for the measure of the resistivity ; (b) Electronic sketch of the quadrupole *ABCD* ; (c) Hall effect on an n-type sample in a magnetic field ; (d) Electronic sketch of the quadrupole *ABCD* under consideration

Hall effect measurements are based on the effect of the Lorentz force exerted on charge particles (electrons for n-type material) moving with speed $\boldsymbol{v}$ in a magnetic field $\boldsymbol{B}$ normal to the surface as shown in Figure 4.20 (c). In equilibrium, a force due

to an internal electric field $\boldsymbol{E}$ (Hall field) balances the Lorentz force so that the net force $\boldsymbol{F}$ is null :

$$\boldsymbol{F} = -q\left(\boldsymbol{E} + \boldsymbol{v} \wedge \boldsymbol{B}\right) \qquad (4.5)$$

where q is the electron charge. When a current, with current density $\boldsymbol{J}$, passes diagonally across the sample, the change in the quadrupole resistance $R_{BD,AC}$ (shown in Figure 4.20 (d) when a magnetic field is applied can be used to calculate the Hall mobility μ_H following the equation [131] :

$$\mu_H = \frac{d}{B}\frac{\Delta R}{\rho} \qquad (4.6)$$

where B is the magnetic field, $\Delta R = R_{BD,AC(\boldsymbol{B=1})} - R_{BD,AC(\boldsymbol{B=0})}$, $\boldsymbol{B=1}$ or $\boldsymbol{B=0}$ when the magnetic field is applied or not respectively.

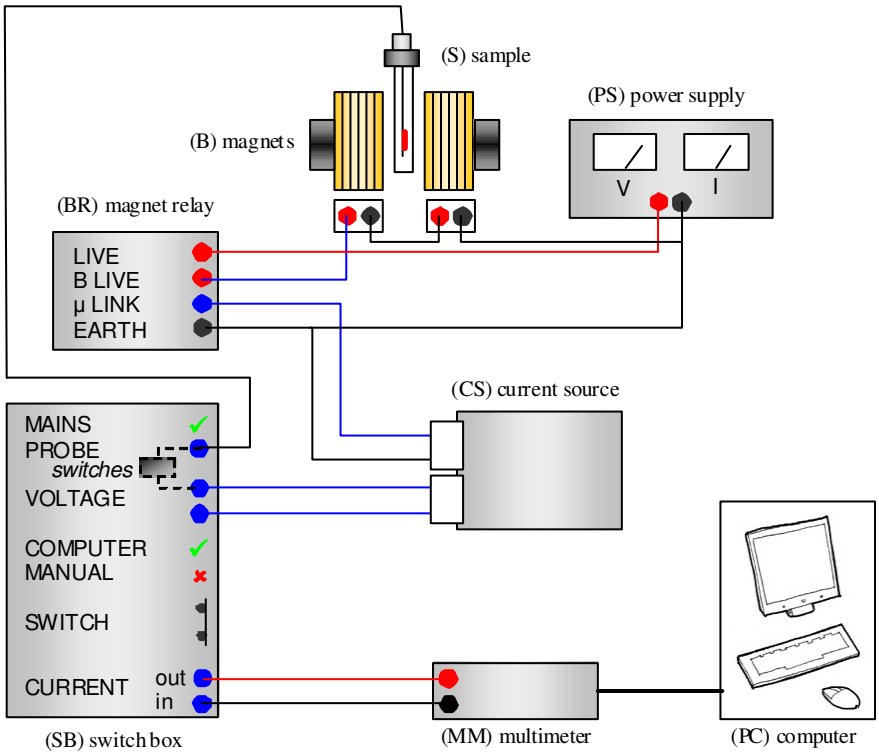

Figure 4.21 Van der Pauw's system for Hall effect measurements

The carrier concentration n (in cm^{-3}) is deduced from :

$$n = \frac{1}{q\,\rho\,\mu_H} \qquad (4.7)$$

where q is the electron charge (in C), ρ the resistivity (in Ω.cm) and μ_H the Hall mobility (in $cm^2V^{-1}s^{-1}$). Equations (4.4), (4.6) and (4.7) can be completed by Petritz's double layer model [133] that takes into account the effect of the parallel conductivity between epilayer and substrate (see Appendix II for details and calculation). A program, originally developed in Turbo Pascal [134], was re-engineered in TestPoint(C) for the computation of resistivity, Hall mobility and carrier concentration.

Van der Pauw's system used to measure the Hall effect is shown in Figure 4.21. Four contact points of a sample (S) connected to an electronic board are alternatively connected in pairs by a computer-controlled switch box (SB) to drive current from a current source (CS) through the sample. Voltages are measured with and without a magnetic field of 0.266 T created by a magnet (B) controlled by a magnet relay (BR).

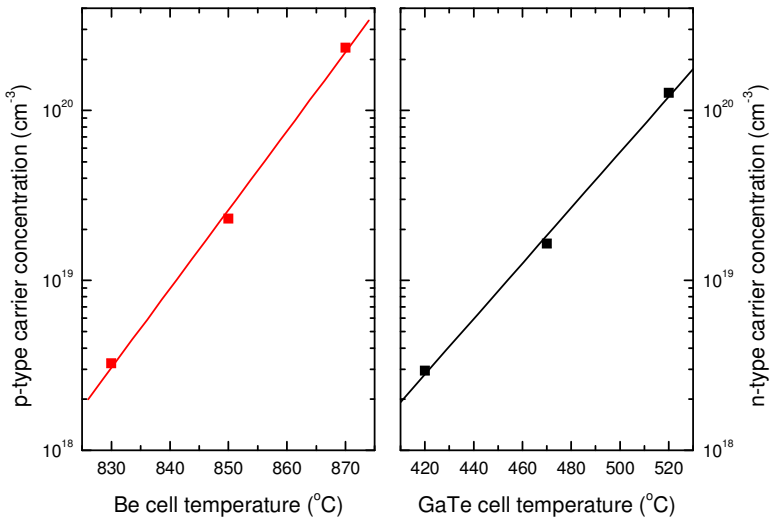

Figure 4.22 Carrier concentration of p- and n-type doped InAs as a function of the cell temperature. Solid lines are linear fits

Doping calibrations were performed with Van der Pauw's measurement system for p- and n-type InAs (Be- and Te-doped respectively). The samples were grown on semi-insulating GaAs substrates (InAs substrates were avoided to prevent parallel conduction). Indium contacts on gold wires were soldered to square-shaped samples with a soldering iron. Doping types can be checked by a hot probe apparatus. Doping calibration results are shown in Figure 4.22 and carrier concentrations are linear functions of the respective cell temperatures.

4.3.2 Current-voltage (I-V) measurements

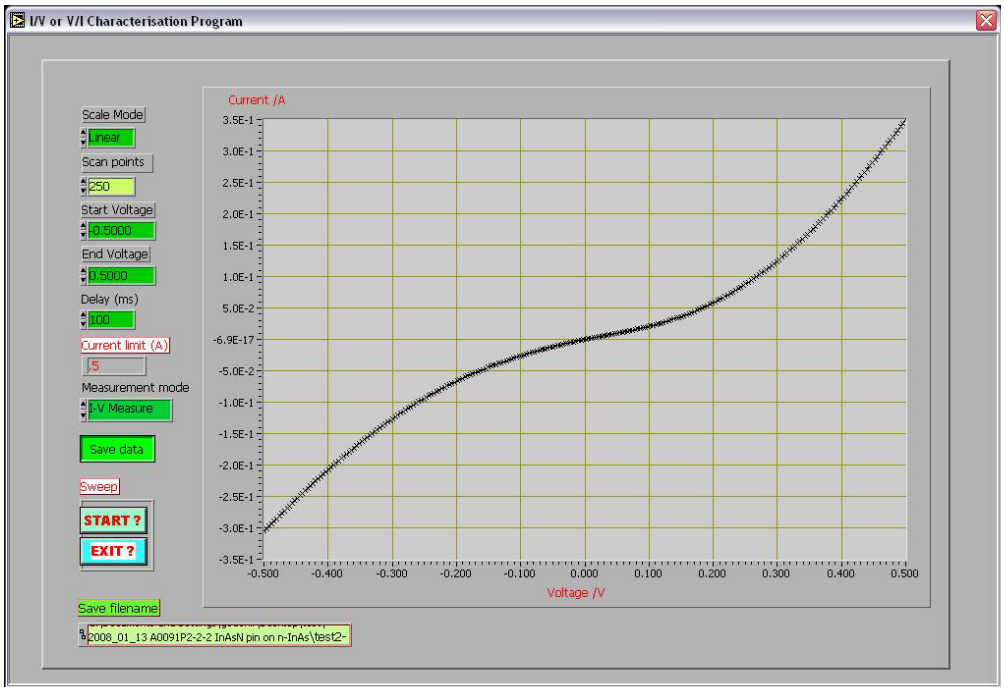

Figure 4.23 Current-voltage (I-V) Labview interface

Current-voltage (I-V) characteristics of devices are easily obtained with a Keithley(C) 2400-LV SourceMeter interfaced to a Labview(C) program that commands the built-in voltage source and measures the current across the device. Measurements at 77 K can be performed when the device is directly immersed in liquid nitrogen. A picture of the Labview(C) interface is shown in Figure 4.23 (it is advised to use a delay

of 100 ms between point, to increase progressively voltage range 0.2 - 1.6 V and to use a current limit 0.1 - 0.8 A to avoid damaging the device).

4.4 Rapid thermal annealing (RTA)

Rapid thermal annealing (RTA) is a commonly used technique consisting of a short time post-growth thermal treatment of a sample at high temperature (i.e. higher than the growth temperature). Post-growth annealing treatment of samples was performed at Sheffield National III-V Facility in a MATTSON(C) Rapid Thermal Annealer following the procedure illustrated in Figure 4.24.

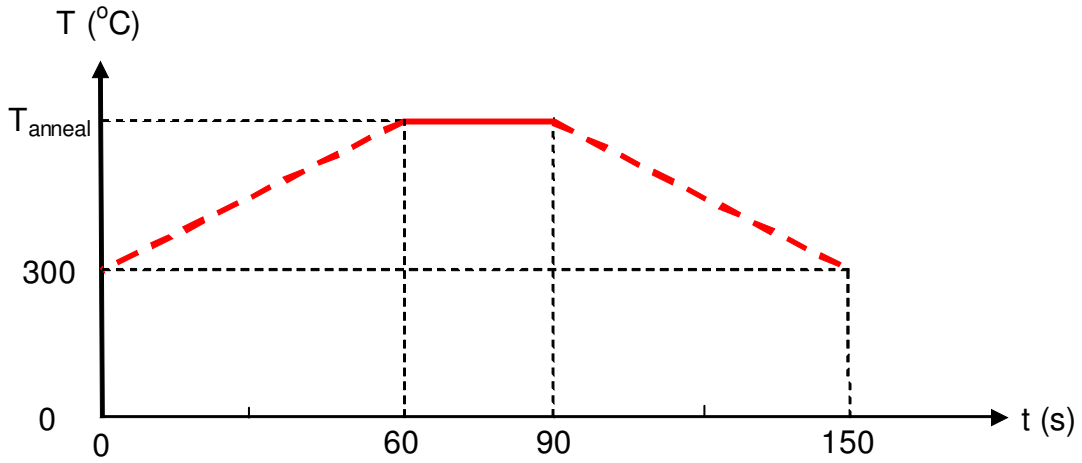

Figure 4.24 Time diagram of a RTA procedure

A purge for 90 s under N atmosphere (10 L.min^{-1}) without heating cleans the chamber atmosphere to avoid interaction between residual (atmospheric) gases and the sample to be annealed. The RTA of InAsN samples can then be performed for 30 s under N atmosphere (2 L.min^{-1}) at a temperature T_{anneal} between 450°C and 650°C reached by a 60 s-ramp. To prevent the desorption of arsenic from the surface, the sample is sandwiched between two GaAs wafers.

4.5 Clean room operations and processing

Cleaning samples is a an important operation before PL measurements, Nomarski microscope, SEM and AFM surface analysis or processing. Instead of the procedure consisting of boiling the sample in trichloroethylene (highly toxic) followed by a dip in isopropanol (IPA), it is better to follow the procedure performed at Sheffield National III-V Facility for safety reasons [135]. After a dip in hot n-butyl acetate, the sample is dipped in acetone then in hot IPA before being blown dry with nitrogen gas. Handling must be done wearing gloves.

The processing of p-i-n structures was performed by Dr R. Airey at Sheffield National III-V Facility. Contacts were realised by conventional photolithography (exposition to UV light of samples coated with photoresist) and gold evaporation ; mesas were formed in a similar way by dip in an acid etch. Devices with diameter of 200 μm to 1 mm were obtained and mounted onto TO-46 headers.

Chapter 5. Investigation of the parameters controlling material quality and nitrogen incorporation in InAsN

Reports on InAsN often state the difficulty to incorporate nitrogen and preserve good material quality. The following chapter presents the properties of InAsN with strongly localised states and the influence of MBE growth conditions on the nitrogen incorporation, structural properties and luminescence of InAsN.

5.1 Preliminary study of dilute nitride InAsN

5.1.1 Generation of defects in InAs by exposure to nitrogen

The growth of good quality InAsN material by means of a nitrogen plasma is rather complicated and can generate defects in InAs instead of optically-active InAsN (where band-to-band transitions dominate the luminescence). A few InAsN epilayers on InAs substrates were grown by MBE at Sheffield and at Lancaster, with thicknesses between 0.2 μm and 0.5 μm. The samples showed mirror-like surface and nitrogen compositions between 0.06 % and 1.10 % were measured by XRD as reported in Table 5.1. As shown in Figure 5.1 (a), the samples with composition below 0.1 % exhibited a shoulder-like epilayer rocking curve while for higher compositions, Pendellösung fringes could be seen, foreshadowing a potentially good interface between InAs buffer and InAsN epilayer. PL measurements of these samples at 4 K are shown in Figure 5.1 (b). A first peak around 2.99 μm corresponding to band-to-band recombination in InAs can be observed for all the samples. Its lineshape is

generally broad, with a FWHM between 11 meV and 33 meV, much broader than 4 meV at low laser excitation power reported for MBE-grown InAs PL [136].

Sample reference	M2774	A0108	A0088	A0077
Nitrogen composition	0.06%	0.08%	0.24%	1.10%
Measured 4 K PL emission (meV)	396	382	379	374
Calculated (BAC) 4 K PL emission (meV)	409	406	390	339

Table 5.1 Details of InAsN samples with defects

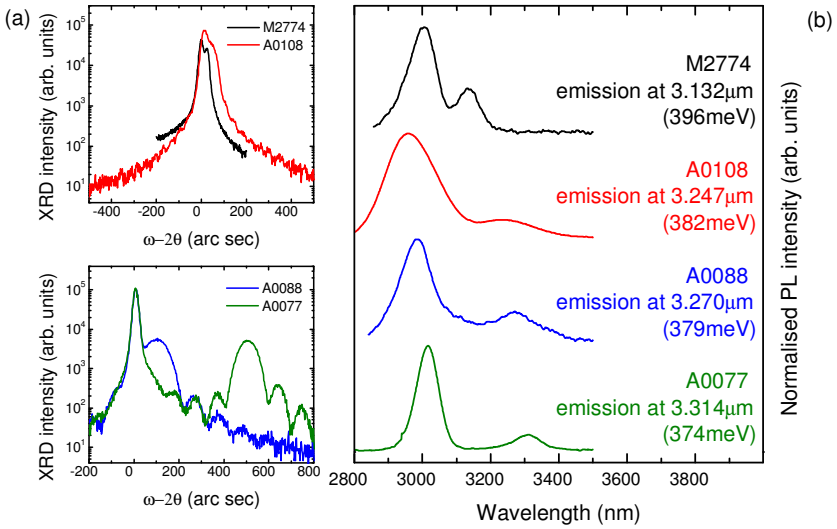

Figure 5.1 (a) XRD measurements of the same samples ; (b) 4 K photoluminescence of defects observed in InAsN epilayers

The most striking feature is the energy of the long wavelength-peak of each sample at 396, 382, 379 and 374 meV. The calculated PL emission at 4 K presented in Table 5.1 – based on the BAC model for InAsN (see Section 6.3) and the composition measured by XRD – does not match with the PL measurements : the photoluminescence observed does not originate from optically active InAsN material. Sample M2774 (0.06 % N) shows a peak at 3.132 μm (396 meV) which exhibited a slight blueshift with increasing excitation power and quenched at 25 K. It can

therefore be attributed to a donor-acceptor pair as the emission labelled DAP_1 observed at 396.5 meV in epitaxial InAs [136, 137] shown in Figure 5.2 (b). Samples A0108 (0.08 % N) and A0088 (0.24 % N) exhibited peaks at 3.247 µm (382 meV) and 3.270 µm (379 meV) respectively. Similarly broad emissions between 378 and 381 meV have been reported in InAs [12, 93] and n-type InAs [136] due to impurities or defects as pictured in Figures 5.2 (c) and (d). The wide lineshape and the saturation of the PL intensity with increasing excitation power (not shown) in the case of samples A0108 and A0088 suggest a donor-acceptor pair recombination as can occur between a shallow donor at the energy E_S 3 meV below the bandgap and a deep acceptor at the energy E_{A2} 35 meV above the valence band in InAs, as illustrated in Figure 5.2 (a) [138]. Last, a broad peak at 3.314 µm (374 meV) was observed in sample A0077 (1.10 % N). Although an emission B_2 in Figure 5.2 (e) has been reported with a FWHM of 24 meV at 374 meV in InAs but with a sharp high-energy edge [137], its origin has not been clearly identified in sample A0077.

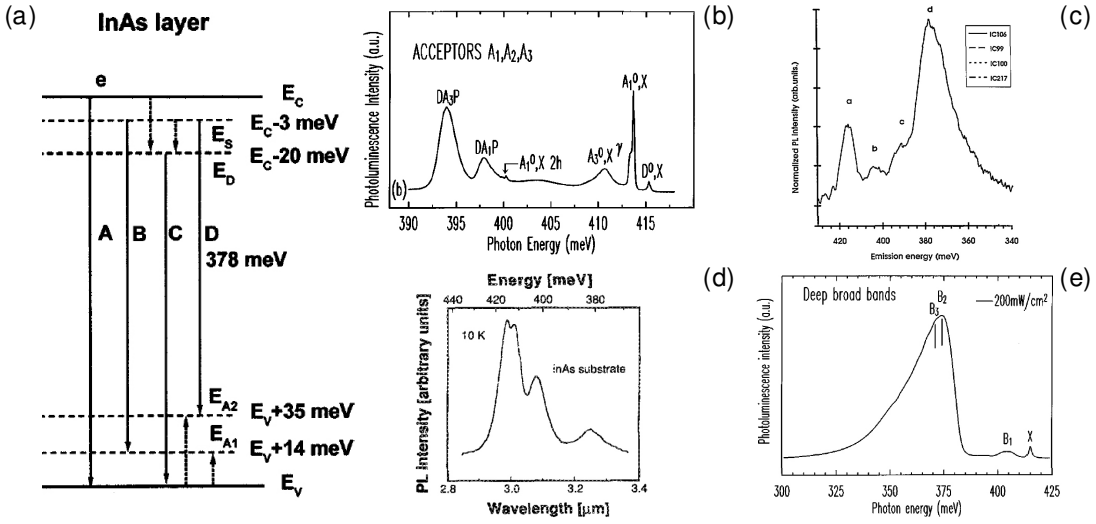

Figure 5.2 Transitions in InAs : (a) E_S - E_{A2} transition [138] ; (b) DAP_1 at 396.5 meV [137] ; (c) peak *d* at 379 meV [93]; (d) peak at 3.25 µm [12] ; (e) B_2 at 374 meV [137]

Emissions at 398 meV and 378 meV are common features in n_0-InAs grown by LPE at Lancaster. Sample M2774 with 0.06 % N hence show n-type dopant behaviour of InAsN for low N concentration [81]. The defects in A0108 (0.08 % N) and A0077 (1.10 % N) may originate from the high nitrogen flux (9.6×10^{-7} mbar) or the high nitrogen plasma power (260 W) used respectively. More generally, they may be due to unoptimised nitrogen plasma operation. Namely, the striking of the plasma was originally performed with the InAs buffer directly facing the plasma, the shutter being closed though. This might cause impacts of N ions when setting the plasma to growth parameters. The growth was also started shortly after the striking of the plasma, thus perhaps not very stable.

Whereas XRD measurements shown in Figure 5.1 (b) evidenced the presence of nitrogen in the material, PL measurements clearly showed that N in these samples does not allow band-to-band transitions. It is likely that most of the nitrogen was incorporated in interstitial sites, but nuclear reaction analysis measurements (NRA) [95, 139] would be needed for further investigation to confirm this.

5.1.2 Nitrogen composition measurements in InAsN

Three early test samples consisting of 0.5 μm-thick InAsN epilayers were grown on (001)-oriented InAs substrates by MBE at Sheffield. XRD measurements on the (004) diffraction plane are shown in Figure 5.3. The peak at 0 arc sec for all three samples is due to the InAs substrate. Based on the epilayer peak at higher diffraction angles, nitrogen composition for samples M2774, M2775 and M2806 was estimated to be 0.06 %, 0.45 % and 0.95 % respectively using Vegard's law. The lattice constant of InAsN decreases and the lattice mismatch to InAs increases with increasing nitrogen. The epilayer peak intensity decreases with increasing nitrogen. In the case of

M2775 and M2806, the XRD peak is broad, a sign of a poor interface, and the XRD FWHM drastically increases above 100 arc sec with higher nitrogen. These two characteristics show the degradation of the interface between substrate and epilayer with increasing nitrogen content and reveal the poor quality of the material.

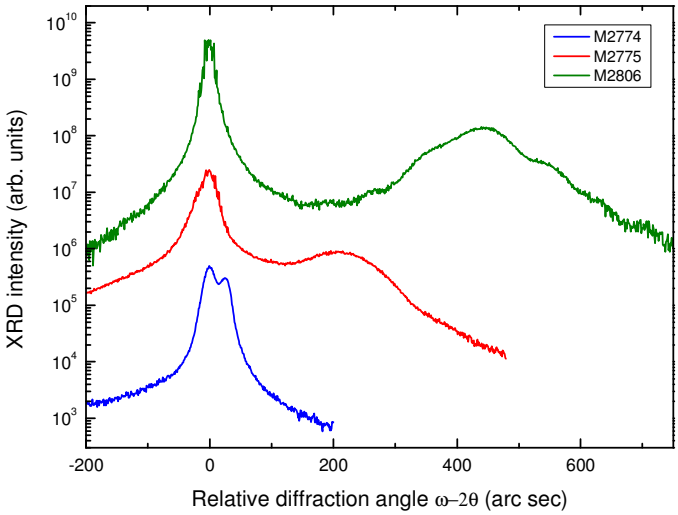

Figure 5.3 XRD measurements on the (004) diffraction plane of InAsN samples containing 0.06 % N (M2774), 0.45 % N (M2775) and 0.95% N (M2806)

Measuring ternary composition by XRD is generally performed by a single scan on the (004) diffraction plane (see Sections 2.2.2 and 4.2.1). Nevertheless, the analysis of the rocking curves requires the knowledge of the amount of relaxation (0 % to 100 %) for the epilayer under study. The mentioned compositions were calculated assuming full strain of the layers but this needs to be proved. Systematic XRD measurements on the (001) and (115) diffraction planes can help to find out the strain-related composition of the material but are time-consuming. Sometimes, the signal from (115) rocking curves is too weak to be detected. Moreover, results given for partially strained layers by analysis of the combined rocking curves with Bede[(C)] PeakSplit software are often questionable.

The comparison between the epilayer thickness and the critical thickness h_c (see Section 2.6.3) can address this issue better and quicker. Schematically, a layer grown with a thickness below the critical thickness is considered to be fully strained (0 % relaxation) and above h_c fully relaxed (100 % relaxation). Based on the critical thickness model developed for $Si_{1-x}Ge_x$ [24], a model on the basis of (2.32) was derived for InAsN. The dependence of the Poisson ratio ν_{InAsN} on the nitrogen composition x was supposed to follow Vegard's law, thus resulting in :

$$\nu_{InAsN}(x) = x\nu_{InN} + (1-x)\nu_{InAs} \qquad (5.1)$$

with $\nu_{InN} = 0.387$ and $\nu_{InAs} = 0.352$ (from Bede[(C)] RADS). Combining in the critical thickness equation (2.32), equations (2.4) for the lattice constant $a(x)$, (2.31) for the lattice mismatch f (a_{layer} taken as $a_{InAsN}(x)$) and (5.1) for the Poisson coefficient ν, the model was set up using a MatLab[(C)] 6.5 routine (see Appendix I). Results are shown by the lines in Figure 5.4.

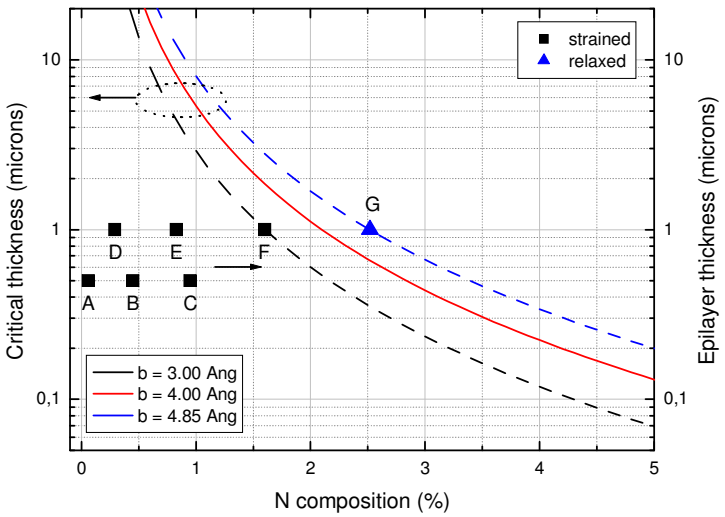

Figure 5.4 Critical thickness for different values of the slip distance b (lines, left axis) and epilayer thickness of strained and relaxed epilayers (scatter, right axis). InAsN samples A - G have different nitrogen composition and were grown with a thickness of 0.5 µm for samples A - C and 1.0 µm for samples D - G

The only parameter omitted mentioning so far is the slip distance *b*. People and Bean [24] used a value of *b* of 4 Å for $Si_{1-x}Ge_x$. Considering the lattice parameters a_{Si_cubic} = 5.4307 Å and a_{Ge_cubic} = 5.6575 Å for the calculation of the lattice constant (based on (2.4)), the slip distance represents ¾ of $Si_{0.5}Ge_{0.5}$ lattice constant. The parameter *b* does not seem to be tabulated for semiconductors. To find out what value to use for InAsN, the epilayer thickness *h* of samples A - G (see caption of Figure 5.4) is plotted on the same graph. Samples A, B, and C are respectively samples M2774, M2775 and M2806 reported earlier. The analysis with Bede$^{(C)}$ PeakSplit software of XRD measurements on the (004) and (115) diffraction planes showed A, B and C to be fully relaxed. Samples D - G are 1.0 µm-thick samples with respective nitrogen composition 0.29 %, 0.83 %, 1.60 % and 2.52 %. Samples D - E all show a smooth surface under the Nomarski microscope while sample G shows cross-hatching (see sample A0156 in Section 6.1.5). It can hence be deduced that 1 µm-thick samples with up to 1.6 % N are fully strained while a 1 µm-thick sample containing 2.52 % N is partially relaxed. One can thus conclude on boundaries for the slip distance *b* : $b > 3$ Å so that $h < h_c$ for the fully strained samples A - F and $b \leq 4.85$ Å so that $h \geq h_c$ for the – at least – partially relaxed sample G. A slip distance of $b = 4$ Å seems thus acceptable for InAsN and the red line in Figure 5.4 represents the critical thickness in InAsN.

5.1.3 Identification of strongly localised states

Two early test samples consisting of 0.5 µm-thick InAsN epilayers were grown on InAs substrates by MBE at Sheffield. 14 K power-dependent PL measurements of these samples along with bulk MBE-grown InAs are shown in Figure 5.5 and compared in Table 5.2. The bulk InAs (sample A0129) in

Figure 5.5 (a) showed a bright and narrow emission at 3.004 µm with a Gaussian lineshape. When the excitation power is increased from 0.2 W to 1.6 W, the associated energy shift $\Delta E_{PL(P)}$ with increasing power (positive for a blueshift, negative for a redshift) is smaller than 1 meV and associated with the band-filling effect [10b]. Higher laser excitation powers increase the number of electron-hole pairs exciting the material, filling progressively the conduction and valence bands where emissions from the bandgap and levels at slightly higher energy occur. Last, it is worth noting that this blueshift is non-existent at 4 K in InAs because of a relatively flat conduction band.

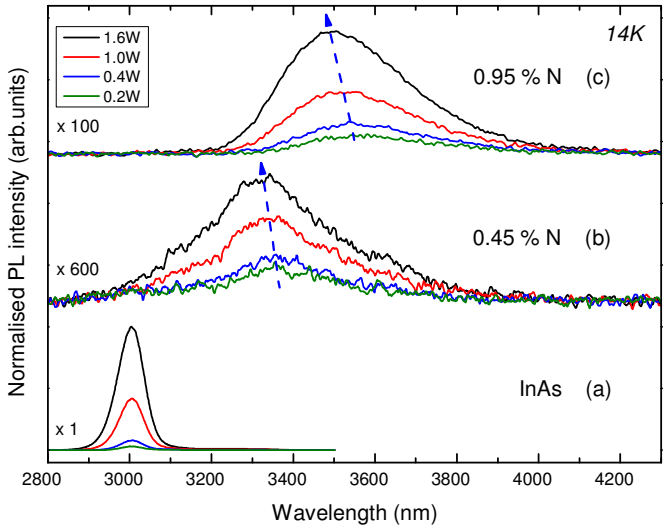

Figure 5.5 14 K power-dependent PL of bulk InAs A0129 (a) and bulk InAsN with different N compositions : (b) 0.45 % (M2775), (c) 0.95 % (M2806)

InAsN samples M2775 (0.45 % N) and M2806 (0.95 % N) plotted in Figure 5.5 (b) and (c) respectively show a single broad asymmetric peak with a long low-energy tail at 14 K with a low luminescence intensity. Emissions at 3.328 µm (~ 373 meV) and 3.504 µm (~ 354 meV) are reported here at 1.6 W laser excitation power for nitrogen compositions of 0.45 % and 0.95 % respectively. One can notice the drastic widening of InAsN lineshape compared to InAs : the PL FWHM at 1.6 W

is more than three times bigger in the case of InAsN epilayers. This is probably due to a high degree of compositional and structural disorder as observed in GaInNAs/GaAs QW with N as low as 1.5 %.

Sample reference	Nitrogen composition (%)	1.6W PL FWHM (meV)	E_0 (meV)	$\Delta E_{PL(P)}$ (meV)	k value
A0129	0.00	10.5	(2.7)	0.7	1.72
M2775	0.45	38.9	25.3	5.0	0.65
M2806	0.95	35.8	17.1	8.1	0.90

Table 5.2 Selected characteristics at 14 K of bulk InAs and bulk InAsN with strongly localised states

The InAsN samples exhibited a low-energy tail. Such a lineshape was previously observed in dilute nitrides such as GaNAs/GaAs bulk and MQW [140, 141] and GaInNAs/GaAs MQW [142-144] and corresponds to the tailing of the density of states (DOS) originating in potential fluctuations of the band edges. The low-energy bandtail observed in PL measurements is generally fitted by [142] :

$$I_{PL}(E) \propto \exp\left(\frac{E}{E_0}\right) \qquad (5.2)$$

where I_{PL} is the PL intensity as a function of the photon energy E and E_0 is a characteristic energy whose value decreases with improved structural properties. In our case, characteristic energies E_0 of 17.1 and 25.3 meV for InAsN samples M2775 and M2806 respectively (at 1.6 W excitation power) indicate strong localisation when compared to InAs sample A0129 (below 3 meV) and reported values with extremes between 3.0 meV [142] and 60 meV [140].

Figure 5.5 presents laser excitation power-varied PL measurements as well. InAsN samples exhibit a strong blueshift with increasing power, as indicated by

$\Delta E_{PL(P)}$ values of 5.0 and 8.1 meV for a power range 0.2 W - 1.6 W. A blueshift with increasing excitation power is a common feature of dilute nitrides such as GaInAsN [145, 146] and GaAsN [14]. These high values are attributed to strongly localised states and the blueshift corresponds to their filling with increasing carrier density [10b]. Analysis of excitation-power dependent PL is commonly performed to investigate the emissions in narrow gap semiconductors [93, 137, 138, 147] and occasionally in nitride materials [145, 148, 149]. The PL intensity I_{PL} shows a variation with increasing excitation L modelled by [147, 150] :

$$I_{PL} \propto L^k \qquad (5.3)$$

where k is an exponent verifying $1 \leq k \leq 2$ for exciton-like transitions (close to the bandgap) and $k < 1$ for free-to-bound transitions (donor-hole hD, electron-acceptor eA) and donor-acceptor pairs (DAP) in near-band-edge photoluminescence studies. This approach is used to compare InAsN to InAs as shown in Figure 5.6.

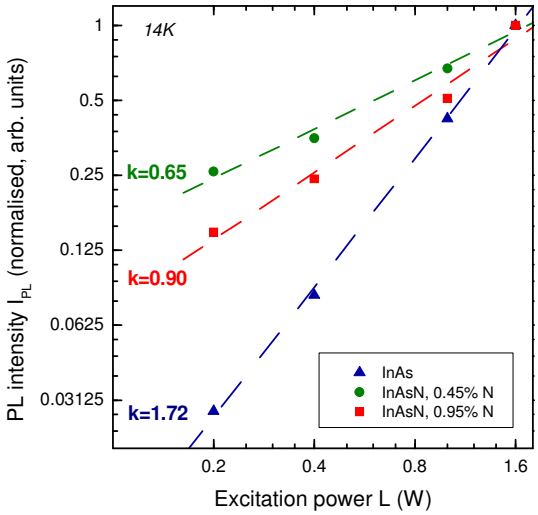

Figure 5.6 Laser excitation power dependence of the 14 K PL intensity (normalised to the value at 1.6 W)

InAs shows a superlinear dependence of the power on the PL intensity with a k value of 1.72 while InAsN showed k values of 0.65 and 0.90 for the samples

containing 0.45 % and 0.95 % nitrogen. In the case of InAs, such a high *k* value is attributed to band-to-band or free carrier recombination whereas we believe *k* values below unity can be associated with localised states in undoped dilute nitride materials. The InAsN samples presented here show a single asymmetric peak of weak intensity and exhibit a blueshift with increasing power and temperature, typical features of dilute nitride material as reported in GaAsN [140, 151] and InGaAsN [152, 153]. The wide lineshape and low-energy tail are attributed to inhomogeneity of the nitrogen distribution and may originate from unoptimised growth conditions. The large energy shift with increasing laser excitation power and high characteristic energies suggests that the nitrogen states are strongly localised.

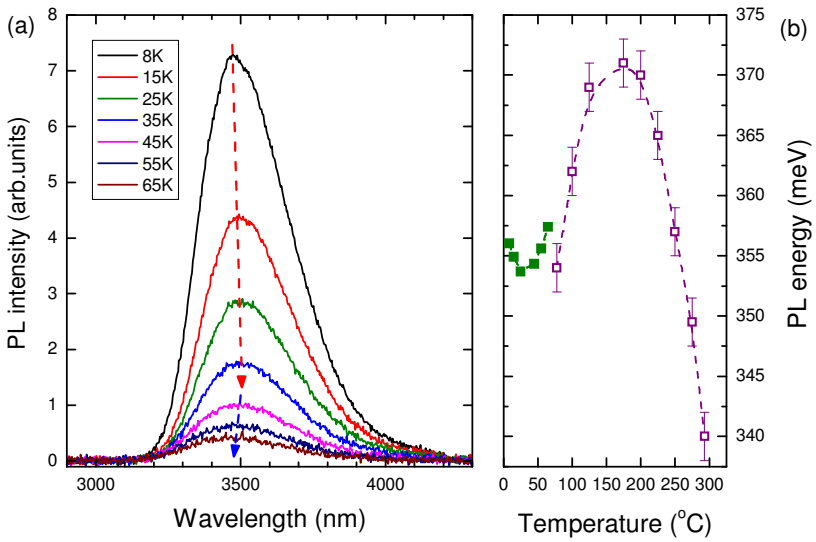

Figure 5.7 Temperature-varied PL of bulk InAsN ([N] = 0.95 %) with strong localised states : (a) PL spectra ; (b) PL energy as a function of the temperature. Green solid symbols are data measured from the sample, open purple symbols are data from [85]

Further evidence of strong localisation is given by the temperature-varied PL of bulk InAsN with nitrogen content of 0.95 % as shown in Figure 5.7 (a). The luminescence quenches at about 70 K and no room-temperature luminescence can be

observed. This is probably due to a high concentration of non-radiative centres. A striking and unusual feature is a 3 meV redshift from 8 K to 35 K followed by a blueshift from 45 K. Compiling these data with the ones from $InAs_{0.99}N_{0.01}$ [85] – the sample is from the same batch indeed through our collaboration with Dr Hopkinson – we report an S-shaped temperature dependence of the PL as shown in Figure 5.7 (b) : a redshift followed by a blueshift up to 175 K, above which a redshift is again observed until room temperature. The so-called S-shape trend was also observed in quantum and bulk structures. In AlAs/GaAs disordered superlattices [154] and dilute nitride quantum structures such as InGaN/GaN MQW [155], GaInNAs/GaAs SQW [156] and MQW [157], it is due to inhomogeneity and carrier localisation in the QW. Band-tail states in the density of states (DOS) are formed as a consequence of nitrogen fluctuations and are responsible for the anomalous temperature dependence. In bulk nitride material $Al_xGa_{1-x}N$, the S-shape emission shift is a sign of disorder and alloy potential inhomogeneities. Time-resolved PL spectroscopy showed that the first redshift is dominated by radiative recombination processes and in the blueshift region, non-radiative recombination is dominant [158].

Preliminary InAsN layers seem to suffer from a degradation of the material quality with the incorporation of as little as one percent nitrogen. Defects in InAsN material with non-optically active nitrogen were identified through their PL emissions. The critical thickness model derived for InAsN is a guide to grow fully strained layers, favoured to the fully relaxed condition to avoid surface cross-hatching inherent to the latter. InAsN alloys can exhibit a low-energy tail and temperature quenching of the luminescence far below room temperature. Strongly localised states were evidenced and poor luminescence may partly be due to a high density of non-radiative

centres. Material disorder was evidenced by the S-shape temperature dependence of the photoemission, which supports the need for optimisation of the growth conditions.

5.2 Growth conditions of InAsN material for enhanced nitrogen incorporation and luminescence

Preliminary InAsN samples were subject to defects or showed poor structural properties and luminescence. A detailed study of the influence of the growth conditions on the material quality is presented in order to enhance nitrogen incorporation and luminescence of InAsN material.

5.2.1 Influence of nitrogen flux and plasma power

An initial step towards the control of the nitrogen composition is to study the influence of the nitrogen flux on the nitrogen composition of layers grown by plasma assisted-MBE (at fixed plasma power). Three sets of InAsN epilayers were grown on InAs substrates with different nitrogen flux at fixed RF powers, growth temperatures and As fluxes. The nitrogen composition of these samples is plotted as a function of the nitrogen flux in Figure 5.8. A first set, grown at 160 W with varying nitrogen flux, shows a linear increase in the nitrogen composition (up to 0.96 %) with increasing N flux. Such a behaviour was previously reported for dilute nitrides grown by plasma assisted-MBE, in GaInNAs/GaAs MQW [42] and GaNAs [121, 159]. Two other batches of samples were grown at RF powers of 210 W and 260 W. A radically different behaviour is observed at higher RF powers and a decrease in the nitrogen composition is observed with increasing N flux.

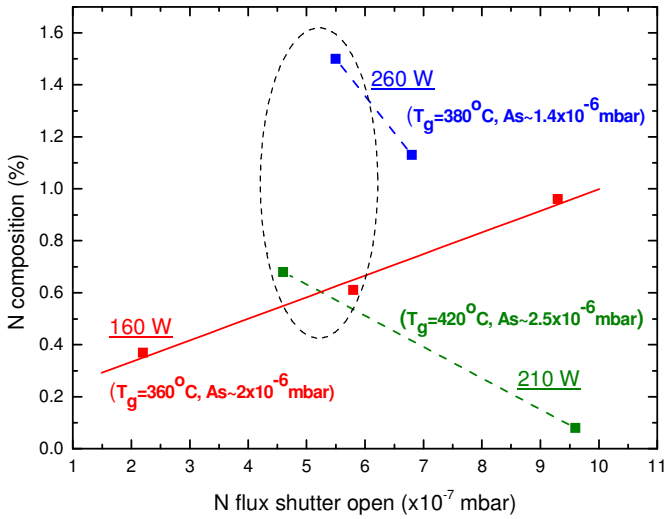

Figure 5.8 Nitrogen composition as a function of the N flux at fixed RF power. The solid line is a linear fit and dashed lines are a guide to the eye

The dependence of the nitrogen composition on the nitrogen flux at fixed RF power can be understood in the light of the nitrogen plasma characterisation by optical spectroscopy presented earlier. At low RF power (160 W), the overall smooth increase of the atomic nitrogen line intensity I_N in Figure 4.12 (a) (see Section 4.1.6) probably leads to a linear increase of atomic nitrogen supplied for N flux from 3 to 8×10^{-7} mbar. On the contrary, plasma characterisations at higher RF powers of 210 W and 260 W showed a drop in atomic nitrogen when the nitrogen flux increased from 5 to 8×10^{-7} mbar. This trend at high RF powers has been reported for bulk GaAsN and GaInAsN MQW grown by RF-MBE [160]. The maximum nitrogen composition achieved at a plasma power of 160 W is inferior to one percent and a higher composition is required for the purpose of this thesis. The comparison of the samples grown with increasing power at ~ 5×10^{-7} mbar N flux (dashed circle) – at different growth temperatures though – suggests that higher powers should help incorporate more nitrogen.

For some nitrogen plasma sources, the RF power controls more effectively the generation of atomic nitrogen than the nitrogen flow rate [161]. To find out whether the nitrogen composition could efficiently be tuned by the variation of RF power at fixed nitrogen flux (all other parameters identical), a set of 200 nm-thick samples were grown with varying RF power at ~ 5×10^{-7} mbar N flux (growth rate ~ 1 µm/h).

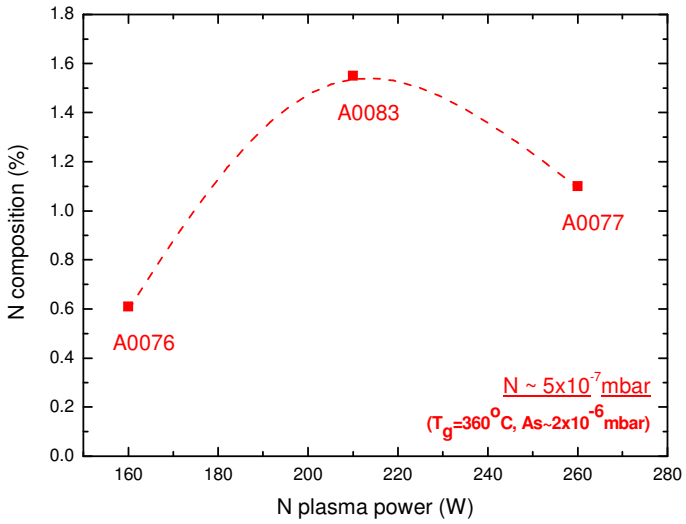

Figure 5.9 Nitrogen composition as a function of the N plasma power. The dashed line is a guide to the eye

The dependence of the nitrogen composition on the plasma power is shown in Figure 5.9. While the characterisation of the nitrogen plasma by optical spectroscopy (see Figure 4.13 (a) in Section 4.1.6) showed atomic nitrogen lines with increasing intensity I_N when the RF power was increased, the nitrogen incorporation in these samples increases by a factor of three up to 210 W (more nitrogen atoms are produced) but drops at RF power of 260 W. This behaviour contradicts the generally reported trend in GaNAs and GaInAsN [121, 126, 159, 160] for which the nitrogen composition increases and saturates with increasing RF power. In our case, the drop can be attributed to a likely decrease in the brightness of the plasma. Indeed, it was shown for GaAsN that the nitrogen composition is a linear function of parameter

C_{SOURCE}, a function of the plasma brightness and expressed as $h \times V_{OPT} / R_{GaAs}$, where h is the number of holes in the aperture plate of the plasma, V_{OPT} the plasma light intensity and R_{GaAs} the GaAs growth rate [162]. At fixed growth rate (as is the case for these samples) and identical plate in front of the plasma cell (all other parameters identical), the nitrogen composition is strictly proportional to the brightness of the plasma. Hence for sample A0077 (1.10 % N), a plasma setting still in the bright mode but with a lower brightness could result in an InAsN epilayer with lower nitrogen composition, due to lower efficiency of the cell in cracking N_2 molecules.

The effective available RF power ranges from 160 W to 380 W. High RF powers produce a higher amount of ionic N species [163] and can damage the crystal as reported for GaInNAs SQW lasers [164] ; they will be avoided. As demonstrated in this section, the plasma set to an inappropriate N flux might operate with reduced efficiency to crack dimers. Finally, it was shown in the characterisation of the plasma (see Figure 4.12 (a), Section 4.1.6) that there is an appropriate flux for each RF power that maximises the generation of atomic nitrogen. InAsN growth will thus be preferred with the plasma operated at optimal setpoints to assure maximum efficiency with RF powers ranging from 160 W to 260 W. Since the variation of the N flux at fixed RF power and the variation of the RF power at fixed N flux does *not* vary regularly the nitrogen composition, the latter can probably be finely tuned by other growth parameters.

5.2.2 Influence of growth temperature

The growth temperature is a crucial parameter to allow the growth of phase segregation-free InAsN material [72]. A series of samples were grown at different growth temperatures, all other parameters fixed (i.e. at RF power 160 W, N flux

~ 5.5×10^{-7} mbar, growth rate ~ 1.0 µm/h, minimum arsenic flux, thickness below 1 µm) and showed a mirror-like surface. Nitrogen composition as a function of the growth temperature is plotted in Figure 5.10 and the characterisation results are compared in Table 5.3. The error in temperature is bigger at higher growth temperature : the growth temperature of samples A0084 (0.56 % N) and A0086 (0.00 % N) was indeed monitored by a pyrometer that was less accurate at high temperature ; the maximum temperature being ~ 400°C, the growth temperature was extrapolated.

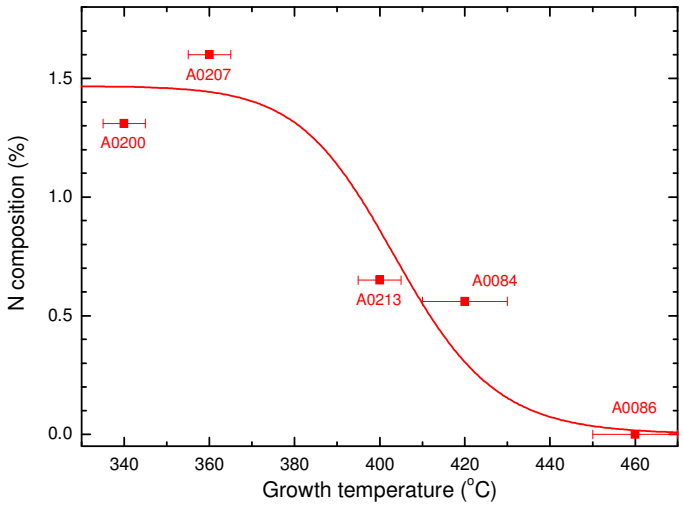

Figure 5.10 Nitrogen composition as a function of the growth temperature. The solid line is the calculation result based on (5.8)

The nitrogen composition levels around 1.5 % at low growth temperatures 340 - 380°C before quickly decreasing at temperatures around 420°C. No nitrogen was incorporated in sample A0086 grown at 460°C. GaNAs and GaInNAs were reported to have an almost unchanged nitrogen composition in the low growth temperature range (400 - 500°C) [159, 165]. In InAsN as well, the little variation of nitrogen composition at growth temperatures below 380°C is attributed here to a weak nitrogen desorption effect over this low temperature range. Decrease in the nitrogen

composition at growth temperatures above 380°C for InAsN can be compared to the same trend occurring in GaNAs and GaInNAs grown by MBE (above 500°C) [159, 165] or by MOVPE [120, 166]. It has been successfully attributed to the combined effects of surface segregation and nitrogen desorption. No nitrogen could be incorporated at 460°C in MBE-grown InAsN on InAs [84]. 4 K PL measurements of sample A0086 (0.00 % N) grown at 460°C showed a peak from InAs along with an emission at 3.295 μm (376 meV) within 2 meV of the reported broad feature B_2 in InAs [137] ; the latter is attributed to a defect and evidences the maximum of the growth temperature window.

Sample reference	A0200	A0207	A0213	A0084	A0086
Growth temperature (°C)	340	360	400	420	460
RHEED pattern	(2 × 1)	(2 × 1)	(2 × 4)	(2 × 3)	(2 × 4)
Nitrogen composition	1.31 %	1.60 %	0.65 %	0.56 %	0.00 %
XRD FWHM (arc sec)	96	101	**31**	106	-

Table 5.3 Characterisation results from XRD and RHEED patterns for varied growth temperatures

RHEED pattern and characterisation results from XRD are presented in Table 5.3 to find out the optimal temperature for the growth of InAsN. RHEED pattern observed during growth is reported as a function of the growth temperature. A (2 × 1) pattern corresponds in our case to high nitrogen composition. It can tentatively be associated with a bidimensional growth mode (i.e. layer by layer) as reported for GaAsN [120]. Reason *et al.* state that a (2 × 1) reconstructed surface for GaAsN material has a significantly greater number of group V sites per unit area than (3 × 1) or (2 × 4) reconstructions and deduce a more effective substitutional incorporation of

N atoms at low growth temperatures [139]. It nevertheless results in a roughening of the surface. It is hence possible that InAsN samples A0200 (1.31 % N) and A0207 (1.60 % N) have a higher proportion of nitrogen atoms in substitutional sites. The (2 × 4) reconstruction observed in A0086 where no nitrogen was incorporated can be associated with the widely reported RHEED pattern for InAs [92].

XRD epilayer peak width (XRD FWHM) is a common indicator of the material quality : the narrower the epilayer peak, the better the material. As shown in Table 5.3, low growth temperatures below 360°C correspond to wide epilayer peaks (above 100 arc sec), while at growth temperature 400°C, an XRD FWHM as narrow as 31 arc sec was observed. This value is very close to the theoretical one of 21 arc sec obtained by simulation. A narrowing of XRD measurements with increasing growth temperature is a common feature in GaN films grown by MBE [167]. Given that the nitrogen composition decreases at higher growth temperature, a narrower XRD linewidth was expected at growth temperature of 420°C than that reported in Table 5.3 for sample A0084 (0.56 % N). Some other samples, grown at 420°C with slightly different growth conditions, showed narrower XRD epilayer peak.

Figure 5.11 (a) shows the PL intensity at 4 K as a function of the temperature. It can be seen in Figure 5.11 (b) that the PL intensity gains an order of magnitude and reaches a maximum for growth temperature of 400°C (sample A0213 with 0.65 % N) before decreasing again at higher temperature. A similar trend with an optimal temperature maximising the PL intensity is usually observed at 450°C for GaInNAs [165] and at 460°C for GaAsN grown at growth rate above 0.4 ML/s (~ 0.5 μm/h) [168]. It is worth noticing that the high PL intensity of the InAsN sample grown at 400°C corresponds to a (2 × 4) surface reconstruction : indeed this RHEED pattern during growth resulted in bright PL for GaAsN bulk material ([N] ~ 1 %) [162]. An

important rule of thumb to keep in mind is that the optimal temperature reduces with decreasing growth rate [162, 168]. PL FWHM is an important criterion, as an indicator of the material quality and for wavelength selectivity in device applications. As shown in Figure 5.11 (b), the PL linewidth decreases continuously as the temperature is increased from 340 to 400°C. Undoubtedly the quality of the material improves to reach an optimum at 400°C. GaAsN PL lineshape shows the same behaviour with increasing growth temperature (at growth rate below 0.8 ML/s) [168]. The widening of the PL at high temperature may be attributed to the onset of three-dimensional growth.

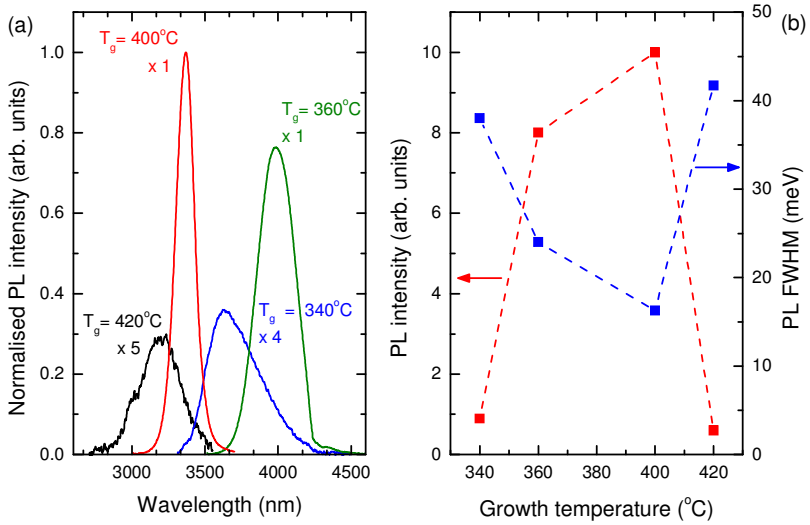

Figure 5.11 (a) 4 K PL spectra of samples grown at different temperatures ; (b) Dependence of the PL intensity and linewidth at 4 K as a function of the growth temperature. Dashed lines are a guide to the eye

A kinetic model was developed to describe the nitrogen incorporation in MBE-grown GaNAs and GaInNAs [165]. An instantaneous surface concentration of nitrogen atoms C_N depends on incoming nitrogen flux and the amount of incorporated and desorbed nitrogen. Its rate of change can be described by :

$$\frac{dC_N}{dt} = J_N - D\,C_N - K\,C_N \qquad (5.4)$$

where J_N is the arrival rate of N, $D\,C_N$ the desorption rate and $K\,C_N$ the incorporation rate. Under equilibrium growth conditions (at the surface), the rate of change is null and the nitrogen density can be expressed as :

$$N_N = \frac{\alpha\, N_{Ga} J_N}{K + D(T_g)} \qquad (5.5)$$

where N_{Ga} is the Ga atom density of GaAs, J_{Ga} the arrival rate of Ga, K the rate constant of incorporation and $D(T_g)$ the desorption rate constant dependent on the growth temperature T_g. The rate constant of incorporation K is proportional to the growth rate (thus J_{Ga}) :

$$K = \alpha\, J_{Ga} \qquad (5.6)$$

The desorption rate constant $D(T_g)$ *is* dependent on the growth temperature T_g (in K) :

$$D(T_g) = D_0 \exp\left(\frac{-E_d}{k_B\, T_g}\right) \qquad (5.7)$$

where D_0 is the inverse of the surface residence lifetime τ_s (5 ms for GaAs), E_d the activation energy for desorption (2.1 eV for GaAs [169]).

As far as InAsN is concerned, the arrival rate of indium J_{In} will be considered instead of J_{Ga}, N_{In} the indium atom density of InAs instead of N_{Ga}. A value of E_d = 3.4 eV for direct desorption from an InAs wetting layer was reported [170]. Due to the lack of reported values, the surface residence lifetime of 5 ms for GaAs will be used for InAs, corroborated by values around 1 ms used for Si [171]. The arrival rate of N atom J_N is proportional to the nitrogen flux, so are J_{In} and N_{In} to the indium flux, both fluxes being fixed for this set of samples. Considering that the nitrogen composition [N] in InAsN is proportional to the nitrogen density N_N, one derives a kinetic model for InAsN from (5.5), (5.6) and (5.7) :

$$[N] \propto \frac{\alpha N_{In} J_N}{\alpha J_{In} + D_0 \exp\left(\frac{-E_d}{k_B T_g}\right)} \qquad (5.8)$$

The model shown by the solid line in Figure 5.10 was calculated from (5.8) with parameters in Table 5.4 and fits well the presented data. Higher growth rate shifts the curve to the left and lower composition. Higher RF power shifts the curve to the left and higher composition.

Kinetic model parameter	$\alpha N_{In} J_N$	αJ_{In}	D_0	E_d
Value for growth temperature fit	1.5×10^{-20} (a.u.)	1.0×10^{-20} (a.u.)	2.0×10^5 s^{-1}	3.4 eV

Table 5.4 Calculated parameters for a fit of the nitrogen composition dependence on growth temperature by the kinetic model

The growth temperature window 360 - 440°C allowing incorporation of nitrogen and luminescence from InAsN epilayers was established by the present study. XRD and PL analyses showed that the best quality is achieved for samples grown between 380°C and 420°C, with bright luminescence and narrow XRD. The reciprocal dependence of the nitrogen composition on the growth temperature was fitted by a kinetic model adapted to InAsN.

5.2.3 Influence of growth rate

Under sufficient As flux, the growth rate in arsenide binaries and ternaries is controlled by the group-III element flux. It will be shown hereafter that the growth rate strongly influences the nitrogen incorporation in InAsN. A series of samples were grown at different growth rates, all other parameters fixed (i.e. at fixed growth temperature 420°C, RF power 210 W, N flux ~ 5.2×10^{-7} mbar, close to minimum

arsenic flux, thickness below 1 µm) and all showed mirror-like surfaces. Nitrogen composition as a function of the inverse growth rate is plotted in Figure 5.12 and characterisation results are compared in Table 5.5.

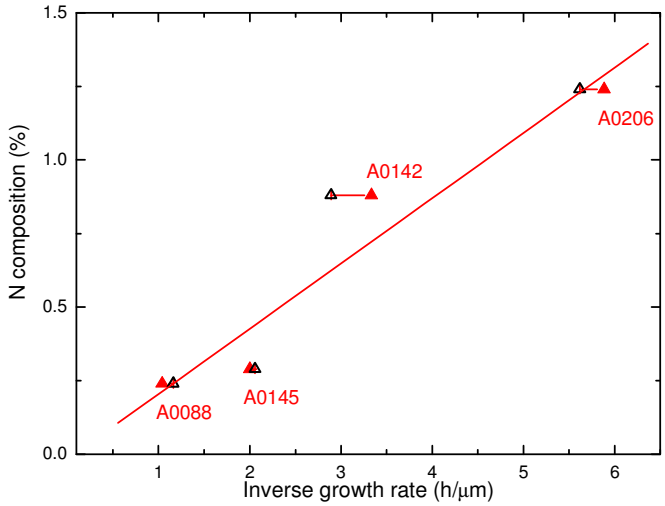

Figure 5.12 Nitrogen composition as a function of the inverse of the growth rate. The solid line is a linear fit. The growth rate was determined by RHEED oscillations (solid red triangles) or from XRD (open black triangles)

Nitrogen composition strongly increases with decreasing growth rate : nitrogen composition as high as 1.24 % is reached for low growth rate of 0.17 µm/h (sample A0206). As shown in Figure 5.12, the nitrogen composition is a reciprocal function of the growth rate. A similar behaviour has been widely reported for GaAsN grown at growth rate in the range 0.125 - 1.0 µm/h [161, 172] and for GaInAsN grown at growth rate between 0.8 and 2.0 µm/h [165]. The nitrogen content in GaAsN sometimes tends to level off at growth rate below 0.5 µm/h [159, 173], which is not the case in the present study. To explain the increase in nitrogen incorporation with reduced growth rate, it can tentatively be proposed that lower growth rates allow more time for N atoms to migrate on the surface and attach to the dangling bonds.

Sample reference	A0206	A0142	A0145	A0088
Growth rate (µm/h)	0.17 (0.178)	0.30 (0.346)	0.50 (0.486)	0.96 (0.86)
Nitrogen composition	1.24 %	0.83 %	0.29 %	0.24 %
RHEED pattern	(1 × 3)	(2 × 4)	(2 × 4)	(2 × 4)
XRD FWHM (arc sec)	58	29+	24	110
Incorporation rate (% N × nm/h)	2.1×10^2	2.5×10^2	1.5×10^2	2.3×10^2

Table 5.5 Characterisation results from XRD and RHEED patterns for varied growth rates. Numbers in brackets in the second row are growth rates determined from XRD (as in Figure 5.12)

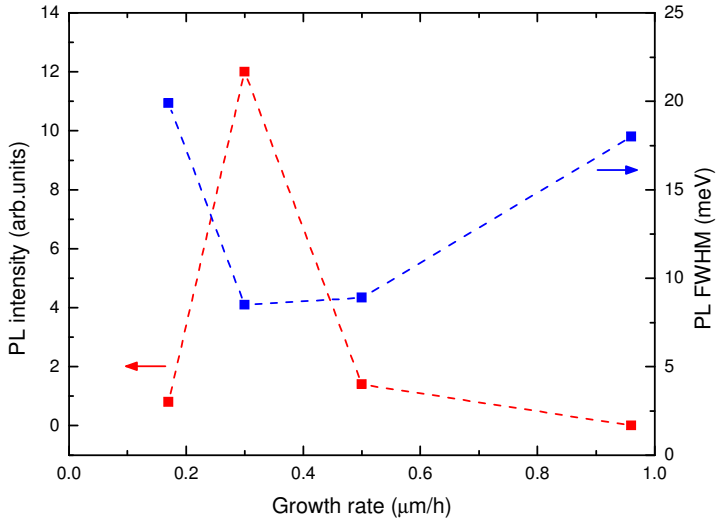

Figure 5.13 Dependence of the PL intensity and linewidth at 4 K as a function of the growth rate. Dashed lines are a guide to the eye

Characterisation results are compared in Table 5.5. For each sample, the first value of the growth rate was measured during growth by RHEED oscillations (see Section 4.1.5) and confirmed by XRD simulation fitting of the Pendellösung fringes when seen and respective substrate and epilayer peak intensities (numbers in brackets). Samples grown at growth rates between 0.3 and 0.5 µm/h present the best features : narrow XRD rocking curves along with (2 × 4) RHEED pattern already mentioned as a indicator of bright PL. PL intensity and linewidth as a function of the growth rate are shown in Figure 5.13. Sample A0206 (1.24 % N) grown at the lowest

growth rate of 0.17 μm/h exhibits rather weak and broad PL ; the (1×3) surface reconstruction can probably be related to a rough surface, explaining the poor luminescence. The highest PL intensity is observed at growth rate 0.3 μm/h. Lower nitrogen compositions are always observed at high growth rate of 1.0 μm/h when compared to lower growth rates, but broad XRD and PL linewidth and weak PL intensity observed for sample A0088 (0.24 % N) is not the general case for samples grown at 1.0 μm/h with slightly different growth conditions.

The incorporation rate of nitrogen in InAsN is expressed as a function of the nitrogen composition [*N*] and InAs growth rate R_{InAs} [51, 174] :

$$incorporation\ \ rate = [N]\, R_{InAs} \qquad (5.9)$$

In a similar manner to GaInNAs [174], the incorporation rate of N in InAsN is found to be independent of the growth rate as shown in Table 5.5 and fixed at ~ 2×10^2 % N × nm/h, lower than 3.7×10^2 % N × nm/h reported for N in GaInNAs. This means that under growth at As flux close to the minimum arsenic flux, N radicals supplied by RF plasma incorporate with a unity sticking coefficient in InAs (like dopant atoms, e.g. Si or Be) – the sticking coefficient of nitrogen being by definition the ratio of flux related to the incorporated nitrogen to the nitrogen flux supplied [175].

The kinetic model developed for InAsN in Section 5.2.2 was employed to fit the nitrogen composition dependence on the growth rate. Indeed, the growth rate R_{InAs} is proportional to the arrival rate of indium J_{In} :

$$R_{InAs} = \beta\, J_{In} \qquad (5.10)$$

Based on the RF plasma characterisation as a function of the power at fixed nitrogen flux of 5×10^{-7} mbar (see Figure 4.13, Section 4.1.6), the intensity ratio

$I_{N\,(210\,W)} / I_{N\,(160\,W)} \sim 1.6$ of the spectroscopic line at 745 nm for RF powers 210 W and 160 W – used respectively for the present growth rate study and the growth temperature study (see Section 5.2.2) – allowed the determination of the parameter $\alpha N_{In} J_N$ at 210 W RF power. The latter is proportional to the arrival rate of nitrogen J_N that changes with RF power, so that $J_{N\,(210\,W)} / J_{N\,(160\,W)} = I_{N\,(210\,W)} / I_{N\,(160\,W)}$.

The kinetic model for InAsN as a function of the growth rate can be derived from (5.8) and (5.10) :

$$[N] \propto \frac{\alpha N_{In} J_N}{\frac{\alpha}{\beta} R_{InAs} + D_0 \exp\left(\frac{-E_d}{k_B T_g}\right)} \qquad (5.11)$$

The dependence of the nitrogen composition as a function of the growth rate is shown in Figure 5.14. The solid line was calculated from equation (5.11) using the parameters in Table 5.6 (J_N being $J_{N\,(210\,W)}$) and convincingly fits the presented data. Lower growth temperature shifts the curve to the right and higher composition.

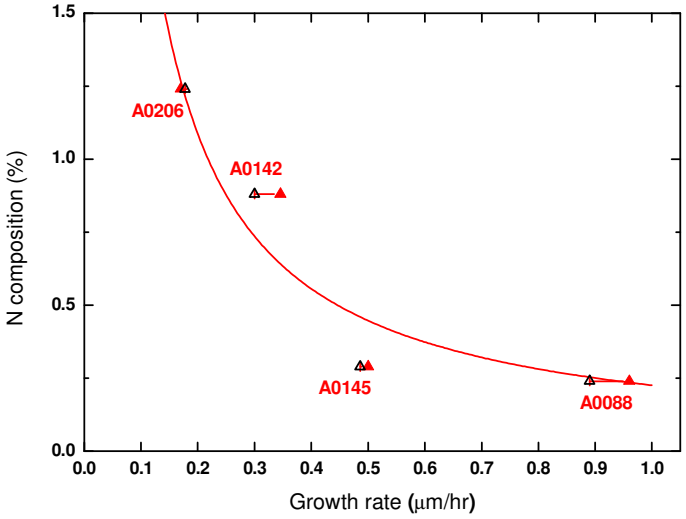

Figure 5.14 Nitrogen composition as a function of the growth rate. The solid line is the calculation result based on (5.11). The growth rate was determined by RHEED oscillations (solid red triangles) or from XRD (open black triangles)

The present study revealed the reciprocal dependence of the nitrogen composition on growth rate. XRD and PL analyses showed that best quality is achieved for samples grown around 0.3 to 0.5 µm/h, with bright luminescence and narrow XRD. The nitrogen composition dependence on the growth rate was fitted by a kinetic model adapted to InAsN.

Kinetic model parameter	$\alpha N_{In} J_N$	α / β	D_0	E_d	T_g
Value for growth rate fit	6.7×10^{-19} (a.u.)	3.9×10^{-18} (a.u.)	2.0×10^{5} s^{-1}	3.4 eV	693 K

Table 5.6 Calculated parameters for a fit of the nitrogen composition dependence on growth rate by the kinetic model

5.2.4 Influence of As flux

As demonstrated in Section 4.1.4 (see Figure 4.8), the minimum arsenic flux As_{min} (the critical As flux for As-terminated InAs growth) is dependent on the growth temperature for a given growth rate, i.e. for a given In flux. In this perspective, discussing the influence of As on the nitrogen composition in terms of As flux or V/III BEP ratio (the As / In ratio) is not relevant and the discussion will be based on the ratio of As flux to minimum arsenic flux As / As_{min}. A series of samples were grown at different arsenic fluxes, all other parameters fixed (i.e. at fixed growth rate ~ 1.0 µm/h, fixed growth temperature 420°C, RF power 210 W, N flux ~ 5.3×10^{-7} mbar, thickness below 1 µm). Nitrogen composition as a function of the inverse As / As_{min} ratio is plotted in Figure 5.15 (a) and characterisation results are compared in Table 5.7. The nitrogen composition strongly increases with decreasing As / As_{min} ratio and sample A0201 (2.29 % N) grown at 0.4 As / As_{min} ratio (In-rich growth) contains more than fives times nitrogen compared to sample A0147 (0.41 % N) grown

at minimum arsenic flux (unity As / As_{min} ratio). The narrowest XRD rocking curve in Figure 5.15 (b) was obtained at unity As / As_{min} ratio and PL with a rather bright emission was measured (see Table 5.7). The absence of PL data for A0091 (0.61 % N) is due to the fact that it is a p-i-n structure.

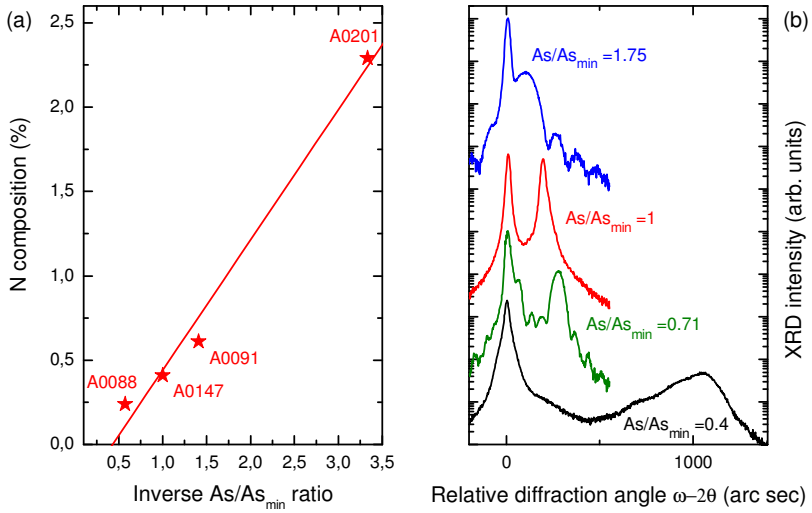

Figure 5.15 (a) Nitrogen composition as a function of the inverse As / As_{min} ratio. The solid line is a linear fit ; (b) XRD rocking curves for InAsN samples grown at different As / As_{min} ratios

Sample reference	A0201	A0091	A0147	A0088
As / As_{min} ratio	0.4	0.71	**1**	1.75
Nitrogen composition	2.29 %	0.61 %	0.41 %	0.24 %
RHEED pattern	(1 × 4)	(2 × 4)	(2 × 4)	(2 × 4)
4 K PL intensity (arb. units)	0	-	720	1

Table 5.7 Growth conditions and characterisation results from XRD and PL for varied As fluxes

The influence of the As / As_{min} ratio on the nitrogen composition can be deduced from data in Table 5.7. On one hand, sample A0201 (2.29 % N) grown at very low As / As_{min} ratio of 0.4 shows no 4 K PL emission related to optically active InAsN but a weak defect emission at 3.117 µm (398 meV), similar to the donor-

acceptor pair DAP_1 identified previously in sample M2774 (see Section 5.1.1). It is likely that the poor PL emission is due to the formation of non-radiative centres through As vacancies. The high nitrogen composition of 2.29 % measured by XRD could probably be attributed to interstitial nitrogen but further investigations are required. This sample is the only one of the batch to show a (1×4) reconstruction pattern, which can easily be related to the milky surface observed with the eye and pictured under Nomarski microscope as shown in Figure 5.16 (a). Disorder is believed to dominate in materials showing 1-by features during growth [118 and references therein]. On the other hand, excess As flux (As-rich growth) reduces the nitrogen composition because the adatom sites are more favourable for As in the competition with N atoms [72]. In GaInNAs, high As flux resulted in constant nitrogen composition [165]. Samples grown at As / As_{min} ratio of 0.71 and above show a mirror-like surface (e.g. Figure 5.16 (b)) along with (2×4) RHEED pattern during growth.

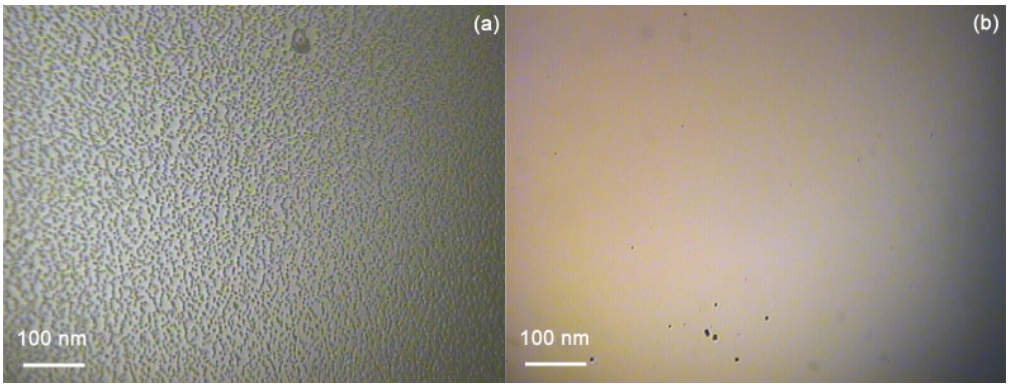

Figure 5.16 Nomarski picture : (a) sample A0201 (2.29 % N) grown at very low As / As_{min} ratio ; (b) sample A0147 (0.41 % N) grown at unity As / As_{min} ratio

A kinetic model evidencing the competition between N and As for group-V sites during growth under overpressure of nitrogen was developed for $GaAs_{1-y}N_y$

[159]. The nitrogen composition y (between 0 and 1) in GaAsN is a function of the arsenic flux Φ_{As} and the nitrogen flux Φ_N :

$$y = \frac{1}{1 + \frac{\Phi_{As}}{C\,\Phi_N}} \qquad (5.12)$$

where the parameter C is expressed as :

$$C = \frac{C_N}{C_{As}} \qquad (5.13)$$

with C_N and C_{As} the incorporation probabilities of N and As respectively, expressed as :

$$C_N = \frac{1}{n_1 + n_2\,\Phi_N} \qquad (5.14)$$

$$C_{As} = \frac{1}{a_1 + a_2\,\Phi_{As}} \qquad (5.15)$$

with the hypothesis that n_1, $a_1 \geq 1$ and n_2, $a_2 > 0$.

For $InAs_{1-x}N_x$, introducing the minimum arsenic flux Φ^0_{As} and combining equations (5.12), (5.13), (5.14) and (5.15), the dependence of the nitrogen composition $[N]$ (in %) on the $As\,/\,As_{min}$ ratio ($\frac{\Phi_{As}}{\Phi^0_{As}}$ in (5.16)) can be expressed as :

$$[N] = 100\,\frac{C_N\Phi_N\left(\frac{a_1}{\Phi^0_{As}} + a_2\frac{\Phi_{As}}{\Phi^0_{As}}\right)}{C_N\Phi_N\frac{a_1}{\Phi^0_{As}} + \left(a_2 C_N\Phi_N + 1\right)\frac{\Phi_{As}}{\Phi^0_{As}}} \qquad (5.16)$$

Kinetic model parameter	Φ_N	Φ^0_{As}	$C_N\,a_1$	$C_N\,a_2$
Value for $As\,/\,As_{min}$ fit	5.3×10^{-7} mbar	2.1×10^{-6} mbar	3.1×10^{-2}	-6.5×10^{3}

Table 5.8 Calculated parameters for a fit of the nitrogen composition dependence on $As\,/\,As_{min}$ by the kinetic model equation (5.16) (blue solid line, Figure 5.17 (a))

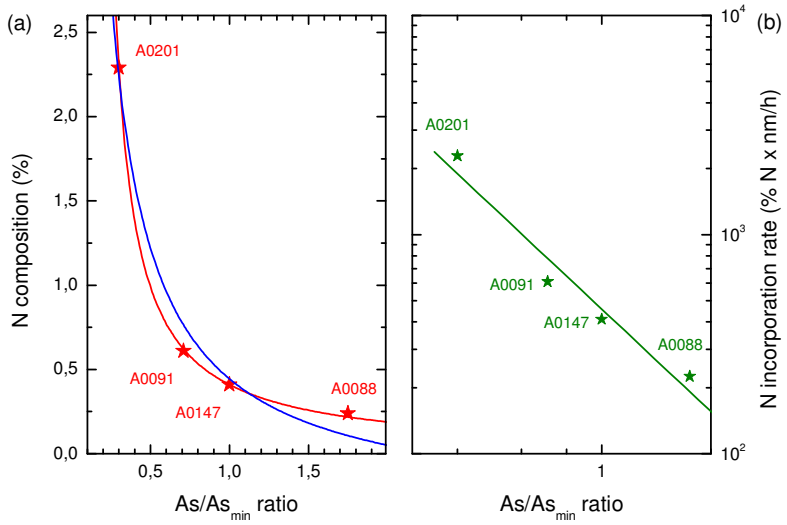

Figure 5.17 (a) Nitrogen composition as a function of the As / As_{min} ratio. The blue solid line is the calculation result based on (5.16) and the red one based on (5.17) ; (b) Incorporation rate of nitrogen in InAsN as a function of the As / As_{min} ratio (in log-log scales). The solid line is a linear fit

The dependence of the nitrogen composition as a function of the As / As_{min} ratio is shown in Figure 5.17 (a). The blue solid line was calculated from equation (5.16) using the parameters in Table 5.8 but does not fit the presented data exactly. The negative value of $C_N a_2$ contradicts the hypothesis $n_2, a_2 > 0$. The samples were not grown under N_2 overpressure indeed (As / N ~ 4) but the kinetic model developed for N_2 underpressure considers that the nitrogen concentration is independent of the As flux [159], which is clearly not the case in this section. It can therefore be assumed that the reciprocal dependence of the As incorporation probability C_{As} in (5.15) is not applicable and it should be considered constant under As overpressure, as corroborated by the growth of InAs of identical quality under various As overpressure fluxes (up to ten times the minimum arsenic flux generally). Hence the parameter C in equation (5.13) is independent of the As flux and the dependence of the nitrogen composition on the As / As_{min} ratio under As overpressure can be derived from (5.12) and simply expressed as :

$$[N] \propto 100 \frac{C \frac{\Phi_N}{\Phi_{As}^0}}{C \frac{\Phi_N}{\Phi_{As}^0} + \frac{\Phi_{As}}{\Phi_{As}^0}} \qquad (5.17)$$

The model shown by the red solid line in Figure 5.17 (a) was calculated from equation (5.17) and fits better the presented data. This trend is confirmed by the linear dependence of the nitrogen composition on the inverse As / As_{min} ratio shown earlier in Figure 5.15. While the incorporation rate of nitrogen in InAsN is independent of the growth rate (see Section 5.2.3), it is shown to be highly dependent on the As / As_{min} ratio as pictured in Figure 5.17 (b). The nitrogen incorporation rate varies reciprocally to the As / As_{min} ratio, corroborating the fact that low As flux should be favoured to increase the nitrogen composition. In the present study, XRD analysis and Nomarski microscope picture showed that best quality is achieved for samples grown around unity As / As_{min} ratio.

5.3 Post-growth treatment of InAsN epilayers

As acknowledged in the literature and demonstrated in the preliminary study of the material, the optical properties of InAsN severely degrade with the introduction of as little as one percent of nitrogen in the InAs lattice. Rapid thermal annealing (RTA), a short time post-growth baking of the sample at high temperature, was proposed to improve the material quality in dilute nitride materials (see Section 3.6). The InAsN epilayer investigated in this study (sample M2806), presented in Sections 5.1.2 and 5.1.3, consists of a 0.5 µm-thick uncapped bulk InAsN epilayer ([N] = 0.95 %) grown on InAs (001) substrate by MBE. The sample was cut into several pieces to investigate the influence of the annealing temperature T_{RTA} (between

450°C and 650°C) on the nitrogen composition over a 30 s-procedure (see Section 4.4 for details).

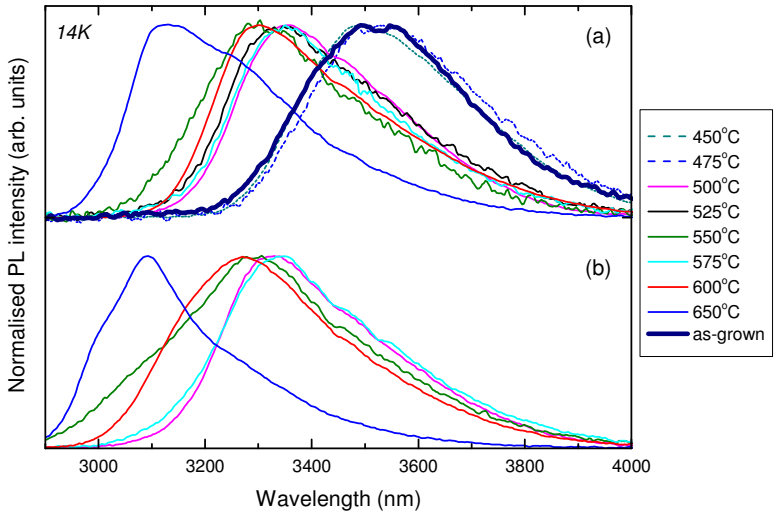

Figure 5.18 14K PL spectra of annealed InAsN : (a) for 30 s ; (b) for 60 s (sample annealed at 525°C was removed for clarity)

14 K PL spectra were recorded for each piece annealed at a different temperature as shown in Figure 5.18 (a). Samples annealed at $450^{o}C \leq T_{RTA} < 500^{o}C$ have an almost identical spectrum to the as-grown sample, with a PL peak around the energy 353 ± 3 meV (3.51 µm ± 0.03 µm). XRD measurements confirm that the nitrogen composition is unchanged. Using a thirty second-rapid thermal annealing at temperatures below 500°C has no effect on bulk InAsN epilayers. Samples annealed for 30 s in the temperature range 500 - 600°C all exhibit a comparable PL emission energy of 372 ± 3 meV (λ ~ 3.333 µm), hence showing about 19 meV blueshift with relation to the as-grown sample. The blueshift in annealed InAsN could be attributed to nitrogen outdiffusion, atomic short range ordering or nitrogen profile homogenisation as identified in InGaNAs [100]. Post-RTA XRD measurements shown in Figure 5.19 reveal a slight decrease in the N composition to values between 0.85 % and 0.95 %. This could be attributed to a relatively small N desorption from

the surface during the annealing process, but the short annealing time makes the loss of nitrogen unlikely and the variation might rather be due to a strain enhancement as observed in annealed GaAsN [14]. Nevertheless, the *calculated* PL peak energy (based on the BAC model for InAsN proposed in Section 6.3) for the nitrogen composition range 0.85 % - 0.95 % is 356 ± 2 meV. Compared to the as-grown sample, the nitrogen desorption is responsible for a blueshift of about 3 meV. Hence, the 16 meV energy difference – far superior to the blueshift arising from nitrogen desorption – indicates that RTA in the temperature range 500 - 600°C is not responsible for a change in the nitrogen composition but mainly for a change in the band structure. The sample annealed at 600°C exhibits the brightest luminescence, superior by a factor of 6 to the as-grown sample.

The sample annealed at 650°C for 30 s shows a severe further 20 meV blueshift to 396 meV accompanied this time by a drastic reduction of the nitrogen composition to 0.59 %. A similar severe blueshift was observed in InAsN/InGaAs SQW when the optimal annealing temperature was exceeded [89]. It seems that annealing temperature of 650°C is too high a temperature that leads to a significant loss of nitrogen by outdiffusion.

To further study the impact of rapid thermal annealing on the material quality, the samples underwent RTA for a second time under the same conditions : for 30 s at all aforementioned temperatures above 500°C (60 s total RTA time). As can be seen in Figure 5.18 (b), 14 K PL spectra similar to the first RTA are observed and no further improvement in the PL intensity was measured. The absence of any further energy shift for the samples annealed below 600°C revealed that the effect of RTA is already saturating after 60 s, faster than the 60 min required in GaInNAs SQW for the blueshift to level off [97]. For the sample annealed at 650°C, XRD rocking curve in

Figure 5.19 shows the reduction of the nitrogen composition to 0.43 % and the apparition of a small peak between those from the substrate and epilayer. Despite the good aspect of the surface, the loss of nitrogen is predominant and phase separation occurs at the RTA temperature of 650°C.

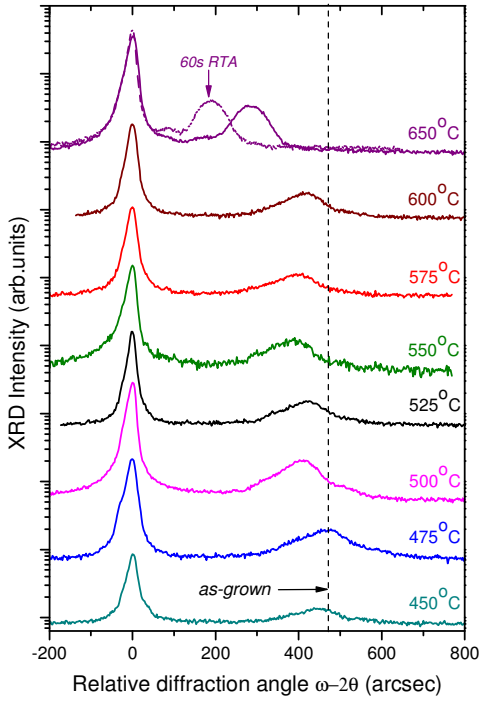

Figure 5.19 XRD measurements of InAsN samples annealed at temperatures between 450°C and 650°C. Solid line is for 30 s-RTA and dotted line for 60 s-RTA

A power-varied PL analysis was performed at 14 K on the samples that underwent a second RTA and the PL peak energy blueshift $\Delta E_{PL(P)}$ between low and high excitation powers (0.2 W and 1.6 W respectively) is plotted in Figure 5.20. While the as-grown sample exhibits a blueshift of 8.1 meV (see Section 5.1.3), the InAsN sample annealed at 525°C has a reduced dependence of the PL peak energy with increasing excitation power $\Delta E_{PL(P)} = 3.1$ meV. For samples annealed at $550°C \leq T_{RTA} \leq 600°C$, $\Delta E_{PL(P)}$ decreases from 3.1 to 0.3 meV with increasing RTA temperature. The reduction in $\Delta E_{PL(P)}$ demonstrates an improvement in InAsN

material quality, given that InAs showed a value of $\Delta E_{PL(P)} \sim 1$ meV. In GaAsN, the reduced dependence of the PL peak energy to increasing laser power (quantified by the blueshift $\Delta E_{PL(P)}$) is most likely related to a homogenisation of the nitrogen profile (flattening the electronic band) which results in a transition energy moved closer to the bandgap [14]. The same mechanism is probably responsible for the reduction in the power-dependent blueshift. The optimal annealing temperature for rapid thermal annealing of bulk InAsN was found to be 600°C, which is higher than the value of 525°C reported for InAsN single quantum wells [89].

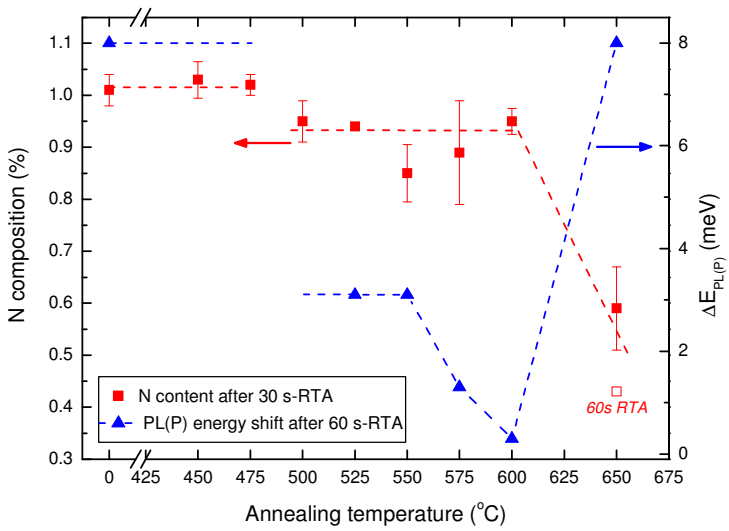

Figure 5.20 Influence of the annealing temperature on nitrogen composition and energy blueshift of the 14 K PL between low and high laser excitation power. Dashed lines are a guide to the eye

For the sample annealed at 650°C for 60 s, a huge PL peak shift $\Delta E_{PL(P)} = 8.0$ meV is observed again, close to the value of the as-grown sample, which corroborates that annealing at 650°C deteriorates the InAsN. No conditions in both annealings seemed to favour a reduction of the PL linewidth as is generally observed in dilute nitrides [89, 98, 176]. The alloy disorder plays a predominant role in the presented sample and a 60 second-rapid thermal annealing treatment at 600°C can enhance InAsN material quality. As a result, the PL intensity was improved by a factor of 6. The related

17 meV blueshift of the 14 K PL spectra is attributed to nitrogen profile homogenisation. Higher annealing temperature leads to strong nitrogen outdiffusion and phase separation.

5.4 Summary

The growth of InAsN by plasma assisted MBE is not simple and requires careful operation to avoid the generation of point defects and of non-optically active InAsN layers. The critical thickness model developed is a guide to the growth of fully strained epilayers. Preliminary samples with as little as one percent nitrogen showed rather poor quality, a low-energy tail and rapid temperature quenching of the luminescence. The low material quality may originate from strongly localised states and material disorder and supports the need for optimisation of the growth conditions.

A study of the growth conditions highlighted that the nitrogen composition is best gradually increased by a reduction in growth temperature, growth rate and arsenic flux. The dependence of the nitrogen composition on these parameters was explained in terms of a kinetic model adapted to InAsN. Rapid thermal annealing can enhance the material quality and luminescence. With the proposed optimal growth conditions, good quality InAsN MBE material should be within reach and will be studied in the following chapter.

Chapter 6. Study of InAsN and InAsNSb materials

Based on the growth conditions study presented in Chapter 5, InAsN layers were grown by MBE to demonstrate the possibility to achieve high material quality, study the properties of InAsN, the potential bandgap engineering of InAsN for mid-infrared applications in the 3 - 5 µm spectral region and the further improvement brought by the addition of antimony.

6.1 Features of InAsN material

6.1.1 Structural characterisation of InAsN

A set of five InAsN samples were grown by MBE with combined progressive reduction in growth temperature and growth rate to vary the nitrogen composition in the layers. Samples consist of 1.0 µm-thick InAsN layers grown on InAs substrate at temperatures between 360°C and 420°C, N plasma powers between 160 W and 210 W, N flux of ~ 5.3×10^{-7} mbar and at minimum arsenic flux (see Table 6.1).

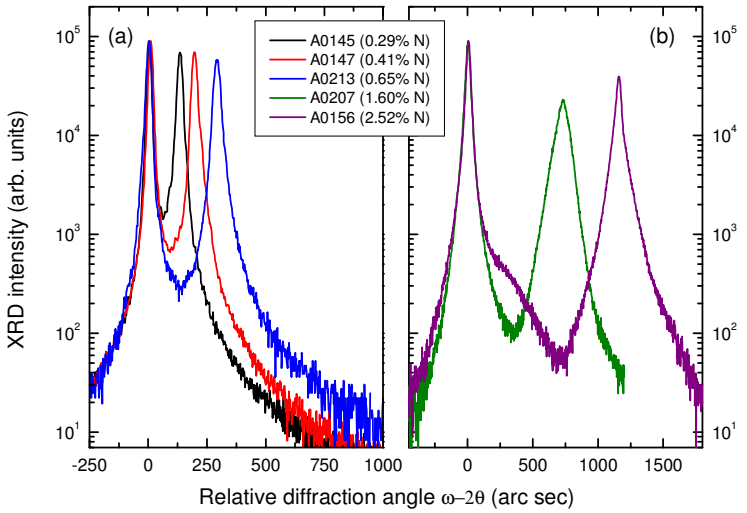

Figure 6.1 XRD rocking curves of InAsN thin films : (a) with N composition below 1 % ; (b) with N composition above 1 %

XRD measurements of the samples under study are shown in Figure 6.1 (the graph is only split for clarity) and the characterisation results are presented in Table 6.1. As can be seen, the nitrogen composition was gradually increased by reducing simultaneously growth temperature from 420°C to 360°C and growth rate from 1.0 μm/h to 0.3 μm/h. This resulted in an increase in the nitrogen composition up to 2.52 % N and the lattice mismatch $\Delta a / a$ increased by one order from 5.2×10^{-4} to 4.5×10^{-3}.

Sample reference	A0145	A0147	A0213	A0207	A0156
Nitrogen composition	0.29 %	0.41 %	0.65 %	1.60 %	2.52 %
Growth temperature (°C)	420	420	400	360	380
Nitrogen plasma power (W)	200	210	160	160	210
Growth rate (μm/h)	0.5	1	1	1	0.3
RHEED pattern	(2 × 4)	(2 × 4)	(2 × 4)	(2 × 1)	(2 × 1)
Lattice mismatch $\Delta a / a$	5.2×10^{-4}	7.3×10^{-4}	1.2×10^{-3}	2.9×10^{-3}	4.5×10^{-3}
XRD FWHM (arc sec)	24	25	31	101*	47

Table 6.1 Growth conditions and XRD characterisation results of InAsN

Samples A0145, A0147 and A0213, shown in Figure 6.1 (a), were grown by reducing the growth temperature from 420°C to 400°C at fixed growth rate of 1.0 μm/h. The (2 × 4) RHEED pattern observed during growth and the mirror-like surface aspect of the sample is a sign of good quality and potential bright PL [162] as discussed in Section 5.2.2. Nitrogen compositions between 0.29 % and 0.65 % were achieved. The XRD peak intensity of the epilayer is very bright, mainly because of the high quality achieved and partly because of the thickness of the layers grown (1 μm). Very little reduction in the epilayer XRD peak intensity is observed with increasing nitrogen composition. The epilayer peak is extremely narrow (24 to 31 arc sec) and

compares very favourably with the theoretical value of 21 arc sec from simulation. Moreover, the material quality is far better than in preliminary InAsN samples presented in Section 5.1.2, where XRD FWHM above 100 arc sec were measured for nitrogen compositions below one percent.

Samples A0207 and A0156, shown in Figure 6.1 (b), were grown at reduced temperature. Nitrogen compositions up to 2.52 % were successfully achieved. Both samples exhibit slightly broader XRD epilayer peaks and the (2 × 1) RHEED pattern observed during growth may correspond to a roughening of the surface, as for GaAsN [139]. Sample A0207 (1.60 % N) has slightly poorer XRD characteristics, attributed to the low growth temperature of 360°C (at 1.0 μm/h growth rate). It is indeed generally observed that lower growth temperatures reduce the material quality of dilute nitrides because of insufficient migration of group-III atoms [165]. To counter this effect, sample A0156 (2.52 % N) was grown at a slightly higher temperature (380°C) to improve the material quality, with a reduced growth rate (0.3 μm/h) to increase the nitrogen incorporation further.

The XRD full width at half maximum (FWHM) of InAsN epilayers grown at Lancaster (red) is compared to the reported InAsN material grown on InAs (blue) by Veal *et al*. [85] in Figure 6.2. In Veal's study (blue dashed line), the XRD FWHM of the epilayers increases exponentially with increasing nitrogen composition, sign of a rapid degradation of the material with nitrogen content over 1 %. On the contrary, the present batch – ignoring A0207 (1.60 % N) grown at too low a temperature – only demonstrates a linear increase in the XRD FWHM with nitrogen composition if the growth temperature is kept between 380°C and 420°C. The much reduced values of the XRD epilayer peak width is a clear sign of the high material quality achieved.

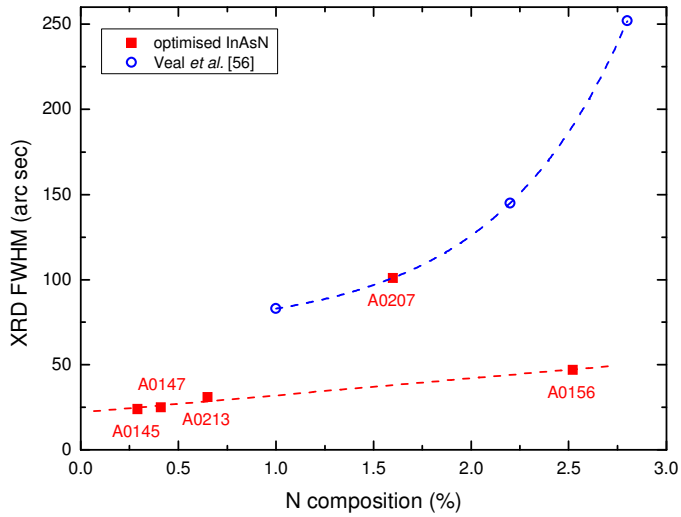

Figure 6.2 Dependence of XRD FWHM on the nitrogen composition in InAsN layers grown at Lancaster (red) and by Veal *et al.* [85] (blue). Dashed lines are linear and exponential fits (red and blue respectively)

6.1.2 Low-temperature luminescence properties of InAsN

Optical characterisation was performed on the set of InAsN samples presented in Section 6.1.1 to investigate the changes in InAsN energy levels as a function of the composition. 4 K PL measurements from thick InAs epilayer grown on (001)-oriented InAs substrate and InAsN samples A0145 - A156 are compared in Figure 6.3. The InAs transition occurs at 3.004 µm at 4 K and presents a single narrow peak of Gaussian shape. For InAsN, the 4 K PL wavelength redshifts from 3.154 µm to 4.505 µm for nitrogen composition from 0.29 % to 2.52 % respectively. This confirms the reduction of InAsN bandgap with increasing nitrogen reported recently [85]. None of them exhibits an InAs-related peak as seen in defect-dominated material (see Section 5.1.1). The lineshape is rather narrow and shows a double peak feature that will be explained in Sections 6.1.3 and 6.1.4. Samples A0207 (1.60 % N) and A0156 (2.52 % N) with nitrogen compositions above 1.5 % are subject to CO_2 absorption. It is indeed evidenced by the transmission spectrum of the molecule

displayed on top of Figure 6.3 (light blue lines, with arbitrary intensity units), whose data are taken from the HITRAN 2004 database [177].

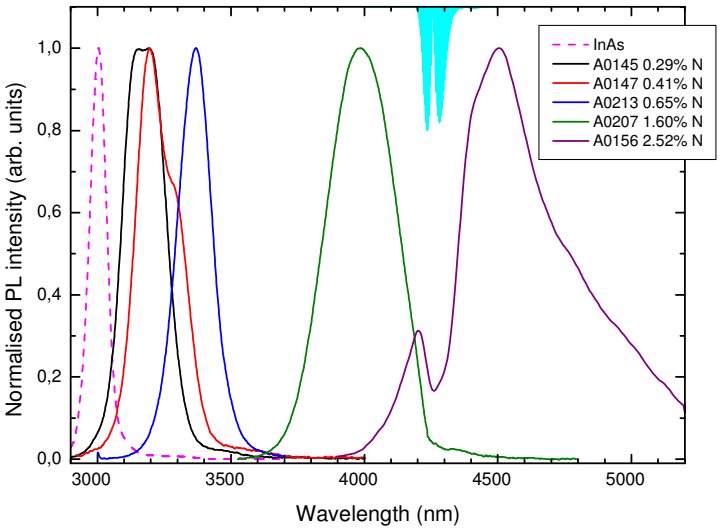

Figure 6.3 4 K PL of InAs (dashed line) and InAsN (solid lines) with various nitrogen compositions. Top : CO_2 molecule transmission spectrum (arbitrary units) from HITRAN 2004 database [177]

The results from 4 K PL are compared in Table 6.2. The PL intensity for these InAsN layers is very bright and shows little variation – a factor of 2 to 3 only – over the nitrogen composition range. Sample A0213 with 0.65 % N is only an order of magnitude less bright than bulk InAs. The material quality presently achieved is good.

Sample reference	A0129	A0145	A0147	A0213	A0207	A0156
Nitrogen composition	0.00 %	0.29 %	0.41 %	0.65 %	1.60 %	2.52 %
4 K PL wavelength (μm)	3.004	3.154	3.188	3.370	3.985	4.505
4 K PL intensity (arb. units)	22.1	0.75	0.51	1	0.76	0.37
1.6 W PL FWHM (meV)	10.2	22.8	22.9	16.3	24.0	30.7
Low energy-tail E_0 (meV)	3.1	5.2	5.3	5.1	4.8	18.3 - 20.9

Table 6.2 Characterisation results from 4 K PL for InAsN

As far as 4 K PL linewidth is concerned, InAsN layers show narrow peaks for nitrogen composition up to 1.6 %. The FWHM varies between 16.3 and 24.0 meV, hardly twice as wide as InAs material. This compares very favourably with preliminary InAsN samples presented in Section 5.1.3 where PL FWHM was above 35 meV for composition below 1 % N. This result points out the improvement in the material quality : radiative transitions occur from a rather well defined energy level with little spreading to surrounding energy levels that material inhomogeneity could bring. Sample A0156 with high nitrogen content (2.52 %) shows a little degradation in the lineshape. It may be related to the high lattice mismatch of 4.5×10^{-3} (see Table 6.1 in Section 6.1.1) which is likely to generate dislocations in the material.

A striking feature of these InAsN layers is the drastic reduction in the band tailing with relation to the preliminary InAsN material, as reflected by weak activation energies of the low energy tail E_0 (calculated by equation (5.2) in Section 5.1.3). All InAsN samples with composition below 2 % N have a value of E_0 between 4.8 and 5.3 meV, less than twice the value of 3.1 meV for the Gaussian-like InAs line. This is a real improvement when compared to preliminary InAsN samples with $E_0 > 17$ meV (see Section 5.1.3) for nitrogen composition below 1 %. It is believed that the reduction in the activation energy of the low energy-bandtail reflects a reduction in the localisation potential and improved structural properties [142]. Nevertheless, InAsN sample A0156 (2.52 % N) shows a noticeable band tailing that is attributed to a slight degradation of the material quality with high nitrogen content.

6.1.3 Evidence of weakly localised states in InAsN

A peculiar double-peak feature mentioned in the previous section was observed in power-varied PL at 4 K as shown in Figure 6.4. This double-peak

emission is different from reported PL spectra for GaAsN [140, 151] and GaInNAs [152, 153]. A single, asymmetric emission peak with a long low-energy bandtail is generally observed at low temperatures in dilute nitrides. The single peak is attributed to the formation of localised states in the material due to the inhomogeneity of the nitrogen distribution. It always exhibits a *strong* blueshift with increasing laser excitation power or temperature [140, 151-153]. Veal *et al.* [85] observed a broad single peak from InAsN at 77 K and assigned it to the combined contributions from free excitons and localised excitons, but the wide lineshape makes questionable the attribution of the transitions to *excitons*. In our case, it is supposed that the short and long wavelength emissions originate respectively from free carrier recombination and localised carrier recombination. In the studied samples, the homogeneity of the nitrogen distribution is improved so that the localised states are shallower. The photogenerated carriers are less trapped by the localised states and the contribution from free carrier recombination was clearly visible at 4 K.

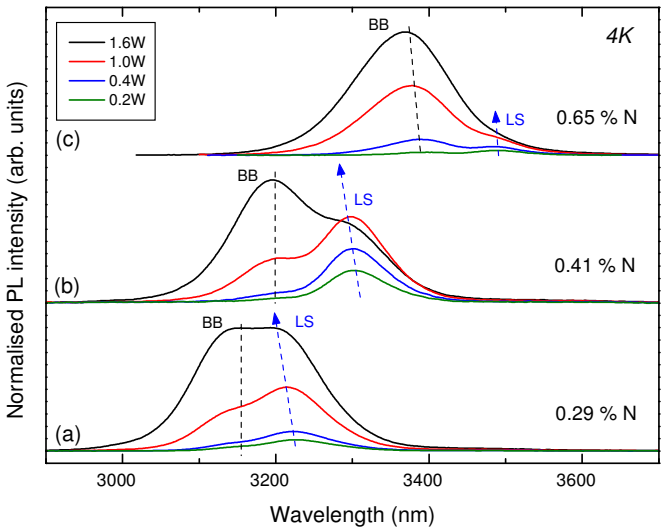

Figure 6.4 Laser excitation power-varied PL at 4 K for InAsN samples with nitrogen composition of : (a) 0.29 % (A0145) ; (b) 0.41 % (A0147) ; (c) 0.65 % (A0213). *BB* are band-to-band transitions, *LS* transitions from the localised states

To further identify the origin of the double peak, results from laser excitation power-varied PL performed at 4 K on InAsN samples with nitrogen composition below one percent are compared to bulk InAs in Table 6.3. Similarly to InAs, the short wavelength in samples A0145 (0.29 % N) and A0147 (0.41 % N) shows no energy shift $\Delta E_{PL(P)}$ with increasing laser power ; sample A0213 (0.65 % N) shows only a small blueshift (3 meV). It can be noticed as well that the PL intensity of the short wavelength peak (*BB*) develops more rapidly than that of the long wavelength emission (*LS*) with increasing excitation power. This is indicative of carrier de-trapping from localized states. This de-trapping leads to a slight peak energy blueshift of the long wavelength emission with increasing excitation power (refer to [178, 179] for details). The dependence of the PL intensity on laser power can be characterised by the parameter *k* from equation (5.3). For the short wavelength peak, *k* is higher than unity for all presented InAsN as for InAs. The short wavelength emission must thus reflect a band-to-band transition.

Sample reference	A0129	A0145	A0147	A0213
Nitrogen composition	0.00 %	0.29 %	0.41 %	0.65 %
Short wavelength $\Delta E_{PL(P)}$ (meV)	0.0	0.0	0.0	3.0
Short wavelength *k* value	1.55	1.17	1.57	1.77
Long wavelength $\Delta E_{PL(P)}$ (meV)	-	4.0	1.9	0.5
Long wavelength *k* value	-	0.72	0.46	0.79

Table 6.3 Characterisation results from excitation power-varied PL at 4 K for InAsN

As for the long wavelength peak, a small blueshift $\Delta E_{PL(P)}$ with increasing laser power and *k* values below unity were observed. The values of *k* above and below unity for short and long wavelength peaks respectively tend to prove that the long

wavelength peak is not a resonant transition of the bandgap as sometimes observed in GaAsN [149]. As already mentioned in Section 5.1.3, we believe $k < 1$ is a signature of localised states. Small characteristic energies E_0 (reported in Table 6.2) and small energy shift $\Delta E_{PL(P)}$ with increasing laser excitation power suggest that the nitrogen states are weakly localised.

6.1.4 Temperature-dependence of InAsN bandgap

The study of the temperature dependence of the bandgap can provide valuable information about the novel InAsN material and has not been convincingly reported so far. It will give a further insight into the double-peak feature presented in the previous section. Temperature-dependent PL measurements were performed on the samples under study from Section 6.1.1 and the luminescence at temperatures from 4 K to 295 K is shown for InAsN sample A0145 (0.29 % N) in Figure 6.5.

The PL spectrum shows two peaks at low temperature. The PL peak energy of the short wavelength emission is constant up to 45 K and then shows the usual redshift due to bandgap reduction with increasing temperature. At 295 K, a broad spectrum is observed and the position of the bandgap-related peak will be analysed further in Section 6.2 (see Figure 6.11). At low temperature, the long wavelength emission exhibits a slight blueshift with increasing temperature, which is typical behaviour of PL emission associated with localised carrier recombination. In dilute nitrides, the two peaks are often not distinguishable, which can result in a blueshift - redshift with increasing temperature [146]. Our observation can explain the common trend observed in dilute nitrides and further clarifies the interpretation of the double-peak emission. The absence of S-shape (redshift - blueshift - redshift) with increasing temperature observed earlier in InAsN with strongly localised states can be interpreted

as a weakening of the localisation potential when compared with preliminary InAsN material presented in Section 5.1.3.

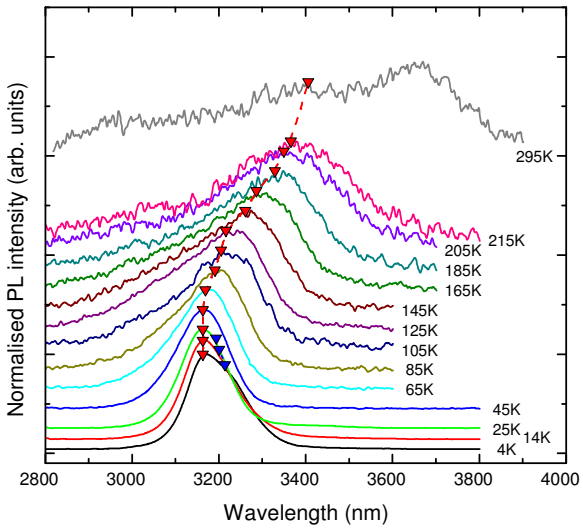

Figure 6.5 Temperature-dependent PL of InAsN sample A0145 (0.29 % N). Red and blue triangles indicate the position of short and long wavelength peaks respectively

Varshni's equation is an empirical model fitting the variation in the bandgap with temperature in semiconductors [13]. Figure 6.6 presents the temperature dependence from 4 K to 300 K of PL peaks from band-to-band recombination (*BB*) in InAsN with various nitrogen compositions and in InAs. All samples show a noticeable reduction of the bandgap with increasing temperature. The localisation depth – energy difference between band-to-band (*BB*) and localisation states (*LS*) at 4 K – increases with increasing nitrogen composition as shown in the inset of Figure 6.6 (a) and means that the repulsion between CB and localised states would increase with the nitrogen content. Further investigations are required.

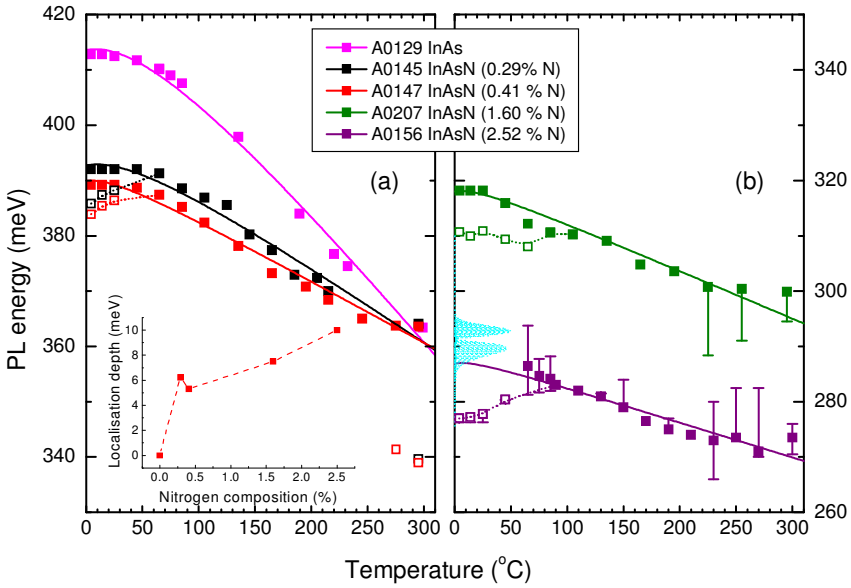

Figure 6.6 Temperature-dependence of the PL energy in InAs and InAsN fitted by Varshni's equation (6.2) and parameters in Table 6.4. Solid symbols are band-to-band transitions (*BB*), open symbols are transitions from the localised states (*LS*). Inset in (a) shows the localisation depth as a function of the nitrogen composition. Light blue lines in (b) represent the CO_2 molecule absorption spectrum (arbitrary units) as a function of energy, from HITRAN 2004 database [177]

The temperature dependence of InAsN bandgap can be fitted by Varshni's equation with parameters shown in Table 6.4. InAs bandgap can be fitted with parameter values very close to $E_{g0} = 415$ meV, $\alpha = 0.276$ meV.K^{-1} and $\beta = 83$ K reported by Fang [12]. In semiconductors, the bandgap energy lies below the PL energy, generally by a factor of ½ k_BT [180, 181]. Fang *et al.* take the bandgap energy as the PL peak energy E_{PL} subtracted by ½ k_BT for binaries, namely InAs, which corresponds to a wave vector-conserving transition :

$$E_g(T) = E_{PL}(T) - \tfrac{1}{2} k_B T \qquad (6.1)$$

Using the same convention for InAsN and Varshni's equation (2.9), the PL peak energy $E_{PL}(T)$ as a function of temperature can be fitted by :

$$E_{PL}(T) = E_{g0} - \frac{\alpha T^2}{\beta + T} + \tfrac{1}{2} k_B T \qquad (6.2)$$

Sample reference	E_{g0} (meV)	α (meV.K^{-1})	β (K)	$\Delta E_g(T)$ (K)
A0129 InAs	413.6	0.296	105	51.8
A0145 InAsN (0.29 % N)	392.7	0.184	69	31.5
A0147 InAsN (0.41 % N)	389.9	0.156	32	28.8
A0207 InAsN (1.60 % N)	318.0	0.130	26	22.6
A0156 InAsN (2.52 % N)	286.9	0.107	21	16.8

Table 6.4 Varshni's parameters and temperature sensitivity for the temperature dependence of InAs and InAsN bandgaps

In Figure 6.6 (a), the slope of the curves fitting the PL energy as a function of the temperature reduces with increasing composition in low-nitrogen containing InAsN samples. The temperature dependence of the PL peak energy for InAsN with nitrogen composition above one percent is compared in Figure 6.6 (b) (the same energy span of 90 meV was employed). CO_2 molecule absorption spectrum [177] is shown as a function of energy (light blue lines) to support the uncertainty in the peak energy when in the range 285 - 295 meV. Despite the uncertainty in energies at certain temperatures influencing the precision in the fitting parameters, one can see from Table 6.4 that α and β both decrease with increasing nitrogen composition. This is similar to GaAsN and GaInNAs where a weakening of the temperature dependence of the bandgap is observed with N composition [18, 19]. The energy shift of InAsN bandgap with temperature is much less than that of InAs as reported by the parameter $\Delta E_g(T)$ in Table 6.4. While InAs bandgap decreases by 51.8 meV when the temperature increases from 4 K to 295 K, InAsN bandgap decreases by only 31.5 to 16.8 meV for nitrogen compositions between 0.29 % and 2.52 % respectively. This is far less than the 75 meV energy shift observed in GaAsN with 3 % N for a rise in temperature from 10 K to room temperature [182]. The higher thermal stability may

be understood in the light of an increase in N-In average bond strength with higher nitrogen content [176, 183].

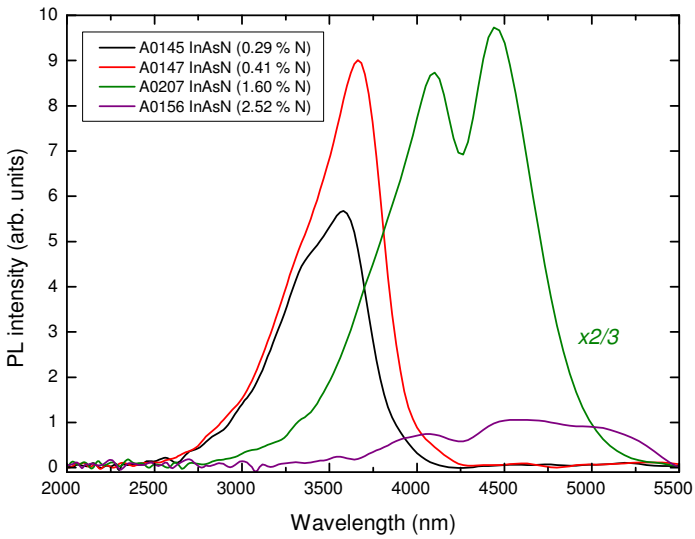

Figure 6.7 Room-temperature FTIR PL of InAsN with various nitrogen compositions

All InAsN samples showed room-temperature luminescence. PL measurements with a Fourier transform infrared spectrometer (FTIR) were performed at Hull University on four InAsN samples with nitrogen composition between 0.29 % and 2.52 % as shown in Figure 6.7. To the best of our knowledge, this is the first report of room-temperature luminescence of InAsN epilayers (see own papers [178, 179]) and it demonstrates once again the material quality achieved through optimisation of the growth conditions. The PL linewidth at room temperature (RT) is 58.4 meV, 52.4 meV, 65.0 meV and 87.7 meV for samples A0145 (0.29 % N), A0147 (0.41 % N), A0207 (1.60 % N) and A0156 (2.52 % N), which corresponds to 2 to 3.5 $k_B T$. It compares very favourably with InAs sample A0129 with RT PL FWHM of 47.9 meV (1.9 $k_B T$).

6.1.5 Surface analysis of InAsN samples

The quality of a material is partially reflected by the quality of its surface. The samples under study in this chapter show mirror-like surfaces but a more detailed look at them can reveal a few new aspects. Figure 6.8 presents Nomarski microscope pictures of InAsN samples with various nitrogen compositions.

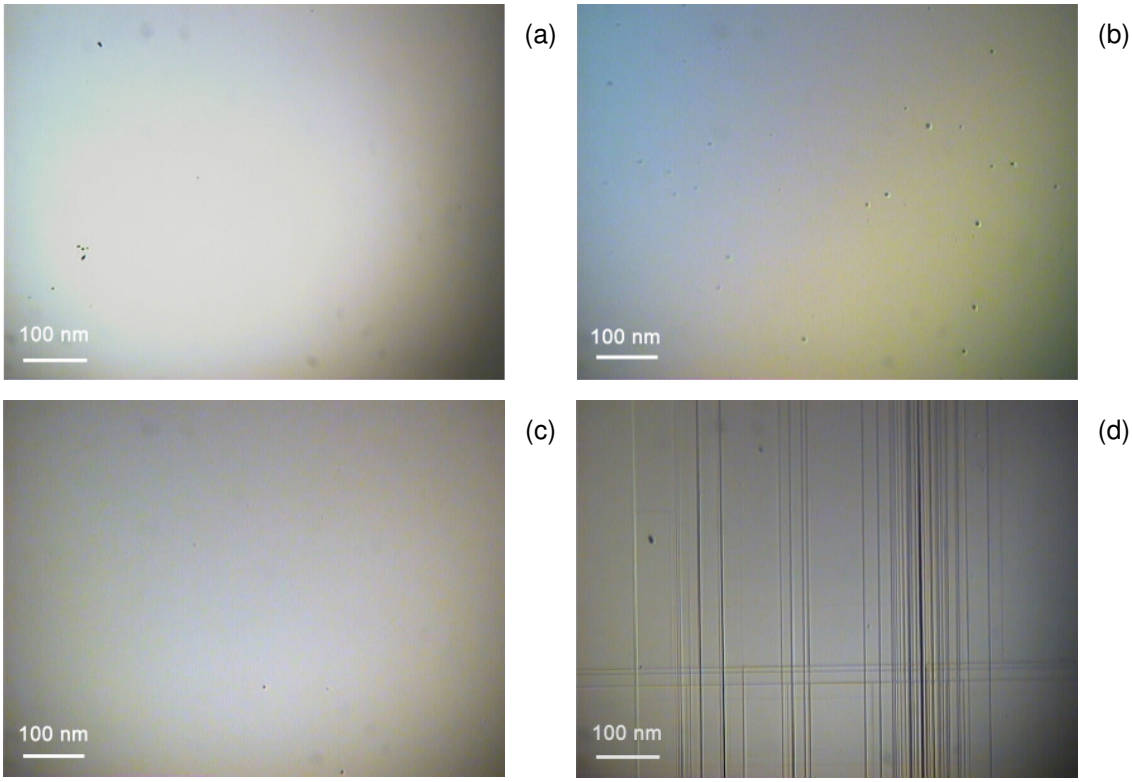

Figure 6.8 Nomarski microscope pictures of InAsN with various nitrogen contents : (a) 0.29 % N, sample A0145 ; (b) 0.65 % N, sample A0213 ; (c) 1.60 % N, sample A0207 ; (d) 2.52 % N, sample A0156

Samples A0145 (0.29 % N), A0213 (0.65 % N) and A0207 (1.60 % N) show very smooth surfaces, as seen in Figures 6.8 (a), (b) and (c). Nevertheless, sample A0213 (0.65 % N) in Figure 6.8 (b) shows a few hole-type features across the whole surface, whose nature has not been elucidated ; these did not prevent a very bright luminescence as mentioned earlier in Section 6.1.2. Sample A0156 (2.52 % N)

pictured in Figure 6.8 (d) shows cross-hatching. This phenomenon is due to misfit dislocations arising from high lattice mismatch (4.5×10^{-3}) of InAsN with 2.52 % N grown on InAs substrate. The strain resulting from the difference in lattice size can be relaxed elastically through dislocations. The roughening of the surface during growth and the presence of contamination of the surface (e.g. N_2 molecules potentially in our case) could cause the formation of mechanical stress concentrators and facilitate dislocation nucleation [25]. A similar effect was observed in previous work in our group for LPE-grown InAsSb bulk layers with 11 % Sb where the lines were much closer than in InAsN sample A0156 (2.52 % N) [184]. Given that the closer the lines the rougher the surface is [25 and references therein], the surface quality is better in InAsN (with 2.52 % N) than in InAsSb (with 11 % Sb) for the same wavelength target of 4.2 µm.

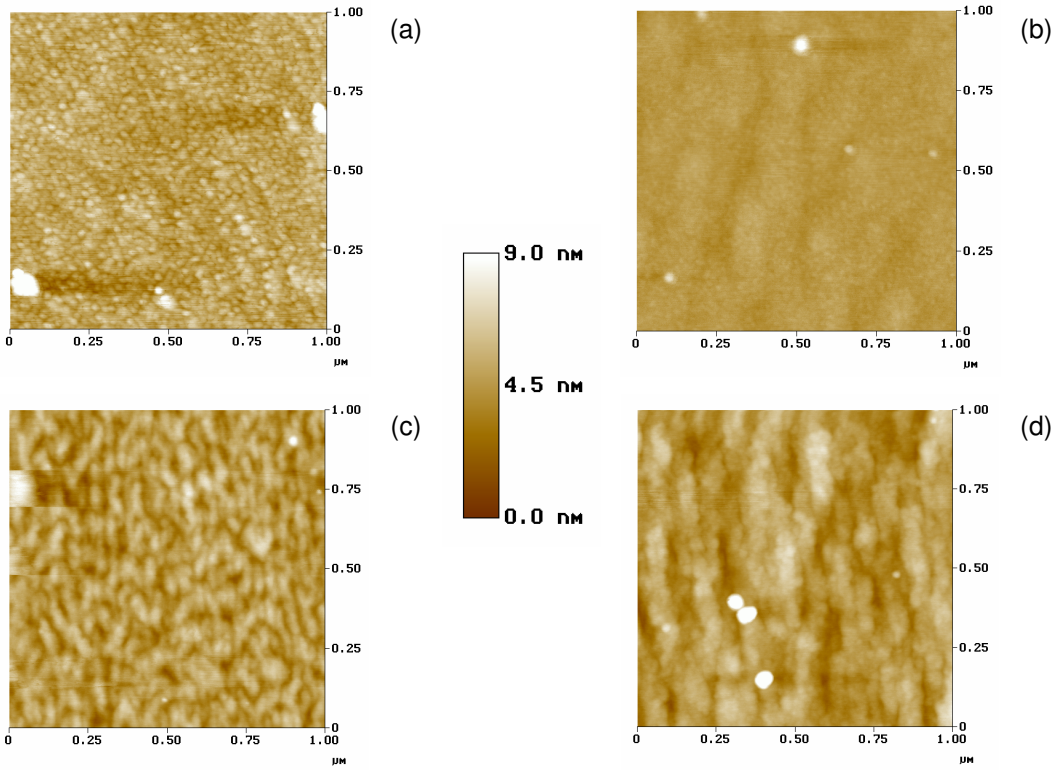

Figure 6.9 AFM pictures of InAsN with various nitrogen content : (a) 0.29 % N, sample A0145 ; (b) 0.65 % N, sample A0213 ; (c) 1.60 % N, sample A0207 ; (d) 2.52 % N, sample A0156

Previous reports of AFM measurements on InAsN layers, grown on GaAs with an InAs buffer, mainly focused on the effect of the growth temperature [82]. A study of the surface quality relative to the nitrogen composition was performed through AFM measurements as shown in Figure 6.9 (the scarce bright white spots on the pictures may correspond to contamination). The surface roughness increases with increasing nitrogen, as is observed in GaAsN [185]. Samples A0145 (0.29 % N) and A0213 (0.65 % N), in Figure 6.9 (a) and (b) respectively, show a relatively smooth surface. This feature corresponds to the (2 × 4) RHEED pattern observed during growth. The slightly smoother surface of sample A0213 (0.65 % N) may be mainly due to the lowering of the nitrogen plasma power from 210 W (for A0145) to 160 W (for A0213), thus reducing the plasma induced damage of the surface by impinging nitrogen species. Samples A0207 (1.60 % N) and A0156 (2.52 % N), in Figures 6.9 (c) and (d) respectively, show a rougher surface that can be related to the (2 × 1) RHEED pattern observed during growth. Peaks and troughs are elongated in one of the crystal directions. The surface of sample A0156 (2.52 % N) reminds one of the surface observed in GaAsN (3.1% N) with wire-like structure [185]. In that case, valleys would correspond to nitrogen deficient regions.

6.2 Rapid thermal annealing treatment of InAsN

The study of rapid thermal annealing (RTA) on InAsN samples with strong localised states presented in Section 5.3 revealed the best parameters to perform this postgrowth treatment. Two InAsN samples of good material quality with nitrogen composition below one percent were annealed at Sheffield III-V Facility Centre for 30 s at 600^{o}C under the conditions presented in Section 4.4. 4 K PL measurements of

as-grown and annealed InAsN samples A0145 (0.29 % N) and A0147 (0.41 % N) are shown in Figure 6.10.

For both samples, annealing preserved the double peak-feature and improved the PL intensity by a factor of six. XRD measurements (not shown) were strictly identical for as-grown and annealed material, hence there was no loss of nitrogen under these annealing conditions. After annealing, sample A0145 (0.29 % N) in Figure 6.10 (a) showed a 6.3 meV blueshift of the short wavelength peak while the long wavelength peak remained at the same energy. The blueshift may be related to an improvement in the nitrogen homogeneity of the crystal, directly affecting the bandgap. It is much less than the 19 meV blueshift observed for annealed InAsN with strong localised states (see Section 5.3).

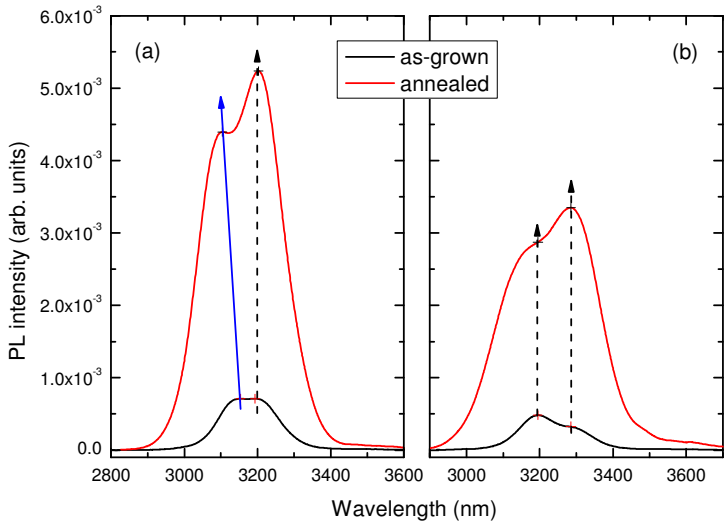

Figure 6.10 Comparison of 4 K PL from as-grown and annealed InAsN : (a) sample A0145 (0.29 % N) ; (b) sample A0147 (0.41 % N)

Annealed sample A0147 (0.41 % N) in Figure 6.10 (b) showed peaks at positions identical to the as-grown material. This further confirms that the quality of the as-grown material was already good since RTA only enhanced the luminescence intensity (perhaps by allowing more N on substitutional sites, but further

investigations are needed). Power-varied PL measurements on these two samples (not shown) demonstrated a behaviour of the peaks with the variation of the excitation power similar to as-grown samples (see Section 6.1.3). Short wavelength peaks are characterised by the exponent $k > 1$ (see equation (5.3)) – 1.37 and 1.54 for samples A0145 (0.29 % N) and A0147 (0.41 % N) respectively – while long wavelength peaks verify $k < 1$ (0.68 and 0.85 for samples A0145 and A0147 respectively). This shows that the nature of the peaks is identical after annealing : band-to-band transition for the short wavelength peak and transition from the localised state for the long wavelength peak.

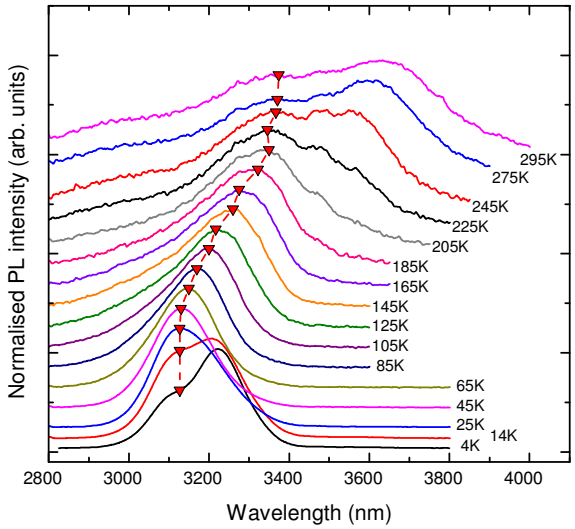

Figure 6.11 Temperature-dependent PL of annealed InAsN sample A0145 (0.29 % N). Red triangles indicate the position of the bandgap related peaks

A temperature-varied PL measurement was performed on sample A0145 (0.29 % N) once annealed, as shown in Figure 6.11. The long wavelength peak (at low temperature), associated with localised states, and the short wavelength peak, associated with InAsN bandgap, behave the same way with temperature as for the as-grown sample. At temperatures above 185 K, two peaks at longer wavelength than the bandgap are clearly visible. Their origins have not been identified. The PL

measurement showed particularly well that the bandgap related-peak lies at a shorter wavelength than the peak of highest intensity at near-room temperatures.

6.3 Enhanced band anticrossing model for InAsN

The band anticrossing (BAC) model is preferred to the tight binding model (inaccurate) or the ***k.p*** model (incomplete) to describe the bandgap in dilute nitride materials because it can predict most of the electronic parameters (see Sections 2.4.2 and 3.5). The conduction band (CB) is split into two subbands E_+ and E_- due to the interaction between the delocalised Γ-minimum of the CB and the nitrogen related level E_N. The transition between $E_-(k)$ at the Γ-point ($k = 0$) and the valence band is the direct bandgap energy E_g ; the study of E_+ is out of the scope of this thesis. Combining equations (2.12) and (2.13), the InAsN bandgap can be derived as :

$$E_g = \frac{1}{2}\left([E_M + E_N] - \sqrt{[E_M - E_N]^2 + 4\left(C_{NM} x^{1/2}\right)^2} \right) \qquad (6.3)$$

where E_M is nothing else but the InAs bandgap and x the nitrogen content in $InAs_{1-x}N_x$ ($0 < x < 1$). At room temperature, Shih, Lin *et al.* [16] estimated the nitrogen level position E_N from its position in GaAs and the valence band offset between GaAs and InAs, so that $E_N = 1.48$ eV in InAsN [16]. The authors obtained a value of $C_{NM} = 1.68$ eV (at 300 K) for InAsN by computation from absorption measurements. Based on InAsN bandgap measurements presented in Section 6.1.4, the compositional dependence of the InAsN bandgap is shown in Figure 6.12. InAsN bandgap was calculated from the PL energy of the band-to-band transitions (short wavelength peaks of the PL spectra) using equation (6.1).

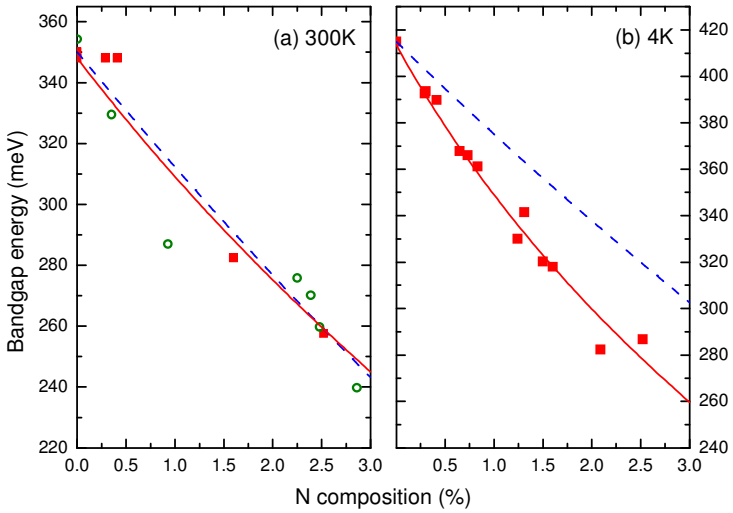

Figure 6.12 Dependence of InAsN bandgap on the nitrogen composition at : (a) 300 K ; (b) 4 K. Blue dashed line and red solid line are based on equations (6.3) and (6.7) respectively. Bandgap values were calculated from PL energies of the band-to-band transitions using equation (6.1). Open circles in (a) are data from [61]

At room temperature, data shown in Figure 6.12 (a) are corroborated by the reported InAsN bandgap obtained from absorption measurements by Kuroda *et al.* [61], as shown by open circles. We thus report a bandgap reduction of 36.9 meV/at.% N at 300 K, in excellent agreement with values of 37 to 38 meV/at.% N in the literature [61, 69] (see Section 3.5.3). At room temperature, the bandgap was fitted with equation (6.3) as shown by the blue dashed line, using parameters presented in Table 6.5. E_M was calculated from Varshni's fit of InAs bandgap (see Section 6.1.4 or [12]). The fit is a reasonable approximation of InAsN bandgap behaviour with increasing nitrogen composition. The 2.1 eV value of C_{NM} is sensible, given that values up to 2.3 eV were obtained by other groups [18]. A better fit of the compositional dependence might be obtained by using a ten-band Hamiltonian [62, 63] but this approach is too complex and was avoided.

Figure 6.12 (b) shows InAsN bandgap at 4 K from all successfully grown-InAsN samples. A higher value of E_M was taken because of the widening of InAs

bandgap at lower temperatures. Nevertheless, the dashed blue line failed to fit convincingly the 4 K compositional dependence of the bandgap with the proposed E_N and C_{NM} parameters. A better model is required, that would account for the behaviour at low temperature. The temperature dependence of InAsN bandgap has not been proposed through the band anticrossing model in the literature ; this issue is addressed in the following paragraph.

Parameters for equation (6.3)	E_M	E_N	C_{NM}
300 K value (eV)	0.351	1.48	2.1
4 K value (eV)	0.415	1.48	2.1

Table 6.5 Band anticrossing model parameters for equation (6.3) shown in Figure 6.12 by blue dashed lines

Variations on the band anticrossing model were proposed to improve it while keeping its simple formulation. The hybridisation parameter C_{NM} is independent of temperature and composition though [186, 187] and cannot be altered to achieve BAC fitting at different temperatures. The position with relation to the valence band of E_M, the conduction band of the host matrix (InAs in the case of InAsN), is obviously independent on the nitrogen composition [19, 188] and its temperature dependence can be modelled by Varshni's equation using the parameters proposed in Section 6.1.4 or [12]. The nitrogen level E_N was found to be dependent on the nitrogen composition* in GaAsN and GaInNAs [60, 188, 189] and increasing nitrogen was found to lower it in GaAsN following the linear approximation [188] :

* E_N is dependent on the pressure [221],[223] and values of 80 meV.GPa^{-1} were reported in GaInNAs. This applies only to pressure dependence measurements of the bandgap and can be neglected for the pressure exerted by the sole strain in the crystal

$$E_N(x) = E^0_{N,x} + \gamma x \qquad (6.4)$$

with γ = -2.52 eV in GaAsN and x the nitrogen composition ($0 < x < 1$).

More recent studies showed that the band anticrossing model gave better temperature-dependence fits when E_N is taken as being linearly dependent on temperature [187, 189] so that :

$$E_N(T) = E^0_{N,T} + \delta T \qquad (6.5)$$

with δ ~ -0.30 meV.K^{-1} in GaInNAs. Combining (6.4) and (6.5), a compositional and temperature dependent $E_N(x,T)$ parameter is proposed :

$$E_N(x,T) = E^0_N + \gamma x + \delta T \qquad (6.6)$$

From these considerations, a temperature-dependent band anticrossing model (BAC) of InAsN bandgap can be derived from equations (2.9), (6.3) and (6.6) :

$$E_g^{InAsN} = \frac{1}{2}\left(\left[E^0_{g,InAs} - \frac{\alpha T^2}{\beta + T} + E^0_N + \gamma x + \delta T\right] - \sqrt{\left[E^0_{g,InAs} - \frac{\alpha T^2}{\beta + T} - E^0_N - \gamma x - \delta T\right]^2 + 4\left(C_{NM} x^{1/2}\right)^2}\right) \qquad (6.7)$$

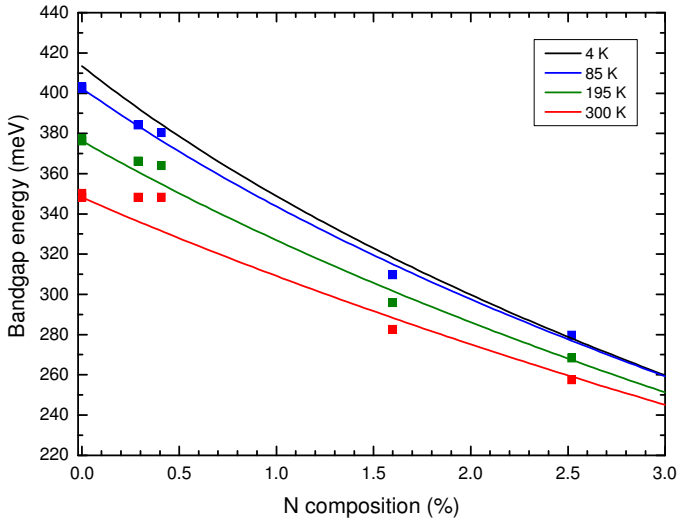

Figure 6.13 InAsN bandgap energy at different temperatures fitted by a temperature-dependent band anticrossing model (6.7)

Figure 6.13 shows the compositional dependence of InAsN bandgap at different temperatures. Using InAsN bandgap of samples with various nitrogen compositions measured at 4 K, the γ parameter was first determined with precision thanks to the large amount of data available, as shown in Figure 6.12 (b). The curve fitting was initiated by keeping γ constant over the temperature range (at this stage, equation (6.5) was not considered yet) ; $E^0_{N,x}$ was found to increase with increasing temperature, supporting the temperature dependence of E_N. Parameter δ was then determined from the temperature dependence of $E^0_{N,x}$. Values of the parameters are summarised in Table 6.6.

$E^0_{g,InAs}$	α	β	E^0_N	γ	δ	C_{NM}
0.415 eV	2.76×10^{-4} eV.K^{-1}	83 K	0.948 eV	4.44 eV	1.4×10^{-3} eV.K^{-1}	2.1 eV

Table 6.6 Band anticrossing model parameters for equation (6.7) shown in Figure 6.12 and Figure 6.13 by solid lines

The values α and β are those used in [12], while C_{NM} is the value found at 300 K (Figure 6.12 (a)). The values of γ and δ are both of opposite sign to the ones found for GaInNAs and GaAsN and two and five times bigger respectively. E^0_N is a mean value within ± 4.7 % of the E^0_N value used in the best fit for each of the temperatures. This confirms that E^0_N is a constant parameter. It is worth mentioning that with the present derivation, $E_N(x,T)$ = 1.41 eV for 1 % N at 300 K is close to the accepted value of E_N = 1.48 eV [16]. The fits are shown by the red solid lines in Figure 6.12 and with increasing temperature in Figure 6.13. The agreement at 4 K is excellent. Only data at 300 K for compositions below 0.5 % show a small

discrepancy, which might be attributed to the uncertainty in determining the bandgap at room temperature as previously stated in Section 6.1.4.

6.4 Achieving 4.2 µm wavelength

6.4.1 Luminescence of InAsN

The major contribution of carbon dioxide to the greenhouse effect makes 4.2 µm wavelength – one of the spectral windows where CO_2 absorption peaks – of particular interest for gas sensing applications. Two 1 µm-thick samples presented in Section 6.1 showed potential to develop sensors – cooled or uncooled – at that particular wavelength. For low temperature applications at 4.2 µm, InAsN sample A0156 with 2.52 % N showed a 4 K PL peak wavelength of 4.505 µm with a clear feature at 4.2 µm associated with CO_2 absorption as shown in Figure 6.14 (a).

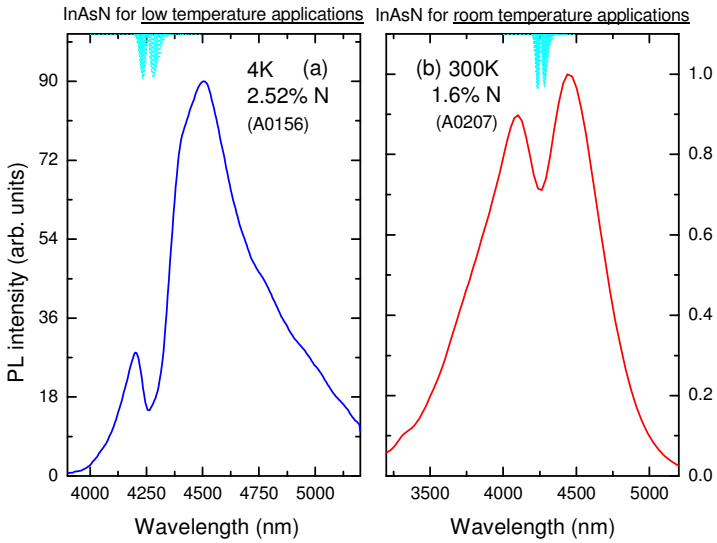

Figure 6.14 InAsN material for 4.2 µm applications at low temperature and room temperature : (a) 4 K PL of InAsN sample A0156 (2.52 % N) ; (b) 300 K PL (FTIR) of InAsN sample A0207 (1.60 % N). Top : Light blue lines represent the CO_2 molecule transmission spectrum (arbitrary units), from HITRAN 2004 database [177]

The sample exhibited a fairly bright PL, with a wide lineshape though. The thickness of the epilayer was 1 μm, a typical value of active region thickness in mid-infrared photodetectors, which is near the critical thickness, explaining why partial strain relaxation resulted in cross-hatching on the surface. For room temperature applications, InAsN sample A0207 with 1.60 % N reaches 4.2 μm at 300 K as shown in Figure 6.14 (b). Nevertheless, the PL intensity of the material at 300 K is rather weak and decreased by more than three orders of magnitude from that at 4 K (as will be evidenced later in Figure 6.21, see Section 6.4.4). The current state of the material would probably lead to poor optical properties of a device and would make cooling necessary to benefit from the best characteristics of InAsN.

Despite the optimisation of the growth conditions, further improvement of InAsN material – such as a narrower PL peak, a PL peak intensity comparable to that of InAs, and lower lattice mismatch – would be needed for 4.2 μm applications. In III-V ternaries, heteroepitaxial growth makes strain a critical parameter to control : as the nitrogen composition increases in InAsN, the lattice size decreases relatively to InAs and increases the tensile strain ; on the contrary, the introduction of Sb into InAs increases lattice size and compressive strain in InAsSb epilayers. Introducing Sb into InAsN could alleviate this issue by balancing the strain. Furthermore, both N and Sb decrease InAs bandgap energy. Finally, the surfactant effect of antimony (see Section 3.7) may improve the luminescence.

6.4.2 InAsNSb material engineering

Our research group has a long experience in InAsSb alloys and so initially InAsNSb was tentatively grown by adding a small amount of nitrogen to InAsSb using optimised growth conditions for the antimonide material. It proved

unsuccessful, probably because the high growth temperature of 440 - 460°C required to grow good quality InAsSb did not correspond with the growth temperature window allowing nitrogen incorporation in InAs. The opposite approach needed to be checked. Starting from the growth conditions used for an InAsN sample A0213 containing 0.65 % N with bright luminescence at 3.37 μm at 4 K (growth temperature 400°C, RF plasma power 160 W, nitrogen flux ~ 5.1×10^{-7} mbar, growth rate 1 μm/h, arsenic minimum flux), an increasing amount of antimony was introduced to grow InAsNSb at fixed nitrogen flux (N ~ 0.65 %) and the influence of Sb on the crystal quality, strain and wavelength was studied. The BEP ratio of As / Sb was varied between 47 and 291, with all other parameters identical, as shown in Table 6.7.

Sample reference	A0210	A0213	A0214	A0209	A0220	A0221
Material	InAsSb	InAsN	InAsNSb	InAsNSb	InAsNSb	InAsNSb
As / Sb BEP ratio	52	-	47	52	112	291

Table 6.7 Growth conditions of InAsNSb samples and InAsSb and InAsN reference samples

XRD measurements performed on InAsNSb are compared to InAsN and InAsSb (As / Sb = 52, grown under identical conditions without nitrogen plasma) in Figure 6.15 (a). While the InAsN epilayer peak is at high ω-2θ angle, the progressive increase in Sb flux reduces the splitting angle and even shifts the epilayer peak to the negative ω-2θ side, to reach InAsNSb at high Sb flux with a bigger lattice constant than InAs. Compared to InAsN, InAsNSb also shows a narrow epilayer peak, much narrower than InAsSb (dashed green line). The evolution of the lattice mismatch is presented in Figure 6.15 (b). InAsNSb grown with an As / Sb BEP ratio of 291 exhibits less mismatch than InAsN (dashed black line). A further increase in the Sb flux changed the strain from tensile to compressive. At high Sb flux, the strain in

InAsNSb is again smaller than in InAsSb (green square) grown at As / Sb BEP ratio of 52. Last, it is demonstrated that InAsNSb can be grown lattice-matched to InAs, for a BEP ratio of As / Sb = 169.

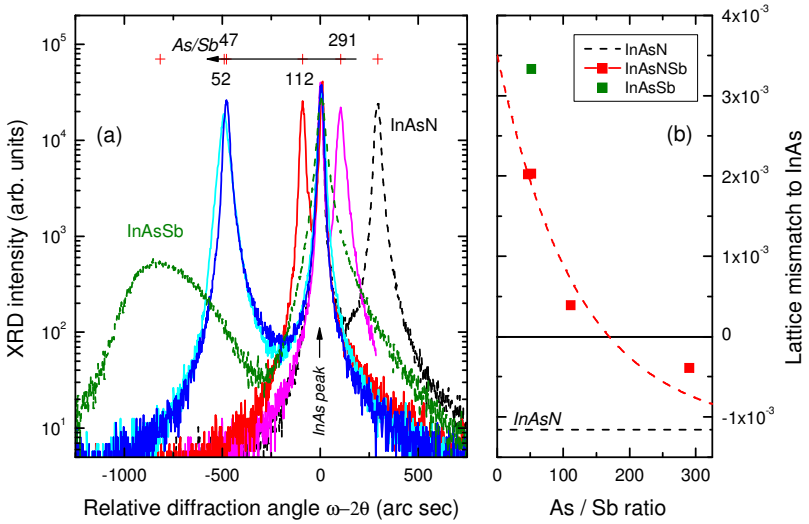

Figure 6.15 (a) XRD measurements of InAsNSb samples with increasing Sb composition. Dashed black and green lines are InAsN and InAsSb respectively ; (b) Lattice mismatch of InAsNSb to InAs as a function of the As / Sb ratio. Dashed red line is a guide to the eye

PL measurements performed on InAsNSb with increasing Sb flux are compared for InAsN and InAsNSb in Figure 6.16 (a). Increasing Sb flux extends the InAsNSb peak to longer wavelength. Compared to InAsN, the PL intensity of InAsNSb was improved three- to four-fold until it dropped for high Sb flux at As / Sb = 47. Similarly, the lineshape of InAsNSb is as narrow as InAsN until high Sb is reached. The InAsNSb PL peak is Gaussian-like, but low excitation power measurements showed that the double peak feature observed in InAsN still existed in InAsNSb. However, the influence of the localised states has reduced since they can hardly be seen at 4 K. Figure 6.16 (b) evidences the reduction of the transition energy with Sb flux. While InAsN showed a PL peak at 368 meV (3.37 μm), the InAsNSb

peak energy decreases from 345 to 268 meV (from 3.592 to 4.628 µm respectively) with increasing Sb flux from As / Sb BEP ratio of 291 to 47.

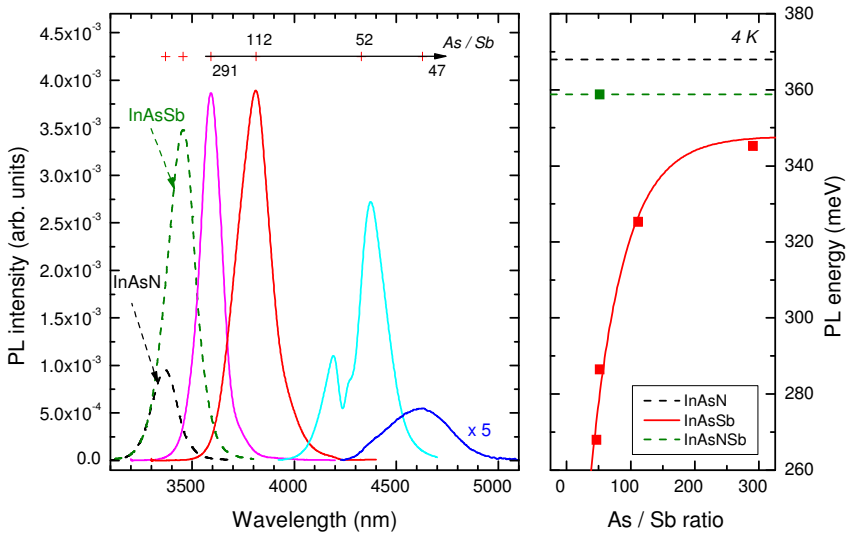

Figure 6.16 (a) 4 K PL measurements of InAsNSb with increasing Sb flux. Dashed lines are InAsN and InAsSb ; (b) 4 K PL energy as a function of As / Sb BEP ratio. The solid red line is a guide to the eye

6.4.3 N and Sb compositions in InAsNSb and bandgap model

Reports on the effects of antimony on the nitrogen incorporation in GaAsN are contradictory, Sb being shown to reduce the nitrogen incorporation in MOVPE-grown GaAsNSb [190] or to increase it in GaAsNSb grown by MBE [106, 191]. The mutual influence of N and Sb on their respective compositions is hence still unknown for InAsNSb and needs to be clarified. Under the assumption of Vegard's law, the lattice constant of $InAs_{1-x-y}N_xSb_y$ follows :

$$a_{InAsNSb}(x,y) = (1-x-y)\,a_{InAs} + x\,a_{InN\_cubic} + y\,a_{InSb} \qquad (6.8)$$

where a_{InAs}, a_{InN_cubic} and a_{InSb} are InAs, InN (cubic) and InSb lattice constants respectively (values are given in Section 2.2.3).

The supply of nitrogen was constant for every InAsNSb sample presented in Section 6.4.2. If the nitrogen composition is supposed to be fixed to 0.65 % N, as measured by XRD in the antimony-free InAsN sample A0213 grown under identical conditions, the antimony composition can be calculated to match the XRD splitting angle measured in InAsNSb. The calculated Sb composition is plotted as a function of As / Sb BEP ratio in Figure 6.17 (a). For samples A0221 (As / Sb = 291) to A0209 (As / Sb = 52), it increases with the Sb flux, along with the decrease in InAsNSb bandgap energy at 4 K shown in Figure 6.17 (b) (here, the PL energy from the band-to-band transition and bandgap energy at 4 K were considered the same since the thermal contribution of the crystal is negligible at low temperature). Nevertheless, such Sb compositions would mean that InAsNSb bandgap decreases by about 17 meV/at.% Sb by the sole effect of antimony, which is unlikely since the bandgap reduction can be evaluated to ~ 8 meV/at.% Sb (based on equation (6.9) later in this section). Moreover, circled data in Figure 6.17 (a) shows that there is no change in the *calculated* Sb composition for samples A0209 and A0214 (grown at the As / Sb ratios of 52 and 47 respectively), which is unexpected with an increase in Sb flux and cannot explain the further reduction in the PL energy. Let us now assume that the antimony content in InAsNSb samples A0209 (As / Sb = 52) and A0214 (As / Sb = 47) is saturated and fixed to 6.0 % Sb, as determined in the nitrogen-free InAsSb sample A0210 grown at As / Sb = 52. The nitrogen composition calculated to satisfy the XRD splitting angle in InAsNSb samples grown at As / Sb ratios of 52 and 47 would vary very little, from 1.19 to 1.20 % N, because both XRD epilayer peaks lie close together (see blue and light blue lines in Figure 6.15). This variation would reduce the bandgap by 0.5 meV in InAsN and cannot account for the 18 meV decrease in the bandgap energy at 4 K in samples A0209 and A0214. Both of the hypotheses, fixed N

composition or fixed Sb composition, are hence wrong and prove that both N and Sb compositions change with As / Sb ratio.

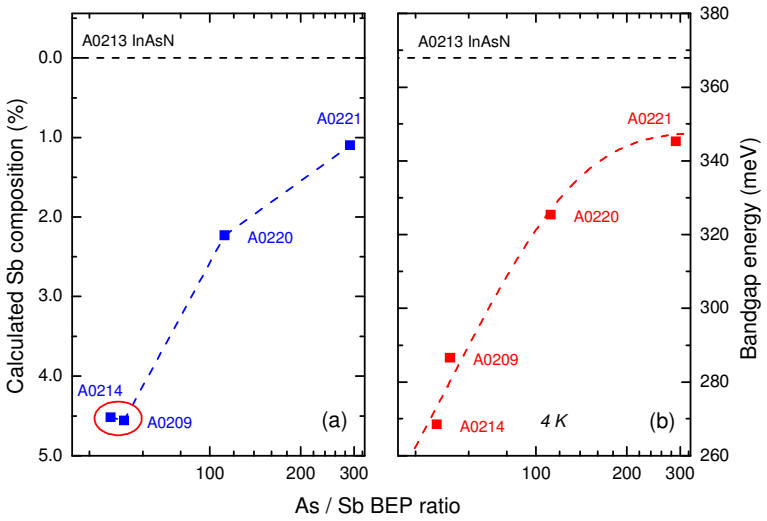

Figure 6.17 (a) Calculated Sb composition as a function of As / Sb ratio, assuming that the nitrogen content in InAsNSb is fixed at 0.65 % ; (b) InAsNSb bandgap energy at 4 K as a function of As / Sb flux ratio

In the literature, N and Sb compositions, when reported, were measured by XRD combined with electron probe microanalysis (EPMA) [110] or secondary ion mass spectroscopy (SIMS) [109]. Since it was not available in our research group, a method to determine N and Sb compositions was developed in-house using 4 K PL measurements and bandgap models. On one hand, XRD measurements performed on quaternaries give a unique information about the splitting angle indicative of the epilayer lattice constant. In InAsNSb, because N and Sb balance the strain, an infinite number of (N,Sb) composition combinations are thus possible. On the other hand, PL measurements on InAsNSb give a transition energy inherent to the combined effect of N and Sb introduced into InAs. InAsNSb has not been modelled yet as a function of the composition and temperature. The $InAs_{1-y}Sb_y$ bandgap has been modelled by Wieder as a function of Sb composition and temperature [192] :

$$E_g^{InAsSb}(y,T) = 0.411 - \frac{3.4\times10^{-4}T^2}{T+210} - 0.876y + 0.7y^2 + 3.4\times10^{-4}Ty(1-y) \qquad (6.9)$$

As for InAsN, the temperature dependent band anticrossing model presented in Section 6.3 gives a precise description of the bandgap as a function of the composition. It is reasonable to assume that the $InAs_{1-x-y}N_xSb_y$ bandgap results from the superposition of the bandgap narrowing $\Delta E^{InAsN}(x)$ and $\Delta E^{InAsSb}(y)$ due to N and Sb respectively that alter the InAs bandgap accordingly :

$$E_g^{InAsNSb}(x,y) = E_g^{InAs} - \Delta E^{InAsN}(x) - \Delta E^{InAsSb}(y) \qquad (6.10)$$

where x and y are the nitrogen and antimony compositions respectively. The temperature dependence of $InAs_{1-x-y}N_xSb_y$ bandgap can be derived from (6.10) as :

$$E_g^{InAsNSb}(x,y,T) = E_g^{InAsN}(x,T) - \left(E_g^{InAs}(T) - E_g^{InAsSb}(y,T)\right) \qquad (6.11)$$

where $E_g^{InAsN}(x,T)$ can be taken as the band anticrossing model equation (6.7), $E_g^{InAs}(T)$ as Varshni's equation (2.9) and $E_g^{InAsSb}(y,T)$ as Wieder's equation (6.9). At 4 K, the bandgap reduction in InAsSb is only ~ 8.5 meV / % Sb. The previous assumption of fixed N incorporation in InAsNSb with increasing Sb flux is thus wrong. For InAsN, the bandgap reduction is ~ 71.3 meV between 0 and 1 % N. By using XRD and PL measurements along with the InAsNSb bandgap model, it is demonstrated in the following the possibility to determine N and Sb compositions in the quaternary InAsNSb by the unique solution to :

$$\begin{cases} a_{InAsNSb}(x,y) = (1-x-y)\,a_{InAs} + x\,a_{InN\_cubic} + y\,a_{InSb} \\ E_g^{InAsNSb}(x,y,4K) = E_g^{InAsN}(x,4K) - \left(E_g^{InAs}(4K) - E_g^{InAsSb}(y,4K)\right) \end{cases} \qquad (6.12)$$

Based on the combination of XRD and bandgap models, the InAsNSb PL energy as a function of N and Sb is shown in Figure 6.18 (a). As the Sb flux increases, the PL energy at 4 K decreases. One can see (as projected on the *xy* plane of Figure 6.18 (a)) that both N and Sb compositions in InAsNSb increase with

increasing Sb flux (numbers in brackets are the *As / Sb* flux ratios). Energy dispersive X-ray spectroscopy (EDAX) measurements performed on InAsNSb, though not precise enough to measure quantitatively the nitrogen composition, confirmed the increasing antimony content in *all* InAsNSb samples grown with increasing Sb flux as shown in Figure 6.18 (b). A striking feature is that Sb enhances by more than two-fold the nitrogen composition (while the supply of nitrogen was constant for all samples), ranging from 0.65 % in the Sb-free InAsN sample to 1.45 % in InAsNSb grown under As / Sb ratio of 47.

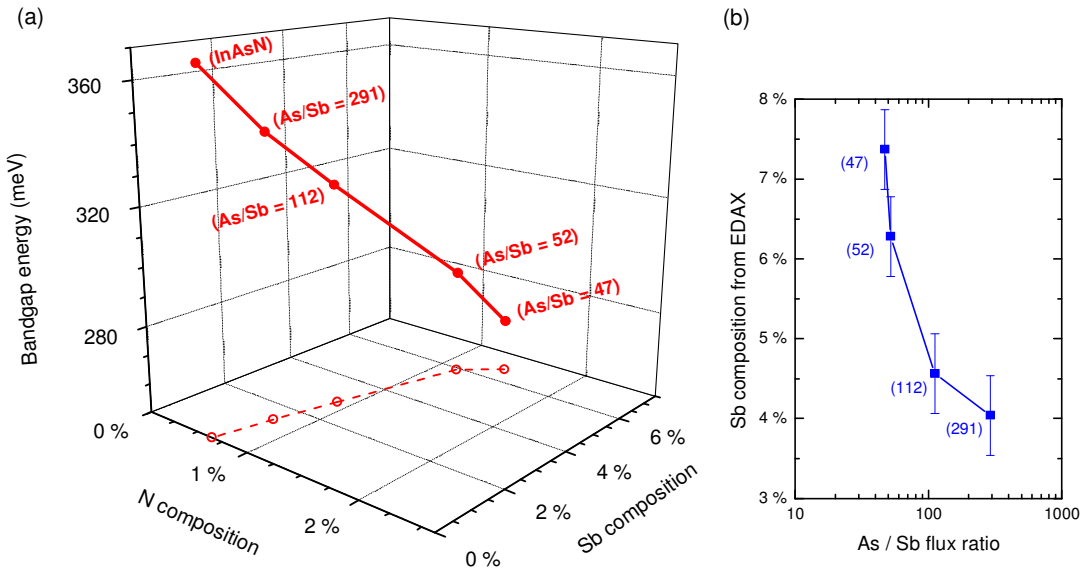

Figure 6.18 (a) InAsNSb bandgap energy at 4 K as a function of N and Sb compositions ; (b) Sb composition determined by EDAX. Numbers in brackets are the *As / Sb* flux ratios

6.4.4 Comparison of InAsNSb and InAsN materials

First, InAsN and InAsNSb are compared in Table 6.8 for 4.2 µm wavelength applications at low temperature. InAsNSb sample A0209 and InAsN sample A0156 (presented in Section 6.1) both reach 4.2 µm wavelength at 4 K as shown in Figure 6.19 (a). The InAsNSb sample has a perfectly Gaussian-like PL peak as

demonstrated by the dashed red line and a peak emission at 4.328 µm was thus computed. The PL peak from InAsNSb sample A0209 (with 1.2 % N and 5.9 % Sb) exhibits a dip due to CO_2 absorption as shown by the light blue lines and is 8.8 times brighter and twice as narrow as the InAsN sample A0156 containing 2.52 % N. The bandtail seen in InAsN was completely suppressed in InAsNSb by the addition of Sb and this is surely related to the improvement in the nitrogen homogeneity of the InAsNSb sample produced by the surfactant effect of Sb.

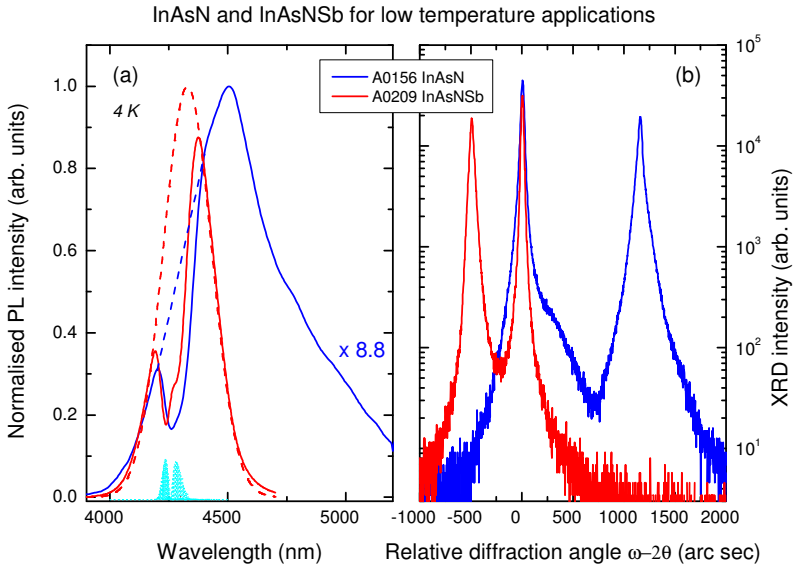

Figure 6.19 Comparison of InAsNSb and InAsN for 4.2 µm wavelength applications at low temperature : (a) 4 K PL measurements of InAsNSb and InAsN samples. Bottom : Light blue lines represent the CO_2 molecule absorption spectrum, from HITRAN 2004 database [177] ; (b) XRD measurements of respective InAsNSb and InAsN samples

XRD measurements performed on the same InAsN and InAsNSb samples are compared in Figure 6.19 (b) and show peaks on each side of the InAs-related peak at zero position. The lattice mismatch in InAsNSb was halved when compared to in InAsN. The epilayer peak is slightly narrower in the case of InAsNSb, which also suggests a better material quality. Finally, a smooth surface was observed by

Nomarski microscope (not shown) for InAsNSb sample A0209, as opposed to the cross-hatched InAsN sample A0156. These features show the clear advantage of growing InAsNSb for mid-infrared applications.

Sample reference	InAsN A0156	InAsNSb A0209
Composition	2.52 % N	1.2 % N, 5.9 % Sb
XRD FWHM (arc sec)	47	42
Lattice mismatch to InAs	-4.5×10^{-3}	2.0×10^{-3}
4 K PL wavelength (μm)	4.505	4.328
4 K PL intensity (arb. units)	1	8.8
4 K PL FWHM (meV)	30.7	16.0
Surface aspect	cross-hatching	smooth

Table 6.8 Summary of InAsNSb and InAsN material characteristics for 4.2 μm wavelength applications at low temperature

InAsNSb and InAsN are now compared for 4.2 μm wavelength applications at room temperature through two other samples. Compared to the InAsN sample A0207 (with 1.6 % N, presented in Section 6.1), the PL from the InAsNSb sample A0220 (containing 0.9 % N and 2.9 % Sb) also reaches 4.2 μm wavelength at 295 K. Temperature varied-PL measurements performed on the InAsNSb sample are shown in Figure 6.20. At low power and low temperature (not shown), localised states could be seen ~ 10 meV above the bandgap related-peak energy, identical to the Sb-free (InAsN) sample A0213 (0.65 % N) used as a "starting point" for the InAsNSb study. The luminescence in InAsNSb was particularly bright all through the temperature range of measurement and demonstrated clear CO_2 absorption at room temperature.

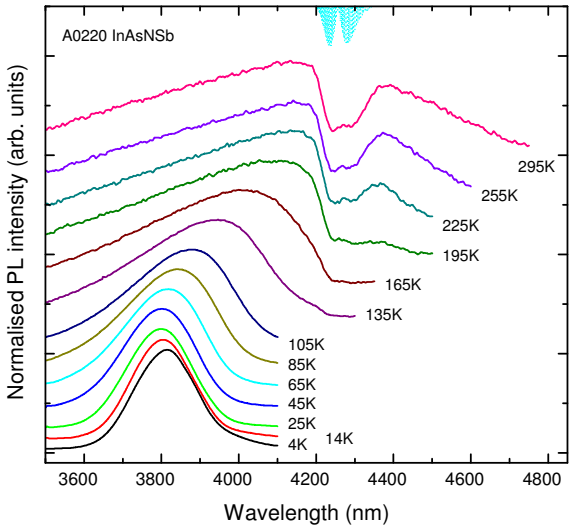

Figure 6.20 PL of InAsNSb sample A0220 (0.9 % N, 2.9 % Sb) at different temperatures showing the characteristic CO_2 absorption feature at room temperature. Light blue lines represent the CO_2 molecule transmission spectrum, from HITRAN 2004 database [177]

A comparison of the temperature dependence of the PL intensity (normalised to the value at 4 K) of InAsNSb and InAsN is shown in Figure 6.21 (a). The trend is that generally observed in III-V compounds [193, 194]. One can see that the PL intensity in InAsNSb decreases by less than two orders of magnitude when the temperature is increased from 4 K to 300 K. This is much less than the decrease of 2.5 and 3.5 orders of magnitude observed in InAs and InAsN respectively. Figure 6.21 (b) shows the temperature dependence of the bandgap energy of InAsN and InAsNSb. The InAsN bandgap energy (sample A0207, 1.6 % N) decreases by ~ 31 meV in the temperature range 4 K - 300 K when that of InAsNSb (sample A0220, with 0.9 % N and 2.9 % Sb) decreases by ~ 45 meV. A value of ~ 37 meV can be calculated for InAsNSb using equation (6.11) where the bandgap variation over the temperature range 4 K - 300 K are $\Delta E^{InAsN}(T)$ ~ 43 meV for InAsN with 0.9 % N, $\Delta E^{InAs}(T)$ ~ 63 meV and $\Delta E^{InAsSb}(T)$ ~ 57 meV for InAsSb with 2.9 % Sb. This calculated value is in rather good agreement with that measured considering the uncertainty in the determination of the bandgap energy for all samples at 300 K.

Indeed, the bandgap energy can be approximated by a linear function of the temperature T when $T > 85$ K, whose slope is given by the parameter Δ in Figure 6.21 (b). While InAsNSb has a value of bandgap reduction with temperature higher than that of InAsN (-2.2×10^{-1} meV.K^{-1} compared to -1.0×10^{-1} meV.K^{-1} respectively), it still outperforms InAs (-2.6×10^{-1} meV.K^{-1}) in terms of temperature stability. Sb allows a higher homogeneity of the material and reduces the strain, which possibly explains the similar or even better properties of InAsNSb when compared to InAsN.

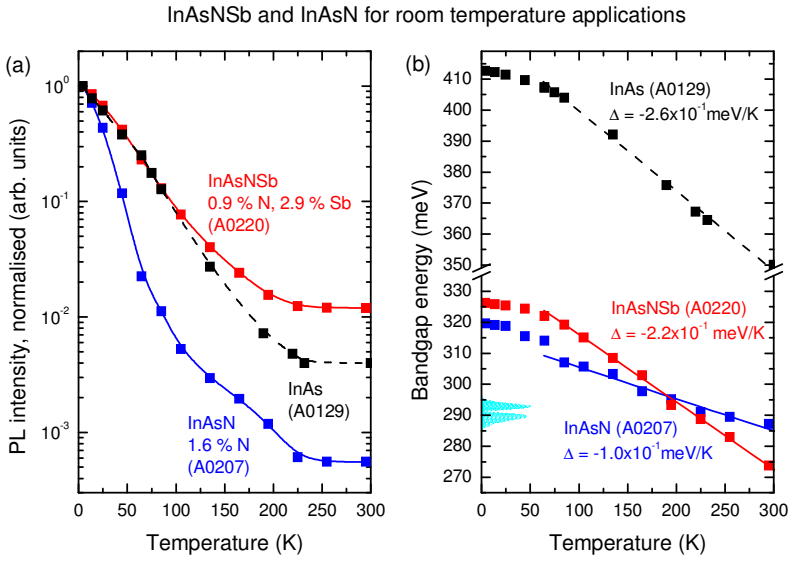

Figure 6.21 Comparison of InAsNSb and InAsN for 4.2 µm applications at room temperature : (a) temperature dependence of the PL intensity (normalised to the value at 4 K) ; (b) temperature dependence of the bandgap. InAs is given for reference. Light blue lines represent the CO2 molecule transmission spectrum, from HITRAN 2004 database [177]

The room temperature luminescence from InAsNSb and InAsN samples is compared in Figure 6.22. The luminescence of $InAs_{0.962}N_{0.009}Sb_{0.029}$ measured by FTIR spectroscopy has been improved by a factor of two when compared to $InAs_{0.984}N_{0.016}$ sample A0207 (in dispersive PL measurements, InAsNSb was up to ten

times as bright as InAsN). Compared with the bulk InAs sample A0129, the room temperature intensity in InAsNSb is only reduced by half (it was seven times less bright than InAs at 4 K). The InAsNSb FWHM is 59.3 meV (~ $2.3k_BT$), rather close to that for InAs, which has a RT FWHM of 47.9 meV (~ $1.9k_BT$). The material quality of InAsNSb alloy was shown to be comparable to that of good quality InAs in terms of luminescence (intensity and linewidth) thanks to the surfactant effect of antimony (see Section 3.7) and demonstrated a reduced temperature sensitivity. The target of 4.2 µm wavelength at room temperature has finally been achieved with a novel quaternary, InAsNSb, which shows bright luminescence with a fairly narrow lineshape.

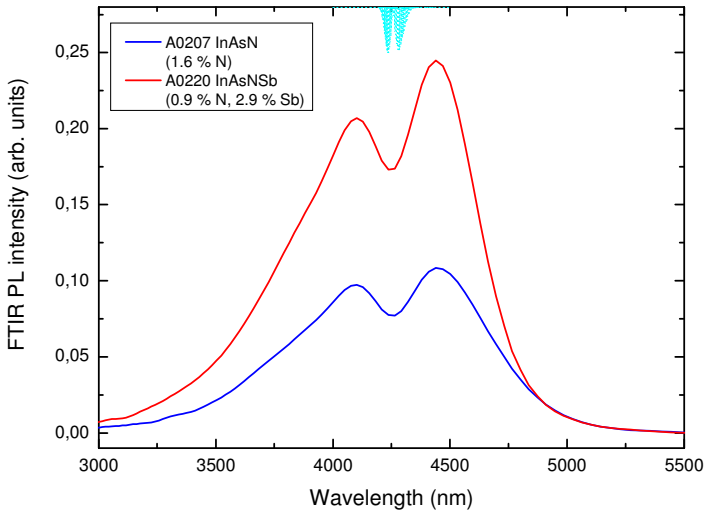

Figure 6.22 295 K FTIR PL of InAsNSb (0.9 % N, 2.9 % Sb) and InAsN (1.6 % N) for 4.2 µm wavelength target at room temperature. Top : Light blue lines represent the CO_2 molecule transmission spectrum, from HITRAN 2004 database [177]

6.5 Summary

InAsN epilayers grown on InAs substrates for the present study showed excellent crystalline structure and contradict the general assumption that a severe degradation of the material quality occurs in dilute nitrides when incorporating more than one percent of nitrogen. Carefully chosen growth parameters based on the study

presented in the previous chapter led to good quality InAsN in which the nitrogen can be increased up to 2.52 % N, causing an increase in the lattice mismatch and a drastic reduction of the bandgap. Emission wavelengths up to 4.5 μm were reached at low temperature and the good material quality helped the samples show strong, narrow photoluminescence up to room temperature, with reduced bandtails and weakly localised states. A double peak-feature in the luminescence of InAsN was attributed to free carrier and localised carrier recombinations. Localised states are subject to carrier de-trapping with increasing excitation power or temperature, leading to their sought-after quenching and the observed blueshift. The temperature dependence of InAsN bandgap was fitted with Varshni's equation (for various nitrogen compositions) and was shown to reduce with increasing nitrogen composition, that is a true advantage in materials for mid-infrared applications. InAsN samples showed a mirror-like surface morphology and only high nitrogen composition (2.52 %) induced cross-hatching on the surface by relaxation of the strain. The surface roughness of InAsN epilayers was shown to increase with nitrogen composition, which clarified the interpretation of the RHEED patterns observed during growth. Rapid thermal annealing favoured an increase in the luminescence intensity with limited blueshift and evidenced further the behaviour of the bandgap related-peak, but did not affect the localisation potential. The small effect of the annealing treatment corroborated further the high quality already achieved in the as-grown material. The InAsN bandgap was successfully described by the band anticrossing model adapted to take into account both temperature and composition dependences.

To achieve the best performance for 4.2 μm wavelength applications (namely carbon dioxide monitoring), quaternary InAsNSb material was developed because of the potential of antimony to balance the strain and improve the material quality.

InAsNSb of excellent crystalline quality was engineered and the lattice mismatch controlled through the addition of antimony. Strong and narrow luminescence was observed up to room temperature. Gaussian-like peaks showed a reduced influence of the localised states on the luminescence. Antimony was shown to extend the InAsNSb wavelength and improve N incorporation and a model of the InAsNSb bandgap was formulated. $InAs_{0.962}N_{0.009}Sb_{0.029}$ was particularly successful in reaching 4.2 μm at room temperature and proved to have brighter luminescence and only slightly higher temperature dependence than InAsN.

Chapter 7. Applications of InAsN and InAsNSb materials to novel devices

"*Knowing is not enough; We must apply. Willing is not enough; We must do.*"
Leonardo da Vinci

The advance made in InAsN and InAsNSb material growth is aimed at a practical application : the fabrication of prototype photodetectors for gas sensing and the detection of carbon dioxide in particular.

7.1 Prototype devices

Simple p-i-n structures were grown at different stages during the InAsN material development but these were unsuccessful, partly because of the material quality and partly because of doping cell-related issues. Some basic InAsN and InAsNSb p-i-n diode structures on InAs substrates, based on the optimisation study of InAsN growth conditions (see Section 5.2) and InAsNSb material engineering (see Section 6.4.2), were grown to investigate the feasibility of detectors with these new materials. Their structure is shown in Figure 7.1 and band offsets were estimated from the literature [23]. An InAsN p-i-n (A0191) was grown n-side up on p-type InAs substrate. As shown in Figure 7.1 (a), a 2.0 μm-thick InAsN active region was grown (at 380^{o}C) and contains 1.05 % N. It is surrounded by p- and n-doped InAs, with the addition of a 20 nm-thick barrier (B1) made of $AlAs_{0.156}Sb_{0.844}$ that is almost lattice-matched to InAs. The barrier is intended to limit diffusion currents in the device to help make it operate in the generation-recombination dominated regime. Undoped (ud) InAs was grown for a few tens of seconds after the InAsN layer to protect the surface while increasing the growth temperature to its optimal value for InAs, that is

~ 485°C (similar action was taken between the barrier growth at 500°C and the InAsN).

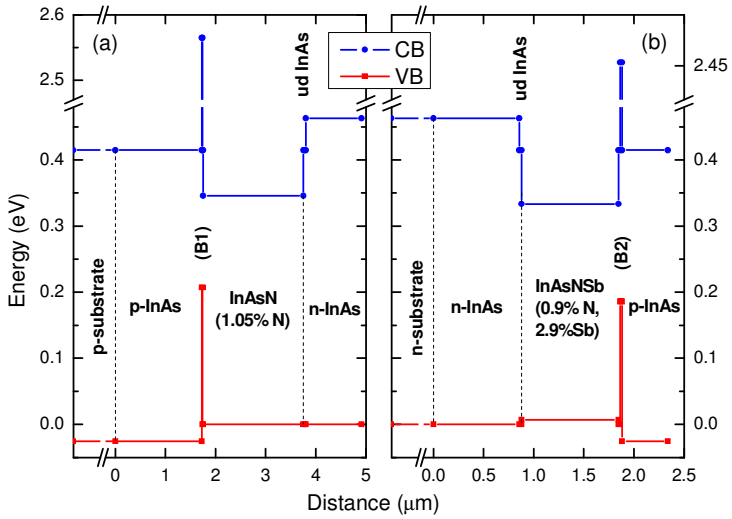

Figure 7.1 Structure and energy bandgap at 4 K of : (a) InAsN A0191 p-i-n ; (b) InAsNSb A0240 p-i-n. Details of barriers (B1) and (B2) are given in the text

A similar structure on n-type InAs substrate was used for the InAsNSb p-i-n diode (A0240, p-side up) but using thinner layers as shown in Figure 7.1 (b). The thickness of InAs cladding layers has been reduced to increase the electric field in the active region and the active region material is an exact copy of the one presented earlier in the study of InAsNSb sample A0220 with 0.9 % N and 2.9 % Sb. A perfectly lattice-matched barrier (B2) was grown on InAs using $Al_{0.87}Ga_{0.13}As_{0.152}Sb_{0.848}$. After growth (that lasted from three to six hours), the p-i-n structures were processed into 400 μm-diameter mesa devices (by Dr. R. Airey) at the Centre for Nanoscience and Technology, University of Sheffield, as shown in Figure 7.2.

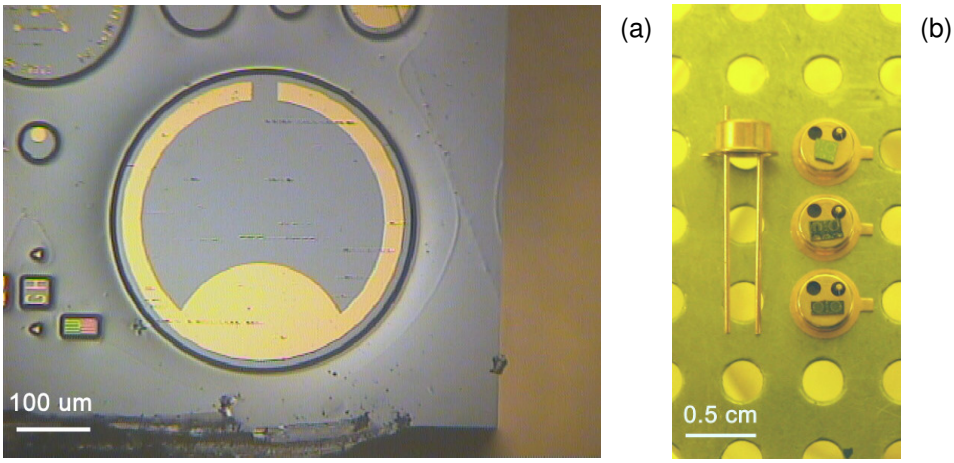

Figure 7.2 (a) Typical 400 µm-diameter mesa before mounting on header ; (b) Typical devices mounted on TO-46 headers

Current-voltage (I-V) characteristics were performed on InAsN and InAsNSb p-i-n devices as shown in Figure 7.3. Both the p-i-n devices exhibited rectification for positive voltages but none of the structures show the expected exponential curve as generally modelled by equation (2.18) in diodes. The deviation from the ideal I-V characteristic can be attributed to the effect of a parallel resistance (in the reverse bias region) and to a series resistance (in the forward bias region) within the material [195]. The InAsN p-i-n showed an I-V characteristic, pictured in the inset of Figure 7.3 (a), where the dark current (the current in the reverse bias region) is ~ 100 mA at 4 K. In Figure 7.3 (b), the shape of the I-V characteristic of the InAsNSb p-i-n shown in the inset is little diode-like. A previous study of InGaAs/InAsSbP photodetectors showed the same behaviour when the doping level was ill-chosen [196a]. Compared to InAsN p-i-n, the dark current at 4 K in the InAsNSb p-i-n is higher. It increases with temperature as is observed in narrow band gap materials when the diffusion current becomes the dominant mechanism at room temperature [196b].

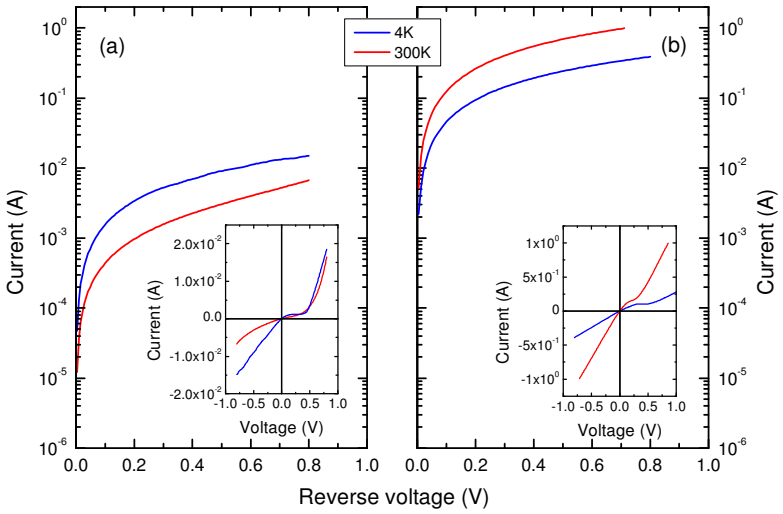

Figure 7.3 Dark current at low and room temperature : (a) InAsN A0191 p-i-n ; (b) InAsNSb A0240 p-i-n. Inset : I-V characteristics

Room temperature photoresponse measurements (see Section 4.2.3) were extremely weak and noisy and showed only a vague peak centred around 3.25 µm as for InAs devices. The devices failed to demonstrate the potential of InAsN and InAsNSb as active regions of *photodetectors*. However, the p-i-n structures were used as *diodes*. Electroluminescence (EL) measurements were performed on the InAsN and InAsNSb p-i-n diodes at various temperatures and currents. The current hardly changed the peak wavelength at 4 K. Spectra at different temperatures are compared in Figure 7.4. The InAsN p-i-n (A0191) showed a narrow peak at 3.27 µm at 4 K and a broader peak around 3.46 µm at 225 K as pictured in Figure 7.4 (a). Unfortunately, these wavelengths correspond rather to emissions from p-type InAs. As for the InAsNSb p-i-n (A0240) shown in Figure 7.4 (b), a very similar behaviour was observed, with peaks at 3.29 µm and 3.57 µm at 4 K and 225 K respectively, but with a much brighter electroluminescence (by a factor of 35). These transitions do not agree with the expected wavelengths from the active region (3.59 µm and 3.80 µm at 4 K for InAsN and InAsNSb respectively), and recombination must again be occurring in the p-type region.

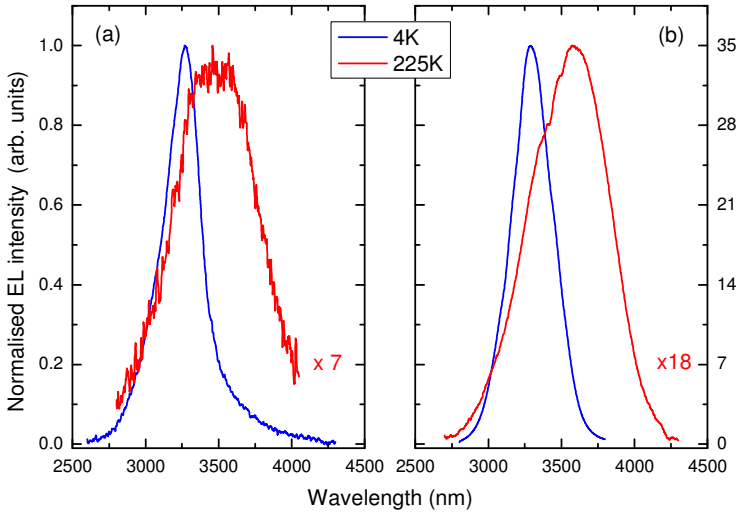

Figure 7.4 EL measurements at 4 K and 225 K : (a) InAsN p-i-n A0191 ; (b) InAsNSb p-i-n A0240

Indeed, a promising result comes from a simple InAsNSb p-i-n structure grown on n-type InAs substrate through a collaboration with National Taiwan University with a lattice mismatch similar to that in sample A0220. The structure of InAsNSb p-i-n C1614 consists of a thin n-type InAs buffer, a 1 µm-thick InAsNSb active region grown at 420°C and a 0.5 µm-thick p-type InAs barrier, without blocking barrier. The antimony composition in InAsNSb is ~ 3 % and the reduction in the XRD splitting angle when compared to a nitrogen-free InAsSb sample (not shown) proved the incorporation of nitrogen (~ 0.8 %). The I-V characteristic at 4 K was similar to that for A0240 with a current step around 300 mA. Low temperature EL measurements are shown in Figure 7.5. While a current of 400 mA induces 4 K electroluminescence at 3.30 µm, most likely from p-InAs, the lowest current possible of 300 mA led to a peak emission of 3.88 µm that surely originates from InAsNSb. Once again, the doping levels determine where recombination occurs and are critical to obtain luminescence from the active region.

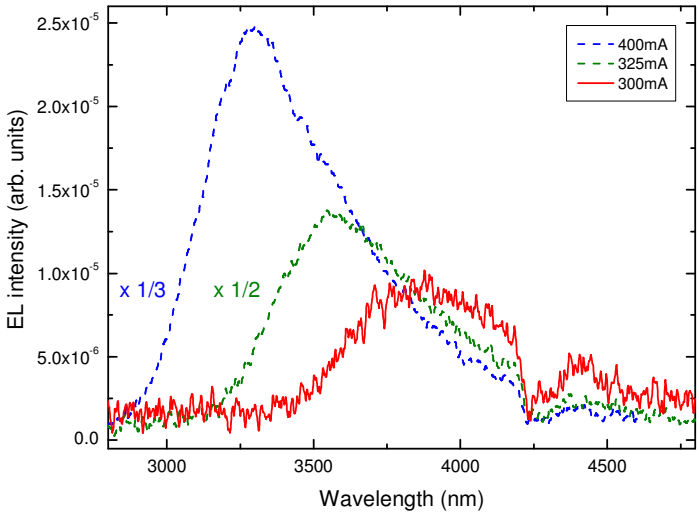

Figure 7.5 4 K EL measurements of InAsNSb p-i-n C1614 at different drive currents, evidencing an InAsNSb-related peak at 300 mA

These first attempts of InAsN and InAsNSb p-i-n structures showed potential to make mid-infrared devices with these novel materials. The high residual carrier concentration in InAsN (~ 10^{15} cm^{-3}, see Section 3.5) might explain why usual doping levels (~ 10^{16} cm^{-3}) did not suffice to make the devices work. Given the good quality of the material attested by previous PL measurements (see Section 6.4), improvements are expected with further device optimisations, i.e. optimisation of doping levels and active region thickness. The choice of the barrier material and the effect of n-side up or p-side up geometries need to be considered. Working devices for 4.2 µm wavelength applications are only a few steps away.

7.2 Summary

Both the InAsN and InAsNSb p-i-n devices exhibited electroluminescence from the p-doped barrier instead of the active region. Nevertheless, emission occurring from the InAsNSb active region was demonstrated at 3.88 µm at 4 K.

Chapter 8. Conclusions and suggestions for further work

"*… but if you haven't got a sort of notion by this time, then I must have been very obscure in my narrative, or you too sleepy to seize upon the sense of my words*"
Lord Jim, Joseph Conrad

8.1 Conclusions on InAsN and InAsNSb materials for mid-infrared applications

Before the start of this study, InAsN was perceived to be a difficult material to grow, with generally poor crystalline quality, exhibiting weak luminescence quenching far below room temperature that originates from poorly understood localised states. As such, no room temperature applications in the mid-infrared spectral range could be considered. The present thesis investigated the optimisation of the MBE growth of InAsN in terms of luminescence, strain and surface quality as well as the parameters controlling the nitrogen incorporation. Weak luminescence in InAsN material of poor quality and S-shape temperature dependence of the photoemission were attributed to strongly localised states and material disorder. High quality InAsN epilayers demonstrated room temperature luminescence at 4.2 μm suitable for CO_2 detection. The crystalline quality and luminescence were both improved by incorporating antimony into InAsN and InAsNSb LEDs were demonstrated.

The main achievements of this thesis are :

- room temperature luminescence up to 4.5 μm was obtained from InAsN of high crystalline quality
- nitrogen incorporation can be controlled and increased by decreasing growth temperature, growth rate and arsenic flux

- InAsN material of good quality demonstrated transitions attributed to band-to-band recombinations and weakly localised states to valence band recombinations
- the temperature dependence of InAsN bandgap was explained with the band anticrossing model by introducing a temperature- and composition-dependent nitrogen level
- strain balance in material for 4.2 μm applications was achieved with the novel InAsNSb alloy
- a way to determine the composition of the quaternary InAsNSb was derived from bandgap models of InAsN and InAsSb, PL and XRD measurements
- the addition of antimony in InAsN was shown to enhance the nitrogen incorporation in InAsNSb
- electroluminescence from InAsNSb diodes at 3.88 μm at 4 K was obtained.

In fact, the growth of InAsN material by nitrogen plasma assisted-molecular beam epitaxy (MBE) is a difficult task. Defects which were identified in InAs are more easily generated in plasma assisted-MBE grown InAsN. Preliminary InAsN samples showed poor structural properties and the weak photoluminescence (PL) originating from strongly localised states quenched at temperature around 80 K. A model was adapted to InAsN to determine the critical thickness. All growths were under the critical thickness to ensure no relaxation occurs. The study of the nitrogen incorporation as a function of the growth parameters revealed that the nitrogen composition is inversely dependent on the growth temperature, the growth rate and the arsenic flux. A kinetic model was adapted to interpret the dependences. The effects of rapid thermal annealing (RTA) on the structural and optical properties of InAsN were investigated and RTA was best performed at 600^{o}C for 30 s. A limited blueshift of the

PL peak position and a reduced dependence of the peak energy with laser excitation power were observed. It was shown that this postgrowth technique had little effect on good quality InAsN material.

It has been demonstrated that high quality InAsN material with nitrogen composition up to 2.5 % can be achieved. The alloy showed good crystalline quality and bright photoluminescence which persisted up to room temperature with a reduced influence of the localised states. Bandgap- and localised state-related transitions were clearly identified and their behaviour with laser excitation power and temperature were clarified : while the bandgap-related transitions are almost independent of the laser excitation power and redshift with temperature, transitions from the localised states blueshift with excitation power and temperature. As for the InAsN bandgap, an explanation of its temperature and nitrogen composition dependences was proposed, based on Varshni's equation and an adapted band anticrossing model.

$InAs_{0.984}N_{0.016}$ suitable for 4.2 μm applications at room temperature was obtained but the properties of the alloy could be improved further by the addition of antimony. InAsNSb showed excellent crystallinity and intense luminescence. The quaternary material can be grown perfectly lattice-matched to InAs. Nitrogen and antimony compositions of the quaternary were determined by a combination of X-ray diffraction measurements and calculation of the InAsNSb bandgap based on Wieder's formula for InAsSb and that presented earlier for InAsN. It was found that antimony enhances the nitrogen incorporation in MBE-grown InAsNSb. $InAs_{0.962}N_{0.009}Sb_{0.029}$ showed improved optical properties at room temperature suitable for CO_2 detection at 4.2 μm. Prototype devices with InAsN and InAsNSb active regions were realised and, despite the need for further optimisation of the doping levels and structure, 4 K electroluminescence was obtained from InAsNSb diodes.

8.2 Suggestions for further work

The main work needed to complete this study lies in the device optimisation. For mid-infrared LEDs, injection, leakage currents and non-radiative recombinations need to be considered. For photodiodes, the thickness of the active region must be chosen for optimised absorption, leakage and dark currents must be reduced as well as the noise to optimise the quantum efficiency and figure of merit $R_0\mathcal{A}$.

More precisely, many growth issues still need to be addressed. Repeatability of the growths is sometimes poor and strongly relies on an accurate temperature measurement. The growth temperature (measuremd indirectly through the reflectivity of the sample surface by a pyrometer) varies according to the actual layer grown and for each substrate holder. The use of an improved measurement of the substrate temperature would increase the repeatability of the temperature-sensitive growth of InAsN. The surface morphology on the nanoscale could still be improved. A better understanding of the nitrogen plasma would help improve InAsN growth. Epitaxial growth with plasma shutter closed may be another effective way to incorporate nitrogen and preserve a smooth surface. As far as the nitrogen plasma is concerned, design considerations on the aperture plate or deviation of ions by application of a bias at the exit of the plasma could help in reducing the amount of species potentially roughening the surface [122, 123]. The stability of the plasma could also be improved further by monitoring the brightness of the plasma mode to increase repeatability and fine tuning of the nitrogen composition. Nitrogen configurations in the alloy could be studied using nuclear reaction analysis (NRA) on the samples already grown to further optimise growth conditions favouring substitutional nitrogen incorporation [95, 139]. Calibrating the EDAX system (with GaN for example) could also help improve the accuracy of the nitrogen composition measured in dilute nitride materials.

The differences in terms of luminescence observed in the numerous InAsN samples raised a few questions. Thick epilayers grown on n-type InAs substrates tend to have a brighter luminescence. Understanding fully the influence on the optical properties of the type of the substrate or the thickness of the epilayer may complete the list of the parameters determining the quality of the InAsN material and devices. The effect of the growth conditions on the depth of the localisation potential are still unknown and a further investigation could help control or suppress the localised states. As far as the nitrogen composition is concerned, being able to determine the nitrogen composition irrespectively of the strain would be of great advantage. To this end, electron probe microanalysis measurements (EPMA) are underway at National Taiwan University (Prof. H.H. Lin) on a set of InAsN samples with various nitrogen compositions to try and measure the nitrogen composition and help deduce the respective strain. This will allow to check the validity of Vegard's law at the same time, namely for InAsN with high nitrogen composition.

The InAsN bandgap dependence on the nitrogen composition has been successfully modelled using the band anticrossing model (BAC) but a few aspects need to be investigated further. The temperature dependence of the BAC was elaborated from four samples at a few temperatures. A systematic study will help in refining the model. Photoreflectance and surface voltage spectroscopy are currently underway at the University of Surrey (Dr T.J.C Hosea) to correlate the dependence of InAsN bandgap with nitrogen composition. Peaks observed below the bandgap energy when nearing room temperature also need to be identified

Wieder's model of the InAsSb bandgap was used to determine the antimony composition in the InAsSb reference sample and InAsNSb epilayers. Nevertheless, differences were observed between antimony compositions obtained through XRD

measurements and this model, hence finding out the reasons why would be useful (material disorder is likely). Despite the many advantages of using InAsNSb material over InAsN, selecting a particular wavelength requires fixing the nitrogen composition and growing a few InAsNSb samples at different As / Sb ratios. A valuable advantage would be the ability to predict the required As / Sb ratio for a particular wavelength and the subsequent nitrogen and antimony compositions at any fixed nitrogen composition *before* growth.

The devices grown at Lancaster and presented in the later section failed to show light emission or photoresponse from the InAsN or InAsNSb active regions. Many factors might be responsible. The absorption coefficient has not been quantitatively reported and its knowledge will help calculate the optimised active region thickness. The residual carrier concentration in early InAsN studies was shown to be very high (~ 1.7×10^{19} cm^{-3} for 2.8 % N) [16]. Its precise determination in the better quality InAsN samples produced later would help in optimising the doping levels for the surrounding barriers. The n and p doping requires better calibration and our Van der Pauw's system could be improved. Moreover, the potential reduction of the leakage current by the choice of an appropriate test sample shape for Hall effect measurements will also increase accuracy [197]. A further improvement would be to implement temperature-varied measurements to access the carrier concentration in InAsN as a function of the temperature. Another parameter to optimise is the thickness of the barriers that controls the achievable electric field within the device [198]. The current thickness of the blocking barrier might not suffice to suppress the current tunnelling.

List of acronyms, abbreviations, symbols and units

Acronyms and abbreviations

3D, 2D, 1D, 0D	three-, two-, one-, zero-dimensional
AFM	atomic force microscopy
BAC	band anti-crossing model
BB	band-to-band
BEP	beam-equivalent pressure
BLIP	background-limited infrared performance
CB	conduction band
CBO	conduction band offset
DAP	donor-acceptor pair
DCXRD	double-crystal X-ray diffraction
DOS	density of states
ECR	electron cyclotron resonance
EDAX	energy-dispersive X-ray spectroscopy
EL	electroluminescence
EPMA	electron probe microanalysis
fcc	face-centred cubic
FE	free exciton
FPA	focal plane array
FTIR	Fourier transform infrared spectroscopy
FWHM	full-width at half-maximum
GSMBE	gas source molecular-beam epitaxy
HBT	heterojunction bipolar transistors
hh	heavy hole band
IPA	isopropanol
IR	infrared
I-V	current-voltage
LE	localised exciton
LED	light-emitting diode
lh	light hole band
LPE	liquid-phase epitaxy
LS	localised state
MBE	molecular-beam epitaxy
MIR	mid-infrared
MOCVD	Metal Organic Chemical Vapour Deposition
MOVPE	Metal Organic Vapour Phase Epitaxy
MQW	multiple quantum wells
NEP	noise equivalent power
NRA	nuclear reaction analysis
OI	optically immersed
PAMBE	plasma-assisted molecular-beam epitaxy
PC	photoconductor
PD	photodiode
PL	photoluminescence
PV	photovoltaic

QD	quantum dots
QDIP	quantum dot infrared photodetector
QW	quantum wells
QWIP	quantum well infrared photodetector
$R_0\mathcal{A}$	zero-bias resistance area product
RF	radio frequency
RF-MBE	radio frequency molecular-beam epitaxy
RHEED	Reflection High-Energy Electron Diffraction
rms	root-mean square
RT	room-temperature
RTA	rapid thermal annealing
SEM	scanning electron microscope
SIMS	secondary ion mass spectroscopy
so	spin-orbit split-off band
SQW	single quantum well
SRH	Shockley-Read-Hall
SSMBE	Solid Source molecular-beam epitaxy
TE	thermo-electric
ud	undoped
UV	ultra-violet
VB	valence band
VBO	valence band offset
VBM	valence band minimum
VCSEL	vertical-cavity surface-emitting laser
XRD	X-ray diffraction

Main symbols

As_{min}	minimum arsenic flux
D^*	specific detectivity
$\Delta E_{PL(P)}$	energy shift with increasing laser excitation power
E_0	characteristic energy of the bandtail
E_g	bandgap energy
E_{PL}	PL energy
η	quantum efficiency
g.r.	growth rate
h_c	critical thickness
k	exponent in equation (5.3)
k_B	Boltzmann constant
λ	wavelength
m_0	free electron mass
T	temperature
T_g	growth temperature
T_{pyro}	temperature given by the pyrometer
T_{sub}	setpoint temperature

Units

A	amp
Å	Angström
arc sec	arc second
a.u.	arbitrary units
^{o}C	degree centrigrade
eV	electron-volt
Hz	hertz
K	Kelvin
L	litre
mbar	millibar
meV/at. % N	meV per atomic percent of nitrogen
min	minute
ML	monolayer
µm/h	micron per hour
Ω	ohm
s	second
sccm	standard cubic centimetre
V	volt
W	watt

Appendix – Conference presentations, articles and collaborations

Conference presentations

MBE grown InAsSb/InAs multi-quantum wells for mid-infrared optoelectronics
Q.D. ZHUANG, A. GODENIR, M. STONE, A. KRIER, G. TSAI, H.H. LIN
III-V Facility Centre Users' day, poster, Sheffield June 2005

Dilute nitride-based photodetectors for gas sensing grown by molecular beam epitaxy
A. GODENIR, Q. ZHUANG, A. KRIER, M. HOPKINSON
Physics Research and the new Parliament, SET for Britain poster competition, Houses of Parliament, London November 2005

Effects of rapid thermal annealing on InAsN alloys grown by molecular beam epitaxy
A. GODENIR, Q. ZHUANG, A. KRIER, M. HOPKINSON, R. AIREY
UK Compound Semiconductor Conference, oral presentation, Sheffield July 2006

Mid-infrared photoluminescence and rapid thermal annealing of bulk InAsN grown by molecular beam epitaxy
A. GODENIR, Q. ZHUANG, A. KRIER, M. HOPKINSON, R. AIREY, G. HILL
MIOMD-VIII International conference, poster, Bad Ischl (Austria) May 2007

Dilute nitride of InAsN - MBE growth and characterization
Q. ZHUANG, A. GODENIR, A. KRIER
MIOMD-VIII International conference, oral presentation, Bad Ischl (Austria) May 2007

Published articles

Room temperature photoluminescence at 4.5 μm from InAsN
Q. ZHUANG, A.M.R. GODENIR, A. KRIER, K.T. LAI, S.K. HAYWOOD
Journal of Applied Physics 103, 063520-1 - 063520-4 (2008)

Photoluminescence in InAsN epilayers grown by molecular beam epitaxy
Q. ZHUANG, A. GODENIR, A. KRIER
Journal of Physics D : Applied Physics 41, 132002-1 - 132002-4 (2008)

Draft articles

Low-temperature photoluminescence and postgrowth rapid thermal annealing of bulk InAsN grown by molecular beam epitaxy
A.M.R. GODENIR, Q.D. ZHUANG, A. KRIER, R. AIREY, G. HILL, M. HOPKINSON

Credits in articles

Mid-infrared electroluminescence at room temperature from InAsSb multiquantum-well light-emitting diodes
A. KRIER, M. STONE, Q.D. ZHUANG, P.W. LIU, G. TSAI, H.H. LIN, Applied Physics Letters volume 89, 091110-1 - 091110-3 (2006)

Group seminars

Towards MBE-grown InAs:N-based devices
A. GODENIR, Q. ZHUANG, A. KRIER
oral presentation for visitors from Taiwan University, Lancaster May 2005

Molecular beam epitaxy-grown dilute nitride-based devices
A. GODENIR, Q. ZHUANG, A. KRIER
oral presentation, Lancaster July 2005
oral presentation at National Taiwan University, Taipei (Taiwan, ROC) July 2005

Optical properties of $InAs_{1-x}Sb_x$/InAs MQW grown by MBE
A. KRIER, M. STONE, A.GODENIR
International Review of Physics and Astronomy, poster, Lancaster October 2005

Mid-infrared lasers based on dilute nitrides
A. KRIER, Q.D. ZHUANG, A. GODENIR, M. STONE, G. TSAI, H.H. LIN
International Review of Physics and Astronomy, poster, Lancaster October 2005

Recent studies in InAsN and InAsSb/InAs multi quantum wells grown by molecular beam epitaxy
A. GODENIR, M. STONE, Q. ZHUANG, A. KRIER
oral presentation for visitors from Taiwan University, Lancaster October 2005

Being a scientist - Doing a PhD in Physics at Lancaster University
A. GODENIR
oral presentation, Lancaster Central High School November 2005

Nanostructures for optoelectronic devices grown using molecular beam epitaxy
M. STONE, Q. ZHUANG, A. GODENIR, R. JONES, A. KRIER
Faculty of Science and Technology Christmas conference, poster competition (runner-up prize), Lancaster December 2005

MBE-grown InAsN : basics, current study and growth perspectives
A. GODENIR, Q. ZHUANG, A. KRIER
oral presentation, Lancaster May 2006

Effects of rapid thermal annealing on InAsN alloys grown by molecular beam epitaxy
A. GODENIR, Q. ZHUANG, A. KRIER, M. HOPKINSON, R. AIREY
oral presentation, Lancaster May 2006

oral presentation, Lancaster July 2006

MBE-grown dilute nitrides - from InAsN to InAsSbN
A. GODENIR, Q. ZHUANG, A. KRIER
oral presentation for visitors from INSA Rennes, Lancaster December 2006

InAsN - A novel dilute nitride-based semiconductor material for mid-infrared operation
A. GODENIR, Q. ZHUANG, A. KRIER, A. HAMMICHE
oral presentation, Lancaster June 2007

Collaborations

National Taiwan University, Taipei (Taiwan, ROC)
Prof. H.H. Lin, Dr. J. Tsai, D.J. Ma, L.C. Tsou. Y.R. Lin

Centre for Nanoscience and Technology, University of Sheffield
Dr. R.J. Airey, Prof. M. Hopkinson, Dr. G. Hill

Advanced Technology Institute, University of Surrey
Dr. T.J.C. Hosea

Department of Engineering, University of Hull
Dr. K.T. Lai, Dr. S.K. Haywood

Department of Physics, University of Warwick
Dr. T. Veal

Appendix I – Critical thickness

Matlab 6.5(c) routine for the calculation of the critical thickness, developed by A. Godenir

```
function y=critical_thickness3(x_min,increment,x_max)

%based on eq. (9a) in "Calculation of critical layer thickness versus lattice mismatch
%for Ge(x)Si(1-x)/Si strained-layer heterostructures, R.PEOPLE, J.C.BEAN,
%Appl. Phys. Letters 47(3), 1 August 1985

%VARIABLES :
%x_min, x_max integer 0<.<1 of N composition in InAsN
%increment is obviously the step between x_min and x_max
%RESULTS :
%a matrix in which each row contains x, 1/A, f, hc
%respectively Nitrogen composition, 1/A, misfit and critical thickness
%resulting hc is given in the metric system

%NB : this calculus is not possible for x=[N]>=0.3

%eq.(9a) similar to hc=(b/A(x))*ln(hc/b), written as
%1/A(x) = ln u / u, where u = hc/b
%ValueOfA calculates the parameter A value for the critical thickness in
%the above equation

x0 = x_min;
inc = increment;
z = x_max;
nmax = (z-x0)/inc+1; %number of iterations of the loop
b = 4e-10; %"slip distance"

for n = 0:nmax
        x = x0+inc*n;
        % -- Poisson coefficient of InAsN --
        nu_InN = 0.387; %from Bede RADS
        nu_InAs = 0.352; %from Bede RADS
        nu = x*nu_InN+(1-x)*nu_InAs;

        % -- InAsN lattice parameter --
        %a_InN_cubic=4.98e-10
        %a_InAs=6.0583e-10
        %a=x*InN_cubic+(1-x)*a_InAs
        a = (6.0583-1.0783*x)*1e-10;

        % -- Misfit f --
        %is indeed the lattice mismatch
        a_InAs = 6.0583e-10;
        f = abs((a-a_InAs)/a_InAs);

        % -- ValueOfA --
        A=(1/b)*((1-nu)/(1+nu))*(1/(16*pi*sqrt(2)))*(b^2/a)*(1/(f^2));
        invA=1/A;

        % -- estimation of the vicinity of the solution, required to use fzero --
        jj=0;
        while log(exp(1)*10^jj)/(exp(1)*10^jj)>invA
```

```
            jj=jj+1;
        end
        point=(10^(jj-1)+10^jj)*exp(1)/2;

        func=['log(x)/x-',num2str(invA)];
        %ln(u)/u decreases from e to infinite
        y1=b*fzero(inline(func),point);
        y(n+1,1)=x;
        y(n+1,2)=invA;
        y(n+1,3)=f;
        y(n+1,4)=y1;
end

['x 1/A f  hc : headers of the columns']
['NB : open the variable "ans" in the Workspace to visualise the result because the display of a
matrix is limited to four digits']

%NB : this calculus is not possible for x=[N]>=.3
%NB2 (very important) : the display of a matrix is limited to 4 digits ; open the variable "ans"
%from the Workspace to visualise the result
```

Appendix II – Hall effect

a. Resistivity

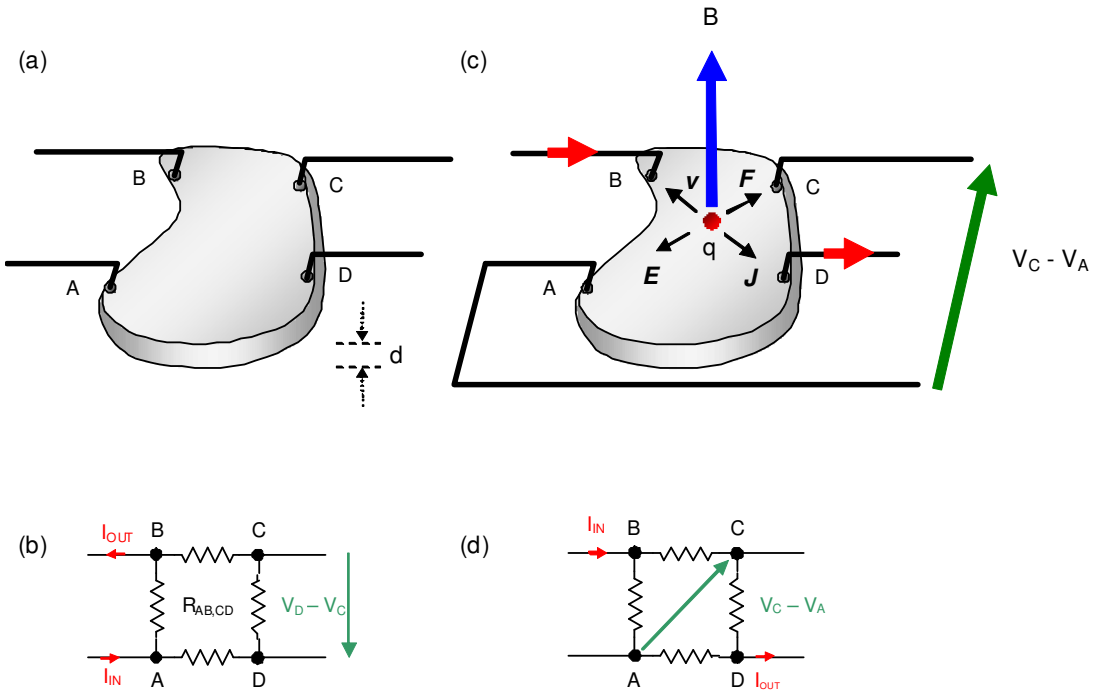

Figure 1 (a) Layer of arbitrary shape with point contacts for the measure of the resistivity ; (b) Electronic sketch of the quadrupole *ABCD* ; (c) Hall effect on an n-type sample in a magnetic field ; (d) Electronic sketch of the quadrupole *ABCD* under consideration

The resistivity ρ of a sheet of conducting material with thickness d can be measured from the potential drop between two contact points C and D when a current is driven through A to B, as illustrated in Figure 1 (a). Under the assumption of a flat, solid, uniformly doped lamella, the resistance values of the quadrupole *ABCD* are linked by the Van der Pauw theorem [131, 132] :

$$\exp\left(\frac{-\pi R_{AB,CD}\, d}{\rho}\right) + \exp\left(\frac{-\pi R_{BC,DA}\, d}{\rho}\right) = 1 \qquad (1)$$

where $R_{ij,kl}$ is the quadrupole resistance with current entering at i and exiting the sample at j and voltage taken as the difference of potential between k and l as shown in Figure 1 (b). The resistivity can be derived as :

$$\rho = \frac{\pi d}{\ln 2}\left(\frac{R_{AB,CD} + R_{BC,DA}}{2}\right) f\left(\frac{R_{AB,CD}}{R_{BC,DA}}\right) \qquad (2)$$

where f verifies the relation :

$$\frac{R_{AB,CD} - R_{BC,DA}}{R_{AB,CD} + R_{BC,DA}} = f \arccos h\left(\frac{1}{2}\exp\left(\frac{\ln 2}{f}\right)\right) \qquad (3)$$

Under the assumption of a symmetrical sample such as a square, a circle, a four-leaf clover shape, $f = 1$. Hence, the resistivity can be written as :

$$\rho = \frac{\pi d}{\ln 2}\frac{\Sigma R}{2} \qquad (4)$$

where $\Sigma R = R_{AB,CD} + R_{BC,DA}$.

b. Hall mobility

For n-type semiconductors, Hall effect measurements are based on the effect of the Lorentz force exerted on charge particles (electrons for n-type material) moving with speed $\boldsymbol{v}$ in a magnetic field $\boldsymbol{B}$ normal to the surface as shown in Figure 1 (c). In equilibrium, a force due to an internal electric field $\boldsymbol{E}$ balances the Lorentz force so that the net force $\boldsymbol{F}$ is null :

$$\boldsymbol{F} = -q\left(\boldsymbol{E} + \boldsymbol{v} \wedge \boldsymbol{B}\right) \qquad (5)$$

where q is the electron charge. When a current, with current density $\boldsymbol{J}$, passes diagonally across the sample, the change in quadrupole resistance $R_{BD,AC}$ (as shown in Figure 1 (d)) when a magnetic field is applied can be used to calculate the Hall mobility μ_H. Indeed, the Hall field $E_{H,y}$ is by definition [199] :

$$E_{H,y} = R_H J_x B_z \qquad (6)$$

where R_H is the Hall coefficient. Given that the current density of electrons flowing with carrier velocity v_x verifies :

$$J_x = -n\,q\,v_x \qquad (7)$$

the Hall coefficient can simply be expressed as :

$$R_H = -\frac{1}{n\,q} \qquad (8)$$

The Hall mobility is defined as [200] :

$$\mu_H = abs(R_H\sigma) = abs\left(\frac{R_H}{\rho}\right) \qquad (9)$$

where σ is the conductivity of the material. Given that :

$$J_x = \frac{dI}{dy\,dz} \qquad (10)$$

$$E_{H,y} = -\frac{dV_H}{dy} \qquad (11)$$

where dI is the difference of current and dV_H the difference of potential across the sample, the Hall mobility can be derived by combining equations (6), (9), (10) and (11) as :

$$\mu_H = \frac{dz}{B_z\rho}abs\left(\frac{dV_H}{dI}\right) \qquad (12)$$

where $\frac{dV_H}{dI}$ is difference of resistance when the magnetic field is applied or not, hence :

$$\mu_H = \frac{d}{B}\frac{\Delta R}{\rho} \qquad (13)$$

where $d = dz$, B is the magnetic field, $\Delta R = R_{BD,AC(\boldsymbol{B=1})} - R_{BD,AC(\boldsymbol{B=0})}$, ***B=1*** or ***B=0*** when the magnetic field is applied or not respectively.

From equations (4) and (13), it is easy to demonstrate that the Hall mobility is independent of the thickness :

$$\mu_H = \frac{d\,\Delta R}{B\,\rho} = \frac{2\ln 2}{\pi B}\frac{\Delta R}{\Sigma R} \qquad (14)$$

c. Petritz's double layer model

A single layer model was initially proposed where Hall parameters were calculated using d as the thickness of the whole sample (epilayer and substrate). This is not a valid approach, moreover when the substrate is semi-insulating as is used for doping calibrations.

For an inhomogeneous sample such as one made of an epilayer grown on a substrate, parameters measured by the Van der Pauw's method must reflect the interaction in the two layers as proposed by Petritz [133]. For a magnetic field perpendicular to the surface of the sample, the conductivity σ is derived as :

$$\sigma = \frac{\sigma_{sub} d_{sub} + \sigma_{epi} d_{epi}}{d_{epi} + d_{sub}} \qquad (15)$$

where σ_i and d_i are the conductivity and the thickness of the substrate ($i = sub$) and the epilayer ($i = epi$). Therefore, the resistivity of the epilayer ρ_{epi} can be derived from the resistivity ρ of the sample measured by Van der Pauw's method as :

$$\rho_{epi} = \frac{d_{epi}}{\dfrac{d_{epi} + d_{sub}}{\rho} - \dfrac{d_{sub}}{\rho_{sub}}} \qquad (16)$$

The Hall coefficient R_H of the whole sample is derived as [133] :

$$R_H = \frac{\left(d_{sub} + d_{epi}\right)\left(R_{H\,sub}\sigma_{sub}^{\,2} d_{sub} + R_{H\,epi}\sigma_{epi}^{\,2} d_{epi}\right)}{\left(\sigma_{sub} d_{sub} + \sigma_{epi} d_{epi}\right)^2} \qquad (17)$$

where $R_{H\,sub}$ and $R_{H\,epi}$ are the Hall coefficients of substrate and epilayer respectively. Using (9) for R_H, $R_{H\,sub}$ and $R_{H\,epi}$, the Hall mobility of the epilayer $\mu_{H\,epi}$ can be derived as :

$$\mu_{H\,epi} = \mu_H \left(1 + \frac{\rho_{epi} d_{sub}}{\rho_{sub} d_{epi}}\right) - \mu_{sub} \frac{\rho_{epi} d_{sub}}{\rho_{sub} d_{epi}} \qquad (18)$$

The resistivity of a semi-insulating substrate is extremely high (10^7 Ω.cm and higher), therefore the following approximations can be considered :

$$\rho_{sub} \to \infty \text{ , hence } \mu_{H\,sub} \to 0$$

Resistivity and Hall mobility of the epilayer can be approximated as :

$$\rho_{epi} \sim \rho \frac{d_{epi}}{d_{epi} + d_{sub}} \qquad (19)$$

$$\mu_{H\,epi} \sim \mu_H \qquad (20)$$

Equations (19) and (20) are used for the computations of resistivity Hall mobility and carrier concentration of the epilayer.

d. Corresponding resistances

	I_{IN}	I_{OUT}	V_-	V_+			R_{eq}
$R_{AB,CD}$	A	B	C	D	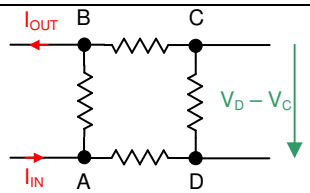	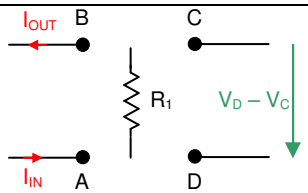	R_1
$R_{AC,BD}$	A	C	B	D	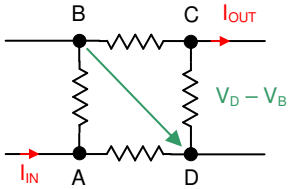	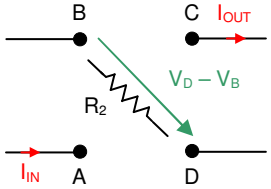	R_2
$R_{AD,CB}$	A	D	C	B	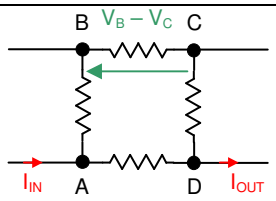	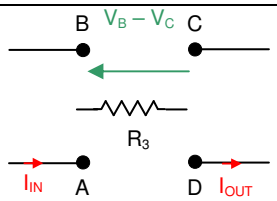	R_3

$R_{CB,AD}$	C	B	A	D	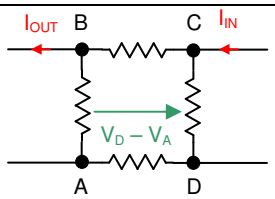	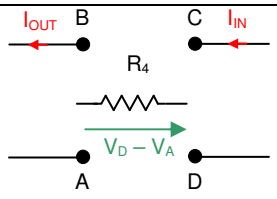	R_4
$R_{DC,BA}$	D	C	B	A	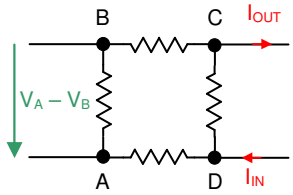	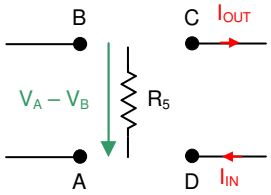	R_5
$R_{DB,CA}$	D	B	C	A	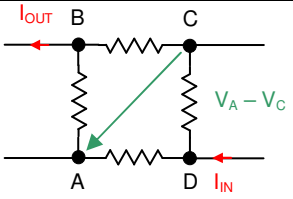	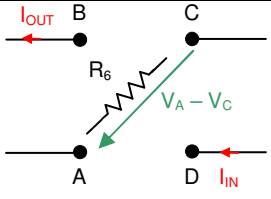	R_6

According to the electrical sketches, we can easily find that :

$$R_{BD,AC} = R_{DB,CA} = R_6 \qquad (21)$$

$$R_2 = -R_6 \qquad (22)$$

Practically, one can write R_1 as a corresponding resistance to $R_{AB,CD}$, as shown in Figure 1 (c), and R'_1 when a magnetic field is applied perpendicular to the surface of the sample. Moreover, the switch box allows six combinations of current and voltage configurations, hence there are six corresponding resistances (R_1, …, R_6) that can be used for averaging. Thus, ΣR and ΔR can be written as :

$$\Sigma R = \frac{R_1 + R_5}{2} + \frac{R_3 + R_4}{2} \qquad (23)$$

$$\Delta R = \frac{R_6 - R_2}{2} - \frac{R'_6 - R'_2}{2} \qquad (24)$$

Combining equation (4) with (23), the resistivity ρ (in Ω.cm) can be derived as :

$$\rho = \frac{\pi}{4.\ln 2} \frac{d_{\mu m}}{10^4} (R_1 + R_3 + R_4 + R_5) \qquad (25)$$

with $d_{\mu m}$ the sample thickness (in μm), R_i the corresponding resistances (in Ω). By combination of equations (13) with (24), the Hall mobility μ_H (in $cm^2V^{-1}s^{-1}$) can be derived as :

$$\mu_H = \frac{d_{\mu m}}{B} \frac{R'_2 - R_2 + R_6 - R'_6}{\rho} \qquad (26)$$

where B is the magnetic field (in T), R_i and R'_i the corresponding resistances (in Ω) without and with applied magnetic field respectively, and ρ the resistivity (in Ω.cm).

Settings for Digital Channel 21 (relay switchbox)

7706 setting	***Digital channel O/P***	I_{IN}	I_{OUT}	V_+	V_-	B_{ON}	B_{OFF}
000	00000000	1	2	3	4	R'_1 (Ω)	R_1 (Ω)
056	00111000	1	3	2	4	R'_2 (Ω)	R_2 (Ω)
035	00100011	1	4	3	2	R'_3 (Ω)	R_3 (Ω)
140	10001100	3	2	1	4	R'_4 (Ω)	R_4 (Ω)
122	01111010	4	3	2	1	R'_5 (Ω)	R_5 (Ω)
066	01000010	4	2	3	1	R'_6 (Ω)	R_6 (Ω)
						T'(°C)	T (°C)
						ΔT'(°C)	ΔT (°C)

Columns B_{ON} and B_{OFF} are the data generated in the output file. T and ΔT are the temperature and variation of the temperature during the measurement respectively.

e. Conditions to be verified

Two conditions must be satisfied to assure the validity of the measured values. The magnetic field must not be too great for the semiconductor under study :

$$\omega_c \tau < 1 \qquad (27)$$

where ω_c is the cyclotron frequency, τ the relaxation time [134]. Cyclotron frequency and relaxation time follow :

$$\omega_c \equiv \frac{qB}{m^*} \qquad (28)$$

$$\tau \approx \frac{m^* \mu}{q} \qquad (29)$$

where m^* is the carrier effective mass. The first condition can be expressed as :

$$\frac{B\mu}{10^4} < 1 \qquad (30)$$

where B is the magnetic field (in T) and μ the mobility (in $cm^2V^{-1}s^{-1}$).

The thermal energy of the system must be greater than the energy of the electron in its shell :

$$kT >> \hbar\omega_c \qquad (31)$$

where $\hbar = \frac{h}{2\pi}$, h being Planck constant. The second condition can be expressed as :

$$kT >> \frac{hqB}{2\pi m^*} \qquad (32)$$

Index of figures and tables

Index of figures

Index of tables

References of papers

[1] ***Toward innovations of gas sensor technology***, N. YAMAZOE, Sensors and Actuators B 108, 2-14 (2005)

[2] ***Mid-infrared Electroluminescence in LEDs based on InAs and related alloys***, A. KRIER, X.L. HUANG, V.V. SHERSTNEV, in Mid-infrared Semiconductor Optoelectronics, ed. A. Krier, Springer Series in Optical Sciences (2006)

[3] Combustible Gas Safety Monitoring: Infrared vs. Catalytic Gas Detectors, www.generalmonitors.com/downloads/white_papers/IR_VS_CATALYTIC.PDF

[4] Chapter 6. Types of semiconductors, in *Semiconductor materials, an introduction to Basic Principles*, B.G. YACOBI, Kluwer Academic/Plenum Publishers, New York (2003)

[5] http://www.dayah.com/periodic/

[6] *Physics of semiconductor devices*, second edition, S.M. SZE, Wiley-Interscience publication, New York (1981)
[6a] Chapter 1. Physics and properties of semiconductors - A résumé
[6b] Chapter 13. Photodetectors
[6c] Appendix F. Lattice constants

[7] ***GaN, AlN, and InN : A review***, S. STRITE H. MORKOÇ, Journal of Vacuum Science & Technology B volume 10 issue 4, 1237-1266 (1992)

[8] ***Handbook series on Semiconductor parameters***, M. LEVINSHTEIN, S. RUMYANTSEV, M. SHUR (ed.), volume1, 147-168 (1996)

[9] *Optoelectronic semiconductor devices*, D. WOOD, Prentice Hall (1994)
[9a] Chapter 1. Basics
[9b] Chapter 6. PIN diodes

[10] *Physical foundations of solid-state devices*, E.F. SCHUBERT, Rensselaer Polytechnic Institute textbook, Troy New York (2005)
[10a] Chapter 12. Density of states
[10b] Chapter 16. High doping effects

[11] ***Band-to-band Auger effect in long wavelength multinary III-V alloy semiconductor lasers***, A. SUGIMURA, IEEE Journal of Quantum Electronics, volume 18 issue 3, 352- 363 (1982)

[12] ***Photoluminescence of InSb, InAs, and InAsSb grown by organometallic vapour phase epitaxy***, Z.M. FANG, K.Y. MA, D.H. JAW, R.M. COHEN, G.B. STRINGFELLOW, Journal of Applied Physics volume 67 number 11, 7034-7039 (1990)

[13] ***Temperature dependence of the energy gap in semiconductors***, Y.P. VARSHNI, Physica volume 34 issue 1, 149-154 (1967)

[14] ***Strain enhancement during annealing of GaAsN alloys***, Q.D. ZHUANG, A. KRIER, C.R. STANLEY, Journal of Applied Physics volume 101, 103536-1 - 103536-4 (2007)

[15] ***Band Anticrossing in III-N-V alloys***, W. SHAN, W. WALUKIEWICZ, K.M. YU, J.W. AGER III, E.E. HALLER, J.F. GEISZ, D.J. FRIEDMAN, J.M. OLSON, S.R. KURTZ, H.P. XIN, C.W. TU, Physica Status Solidi (b) 223, 75-85 (2001)

[16] ***Band gap reduction in InAsN alloys***, D.K. SHIH, H.H. LIN, L.W. SUNG, T.Y. CHU, T.R. YANG, Japanese Journal of Applied Physics volume 42, 375-383 (2003)

[17] ***Band Anticrossing in GaInNAs Alloys***, W. SHAN, W. WALUKIEWICZ, J.W. AGER III, E.E. HALLER, J.F. GEISZ, D.J. FRIEDMAN, J.M. OLSON, S.R. KURTZ, Physical Review Letters volume 82 number 6, 1221-1224 (1999)

[18] ***Band parameters for nitrogen-containing semiconductors***, I. VURGAFTMAN, J.R. MEYER, Journal of Applied Physics volume 94 number 6, 3675-3696 (2003)

[19] ***Electronic Properties of Ga(In)NAs Alloys***, I.A. BUYANOVA, W.M. CHEN, B. MONEMAR, MRS Internet Journal Nitride Semiconductor Research volume 6 number 2, 1-19 (2001)

[20] ***Band structure of highly mismatched semiconductor alloys: Coherent potential approximation***, J. WU, W. WALUKIEWICZ, E.E. HALLER, Physical Review B volume 65, 233210-1 - 233210-4 (2002)

[21] ***A temperature dependent model for the saturation velocity in semiconductor materials***, R. QUAY, C. MOGLESTUE, V. PALANKOVSKI, S. SELBERHERR, Materials Science in Semiconductor Processing 3, 149-155 (2000)

[22] ***Analysis and simulation of a mid-infrared P^+-$InAs_{0.55}Sb_{0.15}P_{0.30}$/$n^0$-$InAs_{0.89}Sb_{0.11}$/$N^+$-$InAs_{0.55}Sb_{0.15}P_{0.30}$ double heterojunction photodetector grown by LPE***, P. CHAKRABARTI, A. KRIER, A.F. MORGAN, IEEE Transactions on electron devices volume 50 number 10, 2049-2058 (2003)

[23] ***Band parameters for III-V compound semiconductors and their alloys***, I. VURGAFTMAN, J.R. MEYER, L.R. RAM-MOHAN, Journal of Applied Physics volume 89 number 11, 5849 (2001)

[24] ***Calculation of critical layer thickness versus lattice mismatch for Ge_xSi_{1-x}/Si strained-layer heterostructures***, R. PEOPLE, J.C. BEAN, Applied Physics Letters 47(3), 322-324 (1985)

[25] ***Dominating nucleation of misfit dislocations from the surface in GeSi/Si(0 0 1) films with a stepwise composition grown by means of molecular-beam epitaxy***, Yu.B. BOLKHOVITYANOV, A.S. DERYABIN, A.K. GUTAKOVSKII, M.A. REVENKO, L.V. SOKOLOV, Journal of Crystal Growth 293, 247-252 (2006)

[26] ***Infrared detectors : an overview***, A. ROGALSKI, Infrared Physics and Technology 43, 187-210 (2002)

[27] http://www.judsontechnologies.com/

[28] http://www.rsc.rockwell.com/infrared_sensors/index.html

[29] http://www.vigo.com.pl/index.php/en

[30] ***High-Speed InSb Photodetectors on GaAs for Mid-IR Applications***, I. KIMUKIN, N. BIYIKLI, T. KARTALOĞLU, O. AYTÜR, E. OZBAY, IEEE Journal of selected topics in quantum electronics volume 10 number 4, 766-770 (2004)

[31] ***Room-temperature $InAs_{0.89}Sb_{0.11}$ photodetectors for CO detection at 4.6 µm***, H.H. GAO, A. KRIER, V.V. SHERSTNEV, Applied Physics Letters volume 77 number 6, 872-874 (2000)

[32] ***Uncooled photodetectors for the 3-5 µm spectral range based on III-V heterojunctions***, A. KRIER, W. SULEIMAN, Applied Physics Letters volume 89, 083512-1 - 083512-3 (2006)

[33] ***Room temperature InAsSb photovoltaic midinfrared detector***, A. RAKOVSKA, V. BERGER, X. MARCADET, B. VINTER, G. GLASTRE, T. OKSENHENDLER, D. KAPLAN, Applied Physics Letters volume 77 number 3 (2000), 397-399

[34] ***Strategy for the design of a non-cryogenic quantum infrared detector***, G. MARRE, B. VINTER, V. BERGER, Semiconductor Science and Technology 18, 284-291 (2003)

[35] ***Quantum well photoconductors in infrared detector technology***, A. ROGALSKI, Journal of Applied Physics volume 93 number 8, 4355-4391 (2003)

[36] ***Quantum dot infrared photodetectors***, H.C. LIU, J.Y. DUBOZ, R. DUDEK, Z.R. WASILEWSKI, S. FAFARD, P. FINNIE, Physica E volume 17, 631 – 633 (2003)

[37] ***Strain compensated InGaAs/InGaP quantum well infrared detector for midwavelength band detection***, S. MAIMON, G.M. COHEN, E. FINKMAN, G. BAHIR, D. RITTER, S.E. SCHACHAM, Applied Physics Letters volume 73 number 6, 800-802 (1998)

[38] ***1024 × 1024 pixel mid-wavelength and long-wavelength infrared QWIP focal plane arrays for imaging applications***, S.D. GUNAPALA, S.V. BANDARA, J.K. LIU, C.J. HILL, S.B. RAFOL, J.M. MUMOLO, J.T. TRINH, M.Z. TIDROW, P.D. LEVAN, Semiconductor Science and Technology 20, 473-480 (2005)

[39] ***Quantum-well infrared photodetectors***, B.F. LEVINE, Journal of Applied Physics volume 74 number 8, R1-R81 (1993)

[40] ***High-detectivity, normal-incidence, mid-infrared (~4 μm)InAs/GaAs quantum-dot detector operating at 150 K***, A.D. STIFF, S. KRISHNA, P. BHATTACHARYA, S. KENNERLY, Applied Physics Letters 79, 421 (2001)

[41] ***Quantum dot infrared photodetectors***, H.C. LIU, M. GAO, J. McCAFFREY, Z.R. WASILEWSKI, S. FAFARD, Applied Physics Letters volume 78 number 1, 79-81 (2001)

[42] ***GaInNAs/GaAs multiple quantum wells grown by gas-source molecular beam epitaxy***, H.P. XIN, C.W. TU, Applied Physics Letters volume 72 number 19, 2442-2444 (1998)

[43] ***Optimization of InAsSb photodetector for non-cryogenic operation in the mid-infrared range***, H. AÏT-KACI, J. NIETO, J.B. RODRIGUEZ, P. GRECH, F. CHEVRIER, A. SALESSE, A. JOULLIÉ, P. CHRISTOL, Physica Status Solidi (a) volume 202 number 4, 647-651 (2005)

[44] ***Passivation of type II InAs/GaSb superlattice photodiodes***, A. GIN, Y. WEI, J. BAE, A. HOOD, J. NAH, M. RAZEGHI, Thin Solid Films 447–448, 489–492 (2004)

[45] ***Uncooled long wavelength infrared photon detectors***, J. PIOTROWSKI, A. ROGALSKI, Infrared Physics & Technology 46, 115-131 (2004)

[46] *Study of Indium Tin Oxide (ITO) for Novel Optoelectronic Devices*, S.A. BASHAR, doctoral thesis, King's College London, University of London (1998), http://www.betelco.com/sb/phd/index.html

[47] Review of Crystal, Thin-Film, and Nanostructure Growth Technologies, Chapter 2 in *Semiconductor Nanostructures for Optoelectronic applications*, Ed. Todd Steiner, Semiconductor Materials and devices series, Artech House, Boston (2004)

[48] ***Interface electroluminescence from InAs quantum well LEDs grown by rapid slider liquid phase epitaxy***, A. KRIER, V.V. SHERSTNEV, Z. LABADI, S.E. KRIER, H.H. GAO, Journal of Physics D: Applied Physics 33, 3156-3160 (2000)

[49] ***Midinfrared photoluminescence of InAsSb quantum dots grown by liquid phase epitaxy***, A. KRIER, X.L. HUANG, A. HAMMICHE, Applied Physics Letters volume 77 number 23, 3791-3793 (2000)

[50] *Growth and characterisation of Semiconductors*, ed. R.A. STRADLING, P.C. KLIPSTEIN, Adam Hilger & IOP Publishing (1990)
[50a] Chapter ***Metal organic chemical vapour deposition (MOCVD) for the preparation of semiconductor materials and devices***, J.O. WILLIAMS

[50b] Chapter ***Growth of thin films and heterostructures of III-V compounds by molecular beam epitaxy***, C.T. FOXON, B.A. JOYCE

[51] ***Molecular beam epitaxy of GaNAs and GaInNAs***, M. KONDOW, T. KITATANI, Semiconductor Science and Technology 17, 746-754 (2002)

[52] ***Current status of research and development of III-N-V semiconductor alloys***, J.W. AGER III, W. WALUKIEWICZ, Semiconductor Science and Technology 17, 741-745 (2002)

[53] ***MBE growth and photoreflectance study of GaAsN alloy films grown on GaAs (0 0 1)***, A. NISHIKAWA, R. KATAYAMA, K. ONABE, Y. SHIRAKI, Journal of Crystal Growth 251, 427-431 (2003)

[54] ***Band gap reduction in GaNSb alloys due to the anion mismatch***, T.D. VEAL, L.F.J. PIPER, S. JOLLANDS, B.R. BENNETT,P.H. JEFFERSON, P.A. THOMAS, C.F. McCONVILLE, B.N. MURDIN, L. BUCKLE, G.W. SMITH, T. ASHLEY, Applied Physics Letters volume 87, 132101-1 - 132101-3 (2005)

[55] ***Luminescence of as-grown and thermally annealed GaAsN/GaAs***, S. FRANCOEUR, G. SIVARAMAN, Y. QIU, S. NIKISHIN, H. TEMKIN, Applied Physics Letters volume 72 number 15, (1998)

[56] ***Pseudopotential theory of dilute III-V nitrides***, P.R.C. KENT, L. BELLAICHE, A. ZUNGER, Semiconductor Science and Technology 17, 851-859 (2002)

[57] ***GaInNAs long-wavelength lasers : progress and challenges***, J.S. HARRIS JR, Semiconductor Science and Technology 17, 880-891 (2002)

[58] ***Experimental studies of the conduction-band structure of GaInNAs alloys***, C. SKIERBISZEWSKI, Semiconductor Science and Technology 17, 803-814 (2002)

[59] ***Conduction band offset and electron effective mass in GaInNAs/GaAs quantum-well structures with low nitrogen concentration***, Z. PAN, L.H. LI, Y. W. LIN, B.Q. SUN, D.S. JIANG, W.K. GE, Applied Physics Letters volume 78 number 15, 2217-2219 (2001)

[60] ***Band anticrossing in highly mismatched III-V semiconductor alloys***, J. WU, W. SHAN, W. WALUKIEWICZ, Semiconductor Science and Technology 17, 860-869 (2002)

[61] ***Growth and characterization of InAsN alloy films and quantum wells***, M. KURODA, A. NISHIKAWA, R. KATAYAMA, K. ONABE, Journal of Crystal Growth 278, 254-258 (2005)

[62] ***Tight-binding and k·p models for the electronic structure of Ga(In)NAs and related alloys***, E.P. O'REILLY, A LINDSAY, S TOMIC, M. KAMAL-SAADI, Semiconductor Science and Technology 17, 870-879 (2002)

[63] ***Derivation of a 10-band k.p model for dilute nitride semiconductors***, A. LINDSAY, S. TOMIC, E.P. O'REILLY, Solid-State Electronics 47, 443-446 (2003)

[64] ***Development of InGaAsN-based 1.3 μm VCSELs***, H. RIECHERT, A. RAMAKRISHNAN, G. STEINLE, Semiconductor Science and Technology volume 17, 892-897 (2002)

[65] ***Solubility of nitrogen in binary III-V systems***, I.H. HO, G.B. STRINGFELLOW, Journal of Crystal Growth 178, 1-7 (1997)

[66] ***MOCVD growth of InN_xAs_{1-x} on GaAs using dimethylhydrazine,*** A.A. EL-EMAWY, H.J. CAO, E. ZHMAYEV, J.H. LEE, D. ZUBIA, M. OSIŃSKI, Physica Status Solidi (b) 228 number 1, 263-267 (2001)

[67] ***InAsN - a new optoelectronic material for mid-infrared applications***, M. OSIŃSKI, Opto-Electronics Review 11(4), 321-326 (2003)

[68] ***InAsN/GaAs quantum dots with an intense and narrow photoluminescence peak at 1.3 μm***, Y.D. JANG, J.S. YIM, U.H. LEE, D. LEE, J.W. JANG, K.H. PARK, W.G. JEONG, J.H. LEE, D.K. OH, Physica E17, 127-128 (2003)

[69] ***MOCVD growth of InAsN for infrared applications***, H. NAOI, Y. NAOI, S. SAKAI, Solid State Electronics volume 41 number 2, 319-321 (1997)

[70] ***Growth of InNAs by low-pressure metalorganic chemical vapor deposition employing microwave-cracked nitrogen and in situ generated arsine radicals***, H. NAOI, D.M. SHAW, Y. NAOI, G.J. COLLINS, S. SAKAI, Journal of Crystal Growth 222, 511-517 (2001)

[71] ***Growth of InNAs on GaAs (1 0 0) substrates by molecular-beam epitaxy***, S. SAKAI, T.S. CHENG, T.C. FOXON, T. SUGAHURA, Y. NAOI, H. NAOI, Journal of Crystal Growth 189/190, 471-475 (1998)

[72] ***Microstructure and composition of InAsN alloys grown by plasma-source molecular beam epitaxy***, R. BERESFORD, K.S. STEVENS, A.F. SCHWARTZMAN, Journal of Vacuum Science and Technology B 16(3), 1293-1296 (1998)

[73] ***Growth of InAsN/InGaAs(P) quantum wells on InP by gas source molecular beam epitaxy***, J.S. WANG, H.H. LIN, L.W. SONG, G.R. CHEN, Journal of Vacuum Science and Technology B 19(1), 202-206 (2001)

[74] ***Bulk InAsN films grown by plasma-assisted gas source molecular beam epitaxy***, D.K. SHIH, H.H. LIN, L.W. SONG, T.Y. CHU, T.R. YANG, 2001 International Conference on Indium Phosphide and Related Materials, Conference Proceedings, 555-558 (2001)

[75] ***$InAs_{0.97}N_{0.03}$/InGaAs/InP multiple quantum well lasers with emission wavelength $\lambda = 2.38$ μm***, D.K. SHIH, H.H. LIN, Y.H. LIN, Electronics Letters volume 37 number 22, 1342-1343 (2001)

[76] ***Tight-binding calculation of electronic structures of InNAs ordered alloys***, T. YANG, S. NAKAJIMA, S. SAKAI, Japanese Journal of Applied Physics volume 36 part 2 number 3B, L320-L322 (1997)

[77] ***GaInNAs : a novel material for long-wavelength-range laser diodes with excellent high-temperature performance***, M. KONDOW, K. UOMI, A. NIWA, T. KITATANI, S. WATAHIKI, Y. YAZAWA, Japanese Journal of Applied Physics volume 35, 1273-1275 (1996)

[78] ***Photoluminescence study of hydrogen passivation in $InAs_{1-x}N_x$/InGaAs single-quantum well on InP***, Y.Y. KE, M.H. YA, Y.F. CHEN, J.S. WANG, H.H. LIN, Applied Physics Letters volume 80 number 19, 3539-3541 (2002)

[79] ***Shubnikov-de Haas oscillations of two-dimensional electron gas in an InAsN/InGaAs single quantum well***, D.R. HANG, C.F. HUANG, W.K. HUNG, Y.H. CHANG, J.C. CHEN, H.C. YANG, Y.F. CHEN, D.K. SHIH, T.Y. CHU, H.H. LIN, Semiconductor Science and Technology (17), 999-1003 (2002)

[80] ***Large effective mass enhancement of the $InAs_{1-x}N_x$ alloys in the dilute limit probed by Shubnikov-de Haas oscillations***, D.R. HANG, D.K. SHIH, C.F. HUANG, W.K. HUNG, Y.H. CHANG, Y.F. CHEN, H.H. LIN, Physica E22, 308-311 (2004)

[81] ***Hall effect measurement of InAsN alloy films grown directly on GaAs(001) substrates by RF-MBE***, M. KURODA, R. KATAYAMA, S. NISHIO, K. ONABE, Y. SHIRAKI, Physica Status Solidi (c) 0 number 7, 2765-2768 (2003)

[82] ***RF-MBE growth of InAsN layers on GaAs (0 0 1) substrates using a thick InAs buffer layer***, S. NISHIO, A. NISHIKAWA, R. KATAYAMA, K. ONABE, Y. SHIRAKI, Journal of Crystal Growth 251, 422-426 (2003)

[83] ***Optical characterization of InAsN single quantum wells grown by RF-MBE***, M. KURODA, R. KATAYAMA, K. ONABE, Y. SHIRAKI, Physica Status Solidi (b) 241 number 12, 2791-2794 (2004)

[84] ***MBE growth of InAsN on (100) InAs substrates,*** V. SALLET, L. LARGEAU, O. MAUGUIN, L. TRAVERS, J. C. HARMAND, Physica Status Solidi (b) 242 No. 6, R43- R45 (2005)

[85] ***Photoluminescence spectroscopy of bandgap reduction in dilute InNAs alloys***, T.D. VEAL, L.F.J. PIPER, P.H. JEFFERSON, I. MAHBOOB, C.F. MCCONVILLE, M. MERRICK, T.J.C. HOSEA, B.N. MURDIN, M. HOPKINSON, Applied Physics Letters 87, 182114-1 - 182114-3 (2005)

[86] ***Nitridation of InAs(1 0 0) surface in a flowing NH3 : formation of InNAs ?***, A. YAMAMOTO, T. SHIN-YA, T. SUGIURA, M. OHKUBO, A. HASHIMOTO, Journal of Crystal Growth 189/190, 476-480 (1998)

[87] ***Auger investigation of group III nitride films grown by molecular beam epitaxy***, S.V. NOVIKOV, C.T. FOXON, T.S. CHENG, T.L. TANSLEY, J.W. ORTON, D.E. LACKLISON, D. JOHNSTON, N. BABA-ALI, S.E. HOOPER, L.C. JENKINS, L. EAVES, Journal of Crystal Growth 146, 340-343 (1995)

[88] ***Nitrogen-induced enhancement of the electron effective mass in InN_xAs_{1-x}***, W.K. HUNG, K.S. CHO, M.Y. CHEM, Y.F. CHEN, D.K. SHIH, H.H. LIN, C.C. LU, T.R. YANG, Applied Physics Letters volume 80 number 5, 796-798 (2002)

[89] ***Growth and postgrowth rapid thermal annealing of InAsN/InGaAs single quantum well on InP grown by gas source molecular beam epitaxy***, J.S. WANG, H.H. LIN, Journal of Vacuum Science and Technology B 17(5), 1997-2000 (1999)

[90] ***Strained InAsN/InGaAs/InP multiple quantum well structures grown by RF-plasma assisted GSMBE for mid-infrared laser applications***, D.K. SHIH, H.H. LIN, Y.H. LIN, IEEE Proceedings-Optoelectronics volume 150 number 3, 253-258 (2003)

[91] ***MOVPE growth of strained InGaAsN/GaAs quantum wells***, H. SAITO, T. MAKIMOTO, N. KOBAYASHI, Journal of Crystal Growth 195, 416-420 (1998)

[92] ***Microscopic mechanisms of surface phase transitions on InAs (001)***, F. GROSSE, W. BARVOSA-CARTER, J.J. ZINCK, M.F. GYURE, Physical Review B 66, 075321-1 - 075321-7 (2002)

[93] ***Excitonic photoluminescence in high-purity InAs MBE epilayers on GaAs substrates***, P.J.P. TANG, C.C. PHILLIPS, R.A. STRADLING, Semiconductor Science and Technology 8, 2135-2142 (1993)

[94] ***The anomalous bandgap bowing in GaAsN***, U. TISCH, E. FINKMAN, J. SALZMAN, Applied Physics Letters volume 81 number 3, 463-465 (2002)

[95] ***Origin of improved luminescence efficiency after annealing of Ga(In)NAs materials grown by molecular-beam epitaxy***, W. LI, M. PESSA, T. AHLGREN, J. DECKER, Applied Physics Letters volume 79 number 8, 1094-1096, (2001)

[96] ***Structural changes during annealing of GaInAsN***, S. KURTZ, J. WEBB, L. GEDVILAS, D. FRIEDMAN, J. GEISZ, J. OLSON, R. KING, D. JOSLIN, N. KARAM, Applied Physics Letters volume 78 number 6, 748-750 (2001)

[97] ***Effects of rapid thermal annealing conditions on GaInNAs band gap blueshift and photoluminescence intensity***, V. LIVERINI, A. RUTZ, U. KELLER, S. SCHÖN, Journal of Applied Physics 99, 113103-1 - 113103-7 (2006)

[98] ***Mechanism for rapid thermal annealing improvements in undoped GaN_xAs_{1-x}/GaAs structures grown by molecular beam epitaxy***, I.A. BUYANOVA, G. POZINA, P.N. HAI, N.Q. THINH, J.P. BERGMAN, W.M. CHEN, H.P. XIN, C.W. TU, Applied Physics Letters volume 77 number 15, 2325-2327 (2000)

[99] ***Effects of rapid thermal annealing on GaInNAs/GaAs multiple quantum wells***, H.P. XIN, K.L. KAVANAGH, M. KONDOW, C.W. TU, Journal of Crystal Growth 201/202, 419-422 (1999)

[100] ***Analysis and optimization of the annealing mechanisms in (In)GaAsN on GaAs***, W.K. CHEAH, W.J. FAN, S.F. YOON, B.S. MA, T.K. NG, R. LIU, A.T.S. WEE, Semiconductor Science and Technology 21, 808-812 (2006)

[101] ***Photoluminescence of rapid-thermal annealed Mg-doped GaN films***, L.S. WANG, W.K. FONG, K.W.CHEAH, W.H. ZHENG, Z.G. WANG, Solid-State Electronics 45, 1153-1157 (2001)

[102] ***Incorporation of nitrogen in nitride-arsenides : origin of improved luminescence efficiency after anneal***, S.G. SPRUYTTE, C.W. COLDREN, J.S. HARRIS, W. WAMPLER, P. KRISPIN, K. PLOOG, M.C. LARSON, Journal of Applied Physics volume 89 number 8, 4401-4406 (2001)

[103] ***Investigations on GaInNAsSb quinary alloy for 1.5 mm laser emission on GaAs***, L.H. LI, V. SALLET, G. PATRIARCHE, L. LARGEAU, S. BOUCHOULE, L. TRAVERS, J.C. HARMAND, Applied Physics Letters volume 83 number 7, 1298-1300 (2003)

[104] ***The opportunities, successes and challenges for GaInNAsSb***, J.S. HARRIS JR., Journal of Crystal Growth 278, 3–17 (2005)

[105] ***Surfactant effect on the surface diffusion length in epitaxial growth***, J. MASSIES, N. GRANDJEAN, Physical Review B volume 48 number 11, 8502-8505 (1993)

[106] ***The role of Sb in the MBE growth of (GaIn)(NAsSb)***, K. VOLZ, V. GAMBIN, W. HA, M.A. WISTEY, H. YUEN, S. BANK, J. S. HARRIS, Journal of Crystal Growth 251, 360-366 (2003)

[107] ***InAsSbN quantum well laser diodes operating at 2-µm-wavelength region grown on InP substrates***, Y. KAWAMURA, T. NAKAGAWA, N. INOUE, Japanese Journal of Applied Physics volume 44 number 35, L1112-L1114 (2005)

[108] ***Properties of InAsSbN quantum well laser diodes operating at 2 µm wavelength region grown on InP substrates***, Y. KAWAMURA, N. INOUE, Journal of Crystal Growth 301-302, 963-966 (2007)

[109] ***Mid-infrared luminescence of an InNAsSb/InAs single quantum well grown by molecular beam epitaxy***, H.B. YUEN, S.M. KIM, F. HATAMI, J.S. HARRIS, A.H. CHIN, Applied Physics Letters volume 89, 121912-1 - 121912-3 (2006)

[110] ***InNAsSb single crystals with cutoff wavelength of 11-13.5 µm grown by melt epitaxy***, Y.Z. GAO, T. YAMAGUCHI, X.Y. GONG, H. KAN, M. AOYAMA, N. DAI, Japanese Journal of Applied Physics volume 42, 4203-4206 (2003)

[111] ***How molecular beam epitaxy (MBE) began and its projection into the future***, A.Y. CHO, Journal of Crystal Growth 201/202, 1-7 (1999)

[112] www.svta.com

[113a] http://www.veeco.com/library/resources_view_sub.php?id=26
[113b] http://www.veeco.com/pdfs.php/264

[114] http://www.wafertech.co.uk/sourcematerials.htm

[115] Structural properties of semiconductors, Chapter 1 in *Electronic and Optoelectronic Properties of Semiconductor Structures*, J. SINGH, Cambridge University Press (2003)

[116] An introduction to MBE growth, A. ANSELM, University of Texas at Austin website, http://www.ece.utexas.edu/projects/ece/mrc/groups/street_mbe/mbechapter.html, (1997)

[117] ***Surface reconstruction phase diagrams for InAs, AlSb, and GaSb***, A.S. BRACKER, M.J. YANG, B.R. BENNETT, J.C. CULBERTSON, W.J. MOORE, Journal of Crystal Growth 220, 384-392 (2000)

[118] ***Enabling electron diffraction as a tool for determining substrate temperature and surface morphology***, V.P. LABELLA, D.W. BULLOCK, C. EMERY, Z. DING, P.M. THIBADO, Applied Physics Letters volume 79 number 19, 3065-3067 (2001)

[119] ***Dynamics of film growth of GaAs by MBE from RHEED observations***, J.H. NEAVE, B.A. JOYCE, P.J. DOBSON, N. NORTON, Applied Physics A : Solid and Surfaces volume 31, 1-8 (1983)

[120] ***High nitrogen incorporation in GaAsN epilayers grown by chemical beam epitaxy using radio-frequency plasma source***, M.A. PINAULT, A. FREUNDLICH, J.A.H. COAQUIRA, A. FOTKATZIKIS, Journal of Applied Physics 98, 023522-1 - 023522-4 (2005)

[121] ***Optical quality of GaNAs and GaInNAs and its dependence on RF cell condition in chemical beam epitaxy***, T. KAGEYAMA, T. MIYAMOTO, S. MAKINO, F. KOYAMA, K. IGA, Journal of Crystal Growth 209, 350-354 (2000)

[122] ***Nitrogen species from radio frequency plasma sources used for molecular beam epitaxy growth of GaN***, A.V. BLANT, O.H. HUGHES, T.S. CHENG, S.V. NOVIKOV, C.T. FOXON, Plasma Sources Sci. Technol. 9, 12-17(2000)

[123] ***Nitrogen plasma optimization for high-quality dilute nitrides***, M.A. WISTEY, S.R. BANK, H.B. YUEN, H. BAE, J.S. HARRIS JR., Journal of Crystal Growth 278 (2005) 229-233

[124] *Dilute nitride semiconductors*, ed. M. HENINI, Elsevier (2005)

[125] ***GaN growth by a controllable RF-excited nitrogen source***, J.M. VAN HOVE, G.J. COSIMINI, E. NELSON, A.M. WOWCHAK, P.P. CHOW, Journal of Crystal Growth 150, 908-911 (1995)

[126] ***RF plasma investigations for plasma-assisted MBE growth of (Ga,In)(As,N) materials***, H. CARRÈRE, A. ARNOULT, A. RICARD, E. BEDEL-PEREIRA, Journal of Crystal Growth 243, 295-301 (2002)

[127] ***Spatial Correlations in GaInAsN Alloys and their Effects on Band-Gap Enhancement and Electron Localization***, K. KIM, A. ZUNGER, Physical Review Letters volume 86 number 12, 2609-2612 (2001)

[128] *Crystals and X-rays*, H.S. Lipson, The Wykeham Science Series, Wykeham Publications (London) (1970)

[129] *Bede QC200 Double crystal diffractometer – Operations manual version 1.00*, T. LAFFORD, Bede Scientific Instruments Ltd. (2000)

[130] Photoluminescence in analysis of surfaces and interfaces, T.H. GFROERER, in *Encyclopaedia of Analytical Chemistry*, edited by R.A. MEYERS, John Wiley & Sons Ltd, Chichester, 9209-9231 (2000)

[131] ***A method of measuring specific resistivity and Hall effect of discs of arbitrary shape***, L.J. VAN DER PAUW, Philips Research Reports volume 13 number 1, 1-9 (1958)

[132] ***A method of measuring the resistivity and Hall coefficient on lamellae of arbitrary shape***, L.J. VAN DER PAUW, Philips Technical Review volume 20 number 8, 220-224 (1958), see http://www.ecse.rpi.edu/~schubert/More-reprints/

[133] ***Theory of an experiment for measuring the mobility and density of carriers in the space-charge region of a semiconductor surface***, R.L. PETRITZ, Physical Review volume 110 number 6, 1254-1262 (1958)

[134] ***Characterisation of III-V semiconductor materials by Van der Pauw's method***, J. RICHARDSON, Lancaster University M.Sc. dissertation (1994)

[135] http://physchem.ox.ac.uk/MSDS/

[136] ***Infrared photoluminescence of InAs epilayers grown on GaAs and Si substrates***, R.D. GROBER, H.D. DREW, J.I. CYI, S. KALEM, H. MORKOÇ, Journal of Applied Physics 65 (10), 4079-4081 (1989)

[137] ***Low-temperature photoluminescence of epitaxial InAs***, Y. LACROIX, C.A. TRAN, S.P. WATKINS, M.L.W. THEWALT, Journal of Applied Physics volume 80 number 11, 6416-6424 (1996)

[138] ***Midinfrared photoluminescence of InAsSb quantum dots grown by liquid phase epitaxy***, A. KRIER, X.L. HUANG, A. HAMMICHE, Applied Physics Letters volume 77 number 23, 3791-3793 (2000)

[139] ***Mechanisms of nitrogen incorporation in GaAsN alloys***, M. REASON, H.A. MCKAY, W. YE, S. HANSON, R.S. GOLDMAN, V. ROTBERG, Applied Physics Letters volume 85 number 10, 1692-1694 (2004)

[140] ***Mechanism for low-temperature photoluminescence in GaNAs/GaAs structures grown by molecular-beam epitaxy***, I.A. BUYANOVA, W.M. CHEN, G. POZINA, J.P. BERGMAN, B. MONEMAR, H.P. XIN, C.W. TU, Applied Physics Letters volume 75 number 4, 501-503 (1999)

[141] ***Hydrogen-induced improvements in optical quality of GaNAs alloys***, I.A. BUYANOVA, M. IZADIFARD, W.M. CHEN, A. POLIMENI, M. CAPIZZI, H.P. XIN, C.W. TU, Applied Physics Letters volume 82 number 21, 3662-3664 (2003)

[142] ***Enhanced optical and structural properties of 1.3 mm GaInNAs/GaAs multiple quantum-well heterostructures with stepped strain-mediating layers***, H.Y. LIU, W.M. SOONG, P. NAVARETTI, M. HOPKINSON, J.P.R. DAVID, Applied Physics Letters volume 86, 062107-1 - 062107-3 (2005)

[143] ***Improving optical properties of 1.55 um GaInNAs/GaAs multiple quantum wells with Ga(In)NAs barrier and space layer***, H.Y. LIU, M. HOPKINSON, P. NAVARETTI, M. GUTIERREZ, J.S. NG, J.P.R. DAVID, Applied Physics Letters volume 83 number 24, 4951-4953 (2003)

[144] ***Effects of insertion of strain-mediating layers on luminescence properties of 1.3-μm GaInNAs/GaNAs/GaAs quantum-well structures***, E.M. PAVELESCU, C.S. PENG, T. JOUHTI, J. KONTTINEN, W. LI, M. PESSA, M. DUMITRESCU, S. SPÂNULESCU, Applied Physics Letters volume 80 number 17, 3054-3056 (2002)

[145] ***Time-resolved photoluminescence studies of $In_xGa_{1-x}As_{1-y}N_y$***, R.A. MAIR, J.Y. LIN, H.X. JIANG, E.D. JONES, A.A. ALLERMAN, S.R. KURTZ, Applied Physics Letters volume 76 number 2, 188-190 (2000)

[146] ***Effect of nitrogen on the temperature dependence of the energy gap in $In_xGa_{1-x}As_{1-y}N_y$/GaAs single quantum wells***, A. POLIMENI, M. CAPIZZI, M. GEDDO, M. FISCHER, M. REINHARDT, A. FORCHEL, Physical Review B volume 63, 195320-1 - 195320-5 (2001)

[147] ***A photoluminescence study of polycrystalline thin-film CdTe/CdS solar cells***, D.P. HALLIDAY, J.M. EGGLESTON, K. DUROSE, Journal of Crystal Growth 186, 543-549 (1998)

[148] ***Photoluminescence study of MBE grown InGaN with intentional indium segregation***, M.C. CHEUNG, G. NAMKOONG, F. CHEN, M. FURIS, H.E. PUDAVAR, A.N. CARTWRIGHT, W.A. DOOLITTLE, Physica Status Solidi (c) 2 number 7, 2779-2782 (2005)

[149] ***Unusual carrier thermalization in a dilute $GaAs_{1-x}N_x$ alloy***, P.H. TAN, Z.Y. XU, X.D. LUO, W.K. GE, Y. ZHANG, A. MASCARENHAS, H.P. XIN, C.W. TU, Applied Physics Letters 90, 061905-1 - 061905-3 (2007)

[150] ***Excitation-power dependence of the near-band-edge photoluminescence of semiconductors***, T. SCHMIDT, K. LISCHKA, W. ZULEHNER, Physical Review B volume 45 number 16, 8989-8994 (1992)

[151] ***On the nature of radiative recombination in GaAsN***, B.Q. SUN, M. GAL, Q. GAO, H.H. TAN, C. JAGADISH, Applied Physics Letters volume 81 number 23, 4368-4370 (2002)

[152] ***Effect of temperature on the optical properties of (InGa)(AsN)/GaAs single quantum wells***, A. POLIMENI, M. CAPIZZI, M. GEDDO, M. FISCHER, M. REINHARDT, A. FORCHEL, Applied Physics Letters volume 77 number 18, 2870-2872 (2000)

[153] ***Optical characteristics of 1.55 mm GaInNAs multiple quantum wells***, H.D. SUN, A.H. CLARK, H.Y. LIU, M. HOPKINSON, S. CALVEZ, M.D. DAWSON, Y.N. QIU, J.M. RORISON, Applied Physics Letters volume 85 number 18, 4013-4015 (2004)

[154] ***Photoluminescent properties and optical absorption of AlAs/GaAs disordered superlattices***, T. YAMAMOTO, M. KASU, S. NODA, A. SASAKI, Journal of Applied Physics volume 68 number 10, 5318-5323 (1990)

[155] ***''S-shaped'' temperature-dependent emission shift and carrier dynamics in InGaN/GaN multiple quantum wells***, Y.H. CHO, G.H. GAINER, A.J. FISCHER, J.J. SONG, S. KELLER, U.K. MISHRA, S.P. DENBAARS, Applied Physics Letters volume 73 number 10, 1370-1372 (1998)

[156] ***Evidence of strong carrier localization below 100 K in a GaInNAs/GaAs single quantum well***, L. GRENOUILLET, C. BRU-CHEVALLIER, G. GUILLOT, P. GILET, P. DUVAUT, C. VANNUFFEL, A. MILLION, A. CHENEVAS-PAULE, Applied Physics Letters volume 76 number 16, 2241-2243 (2000)

[157] ***Recombination mechanisms in GaInNAs/GaAs multiple quantum wells***, A. KASCHNER, T. LUTTGERT, H. BORN, A. HOFFMANN, A.YU. EGOROV, H. RIECHERT, Applied Physics Letters volume 78 number 10, 1391-1393 (2001)

[158] ***Dynamics of anomalous optical transitions in $Al_xGa_{1-x}N$ alloys***, Y.H. CHO, G.H. GAINER, J.B. LAM, J.J. SONG, W. YANG, W. JHE, Physical Review B volume 61 number 11, 7203-7206 (2000)

[159] ***Incorporation of N into GaAsN under N overpressure and underpressure conditions***, S. ZHONGZHE, Y.S. FATT, Y.K. CHUIN, L.W. KHAI, F. WEIJUN, W. SHANZHONG, N.T. KHEE, Journal of Applied Physics volume 94 number 2, 1069-1073 (2003)

[160] ***Nitrogen-plasma study for plasma-assisted MBE growth of 1.3 μm laser diodes***, H. CARRÈRE, A. ARNOULT, A. RICARD, X. MARIE, TH. AMAND, E. BEDEL-PEREIRA, Solid-State Electronics 47, 419-423 (2003)

[161] ***Nitrogen incorporation in group III-nitride-arsenide materials grown by elemental source molecular beam epitaxy***, S.G. SPRUYTTE, M.C. LARSON, W. WAMPLER, C.W. COLDREN, H.E. PETERSEN, J.S. HARRIS, Journal of Crystal Growth 227-228, 506-515 (2001)

[162] ***MBE growth of high-quality GaAsN bulk layers***, J.S. WANG, A.R. KOVSH, L. WEI, J.Y. CHI, Y.T. WU, P.Y. WANG, V.M. USTINOV, Nanotechnology 12, 430-433 (2001)

[163] ***Role of N ions in the optical and morphological properties of InGaAsN quantum wells for 1.3-1.5 μm applications***, J. MIGUEL-SÁNCHEZ, A. GUZMÁN, E. MUÑOZ, Applied Physics Letters volume 85 number 11, 1940-1942 (2004)

[164] ***Very low threshold current density 1.3 μm GaInNAs single-quantum well lasers grown by molecular beam epitaxy***, S.M. WANG, Y.Q. WEI, X.D. WANG, Q.X. ZHAO, M. SADEGHI, A. LARSSON, Journal of Crystal Growth 278, 734-738 (2005)

[165] ***Kinetic modeling of N incorporation in GaInNAs growth by plasma-assisted molecular-beam epitaxy***, Z. PAN, L.H. LI, W. ZHANG, Y.W. LIN, R.H. WU, Applied Physics Letters volume 77 number 2, 214-216 (2000)

[166] ***Nitrogen incorporation into GaAs(N), $Al_{0.3}Ga_{0.7}As(N)$ and $In_{0.15}Ga_{0.85}As(N)$ by chemical beam epitaxy (CBE) using 1,1-dimethylhydrazine***, J.O. MACLEAN, D.J. WALLIS, T. MARTIN, M.R. HOULTON, A.J. SIMONS, Journal of Crystal Growth 231, 31-40 (2001)

[167] *Group III nitride semiconductor compounds - Physics and Applications*, edited by B. GIL, Oxford Science Publications, Clarendon Press (1998) ; chapter 2

[168] ***Influence of alloy stability on the photoluminescence properties of GaAsN/GaAs quantum wells grown by molecular beam epitaxy***, M.A. PINAULT, E. TOURNIÉ, Applied Physics Letters volume 79 number 21, 3404-3407 (2001)

[169] ***Kinetic modeling of microscopic processes during electron cyclotron resonance microwave plasma-assisted molecular beam epitaxial growth of GaN/GaAs-based heterostructures***, Z.Z. BANDIĆ, R.J. HAUENSTEIN, M.L. O'STEEN, T.C. MCGILL, Applied Physics Letters volume 68 number 11, 1510-1512 (1996)

[170] ***Formation and dissolution of InAs quantum dots on GaAs***, CH. HEYN, D. ENDLER, K. ZHANG, W. HANSEN, Journal of Crystal Growth 210, 421-428 (2000)

[171] *Near-infrared photodetectors based on Si/SiGe nanostructures*, A. ELFVING, doctoral thesis, Department of Physics, Chemistry and Biology, Linköping University, Sweden (2006) www.diva-portal.org/diva/getDocument?urn_nbn_se_liu_diva-5909-1__fulltext.pdf

[172] ***Nitrogen incorporation in GaNAs layers grown by molecular beam epitaxy***, Q.X. ZHAO, S.M. WANG, M. SADEGHI, A. LARSSON, M. FRIESEL, M. WILLANDER, Applied Physics Letters 89, 031907-1 - 031907-3 (2006)

[173] ***Thermodynamic Analysis of the Growth of GaAsN Ternary Compounds by Molecular Beam Epitaxy***, V.A. ODNOBLYUDOV, A.R. KOVSH, A.E. ZHUKOV, N.A. MALEEV, E.S. SEMENOVA, V.M. USTINOV, Semiconductors volume 35 number 5, 533-538 (2001)

[174] ***Nitrogen incorporation rate, optimal growth temperature, and AsH_3-flow rate in GaInNAs growth by gas-source MBE using N-radicals as an N-source***, T. KITATANI, M. KONDOW, K. NAKAHARA, M.C. LARSON, Y. YAZAWA, M. OKAI, K. UOMI, Journal of Crystal Growth 201/202, 351-354 (1999)

[175] ***Thermodynamic analysis of the MBE growth of GaInAsN***, V.A. ODNOBLYUDOV, A.YU. EGOROV, A.R. KOVSH, A.E. ZHUKOV, N.A. MALEEV, E.S. SEMENOVA, V.M. USTINOV, Semiconductor Science and Technology 16, 831-835 (2001)

[176] ***Optical properties of as-grown and annealed InAs(N)/InGaAsP strained multiple quantum wells***, G.R. CHEN, H.H. LIN, J.S. WANG, D.K. SHIH, Journal of Applied Physics volume 90 number 12, 6230-6235 (2001)

[177] ***The HITRAN 2004 molecular spectroscopic database***, L.S. ROTHMAN, D. JACQUEMART, A. BARBE, D. CHRIS BENNER, M. BIRK, L.R. BROWN, M.R. CARLEER, C. CHACKERIAN JR., K. CHANCE, L.H. COUDERT, V. DANA, V.M. DEVI, J.M. FLAUD, R.R. GAMACHE, A. GOLDMAN, J.M. HARTMANN, K.W. JUCKS, A.G. MAKI, J.Y. MANDIN, S.T. MASSIE, J. ORPHAL, A. PERRIN, C.P. RINSLAND, M.A.H. SMITH, J. TENNYSON, R.N. TOLCHENOV, R.A. TOTH, J. VANDER AUWERA, P. VARANASI, G. WAGNER, Journal of Quantitative Spectroscopy & Radiative Transfer 96, 139-204 (2005)

[178] ***Room Temperature Photoluminescence at 4.5 μm from InAsN***, Q. ZHUANG, A.M.R. GODENIR, A. KRIER, K.T. LAI, S. K. HAYWOOD, Journal of Applied Physics 103, 063520-1 - 063520-4 (2008)

[179] Photoluminescence in InAsN epilayers grown by molecular beam epitaxy, Q. ZHUANG, A. GODENIR, A. KRIER, Journal of Physics D : Applied Physics 41, 132002-1 - 132002-4

[180] Photoluminescence theory, H.B. BEBB, E.W. WILLIAMS, in *Semiconductors and Semimetals*, ed. R.K. WILLARDSON, A.C. BEER, Academic Press (London) volume 8 chapter 4, p.238 (1972)

[181] *Semiconductor lasers and heterojunction LEDs*, H. KRESSEL, J.K. BUTLER, Academic Press (London), chapter 1 (1977)

[182] ***Metal organic vapor phase epitaxy growth of GaAsN on GaAs using dimethylhydrazine and tertiarybutylarsine***, A. OUGAZZADEN, Y. LE BELLEGO, E.V.K. RAO, M.JUHEL, L. LEPRINCE, G. PATRIARCHE, Applied Physics Letters volume 70 number 21, 2861-2863 (1997)

[183] ***Chemical bonding of nitrogen in dilute InAsN and high In-content GaInAsN***, D.N. TALWAR, Physica Status Solidi (c) volume 4 number 2, 674- 677 (2007)

[184] *Fabrication and optimisation of novel infrared detectors*, W. SULEIMAN, doctoral thesis, Physics Department, Lancaster University, chapter 5 (2007)

[185] ***Growth and structural characterization of III-N-V semiconductor alloys***, I. SUEMUNE, K. UESUGI, T.Y. SEONG, Semiconductor Science and Technology 17, 755-761 (2002)

[186] ***Band structure and optical properties of $In_yGa_{1-y}As_{1-x}N_x$ alloys***, C. SKIERBISZEWSKI, P. PERLIN, P. WISNIEWSKI, T. SUSKI, J.F. GEISZ, K. HINGERL, W. JANTSCH, D.E. MARS, W. WALUKIEWICZ, Physical Review B volume 65, 035207-1 - 035207-10 (2001)

[187] ***Experimental studies of the conduction-band structure of GaInNAs alloys***, C. SKIERBISZEWSKI, Semiconductor Science and Technology 17, 803-814 (2002)

[188] ***Theory of enhanced bandgap non-parabolicity in GaN_xAs_{1-x} and related alloys***, A. LINDSAY, E.P. O'REILLY, Solid State Communications 112, 443-447 (1999)

[189] ***Boundary conditions for the electron wavefunction in GaInNAs-based quantum wells and modelling of the temperature-dependent bandgap***, M. HETTERICH, A. GRAU, A.YU. EGOROV, H. RIECHERT, Journal of Physics : Condensed Matter 16, S3151-S3159 (2004)

[190] ***Influence of Sb, Bi, Tl, and B on the incorporation of N in GaAs***, F. DIMROTH, A. HOWARD, J. K. SHURTLEFF, G. B. STRINGFELLOW, Journal of Applied Physics volume 91 number 6, 3687-3692 (2002)

[191] ***Comparison of nitrogen incorporation in molecular-beam epitaxy of GaAsN, GaInAsN, and GaAsSbN***, J.C. HARMAND, G. UNGARO, L. LARGEAU, G. LE ROUX, Applied Physics Letters volume 77 number 16, 2482-2484 (2000)

[192] ***Photo-electronic properties of $InAs_{0.07}Sb_{0.93}$ films***, H.H. WIEDER, A.R. CLAWSON, Thin Solid Films volume 15 issue 2, 217-221 (1973)

[193] ***Growth of high quality InGaAsN heterostructures and their laser application***, A.YU. EGOROV, D. BERNKLAU, B. BORCHERT, S. ILLEK, D. LIVSHITS, A. RUCKI, M. SCHUSTER, A. KASCHNER, A. HOFFMANN, GH. DUMITRAS, M.C. AMANN, H. RIECHERT, Journal of Crystal Growth 227-228, 545-552 (2001)

[194] ***Photoluminescence of MBE-grown $InAs_{1-x}Sb_x$ lattice mismatched to GaAs***, S. ELIES, A. KRIER, I.R. CLEVERLEY, K. SINGER, Journal of Applied Physics D issue 26, 159-162 (1993)

[195] *Light Emitting Diodes*, E.F. SCHUBERT, second edition, Cambridge University Press (2006)
http://www.ecse.rpi.edu/~schubert/Light-Emitting-Diodes-dot-org/chap04/chap04.htm

[196] *Epitaxial growth and fabrication of mid-infrared photodetectors for use in gas sensors*, H.H. GAO, doctoral thesis, Physics Department, Lancaster University (1999)
[196a] Chapter 7 : The investigation of $InGa_{0.97}As_{0.03}/InAs_{0.36}Sb_{0.20}P_{0.44}$
[196b] Chapter 8 : The investigation of 4.6 µm photodetectors and light emitting diodes

[197] ***Electrical measurements on semiconductor materials***, C. MELLOR, Experimental Techniques of Semiconductor Research, Institute of Physics Conference, Nottingham (2005)

[198] *Introduction to semiconductors* (Introduction aux semiconducteurs), S. MOTTET, E.N.S.S.A.T. course notes, OPT2 (2002)

[199] Material and device evaluation technique, appendix 1 in *An introduction to semiconductor microtechnology*, second edition, D.V. MORGAN, K. BOARD, John Wiley and Sons, Chichester (1983)

[200] *The electrical characterization of semiconductors*, J.W. ORTON, P. BLOOD, Academic Press, 97 (1992)

"*An expert is a man who has made all the mistakes, which can be made, in a very narrow field.*"

Niels Bohr